MECHANICAL ENGINEERING SERIES

P.A. Lakshminarayanan
Yogesh V. Aghav

Modelling Diesel Combustion

Springer

Modelling Diesel Combustion

Mechanical Engineering Series

Frederick F. Ling
Editor-in-Chief

The Mechanical Engineering Series features graduate texts and research monographs to address the need for information in contemporary mechanical engineering, including areas of concentration of applied mechanics, biomechanics, computational mechanics, dynamical systems and control, energetics, mechanics of materials, processing, production systems, thermal science, and tribology.

Advisory Board/Series Editors

Applied Mechanics	F.A. Leckie University of California, Santa Barbara
	D. Gross Technical University of Darmstadt
Biomechanics	V.C. Mow Columbia University
Computational Mechanics	H.T. Yang University of California, Santa Barbara
Dynamic Systems and Control/ Mechatronics	D. Bryant University of Texas at Austin
Energetics	J.R. Welty University of Oregon, Eugene
Mechanics of Materials	I. Finnie University of California, Berkeley
Processing	K.K. Wang Cornell University
Production Systems	G.-A. Klutke Texas A&M University
Thermal Science	A.E. Bergles Rensselaer Polytechnic Institute
Tribology	W.O. Winer Georgia Institute of Technology

For other titles published in this series, go to
http://www.springer.com/1161

P.A. Lakshminarayanan • Yogesh V. Aghav

Modelling Diesel Combustion

With Contributions by Yu Shi and Rolf Reitz

Springer

P.A. Lakshminarayanan
Ashok Leyland Ltd.
175, SIPCOT Industrial Complex
Hosur-635126
India
lakshminarayanan.pa@ashokleyland.com

Yogesh V. Aghav
Kirloskar Oil Engines Ltd.
L.K. Marg, Khadki
Pune-411003
India
Yogesh.Aghav@kirloskar.com

ISSN 0941-5122
ISBN 978-90-481-3884-5 e-ISBN 978-90-481-3885-2
DOI 10.1007/978-90-481-3885-2
Springer Dordrecht Heidelberg London New York

Library of Congress Control Number: 2009943995

Cover design: eStudio Calamar S.L.

Printed on acid-free paper

Springer is part of Springer Science+Business Media (www.springer.com)

Modelling Diesel Combustion

P. A. Lakshminarayanan

Yogesh V. Aghav

16 June 2009

Modelling Diesel Combustion

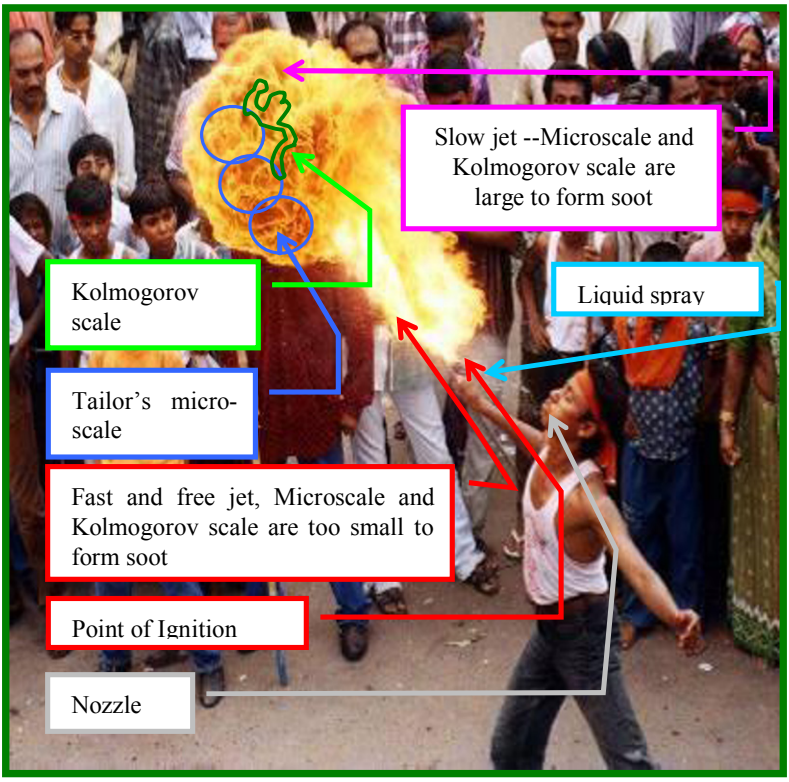

P. A. Lakshminarayanan

Yogesh V. Aghav

16 June 2009

Acknowledgments

Our work at the Indian Institutes of Technology, Madras and Delhi and at Loughborough University, and later at the industrial R&Ds of Ashok Leyland, Ltd. and Kirloskar Oil Engines, Ltd. for the last 4 decades forms the basis of the phenomenological models presented in the book. We are grateful to these great institutions for the constant encouragement and guidance we received. We express our thanks to FEV, India for their kind support during the preparation of the book.

The book is complete only with the last two chapters on the reviews and applications of modern methods of simulating diesel engines by Dr. Yu Shi and Prof. Dr. Rolf Reitz of Engine Research Centre at the University of Wisconsin, Madison. They acceded to our request spontaneously and gracefully to provide the material. We express our profound gratitude to them for showing magnanimity.

We thank our Professors Dr. B.S. Murthy, Dr. J.C. Dent, Dr. P.A. Janakiraman, Dr. M.K. Gajendra Babu and Dr. U.P. Nagpurkar, Dr. M.N. Kumar, Dr. Rainer Thiele, Mr. P.G. Bhat, and Mr. A.D. Dani for decisively influencing our formative years and subsequent research.

While writing the book, we heavily leaned on various research work carried out by us with our co-authors of papers published in many learned journals. We are indebted to them.

We thank Mr. R. Seshsayee, Ashok Leyland and Mr. R.R. Deshpande, Kirloskar Oil Engines, Ltd. for encouraging us to write this book.

We thank the Society of Automotive Engineers (SAE), American Society of Mechanical Engineers (ASME) and Institute of Mechanical Engineers, London (IMechE) for allowing us to use the figures and other material published by us in their learned journals. We thank the publishers Springer for giving us a chance to write this book.

We are thankful to our families for their support and understanding throughout the research work and the preparation of the book.

P. A. Lakshminarayanan *Yogesh V. Aghav*
June 16, 2009

Preface

Phenomenology of Diesel Combustion and Modeling

Diesel is the most efficient combustion engine today and it plays an important role in transport of goods and passengers on land and on high seas. The emissions must be controlled as stipulated by the society without sacrificing the legendary fuel economy of the diesel engines. These important drivers caused innovations in diesel engineering like re-entrant combustion chambers in the piston, lower swirl support and high pressure injection, in turn reducing the ignition delay and hence the nitric oxides. The limits on emissions are being continually reduced. Therefore, the required accuracy of the models to predict the emissions and efficiency of the engines is high. The phenomenological combustion models based on physical and chemical description of the processes in the engine are practical to describe diesel engine combustion and to carry out parametric studies. This is because the injection process, which can be relatively well predicted, has the dominant effect on mixture formation and subsequent course of combustion. The need for improving these models by incorporating new developments in engine designs is explained in Chapter 2. With "model based control programs" used in the Electronic Control Units of the engines, phenomenological models are assuming more importance now because the detailed CFD based models are too slow to be handled by the Electronic Control Units.

Experimental work is necessary to develop the basic understanding of the processes. Chapter 3 describes the experimental set up of the bomb for interferometry and real engine studies for validation of the phenomenological models. This chapter also includes the details of the measurement techniques for obtaining the experimental data needed for validating the phenomenology. Empirical relations have been obtained in Chapter 4 to describe the axial and radial variations of fuel concentration in the vaporising and burning sprays, and to evaluate penetration and air entrainment of the free and wall jet regions. The movement of the 'tail' of the spray in the post injection period has been studied. These equations form the basis for building the phenomenological models of ignition delay, emissions and heat release rate in subsequent chapters.

The norms for NO_x and HC emissions are so tight that prediction of ignition delay has become necessary. In Chapter 5, phenomenological calculations of the cooling of spray surface have shown that the physical parameters and fuel type influence the temperature of the mixture of air and the fuel vapour throughout its life up to the end of ignition delay. A model is proposed in Chapter 6 to predict rapid convective heat transfer between spray and wall by extending the analogy adopted by Woschni.

The rate of heat release in an indirect injection engine is modelled on the lines of its observed rate in a direct injection engine. The diffusion combustion is modeled as proportional to the available fuel and rate of air entrainment in Chapter 7. Chapter 8 introduces the concept of air useful for combustion. The ratio of

momentum of the useful air to the total momentum of injected fuel near TDC at the end of ignition delay period is found to bear a universal relationship with the indicated efficiency and dry soot emissions in case of combustion chambers supported by air swirl. In Chapter 9, the combustion rate is precisely described using the concept developed in Chapter 7 by relating the fuel air mixing rate to the turbulent energy created at the exit of the nozzle as a function of the injection velocity and by considering the dissipation of energy in free air and along the wall. The absence of adjustable constants distinguishes the model from the other zero-dimensional or pseudo multi-dimensional models.

Hydrocarbon (HC) emissions from direct injection diesel engines are mainly due to fuel injected and mixed beyond lean combustion limit during ignition delay and fuel effusing from the nozzle sac at low pressure. The concept has been developed in Chapter 10 to provide an elegant model to predict the HC emissions. To contrast the phenomenon of HC formation in a Diesel and in a spark ignition engine, Chapter 11 is included. The absorption and desorption of fuel by cylinder lubricating oil films has been modelled using principles of mass transfer.

A new model for smoke explained in Chapter 12 characterizes the smoke emitted at higher loads from the wall spray formed after impingement. Smoke has been treated by ignoring the fast chemistry, as the slow physical mixing seems to be controlling. A new phenomenological model for NO_x emission is developed based on mixing controlled combustion incorporating localized wall heat transfer in Chapter 13. Based on the smoke formation and oil consumption, an estimate of the particulate matter is made in Chapter 14.

Chapter 15 and 16 on the modern methods of simulating diesel engines are contributed by Dr. Yu Shi and Prof. Dr. Rolf Reitz of Engine Research Centre at the University of Wisconsin, Madison. Chapter 15 reviews the basic approach of multi-dimensional CFD modelling of diesel combustion, and focusing on the advanced turbulence and combustion models. Recent efforts for reducing the computational expense of multi-dimensional CFD modelling are also discussed. CFD tools reveal details about invisible or technically difficult or costly in-cylinder processes of diesel combustion, so that guidance can be provided to improve engine designs in terms of emissions reduction and fuel economy; innovative combustion concepts can be evaluated numerically prior to experimental tests to reduce the number of investigated parameters and thus costs; important design parameters can be discovered by modelling engines of different sizes to establish engine size-scaling relationships and thus non-dimensionalizing engine designs; by integration with optimization methodologies, CFD tools can also directly impact the design of optimum engine systems, such as piston geometry and injection parameters. Each of these aspects is described by relevant case studies in Chapter 16.

Contents

1 Introduction

Abstract The Internal Combustion (IC) engines play a dominant role in the fields of transportation of goods and passengers, agricultural and industry. They develop power by consuming precious fossil fuels and cause pollution. Among different types of engines, the direct-injection (DI) diesel engine exhibits the best fuel economy along with lowest engine-out emissions. Efforts have been put to improve exhaust emissions and fuel economy continuously. The complex task of improving IC engines, which have reached a higher degree of sophistication, can be achieved by combination of advanced experiments and computational studies. Modern methods of experimental investigations are being developed to provide more insight. The modelling of combustion engine processes is useful to carry out extensive parametric studies, rather than hardware development and experimentation. Depending on the various possible applications, different types of models for engine combustion processes have been developed. Therefore, theoretical and applied understanding of the engine processes is also developing at faster rate.

Role of Internal Combustion Engines

Rapid Increase in pollution levels, escalation of fuel prices, and depletion of hydrocarbon reserves of the world have forced the engineers to look for appropriate technology and alternative fuels to cater to the ever-increasing demands of energy. The Internal Combustion (IC) engines form an indispensable part of industrial growth. IC engines play a dominant role in the fields of propulsion, power and energy. They also contribute in our modernized agricultural sector and transportation of goods and passengers. It is impossible to do without the IC engines and hence means must be sought to improve the designs.

It has been estimated that the present fossil fuel demand is expected to double between now and 2050. At present, about two-thirds of world energy demand is met by fluid fossil fuels because of their availability and convenience of use in existing design of several prime movers such as internal combustion engines. In future, the energy scenario is likely to be several times worse than the two oil crises of 1970s. The second predicament involving the fossil fuels is the environmental damage caused by combustion of fossil fuels. Technologies for fossil fuel extraction, transportation, processing and particularly their combustion have harmful impacts on the environment. The fossil fuels which constitute carbon and hydrogen in addition to traces of sulphur and quality enhancer additives like oxygenates produce various gases, soot, ash and other organic compounds during combustion and when released into atmosphere cause degradation of air quality (Walsh 2000, Fiaz and Sturm 2000). These pollutants when mixed with water and other atmospheric

P.A. Lakshminarayanan and Y.V. Aghav, *Modelling Diesel Combustion*,
Mechanical Engineering Series, DOI 10.1007/978-90-481-3885-2_1,

compounds or triggered by sunlight, change their form and become pollutants like ozone, aerosols, peroxyacetyl nitrates, various acids causing damage to the aquatic and terrestrial ecosystem, affecting humans, animals, vegetation and structure.

In IC engines, the chemical energy of the fuel is released inside the cylinder to produce mechanical power. Spark ignited (SI) gasoline and compression ignited (CI) diesel engines are the main types of IC engines. In 1876, Otto invented SI engine and later in 1892 Diesel developed CI engine. Traditionally, SI gasoline engines are employed for light duty applications, as they are compact with simple construction for lower power range. On the other hand, CI diesel engines are for heavy-duty usage as they can develop more power at lesser fuel consumption. Different methods of fuel supply are used for CI engines, namely indirect and direct type. Out of these different types of engines, the direct-injection (DI) diesel engine exhibits the best fuel economy along with lowest engine-out emissions. Therefore, it is emerging as the engine of the future. The packing of higher power also improves the power to weight ratio to make the engine more compact. Traditionally, considered as heavy-duty, the DI diesel engines are also now capturing the in passenger car market. The best fuel economy car consuming only 3 L of fuel for 100 km is developed with the modern DI diesel engine. This trend is facilitated by the development of contemporary injection systems that are more flexible, and generate higher injection pressures for better spray atomisation and combustion characteristics than their predecessors. The modern DI diesel engines satisfy stringent emission norms of Euro III without after treatment. The DI diesel engine is now recognized as environment friendly, powerful, and smooth running (Krieger *et al*. 2000).

Developments in DI Diesel Engines

In DI diesel engines, the fuel is sprayed at higher pressure directly into the main combustion chamber where it ignites by mixing with hot air produced by isentropic compression. The stoichiometric air to fuel ratio is 14.7 for diesel fuel. However, the diesel engines work satisfactorily above air to fuel ratio of 19, i.e. always with some excess air. As the fuel is directly sprayed into the cylinder, sufficient time is not available for mixing, which results in smoke in zones of lower air to fuel ratios. The higher compression ratio is helpful in improving the efficiency of diesel engines at higher loads. They are also more economical than gasoline engines at lower loads because they can work at very lean mixtures avoiding throttling losses of charge air. Due to their lower heat losses, diesel engines have a lower risk of gradually overheating if left idling for long periods. In many applications, such as marine, agriculture and railways, diesels are left idling unattended for many hours. These advantages are especially attractive in locomotives.

A naturally aspirated diesel engine produces less power density i.e., power in a given volume, compared to gasoline engines. The power of the diesel engine is always limited by the air available. Therefore, they are often turbocharged to improve power density. The turbocharged versions can produce more power than petrol engines limited by mechanical capability. The diesel engines do not face knocking problem. A turbocharger consists of a turbine and a compressor linked by a shared axle. The turbine inlet receives exhaust gases from the engine exhaust manifold causing the turbine wheel to rotate. This rotation drives the compressor, compressing ambient air and delivering it to the intake of the engine; this allows more fuel to burn in the cylinder. At higher boost, the benefit of more air mass diminishes as the density drops substantially. Inter-cooling by using atmospheric air or engine jacket water helps to recover the density by bringing down the temperature of the charge. The charge air is not throttled in diesel engines; therefore, a governor is used to control fuel supply quantity. A sophisticated fuel supply system consisting of pumping unit, multi-hole injector and governor are employed in DI diesel engines to inject the correct amount of fuel at the required time under favourable conditions for combustion.

Early DI diesel engines operated at relatively low compression ratios and low injection pressures. Hence, they demanded very advanced injection timings in commensurate with the large ignition delay. During the ignition delay period at the beginning of combustion, up to about 20% of the injected fuel is prepared to stoichiometric proportion. Due to high flame speed, the prepared mixture burns at high temperature to produce nitrogen oxides and explosive noise characteristic of a diesel engine (Fig. 1.1). This period of combustion is said to be premixed phase governed by chemical kinetics. On the other hand, the rest of the fuel burns as and when the mixture is prepared because the delay is absent with hot gases and radicals available in the vicinity, remnant of the fuel burnt earlier. This second part is called diffusive phase and the rate of combustion of the majority of fuel is controlled by the physical mixing processes in the spray. The third or the last stage corresponds to the tail of heat release diagram in which a small but distinguishable rate of heat release persists well into the expansion stroke (Heywood 1988). Such a design was the result of the available technology and lack of norms for noise and emissions.

During last 50 years, the design of DI engines has undergone a sea change because of social and economical aspects (Bosch 2000). With the advent of new emission norms, reduction in ignition delay held the key to solve twin problems of NO_x emission and noise. Higher temperature at the beginning of injection by increased compression ratio reduced the delay period and subsequent premixed combustion phase substantially. Higher injection pressures and turbulence were introduced to improve the mixing rate and hence to maintain the combustion duration within a reasonable limit, in spite of the loss of fast burning premixed combustion process. User demands of improving fuel economy and legal requirement of reduction in emissions are driving the engine development persistently. The advancements in design are summarized in Table 1.1.

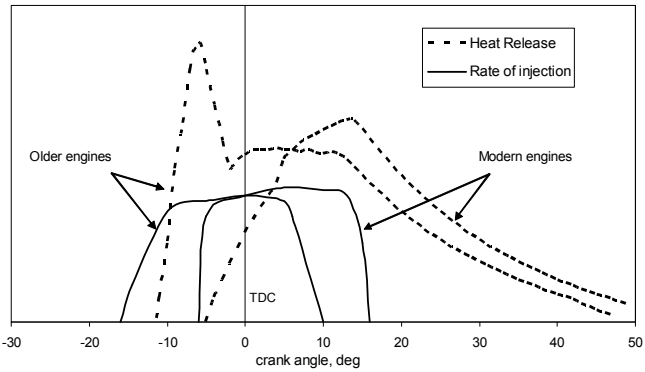

Fig. 1.1 Combustion in DI diesel engine

Table 1.1 Advancements in DI diesel engines

Period	Advancements	Events
Early 1970s	Main problems were life of engine and visible smoke	Improve design engine components, avoid secondary injection
Late 1970s to early 1980s	Improve fuel economy	Improved design of combustion chamber, valve train
Mid-1980s to early 1990s	Reduction in noise	Improved compression ratios
	Reduction in NO_x, HC, CO	Very low nozzle sac volumes or valve-closed orifice (VCO) nozzles
		Increase injection pressure capability even more, specially at lower speed
		Increase injection timing flexibility
1990–2000	Reduction in particulate	Turbo-charging, Electronic control of injection rate, injection timing
	Improving power packing	
2000–2006	Stricter emission laws, Rapid escalation and shortages of fuel	Heavy boosting and inter-cooling, Higher injection pressure, Oxygenated fuels

The DI diesel engines are regulated by government laws for gaseous emissions like HC, CO and NO_x as well as for solid emissions known as particulate matter and smoke. In diesel engines, both HC and CO emissions are a small fraction of those found in a gasoline engine. Even engine-out NO_x emissions in a diesel are less than their corresponding gasoline emissions. However, modern gasoline engines operate at a stoichiometric ratio where the three-way catalyst performs at its highest conversion efficiency resulting in extremely low HC, CO, and NOx emissions. Unfortunately, diesel exhaust is very lean and reducing NO_x in an oxygen-rich environment is a very challenging task. The catalyst industry is developing solutions like DeNOx catalyst or selective catalytic reduction (SCR) for the diesel NO_x problem. Another problematic pollutant associated with diesel engines is the particulate matter. The casual observer is made aware of this pollutant in the form of black smoke or soot emitted from either the tail pipes of many diesel-equipped

passenger cars or the stacks of diesel-powered heavy-duty vehicles. Emission of soot is also accompanied with other matter suspended in the exhaust, such as: unburned lube oil, unburned fuel, trace metals, and sulphur by-products. Emission of soot in particulate matter results from the nature of the heterogeneous combustion process or diffusion type combustion that is prevalent in diesel engines. Preparation of fuel and air mixture in modern diesel engines has greatly reduced this problem. The development of diesel particulate filters promises to eliminate it altogether.

There are a number of serious reasons for considering bio-fuels like vegetable oil based bio-diesel, alcohols, as alternatives for petroleum based diesel fuel, e.g. expected growth of prices of fossil liquid fuels in the near future and gradual exhaustion of crude oil sources in the next 80–100 years. Governments of many countries have started thinking that bio-fuels will provide boost to agricultural industry. In addition, the oxygenated fuels have attracted increasing attention in engine development owing to its excellent combustion characteristics in reducing emissions (Miyamoto *et al*. 1998, Xiao *et al*. 2000). Therefore, oxygenated fuels would find way as a supplement and substitute for diesel fuels for regular usage.

Heavy turbo-charging along with intercooling, higher injection pressures with finer sprays, flexible injection timing, exhaust gas recirculation and electronic control unit are the main features of modern DI diesel engines. The modern DI diesel engines are compact, smooth, reliable and sturdy (Fig. 1.2). To accomplish better air fuel mixing, reduced premixed phase of combustion and minimize the tail in the heat release diagram modern DI diesel engine employ:

- Higher compression ratios
- Turbo-charging and inter-cooling
- Down-sizing and up-rating
- Smaller fuel orifice sizes and sac volume
- Oxygenated fuels

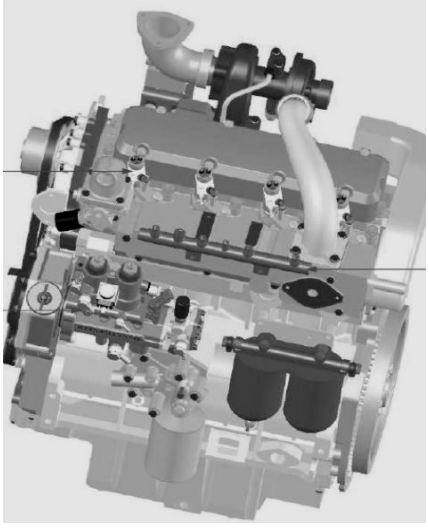

Fig. 1.2 Modern DI diesel engine

Modelling of Combustion in DI Diesel Engines

The complex task of improving IC engines, which have reached a higher degree of sophistication, can be achieved by combination of advanced experiments and computational studies. Despite the quantitative uncertainties of numerical simulations, which are often greater than those of experiments are, the modelling of combustion engine processes has some significant advantages that make its utilization in engine development a necessity. In this regard, it is obvious that numerical simulations are especially suited to carry out extensive parametric studies, since they are more effective than the alternative construction and investigation of numerous prototypes (Stiesch 2003).

The advantages of engine modelling are: (a) parametric studies of each variable can be done, (b) wide range of boundary conditions can be analysed, (c) separation of each sub-process from other, (d) detailed information is available as output, (e) effective in terms of time and cost.

Depending on the various possible applications, different types of models for engine combustion processes have been developed. Three different model categories are typically distinguished. In an order of increasing complexity and increasing requirements with respect to computer power, these are zero-dimensional thermodynamic models, quasi-dimensional phenomenological models and multi-dimensional computational fluid dynamics (CFD) models.

In thermodynamic models, the heat release by combustion cannot be easily derived by a detailed modelling of physical and chemical sub-processes, because these processes are strongly affected by the distribution of unresolved spatial temperature and composition. Because the combustion chamber is taken as zero-dimensional, it is mandatory to model the heat release rate by empirical sub-models using simple mathematical equations. On the other hand, the multidimensional CFD models are based on locally resolved solution of conservation of mass, energy, momentum, and include detailed sub-models for spray and combustion phenomena. With these models, the gas flow patterns can be predicted best and prediction of fuel spray are less complete and combustion calculations present considerable difficulties. The CFD models are of immense use to appreciate the inner mechanism of diesel sprays, but are very difficult to comprehend during the complete simulation of a diesel engine. Therefore, there is a need for a third category of model that allows to execute efficient, fast and economic preliminary calculations of heat release models and exhaust emissions as a function of important engine parameters like injection pressure, injection timing, swirl ratio and boost pressure. These models based on physical and chemical sub-models, for local processes like spray formation, air fuel mixing, ignition and combustion including emission formation are termed as phenomenological models. Therefore, these models are more comprehensive compared to thermodynamic models and consume less computational resources compared to CFD models. It should be noted that phenomenological models are the most practical to describe diesel engine combustion (Stiesch 2003).

This is because the injection process, which can be relatively well predicted with the phenomenological approach, has the dominant effect on mixture formation and subsequent course of combustion. Therefore, these models are widely used as predictive tools for carrying out parametric studies during engine development.

Many experimental investigations are also being carried out to provide better insight of the combustion process happening under engine environment. More recently, the development of laser-based diagnostics has provided a means for making detailed insitu measurements of the processes occurring inside a reacting diesel fuel jet. These diagnostics allow specific species within the reacting jet to be measured at multiple points simultaneously with high spatial and temporal resolution.

Even though the IC engine was invented a century ago, its development is continuing, as new technology is available and new demands are arising. Although the DI diesel engine is a better choice among different types of IC engines as a prime mover considering fuel economy and exhaust emissions, efforts are being put to improve them further to meet future stringent demands of fuel economy and pollution. Alternative technologies and fuels are being implemented in these engines. Therefore, theoretical and applied understanding of the engine processes is also developing at faster rate.

References

Bosch Automotive Handbook. Bosch, 5th Edition, 2000

Fiaz A, Sturm PJ (2000) New Directions, Road Traffic in Developing Countries, Journal of Atmospheric Environment 2000; 34: 4745–4746

Heywood JB (1988) A text book on Internal Combustion engine fundamentals. McGraw-Hill International edition

Krieger K, Hummel HG and Naik LM (2000) Diesel Fuel Injection Technology: An essential contribution towards an environment friendly powerful diesel engine. SAE 2000-01-1429

Miyamoto N, Ogawa H, Nurun NM, Obata K, Arimes T (1998) Smokeless, low NOx, high thermal efficiency and low noise diesel combustion with oxygenated agents as main fuel. SAE 980506

Stiesch G (2003) Modelling engine spray and combustion processes, Springer

Walsh MP (2000) Global Trends in motor Vehicle Pollution Control, Accomplishments to Date and Challenges for New Millennium. Paper No. F2000PH02, Proceedings of FISITA-2000, Seoul, Korea

Xiao Z, Ladommatos N, Zhao H (2000) The effect of aromatic hydrocarbon and oxygenates on diesel engine emissions. IMechE 214, Part D

2 Phenomenology of Diesel Combustion and Modelling

Abstract Diesel is the most efficient combustion engine today and it plays an important role in transport of goods and passengers on road and on high seas. It is expected that the diesel engine will be active for another 100 years as increasingly economical sources are found with the increase in oil prices offering incentive to the explorers. The emissions must be controlled as demanded by the society without sacrificing the legendary fuel economy of the diesel engines. These important drivers caused innovations in diesel engineering like re-entrant combustion chambers in the piston, lower swirl support and high pressure injection, in turn reducing the ignition delay and hence the Nitric Oxides (NO_x). From 16 g/kWh in 1988, the limit on NO_x is reduced today to as low as 2.0 and PM limit is reduced from 0.8 g/kWh to 0.02. These limits are being continually reduced. Therefore, the required accuracy of the models to predict PM, NO_x and efficiency of the engines is high. The phenomenological combustion models are practical to describe diesel engine combustion and to carry out parametric studies. This is because the injection process, which can be relatively well predicted with the phenomenological approach, has the dominant effect on mixture formation and subsequent course of combustion. The need for improving these models was also established by incorporating developments happening in engine designs. A phenomenological model consisting of sub-models for combustion and emissions are proposed in detail in this chapter. With more and more "model based control programs" used in the ECU controlling the engines, phenomenological models are assuming importance now. The full CFD based models though give detailed insight into the combustion phenomena and guide the design engineer, they are too slow to be handled by the ECU's or for laying out the engine design. Therefore, phenomenological models have a bright future hand in hand with the sophisticated models. The diesel combustion is modelled by studying the structure of the spray, ignition delay, heat transfer, air-fuel mixing and heat release. These contribute to smoke, NO_x and engine performance.

The Phenomenological Combustion Models are very practical to describe diesel combustion and to carry out parametric studies. This is because the injection process. The models are improved by incorporating new developments in engine designs.

The combustion in modern DI diesel engines is mainly divided in two phases: (a) a small ignition delay event in which pre-flame activities take place followed by (b) main heat release event in which actual combustion happens. These events are modelled differently considering prominent role of chemical kinetics during ignition and physical mixing rate during heat release. This approach is described

P.A. Lakshminarayanan and Y.V. Aghav, *Modelling Diesel Combustion*, Mechanical Engineering Series, DOI 10.1007/978-90-481-3885-2_2,

in detail in the following sections. This chapter summarizes different types of models along with description of popular models.

Combustion Model

The combustion starts almost at the onset of fuel injection because the ignition delay in modern DI diesel engines is very small with high compression ratio and highly retarded injection timing enabling substantial reduction in noise, NO_x and HC. The heat release estimated with this assumption predicts satisfactorily the important instantaneous parameters used by a designer e.g. heat transfer, fuel consumption, and the performance turbocharger and piston. On the same tenor, ignition delay cannot be neglected while estimating emissions however small it may be.

Ignition delay

In direct injection diesel engines, estimation of ignition delay is of great importance because of its effect on startability, noise and formation of NO_x. The ignition delay in a diesel engine is defined as the time interval between the start of injection and the start of combustion. This delay period consists of (a) physical delay, wherein atomisation, vaporization and mixing of air fuel occur and (b) chemical delay attributed to pre-combustion reactions. Both physical and chemical delays occur simultaneously. Early DI diesel engines operated at relatively low compression ratios and low injection pressures with very advanced injection timings in commensurate with the large ignition delay (Lakshminarayanan *et al.* 2002a). Reduction in ignition delay held the key to solving emission and noise problems. Higher temperature at the beginning of injection by increased compression-ratio reduces the delay period substantially.

Numerous ignition delay correlations have been proposed based on experiments carried out in constant volume bombs, steady state reactors, rapid compression machines and engines. Wolfer (1938) developed the earliest correlation for predicting ignition delay. The equation was in the form of an Arrehenius expression representing a single stage reaction. Kadota *et al*. (1976) related results of combustion bomb experiments to an Arrehenius type expression by introducing dependence of equivalence ratio. Lahiri *et al*. (1997) modified this equivalence ratio to fuel-oxygen ratio, attempting to make it suitable for oxygenated fuels. However, these correlations fail to predict the ignition delay under unsteady diesel engine conditions as they are based on experiments conducted in a constant volume bomb. On the other hand, a few correlations have been developed considering engine data (Hardenberg and Hase 1979, Watson *et al*. 1980). These correlations also were not successful in yields, satisfactory predictions under widely varying operating conditions as they have ignored the effect of mixture quality. Recently Assanis *et al*. (1999) have compared these correlations and found better predictability using the Watson correlation (1980). They improved the correlation by

introducing the equivalence ratio and tuning the empirical constants. They postulated that the introduction of the dependency of ignition delay on overall equivalence ratio makes the correlation more dynamic.

The time taken for visible fire to appear in the pre-mixed zone of spray is a strong function of pressure and temperature of the ambient. In addition, the physical properties such as Cetane number, viscosity of fuel, nozzle-hole size, injected quantity and injection pressure contribute to the delay phenomenon in diesel engines (Chandorkar *et al*. 1988).

Heat release

The shaft work by a diesel engine is the sum of work on the piston by the pressure produced by the heat released by combustion and the losses due to pumping, heat transfer and friction. While the flow losses and friction work could be reasonably comprehended, the heat release is dependent on the complex turbulent mixing of fuel and air at high temperature after compression. The variety of combustion chambers and types of fuel injection equipments influence the heat release rate characteristically.

Models based on fluid dynamics

These types of models are often called as multidimensional models due to their inherent ability to provide detailed geometric information on the flow field based on the solution of the governing equations. In the numerical calculations of reacting flows, computer time and storage constraints severely restrict the complexity of the reaction mechanism that can be incorporated. They use simplified model for predicting combustion, which is mixing controlled and kinetically controlled. The choice between these two models is made by the ratio of the chemical reaction time to the turbulent mixing time. Several three-dimensional simulation models of injection, mixing and burning in diesel engines exist (Cartillieri and Johns 1983, Gosman *et al*. 1985) describing various phenomena in the engine and providing possibilities of understanding the inner mechanism of diesel sprays. However, the volume of computation in multi-dimensional models is too prohibitive to carry out many parametric studies. In addition, their sub-models require a thorough validation with detailed experiments before employing them confidently in engine design work.

Phenomenological models

In these types of models, details of different phenomenon happening during combustion are added to basic equation of energy conservation. In the simplest approach, Rife and Heywood (1974) assumed the growth and motion of the spray within the chamber and analysed it as a quasi-steady one-dimensional turbulent gaseous jet. Shahed *et al*. (1973), Dent and Mehta (1981), and Hiroyasu *et al*. (1983) found that the spray structure offered the clue to better heat release predictions. In these investigations, detailed two-dimensional axisymmetric spray calculations are attempted using the mixing of the injected fuel with the surrounding air entrained due to high shear velocity of the jet (Fig. 2.1). A criterion of stoichiometric

burning of the fuel in ignitable elements has been used in these models by spray-mixing approach.

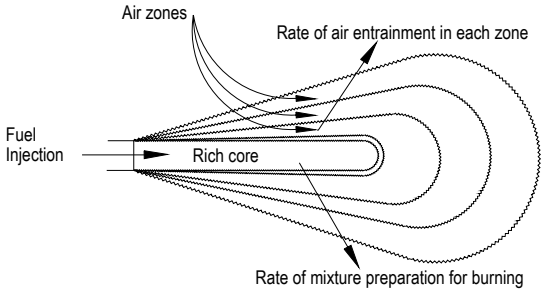

Fig. 2.1 Multi zone spray model

Zero-dimensional models

This type of models is more attractive due to their simplicity as they use simple algebraic equations to describe heat release rate. Lyn's work (Austen and Lyn 1960) is the earliest in identifying a strong relationship between fuel injection and heat release rates. The rate of injection diagram was subdivided into elemental fuel packets emanating as rectangular pulses, which results in exponentially decaying heat energy function. The convolution integral of the heat release from the individual packets summed neatly to the net heat release rate (Fig. 2.2). Due to the absence of universal decay constants for elemental heat-release rates in different types of engines and their operating conditions, the application of this elegant idea posed difficulty.

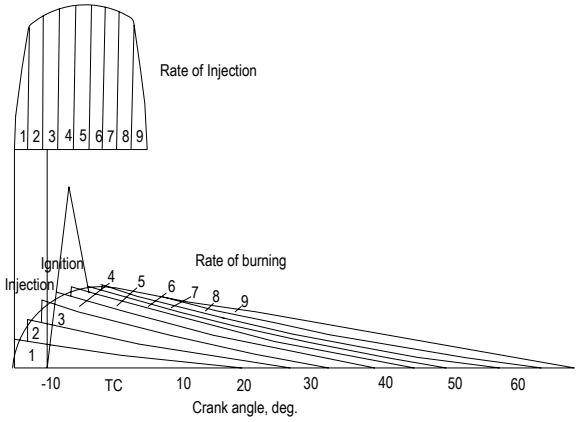

Fig. 2.2 Relation between rate of injection and rate of burning

In this regard, the global heat release rate function of Wiebe (1970) earned much wider acceptance in diesel engine simulation for several years now (Fig. 2.3). The Wiebe's function, however, requires two adjustable constants for a given engine

type and even then fails to explain the effects of speed and load. In addition, this function does not reflect the effects of the shape of the combustion chamber and the fuel injection rate on the history of heat release as desired in current engine development.

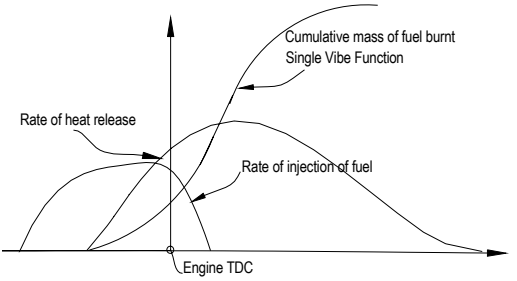

Fig. 2.3 Wiebe's model

The limitations of Wiebe's function to predict the rate of heat release during early premixed period was somewhat overcome by Watson *et al*. (1980) through the concept of double Wiebe function. This however, added more number of adjustable constants that are dependent on the engine type. While such algebraic functions are easy to compute, there are various other complex models (Table 2.1).

Table 2.1 Combustion models

Author (year)	Specialty of model	Remark
Austen and Lyn (1960)	Direct relation between fuel injection pump and heat release rate	Absence of universal constants
Wiebe (1970)	Exponential decay function with empirical constants	No effect of injection rate and combustion chamber
Shahed *et al*. (1973)	Detailed computation of two-dimensional axisymmetric spray	Engine dependant constant
Dent and Mehta (1981)		No effect of load and speed
Hiroyasu *et al*. (1983)		
Cartillieri and Johns (1983)	Three-dimensional finite volume technique	Large volume of calculation
Gosman *et al*. (1985)		
Chmela and Orthaber (1999)	Mixing controlled combustion	No effect of wall impingement

In a simpler approach, avoiding necessity of engine dependant tuning constants, Chmela and Orthaber (1999) proposed an innovative model on the premise that the fuel-air mixing, and hence the burning in diesel engines, is proportional to the average turbulent kinetic energy associated with the fuel injection rate. In addition, the turbulent energy decay in time is proportional to the total kinetic energy of the injected fuel itself. It is observed that this model predicts the trend of heat release quite closely if only there is no impingement of sprays on the piston.

A comparison of the predicted and the experimental results is not satisfactory in case of spray impinging on the wall. This situation arises in engines of capacities less than 2 L per cylinder operating at more than half load, where majority of diesel engines belongs. Therefore, an attempt has been made in this book to enhance this model by encompassing the phenomena at the wall and the instantaneous injection rate derived from the indicated performance of fuel injection equipment (Lakshminarayanan *et al*. 2002a).

Emission Models

DI diesel engines emit smoke, hydrocarbons, nitric oxides, carbon monoxide and particulate matter are mainly regulated. They are formed in different phases of combustion as described below.

Hydrocarbons
The fuel leaned beyond flammability limits (Greeves *et al*. 1977), bulk quenching during expansion, fuel effusing from nozzle sac after completion of injection (Yu *et al*. 1980) are the most important reasons for Hydrocarbon (HC) emissions. A semi-empirical phenomenological model was successfully made for HC emissions considering the fuel injected and mixed beyond the lean combustion limit during ignition delay and fuel effusing from the nozzle sac at low pressure (Lakshminarayanan *et al.* 2002b). Exhaust gas recirculation (EGR), a well-accepted method of NO_x reduction, alters ignition delay and HC emissions. The oxygen-enriched fuels that attract great attention worldwide owing to its excellent combustion characteristics, exhibit different behaviour especially in case of ignition delay and HC emissions.

Oxides of nitrogen
Considering the heterogeneous nature of fuel-air mixture in diesel engines, NO_x and particulate matter (PM) are important emissions. Continuous efforts are being made to minimize the quantities of these two pollutants from the diesel engine exhaust. Vioculescu and Borman (1978) carried out gas sampling from within the cylinder of a naturally aspirated direct injection (DI) diesel engine using a rapid acting sampling valve. This resulted in a plot showing time history of ratio of the average cylinder NO_x concentration in the exhaust during the combustion process. Similar modelling and gas sampling studies have been done with indirect injection (IDI) diesel engines, which suggest that prechamber is the prominent location for formation of nitrogen oxides (Mansouri *et al*. 1982). Duggal *et al.* (1978) plotted the NO concentrations and equivalence ratios as a function of crank angle using a rapid-acing sampling valve at different locations within the prechamber of a swirl chamber IDI engine. There are a number of potential mechanisms responsible for NO in combustion processes. The relative importance of these different mechanisms is strongly affected by the temperature, fuel-air equivalence ratio, pressure, flame

conditions, residence time and concentrations of key reacting species. Rapid NO_x formation begins after the start of heat release. Shortly after the end of heat release, the period of rapid NO_x formation ends because temperatures of the burned gas decrease due to mixing with cool bulk gas and expansion of the charge (Kitamura *et al*. 2005). Fuel-Air equivalence ratio is another important factor influencing NO_x formation. As the equivalence ratio becomes leaner, NO and NO_x decrease significantly as expected. NO_2 however shows an opposite trend to that of NO that causes the NO_2/NO_x ratio to increase at leaner conditions. The NO_2 peaks at an equivalence ratio near 0.25. Leaner equivalence ratio is indicative of lower loads and lower bulk gas temperatures that are conducive to the formation of NO_2 (Pipho *et al*. 1991).

Advancing injection timing or increasing injection pressure improves combustion efficiency raises combustion temperature. In general, higher combustion temperatures lead to higher NO_x formation (Henein and Patterson 1972). Addition of diluents to the engine intake air is considered as an effective mean to reduce the NO formation rate and hence the exhaust NO_x levels. The effect is primarily one of reducing the peak flame temperature, which is the driving factor for NO_x formation. Diluents such as N_2, CO_2 and exhaust gas were added to the intake air of direct injection (DI) engine to study their effect on NO_x reduction (Challen and Baranescu 1999). Similar studies done in indirect injection (IDI) engine showed similar trends (Yu and Shahed 1981). Plee *et al*. (1981, 1983) established a correlation showing the effect of changes in intake air composition and temperature on NO_x emissions.

NO_x emissions comprise of NO and NO_2. The NO_2 is formed via NO molecule. Therefore, the modelling of NO_x formation is most often reduced to studying the formation of NO. It is widely accepted that in diesel engines the major portion of NO is formed via thermal path (Ahmed and Plee 1983). Many multi-dimensional and multi-zone phenomenological models use extended Zeldovich mechanism (Heywood 1988). This mechanism was postulated by Zeldovich (1946) and improved by Lavoie *et al.* (1970). Khan *et al.* (1973) related FIE and engine operating conditions to NO formation and developed a method of calculation for emissions (Khan *et al.* 1973). They concluded that an increased rate of injection or increased air swirl reduces the amount of exhaust smoke and increases NO_x.

All these models utilize empirical heat transfer correlation, which are mass averaged. During combustion, the heat loss is caused partly by convection from burned gases at high temperature and partly by radiation from soot particles formed during the diffusion flame. Due to the short distance between the nozzle and the combustion chamber wall under typical operating conditions, diesel fuel impinges on the wall in the form of liquid followed by fuel vapour and flame after onset of auto-ignition. The peak radiant heat flux is always less than 20% total heat flux confirming the dominant role of spray and flame interaction with piston bowl (Arcoumenis *et al*. 1998).

The contribution of convective mode of heat transfer is about 80% to total engine heat transfer (Heywood 1988, Stiesch 2003). However, it is known that in

diesel engines radiative heat transfer may have a significant contribution in addition to convective heat transfer. The radiative heat transfer in diesel engines is caused by both radiation of hot gases and by radiation of soot particles within the diffusion flame. It is agreed in the literature that the latter has a significantly greater impact on the radiative heat flux, and thus most heat transfer models concentrate on the radiation of soot only. It should be noted though, that a general difficulty in the evaluation of soot radiation exists in that the prediction of the soot concentration itself is typically subject to significant uncertainties (Stiesch 2003). Therefore, the empirical heat transfer correlations focused mainly on convective mode.

The heat transfer coefficient has been derived by many researchers by assuming an analogy with a steady turbulent flow over a solid wall. The colour pyrometer and fast response thermocouples were employed for experimental investigations. Annand (1963) developed correlation for convective heat transfer but it was based on experiments conducted on only cylinder head. Probably, the most widely used approach in this category is the one suggested by Woschni (1967). Hohenberg (1979) improved the above correlation by using a length based on instantaneous cylinder volume and exponent of the temperature term. This approach gives an estimate of the surface-averaged heat transfer coefficient history in terms of the bulk gas temperature and a surface-averaged or total heat flux (Ikegami *et al.* 1986, Nishiwaki 1998). However, this approach cannot give the kind of information necessary to design modern engines. The empirical correlations underestimate to varying degrees the heat transfer during combustion. The investigations have revealed that during the combustion period the wall heat flux is substantial locally in space and time, due to the transient nature of the flame propagation. In particular, during combustion the heat flux increases rapidly after impingement on the wall (Kleemann *et al.* 2001). The characteristics of injected spray and its interaction with the swirling air and the wall of the combustion chamber determine the efficiency and the exhaust emissions. In Chapter 14, a phenomenological model for NO_x prediction is proposed based on spray combustion incorporating localised effect of heat transfer in wall spray and exhaust gas recirculation.

Smoke and particulate matter

The characterization of diesel smoke has remained a challenge in engine development and modeling work. Effect of different parameters of combustion chamber and injection on soot and NOx emissions were investigated by De Risi *et al.* (1999, 2005). Kurtz and Foster (2004) identified critical time for mixing in diesel engine and its effect on emissions. Based on in-situ laser diagnostics, a conceptual model of burning jet was developed (John Dec 1997). Khan et al (1973) first presented a model for the prediction of soot related to engine operating condition. Hiroyasu *et al*. (1976) proposed a two-step semi empirical model and applied it to the multipacket combustion model. Later on, the model was extended up to a simple three-dimensional model (Nishida K, Hiroyasu H 1989). Fusco *et al*. (1994) proposed that either pyrolysis of fuel could result in soot precursor radicals or growth species with possibilities of oxidation at intermediate stages. There is a principal mathematical problem in the modeling of the engine-out soot emissions by using

formation and oxidation methodology (Stiesch G 2003). Since the soot mass in the exhaust is the very small difference between two nearly equal large quantities i.e. between formation and oxidation, a significant error will result if only a small deviation in either the production or the formation rate. Magnussen *et al*. (1976) carried out experiments on steady state free diffusion flames and concluded that soot was formed and contained in the turbulent eddies within the flame. The burn up of the soot was related to the dissipation of turbulence. In this view, Dent's work (1980) was unique. The importance of turbulent energy dissipation rate on smoke in quiescent chamber diesel engines was identified quantitatively. Recently, Dec and Tree (2001a, 2001b) investigated interactions of combusting fuel jet free in air and at the wall using laser diagnostics. They found that soot deposition on the wall and blow-off are not the major contributors to engine-out soot emissions. In chapter 12, a model that clearly distinguishes the free jet and wall jet regimes of a diesel-engine spray and their turbulence structure is developed to explain the smoke.

Diesel particulates consist principally of carbonaceous material (soot from smoke) generated by combustion on which some organic compounds have become absorbed. Most of the particulate material results from incomplete combustion of fuel hydrocarbons; some is contributed by the lubricating oil (Heywood 1988). Diesel particulate matter is therefore a complex mixture of organic and inorganic compounds in solid and liquid phases (Johnson *et al.* 1994). The basic measurement of particulate matter is by its mass and it can be described as any exhaust components other than uncombined water that collects on a filter in a dilution tunnel at a temperature less than 53°C. In the standard procedure of measurement of mass emission, dilution tunnels are used to simulate the physical and chemical processes the particulate emissions undergo in the atmosphere. In the dilution tunnel, the raw exhaust gases are diluted with the ambient air to a temperature of 53°C or less and the sample stream from the diluted exhaust is filtered to remove the particulate matter. The mathematical modelling of particulate matter is always concentrated around soot because of its complex nature. Different studies have been carried out to establish contributions of soot, unburnt HC from fuel and lubricating oil (Cartillieri and Trittari 1984, Cartillieri and Wachter 1987, Cartillieri and Herzog 1988). Most of the PM correlations consider only soot to estimate particulate matter. Recently one phenomenological model is proposed for PM based on soot and unburnt HC from fuel (Tan *et al.* 2007). However, this model requires tuning of engine and load dependent constants. It does not account for SOF from lubricating oil and IOF from sulphates.

Theme of the Book

The literature survey highlighted some of the limitations of present phenomenological models for application to modern engines. The available models require many engine-dependent empirical constants and consideration is given to neither

spray-wall interaction nor the effect of oxygenated fuels. The book presents the results of the research work based on comprehensive experimental work undertaken for improving phenomenological modelling of combustion in modern engines.

The highlights of the phenomenology of diesel combustion considered in the following chapters are as follows.

- Analysis of modern in-cylinder emission control technologies
- Turbulence structure for engine sprays
- Spray-wall interaction and its effect
- Mixing controlled combustion
- Localized heat transfer
- Quasi one-dimensional approach to the heat release in DI engines
- Consideration to fuel bound oxygen
- Avoid engine dependent constants
- Sub-model for prediction of combustion
- Sub-models for important exhaust emissions

About 50 modern engines (Table 3.2) from 21 different engine families with widely varying features like bore-sizes, aspiration and cooling system are selected for experimental work. These engines meet current emission norms and are capable of upgrading to next stage with minor changes. Observations pertaining to fuel injection, emissions and engine performance were collected simultaneously using experimental set up specially developed. Additional experiments were also carried out to study the effect of oxygenated fuels and exhaust gas recirculation on a few engines. The new models are thoroughly validated by using a large number of data collected from many experimental data. In addition, the results of new models are compared with 1-D engine cycle simulation tools like 'AVL Boost (2005) which are being extensively used for engine development. The objectives of research work are:

- To improve understanding of ignition delay and mixing controlled combustion
- Develop turbulence structure for engine spray
- Estimation of combustion cavity – spray interaction
- Wall impingement of sprays causing loss of kinetic energy and intense heat transfer
- Effect of exhaust gas recirculation, EGR on combustion
- Effect of fuel bound oxygen on combustion and emission
- Effect of injection characteristics and nozzle features

To meet above objectives, a research scheme was developed as shown schematically in the Fig. 2.4.

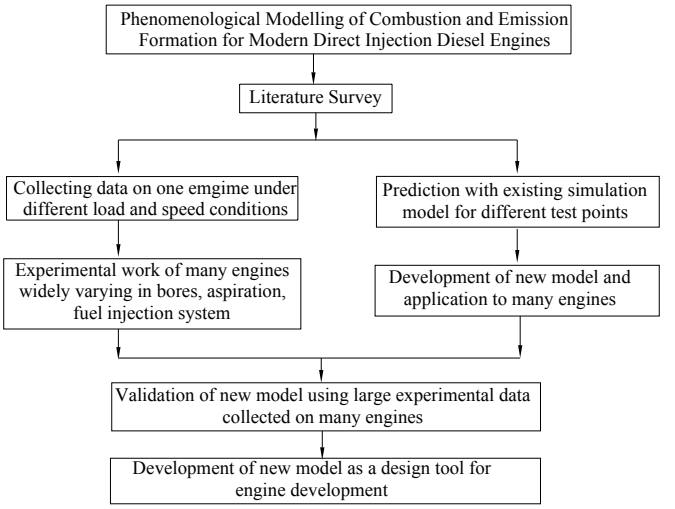

Fig. 2.4 Book scheme

References

Ahmed, T. and Plee, S. L., 1983 "Application of Flame Temperature Correlations to Emissions from a Direct-Injection Diesel Engine," SAE paper 831734

Annand WJD (1963) Heat Transfer in the Cylinders of Reciprocating Internal Combustion Engines. Proc. IMechE, 177:973990

Arcoumenis C, Cuter P, Whitelaw DS (1998) Heat transfer process in diesel engines. IChemE, 176, Part A

Assanis DN, Filipi ZS, Fiveland SB, Syrimis M (1999) A Predictive Ignition Delay Correlation under Steady State and Transient Operation of a Direct Injection Diesel Engine. ASME-ICE Fall Technical Conference

Austen AEW, Lyn WT (1960) Relation between fuel injection and heat release in a direct injection engine and the nature of the combustion process. Proceedings of the IMechE

Cartillieri W, Johns RJR (1983) Multidimensional Modelling of Engine Processes: Progress and Prospects. Fifteenth CIMAC Congress, Paris

Cartillieri W, Trittari P (1984) Particulate Analysis of light duty diesel engines [IDI and DI] with particular reference to lubricating oil particulate fraction. SAE 840418

Cartillieri W, Wachter WF (1987) Status report on preliminary survey of strategies to meet US-1991 HD diesel emission standards without exhaust gas after treatment SAE 870342

Cartillieri W, Herzog PL (1988) Swirl supported of quiescent combustion for 1990's heavy duty DI diesel engines – An analysis. SAE 880342

Challen B, Baranescu R (1999) Diesel Engine Reference Book, SAE, Warrendale, PA, 2nd edition

Chandorkar SB, Dani AD, Lakshminarayanan PA (1988) Effects of injection parameters, fuel quality and ambient on the ignition delay and the location of the flame Kernel in a diesel spray in a quiescent chamber. SAE 881227

Chmela FG, Orthaber GC (1999) Rate of heat release prediction for a direct injection diesel engine based on purely mixing controlled combustion. SAE 99010186

Dec JE (1997) A conceptual model of D I diesel combustion based on Laser Sheet imaging. SAE 970873

Dec JE, Tree DR (2001) Diffusion-Flame Wall Interactions in a Heavy-Duty DI Diesel engine. SAE 2001-01-1295

Dent JC (1980) Turbulent mixing rate - Its effect on smoke and hydrocarbon emissions from Diesel Engines. SAE 800092

Dent JC, Mehta PS (1981) Phenomenological combustion model for a quiescent chamber diesel engine. SAE 811235

DeRisi, A, Manieri D, Laforgia D (1999) A Theoretical Investigation on the Effects of Combustion Chamber Geometry and Engine Speed on Soot and NOx Emissions. ASME-ICE, Paper No. 99-ICE-207, 33-1

DeRisi A, Donabeo T, Laforgia D (2005) An Innovative methodology to improve the design and the performance of direct injection diesel engine. Int J Eng Research, IMechE, 5

Duggal VK, Priede T, Khan IM (1978) A Study of Pollutant Formation within the Combustion Space of a Diesel Engine. SAE paper 780227

Fusco A, Knox-Kelecy AL, Foster DE (1994) Application of a phenomenological soot model to Diesel Engine Combustion. 3rd International Symposium, COMODIA

Gosman AD, Tsui YY, Watkins AP (1985) Calculation of Unsteady Three-dimensional Flow in a Model Motored reciprocating Engine and Comparison with Experiment. Fifth International Turbulent Shear Flow Meeting, Cornell University

Greeves G, Khan IM, Wang CTH, Fenne I (1977) Origins of Hydrocarbon emissions from diesel engines. SAE 770259

Hardenberg HO, and Hase, FW (1979) An Empirical Formula for Computing the Pressure Rise Delay of a Fuel From Its Cetane Number and From the Relevant Parameters of Direct-Injection Diesel Engines. SAE 790493

Henein NA, Patterson DJ (1972) Emissions From Combustion Engines And Their Control. Ann Arbor Science Publishers

Heywood JB (1988) A text book on Internal Combustion engine fundamentals. McGraw-Hill Int ed

Hiroyasu H *et al.* (1983) Development and use of a spray combustion modelling to predict diesel engine efficiency and pollutant emissions. Bull JSME 26: 214

Hiroyasu, Kadota (1976) Models for combustion and formation of nitric oxide and soot in direct injection diesel engines. SAE 760129

Hohenberg GF (1979) Advanced approaches for heat transfer calculations. SAE 790825

Ikegami M, Kidoguchi Y, Nishiwaki K (1986) A Multidimensional Model Prediction of Heat Transfer in Non-Fired Engines. SAE 860467

Johnson JH, Bagley ST, Gratz LD, Leddy DG (1994) A review of diesel particulate control technology and emission effects. SAE 940233

Kadota T, Hiroyasu H, and Oya H (1976) Spontaneous Ignition Delay of a Fuel Droplet in High Pressure High Temperature Gaseous Environments. Bull. JSME, 19~130, Paper No. 536.46, pp. 437–445.

Khan IM, Greeves G, Wang CHT (1973) Factors Affecting Smoke and Gaseous Emissions From Direct Injection Engines and a Method of Calculation, SAE 730169

Kitamura Y, Mohammadi A, Ishiyama T, Shioji M (2005) Fundamental Investigation of NO_x Formation in Diesel Combustion under Supercharged and EGR Conditions, SAE 2005-01-0364

Kleemann AP, Gosman AD, Binder KB (2001) Heat Transfer in Diesel Engines: A CFD Evaluation Study. COMODIA 2001, pp. 123–134, Nagoya

Kurtz, EM, Foster DE (2004) Identifying a critical time for mixing in a direct injection diesel engine through the study of increased in-cylinder mixing and its effect on emissions through study of increased in-cylinder mixing and its effects on emissions. Int J Eng Research, IMechE, 5

Lahiri D, Mehta P, Poola R, Sekar R (1997) Utilization of Oxygen-Enriched Air in Diesel Engines: Fundamental Considerations. ASME Paper No. 97-ICE-72, New York

Lakshminarayanan PA, Aghav YV, Dani AD, Mehta PS (2002a) Accurate prediction of the rate of heat release in a modern direct injection diesel engine. IMechE, 216, J Auto Eng

Lakshminarayanan PA, Nayak N, Dingre SV, Dani AD (2002b) Predicting Hydrocarbon Emissions From Direct Injection Diesel Engine. ASME J Power of Gas Turbine, 124

Lavoie GA, Heywood JB, Keck JC (1970) Experimental and Theoretical investigation of Nitric Oxide Formation in internal combustion engine. Combust Sci Tech, 1

Magnussen BF, Hjertager BH (1976) On mathematical modelling of turbulent combustion with special emphasis on soot formation and combustion. Int symposium on combustion

Mansouri SH, Heywood JB, Radhakrishnan K (1982) Divided-Chamber Diesel Engine, Part I: Cycle-Simulation Which Predicts Performance and Emissions. SAE 820273

Nishida K, Hiroyasu H (1989) Simplified three-dimensional modelling of mixture formation and combustion in a DI diesel engine. SAE 890269

Nishiwaki K (1998) Modeling Engine Heat Transfer and Flame-Wall Interaction. Proc. COMODIA 98, pp. 35–44

Pipho, MJ *et al.* (1991) NO_2 Formation in a Diesel Engine. SAE 910231

Plee SL, Ahmed T, Myers JP (1983) Diesel NOx Emissions-A Simple Correlation Technique for Intake Air Effects. Proceedings Nineteenth Int Symposium on Combustion, pp. 1495-1502, The Combustion Institute, Pittsburgh,

Plee SL, Myers JP, Ahmed T (1981) Flame Temperature Correlation for the Effects of Exhaust Gas Recirculation on Diesel Particulate and NOx Emissions. SAE 811195

Rife JM, Heywood JB (1974) Photographic and performance studies of diesel combustion with a rapid combustion machine. SAE 740948

Shahed SM, Chiu WS, Yumlu VS (1973) A preliminary model for the formation of nitric oxides in D I diesel engine and its application in parametric studies. SAE 730083

Stiesch G (2003) Modelling engine spray and combustion processes, Springer

Tan PQ, Hu ZY, Deng KY, Lu JX, Lou DM, Wan G (2007) Particulate matter emission modelling based on soot and SOF from direct injection diesel engines. Int J Energy Conversion and Management, 48, pp. 510–518.

Tree DR, Dec JE (2001) Extinction Diesel Combustion: An integrated view combining laser diagnostics, chemical kinetics and empirical validation. SAE 2001-01-1296

Users Guide, AVL Boost 4.1, July 2005.

Wiebe IT (1970) Brennverlauf und Kreisprozeb von Verbrennungsmotoren. VEB Verlag Technik, Berlin

Vioculescu IA, Borman GL (1978) An Experimental Study of Diesel Engine Cylinder-Averaged NOx Histories. SAE 780228

Watson N, Pilley AD, and Marzouk M (1980) A Combustion Correlation for Diesel Engine Simulation. SAE 800029

Wolfer, HH (1938) Ignition Lag in Diesel Engines. VDI-Forschungsheft 392, translated by Royal Aircraft Establishment, Aug. 1959, Farnborough Library No. 358, UDC 621-436.047.

Woschni G (1967) A Universally Applicable Equation for the Instantaneous Heat Transfer Coefficient in the Internal Combustion Engine. SAE 670931

Yu RC, Shahed SM (1981) Effects of Injection Timing and Exhaust Gas Recirculation on Emissions from a D.I. Diesel Engine. SAE 811234

Yu RC, Wong VW, Shahed SM (1980) Sources of Hydrocarbon emissions from direct injection diesel engines. SAE 800048

Zeldovich YB (1946) The Oxidation of Nitrogen in Combustion and Explosions. Acta Physicochimica, USSR, 21

3 Experiments

Abstract Experimental work is necessary to develop the basic understanding of the processes in the engine. This chapter describes the experimental set up of the bomb for experimental interferometry, engine studies and details of the engines used in the book for validation of the phenomenological models. The details of the experimental techniques for obtaining the experimental data needed for validating the phenomenology are included.

The phenomenological models are based on physical and chemical description of the processes in the engine. Experimental work helps in collecting some data used as input for phenomenological model and in validating them. This chapter describes the set up of the bomb and engines for developing the phenomenology of combustion.

Studies in a Bomb

Holographic interferometry is attractive as the concentration and temperature fields within a transient vapourising fuel spray with or without combustion can be obtained in principle (Dent *et al.* 1977, Dent 1980). Using a double exposure pulsed laser technique the transient development of the injected fuel spray and its combustion can be frozen at any instant, and recorded on a holographic plate as a two-dimensional interference fringe field, which is a result of refractive index changes arising from optical path length variation through the spray. Later analysis and inversion of the interference fringe field yields the local refractive index within the spray plume.

The refractive index is dependent on both species concentration and temperature. The decoupling of these individual contributions to the absolute value of the refractive index is used to obtain the concentration and temperature fields within the spray (Dent *et al.* 1977, Dent 1980). The schematic of experimental set up is shown in Fig. 3.1.

The experimental study in the bomb is considered in two parts (Lakshminarayanan and Dent 1983). The first deals with vaporising sprays in the absence of combustion, establishes equations for the description of concentration and temperature fields within a transient spray, particularly the behaviour following detachment of the jet from the injector nozzle at the end of injection. The data reduction procedure for the evaluation of concentration and temperature from the refractive index field is discussed in references (Dent 1980).

P.A. Lakshminarayanan and Y.V. Aghav, *Modelling Diesel Combustion*,
Mechanical Engineering Series, DOI 10.1007/978-90-481-3885-2_3,

The second part of the study deals with autoignited sprays of injected fuel into high temperature air. In decoupling the contributions of species concentration and temperature to the refractive index field, the equations obtained in the first phase of the work are used to determine local stoichiometry within the spray. During the evaluation of local species concentration and burned gas temperature, chemical equilibrium of the combustion reaction is assumed.

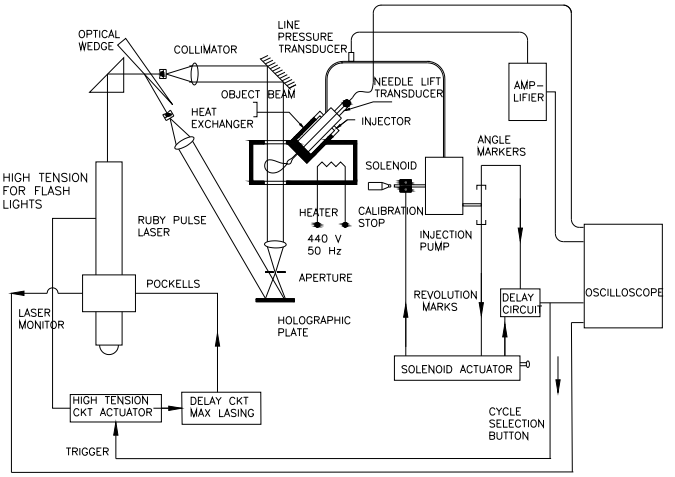

Fig. 3.1 Test set up for bomb experiments

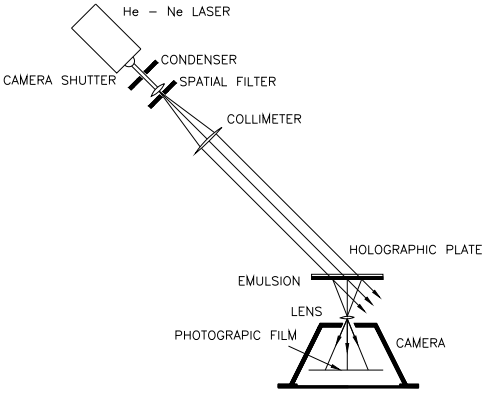

Fig. 3.2 Reconstruction of hologram

Attractive as holographic interferometry is, it suffers from disadvantages if applied directly to a typical Diesel engine. High interference fringe density at high compression ratios coupled with laser speckle noise makes fringe interpretation difficult. The problem is compounded if the gas motion within the engine is highly turbulent, due to high swirl and squish. This causes corruption of the background fringe field.

A quiescent chamber diesel engine is simulated. A suitable set of scaling parameters have been used to relate the fuel air mixing process in a constant volume bomb to those within an actual engine cylinder.

To initiate auto-ignition and combustion in the bomb with ignition delay typically observed in engines, diethyl ether doped with an ignition improver was used as the injected fuel. The experimental rig (Fig. 3.1) consisted of a stainless steel bomb (Chiu 1973) with good optical access (70 mm thick quartz windows), the centrally mounted injector with a single-hole nozzle produced a spray plume directed radially across the bomb within the full view of the windows. A flat impingement surface was provided at a distance of 60 mm from the nozzle to enable the study of transient wall jet behaviour following jet impingement. An electronically controlled jerk pump system enabled single injections of fuel to be achieved with good repeatability.

The beam from a 300 mJ pulsed ruby laser was split with an optical wedge and the two resultant beams collimated to the size of the optical windows. The object beam was transmitted through the bomb, a condensing lens and aperture, and finally combined with the reference beam at the holographic plate. Because of the transmission optical arrangement used, a dark field interferogram (Matulka 1970) is obtained, which improves fringe contrast and resolution.

The air to the bomb was from the laboratory supply at a pressure of 7-bar. For the vaporisation studies, the air was pre-heated in an electric furnace and bled slowly through the bomb, this produced a quiescent condition in the bomb with air temperatures reaching about 420 K. The combustion studies required modification to the bomb to incorporate a 2.5 kW heating element within the cavity, this enabled the air temperature to be increased to 720 K. However, the presence of strong free convective flows was observed in the cavity. Double exposure holographic interferometry was used, image reconstruction and photography is indicated schematically in Fig. 3.2.

Engine – bomb similarity

It has been shown (Dent *et al.* 1977, Dent 1980) that similarity between a quiescent chamber engine and its simulation is achieved when the two parameters below are equal for the engine and the simulation.

$$Fuel\ Injection\ \ Engine\ Scale = \frac{U_j d_e}{L} \tag{3.1}$$

$$Fuel\ Vaporisation = \left(\frac{k}{C_p}\right)_{mix} \left(\frac{\rho^{0.69}}{\mu^{0.63}}\right)_{air} \frac{B}{1+B}\left(1+d_e\right) \tag{3.2}$$

Assuming a naturally aspirated engine and an injection timing of 20° bTDC Fig. 3.3 shows the Fuel Vaporisation parameter plotted against engine compression

ratio. The experimental points for the vaporisation and combustion studies are (A, B, C, D, E, G) and (K, J) respectively.

Vaporisation studies

n-Pentane was used because of its low boiling point. The experimental conditions were (A, B, C, D, E and G) as listed in Table 3.1. Typical interferograms obtained at different instants at experimental condition E are shown in Fig. 3.4. Enlarged photographic prints of the interferograms were used for fringe counting, from the periphery of the jet to its axis. The inversion of the fringe count data to yield local refractive index difference ($n_r - n_m$) relative to the air reference state refractive index n_r, n_m, and the derivation of the local fuel vapour concentration C_f which is

$$C_{f_r} = \frac{\left(T_\infty / T_r - 1\right) - \dfrac{n_r - n_m}{\rho_\infty K_\infty}}{\left(\dfrac{M_\infty}{M_f} - 1\right)\dfrac{\left(n_r - n_\infty\right)}{\left(\rho_\infty K_\infty + 1\right)} - \dfrac{T_\infty}{T_r}\left(\dfrac{K_f}{K_m} - 1\right)} \tag{3.3}$$

follow directly from references (Dent 1980, Lakshminarayanan and Dent 1983). The local temperature T_r can be expressed as:

$$T_r = C_{f_r} T_s + (1 - C_{f_r}) T_\infty \tag{3.4}$$

Table 3.1 Experimental conditions, nozzle (single) hole diameter = 0.21 mm

					Bomb conditions			Similar engine conditions 100 mm bore at 20 BTDC			
Study code	Fuel	Nozzle opening pressure	Injection quantity /nozzle hole (mm^3)	Injection duration (ms)	Pressure (bar)	Temperature (K)	Density (kg/m^3)	Pressure (bars)	Temperature (K)	Density (kg/m^3)	Compression ra-
A	n-Pentane	110	7	1.2	3	433	2.36	15.0	651	7.87	10
B	n-Pentane	110	7	1.2	3	403	2.54	12.4	618	6.85	9
C	n-Pentane	110	11	1.5	3	403	2.54	12.4	618	6.85	9
D	n-Pentane	110	11	1.5	6	403	5.08	20.0	703	9.72	15
E	n-Pentane	110	7	1.2	6	403	5.08	20.0	703	9.72	15
G	n-Pentane	165	11	1.5	6	403	3.08	20.0	703	9.72	15
J	Diethyl ether[a]	130	10	1.5	7	723	3.08	25.0	736	12.0	20
K	Diethyl ether[a]	130	7	1.5	7	723	3.08	25.0	736	12.0	20

[a]1.5% Nitromethane is added to reduce delay to 0.75 ms

Here, T_s is the saturated vapour temperature. For every point r, equations (3.3) and (3.4) were solved using a predictor corrector iteration procedure to obtain C_{fr} and T_r. Typical contour-plots of $C_{f\,\mathrm{r}}$ and T_r are shown in Fig. 3.5a and b.

Combustion studies

In a real engine, a jet of diesel fuel burns in an atmosphere of varying pressure. In the interferometric technique described earlier, the condition of the surroundings should be the same in the two exposures. Therefore, a constant pressure burning jet was studied. In addition, the ignition delay should be of the order of 1 ms as in a real engine. To achieve this, a fuel mixture of diethyl ether and 1.5% nitromethane was added. Initial studies of high-speed movies of a combusting jet confirmed a small ignition delay. Data J and K in Table 3.1 correspond to the combustion studies. Interferograms of the burning jet were analysed as follows.

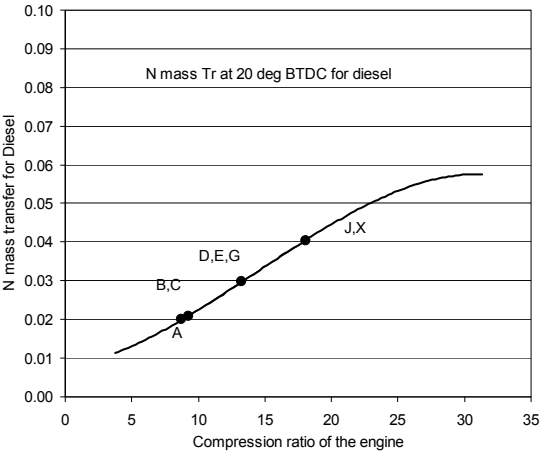

Fig. 3.3 Similarity between bomb and engine experiments

The bomb reference state condition was considered when the air temperature in the bomb had stabilized prior to injection. The object state condition was taken at times after ignition delay. Because of the large capacity of the bomb and small quantity of fuel injected, the pressure change due to combustion was of the order of 0.01 bar.

The value of equivalent diameter d_e is given (Beer and Chigier 1972) by

$$d_e = d_o\,[\text{density of fuel/density of combustion products at flame temperature}]^{1/2} \tag{3.5}$$

To find the temperature using the fringe count data a chart of T, $n-1$, Φ (temperature, refractivity and equivalence ratio) was prepared (Fig. 3.6) using the following principle (Dent 1980). With combustion present, in a burning air fuel-vapour region at the outer edge of the spray at radius r, the products of

combustion are assumed to be in equilibrium. The major species present are CO_2, CO, H_2O, N_2, O_2 and H_2. The reactions (Martin and Heywood 1977) considered are

$$C_xH_yO_z + q(O_2 + 3.76\,N_2) \rightarrow uCO_2 + (x-u)\,CO + v\,H_2O + (y/2 - v)\,H_2 + \left[q + \frac{1}{2}z - \frac{1}{2}(x+y+v)\right] O_2 + 3.76\;q\;N_2 \tag{3.6}$$

$$CO_2 \longleftrightarrow CO + O_2 \tag{3.7}$$

$$H_2O \longleftrightarrow H_2 + O_2$$

In the products of reaction with equivalence ratio greater than 1.5, CO_2 is absent. In addition, beyond the rich limit of combustion (equivalence ratio 3 for diethyl ether), fuel vapour coexists with the products of combustion at the rich limit (Bradshaw *et al.* 1981). For a given equivalence ratio, Φ, temperature, T and type of fuel using equations (3.6) and (3.7) the concentration $C_{i,r}$, of various species, i, and the density of the products ρ_{rg} can be calculated. The refractive index, n_{rB} is given by:

$$n_{r_B} = \rho_{r_B} \sum C_{i,r} K_i + 1 \tag{3.8}$$

Fig. 3.4 Interferogram for Data E, at 1.5 ms after start of injection

Here K_i (Tennent 1971) is the Gladstone-Dale constant for a specie, i. Thus, a table or a chart of T, $n–1$, Φ (Fig. 3.6) can be prepared. Table 3.1 gives a complete listing of the experimental conditions. It should be noted that the Fuel Injection – Engine Scale parameter was approximately satisfied in all tests.

Real Engine Studies

The newly developed phenomenological models were applied to many modern DI diesel engines to predict the rate of heat release and the exhaust emissions. Experimental results were also collected from these engines using experimental set up compliant to ISO 8178. Then, the predicted and experimental values are compared and analysed to understand the process of combustion and formation of pollutants. This helped in assessing and improving predictability by the models

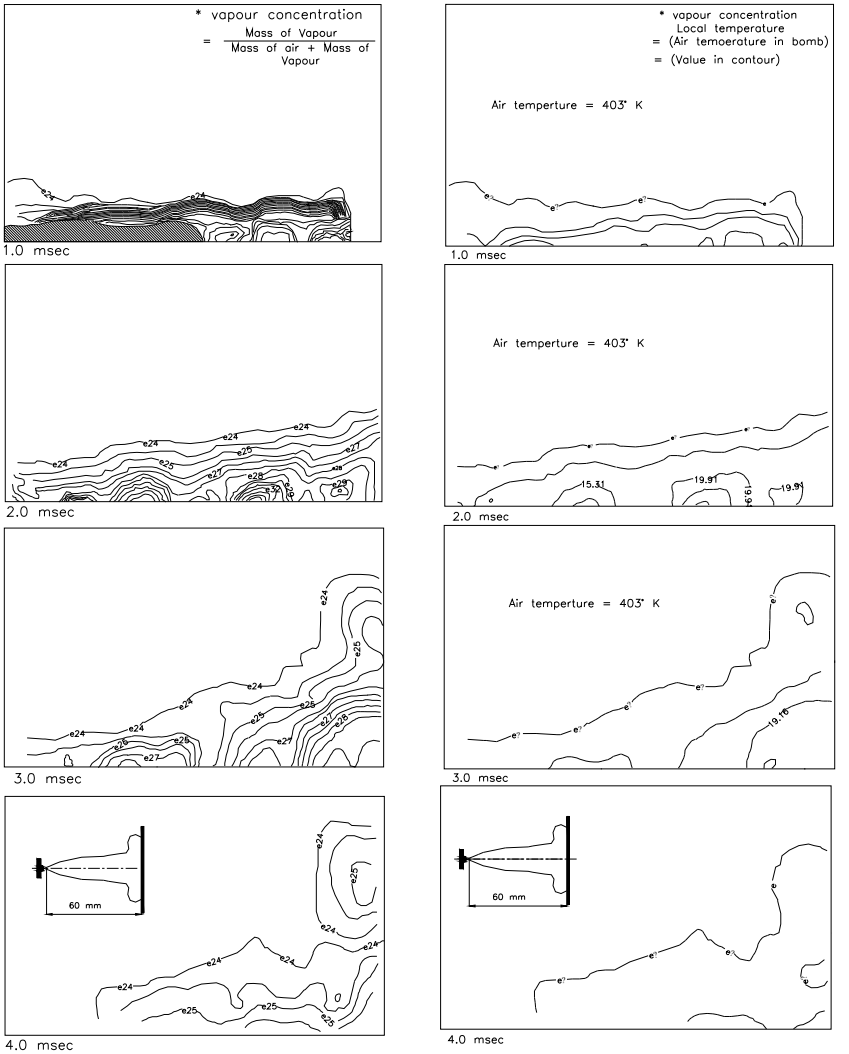

Fig. 3.5 Concentration contours

Engines A9 to E10 and A10 to G10, Table 3.2 are of modern type designed for low emissions of NOx and hydrocarbons. The compression ratio was relatively higher to enable injection delayed with respect to the previous generation of engines to which engine G10 belongs. The decrease in ignition delay in such engines resulted in lower premixed burning fraction and hence the sharp first peak is missing in the heat release diagrams (Chmela and Orthaber 1986). These engines used Bosch jerk type fuel injection system. To cover a wide range of engines in the study of HC emissions, the engine, E10 used by Chmela and Orthaber (1986) and engine, H10 (PT-fuel Injection system) used by Yu *et al.* (1980) are also studied using the integrated parameters such as ignition delay, nozzle hole-size and injected quantity.

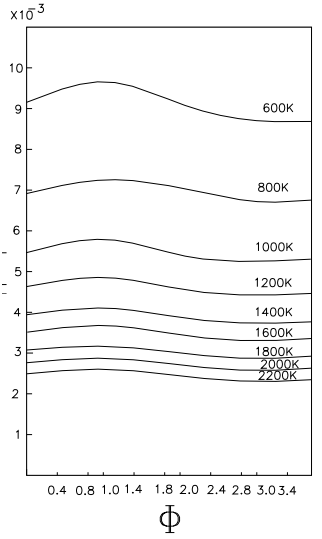

Fig. 3.6 Φ, n–1, T chart

Table 3.2 Specifications of engines used in the book. Number suffix of engine type refers to the chapter

Engine type	Aspiration	Cylinders	Bore (mm)	Stroke (mm)	Rated speed (rpm/1,000)	Nozzle holes	Hole diameter (μm)	Sac volume (mm^3)	Injection pressure press	Injection quantity (mm^3/str)	Fuel pump	Fuel timing (bTDC)	Combustion chamber (Fig. no)	Pistin Cavity diameter (mm)	Impingement distance	Boost ratio	Swirl number	no. of valves	Emission Norms	Compression Ratio	Bmep (bar)
A6	NA	1	130.0	150.0	1.4	8	–	–	1000	96	–	9	–	88	45	2.9	–	4	–	17.3	19.0
RE7	NA	4	90.0	94.0	3.5	1	P	–	180	32	A		SC	–	–	1.0	–	2	–	22.0	5.1
A8	NA	1	75.0	76.0	2.2	4	220	1.37	500	17	Q		8.7a	–	–	1.0	2.70	2	–	18.0	6.1
B8	NA	6	100.0	120.0	2.3	4	280	0.30	450	60	E	32	8.7b	55	30	1.0	2.70	2	–	17.5	7.8

C8	NA	4	110.0	116.0	2	4	280	1.37	550	77	E	28	8.7c	74	42	1.8	2.20	2	–	17.5	9.2
D8	NA	3	100.0	110.0	2	5	250	1.37	450	36	E	r	8.7d	60	33	1.0	2.50	2	–	17.5	5.6
E8	NA	1	68.0	76.0	3	1	P	–	180	14	A		S	–	–	1.0	–	2	–	19.0	5.4
F8	NA	1	80.0	95.0	1.5	3	286	1.69	200	26	A	24	8.7c	45	24	1.0	3.30	2	–	17.0	6.3
G8	NA	4	100.0	120.0	2	4	280	0.30	400	50	E	28	8.7b	55	–	1.0	2.70	2	–	17.5	7.2
H8	TA	9	280.0	290.0	1	9	450	m	1000	2250	A		9.9	220	120	4.0	0.80	4	–	12.0	20.2
J8	TA	6	175.0	220.0	1	8	330	m	800	570	Z		9.9	130	70	2.5	1.00	4	–	13.5	17.0
K8	NA	1	80.0	110.0	1.5	3	286	1.69	300	29	A		8.7c	45	24	1.0	3.30	2	–	17.0	6.3
L8	NA	4	100.0	120.0	1.5	4	280	0.30	400	48	E	20	8.7b	55	30	1.0	2.70	2	–	17.5	7.2
M8	NA	3	110.0	116.0	2	5	280	0.30	450	44	E	24	8.7c	74	42	1.0	1.80	2	–	17.5	5.6
N8	NA	1	87.5	110.0	1.5	3	286	1.69	200	35	A		8.7c	48	25	1.0	3.30	2	–	17.0	6.3
R	NA	1	88.0	85.5	2.4	5	220	–	–	–	A		8.1	44	23	1.0	3.30	2	e	17.0	–
S1	NA	1	88.0	85.5	2.4	5	220	–	–	–	A		8.1	44	23	1.0	3.30	2	E	17.0	–
S2	NA	1	88.0	85.5	2.4	5	220	–	–	–	A		8.1	44	23	1.0	3.30	2	e	17.0	–
A9	NA	4	105.0	120.0	2.7	5	200	1.37	800	55	V	q	9.9	60	33	1.0	2.10	2	–	18.0	7.0
B9	T	4	105.0	120.0	2.5	5	240	1.37	600	75	E	t	9.9	62	36	1.8	2.10	2	–	18.0	9.5
C9	TA	6	175.0	220.0	1.5	8	330	M	800	600	Z		9.9	130	70	2.5	1.00	4	–	14.5	17.0
D9	TA	8	280.0	320.0	0.8	8	550	M	700	3200	A		9.9	220	120	4.0	0.80	4	–	11.0	24.4
E9	TA	1	124.0	165.0	1	8	240	–	800	255	C		–	100	55	2.5	1.80	4	–	18.0	22.0
A10	NA	4	105.0	120.0	2.2	5	200	0.59	680	60	E	t	9.9	60	33	1.0	2.10	2	–	18.0	7.5
C10	TA	4	110.0	116.0	2.2	5	200	1.37	650	65	E	28	8.7c	74	42	1.5	1.80	2	–	17.0	8.3
D10	TA	9	280.0	320.0	1	8	550	m	1000	2350	A		9.9	220	120	4.0	0.80	4	–	12.0	18.3
E10	TA	6	118.0	135.0	1.5	4	350	0.60	600	105	E	18	–	63	34	2.0	2.20	2	–	17.0	10.2
F10	NA	6	100.0	120.0	2.5	4	290	0.59	600	57	E	32	8.7b	55	30	1.0	2.70	2	–	17.5	7.1
G10	TA	6	102.0	120.0	2.5	6	260	1.37	600	85	E		8.7b	56	30	1.8	–	2	–	17.5	9.8
H10	NA	1	140.0	152.0	1.5	8	203	0.62	p	p	T		–	–		1.0	–	2	e	14.1	–
B10	T	4	105.0	120.0	2.2	5	240	0.38	485	75	E	t	9.9, 12.3	62	36	2.0	2.50	2	TI	18.0	10.3
A11	NA	1	82.5	114.3	1.3	–	–	–	–	–	–	35*	SI	–	–	–	–	–	e	7.0	3.8**
C12	NA	4	105.0	120.0	1.5	5	200	0.59	600	58	E	18	12.3	60	33	1.0	2.50	2	TI	18.0	8.1
D12	T	4	105.0	120.0	1.5	5	240	0.38	650	88	E	22	12.3	62	36	2.0	2.50	2	TI	18.0	12.0
E12	NA	6	100.0	120.0	1.5	5	180	z	550	57	E	10	12.3	55	30	1.0	2.70	2	TII	17.5	8.1
F12	NA	1	124.0	130.0	2.3	5	226	z	675	80	F	11	12.3	74	40	1.0	2.70	2	TII	18.0	6.4
G12	T	4	105.0	125.0	2.5	5	240	0.38	700	72	E	22	12.3	62	36	2.0	2.50	2	TI	18.0	8.7
H12	TA	4	105.0	125.0	2.5	5	240	0.38	725	75	E	22	12.3	62	36	2.1	2.50	2	TI	18.0	9.1
I12	TA	4	105.0	125.0	2.5	5	250	0.38	725	75	E	22	12.3	62	36	2.3	2.50	2	TI	18.0	9.1
K12	TA	4	105.0	120.0	1.5	5	240	0.38	525	112	E	15	12.3	62	36	2.3	2.50	2	TI	18.0	15.2
L12	TA	6	104.0	113.0	2.4	5	225	z	463	61	V	12	12.3	62	27	2.1	2.30	2	EII	17.5	8.6
M12	TA	6	104.0	113.0	2.4	5	228	z	775	76	V	12	12.3	62	27	1.9	2.30	2	EII	17.5	10.8
N12	TA	6	104.0	113.0	2.4	5	228	z	834	82	V	12	12.3	62	27	1.9	2.30	2	EII	17.5	11.7
O12	TA	6	107.3	121.0	2.4	6	175	z	802	64	V	11	12.3	64	28	2.0	2.50	2	EII	17.5	7.8
P12	TA	6	107.3	121.0	2.4	6	190	z	812	76	V	11	12.3	64	28	2.2	2.50	2	EII	17.5	9.2
L16	TA	1	137.2	165.1	2.1	6	158	m	1500	114	C	x	16.13	98	e	e	0.50	4	e	15.5	–

M16	TA	1	82.0	90.4	4	7	141	m	860	16	C	y	16.1	46	e	e	2.2	4	e	16.6	–
S16	TA	1	82.0	90.4	4	8	133	m	1600	22	C	z	16.13	51.3	e	e	vs	4	e	14.3	–
H16	TA	1	137.2	165.1	2.1	8	217	m	1600	274	C	w	16.13	97.8	e	e	0.5	4	e	16.1	–

Varied swirl	vs	2.2–5.6
Emission norms	EII	Euro-2 on road
	TI	US Tier -1 off road
	TII	US Tier -2 off road
Engine	e	experimental engine
Fuel pump	V	rotary distributor type pump, VE
	E	inline block pump, PE-A
	Q	individual fuel pump submerged in the crank case, PF-Q
	A	individual fuel pump above the crank case, PF-A
	Z	large Individual fuel pump above the crank case, PF-Z
	C	common rail system, CRS
	T	Cummins PT injection system
Nozzle	m	minisac
	z	zero sac, with 10% hydro eroded holes
	P	Pintle type
Fuel timing	x	–35 to –5
	y	–39 to –21
	z	–35 to –5
	w	–10 to 10
	t	15–22
	q	10–12
	r	13–20
	*	spark ignition timing
Valves	4	for engine types H8, J8, C9, D9, D10
	2	rest of the engines
Aspiration	NA	naturally aspirated
	T	turbocharged
	TA	turbocharged aftercooled
Combustion chamber	SC	prechamber type with swirl chamber, IDI
	S	saurer combustion chamber in the piston with pintle nozzle
	SI	spark ignition
	others	direct injection type with combustion chamber in the piston
General	–	not relevant for analysis or not applicable
	p	variable
	**	imep

The cylinder pressure was measured using uncooled AVL piezoelectric pressure transducer of type GM11D or AVL cooled pressure transducer of type GM12D in engines. Here the length of the duct leading the pressure from the cylinder to the transducer was very short. In the engines was used. The line pressure was measured using strain gage type pressure transducer from AVL of type 31DP2000-2.0, GG0443. The needle lift was measured using by building in a linearly variable differential transformer. The crank angle position was sensed using an angle encoder. The engine is loaded using an eddy current brake. All the transient signals from different transducers and the encoder are fed into an indicating system. Here, there are signal conditioners and amplifiers and a computer to process all the signals for calculating thermodynamics like heat release rate and other details like the duration of injection, ignition delay and peak values of various pressures.

Injection characteristics and the indicated diagrams

A schematic diagram of the experimental set up is shown in Fig. 3.7. Further, to filter out the fluctuations in pressure due to physical effects in the cylinder, and the duct leading the pressure to the transducer, a moderate smoothening of the pressure diagram is optionally carried out using the moving average software in the indicating system. However, since the smoothening was done over a duration of 2° crank angle the missing of first peak is more due to higher compression ratio and delayed fuel injection than due to smoothening.

Figure 3.8 shows typical traces of line pressure, cylinder pressure, needle lift and apparent heat release of the turbocharged engine, B10 at 90% load.

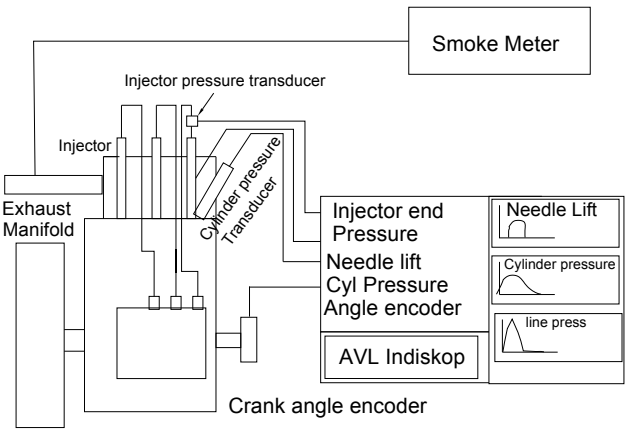

Fig. 3.7 Experimental set up

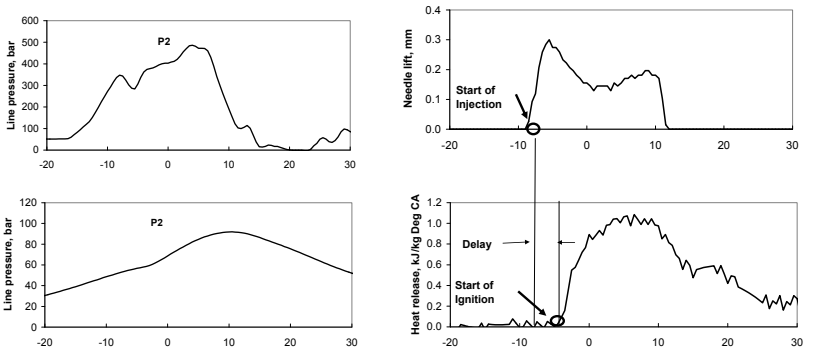

Fig. 3.8 Injector and in-cylinder characteristics of turbocharged engine, B10 at 90% load

Exhaust raw gas analysis

The gaseous emissions, smoke and particulate sampling probes were fitted at least 0.5 m or three times the diameter of the exhaust pipe as to ensure an exhaust gas temperature of at least 343 K (70°C) at the probe. In the case of a multi-cylinder engine with a branched exhaust manifold, the inlet of the probe was located sufficiently far downstream so as to ensure that the sample is representative of the average exhaust emissions from all cylinders. The test set up meets the requirements of ISO 8178 for intake air, fuel and emission measurements. Commercially available gas analysers were used.

Hydrocarbon (HC) measurement

Gaseous HC emissions from diesels are measured using a hot particulate filter at 190°C and a heated FID. Thus, the HC constituents varying from methane to the heaviest hydrocarbons remain in the vapour phase in the heated sampling line which is also maintained at about 190°C. Any hydrocarbons heavier than this are therefore condensed and with the solid phase soot, are filtered from the exhaust gas stream upstream of the detector. Figure 3.9 shows the heated Flame ionisation detector used for the analysis of HC emission. The flame in an FID instrument is usually generated by combusting a 40% H_2/60% He mixture in air. Any oxygen present in the sample influences FID analyzer. To minimize this effect, zero and reference gases are used with O_2 content close to that of the gas to be measured. FID instruments are unaffected by the water vapor in the analysed gas.

Oxides of nitrogen (NO_x) measurement

$$NO + O_3 \rightarrow NO_2^* + O_2$$

where NO_2^* represents the excited state molecule.

Only about 20% of the NO_2 that is formed is in the excited state. This NO_2^* reverts back to the ground state while emitting electromagnetic radiation.

$$NO_2^* \rightarrow NO_2 + hv$$

The *hv* represents the radiated electromagnetic emission, which is in the wavelength range between 600 and 3,000 nm, with intensity maximum at approximately 1,200 nm. The light emission is filtered to eliminate interference from other gases, such as CO, SO_2 and unsaturated hydrocarbons. This chemiluminescence signal is detected photo-electrically by a photo multiplier tube. This signal is proportional to the NO concentration in the sample gas. When NO_x measurement is to be done, the exhaust sample is first rooted through a converter heated to a specific temperature. The temperature of the converter is typically between 350°C and 650°C. The converter reduces NO_2 present in the exhaust to NO. Then the exhaust containing only NO is rooted to reaction chamber and measurement is done as explained earlier. Figure 3.10 shows the schematic diagram of a typical NO_x analyser used for measurement of emissions.

Smoke evaluation

Smoke is evaluated by using opacity principle as well as filtering method. In current study, AVL Opacimeter-439 and Bosch smoke gun were used to collect smoke data. Opacimeter measures the opacity of a sample of the exhaust gas extracted from the exhaust pipe and passed through a heated measurement-chamber. Since condensation of hydrocarbon and water is avoided, due to heating of the exhaust the measured opacity is only by black carbon. Figure 3.11 illustrates the operating principle, which involves measuring the opacity of a portion of exhaust gas continuously flowing through the sample tube. Zero reference is achieved by a switching arrangement utilizing a second tube containing clean air, free of smoke. An internal electric fan purges the instrument case and clears soot from the light source and photocell. The calibrated ammeter reads in units from 0 (clear) to 100 (opaque). Since the length of the smoke-tube is fixed and known, these readings can be related to measurements made with other instruments by means of the Beer-Lambert law. The smoke reading is not affected by exhaust pipe diameter. Transient response is limited to the time required to fill the sampling tube.

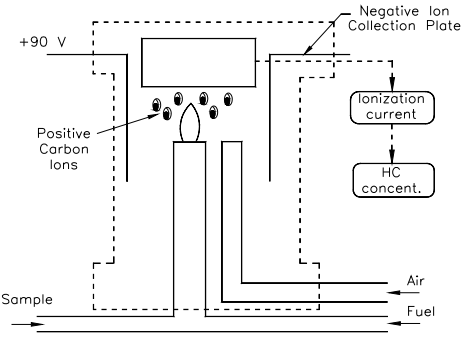

Fig. 3.9 Flame ionisation detector for HC measurement

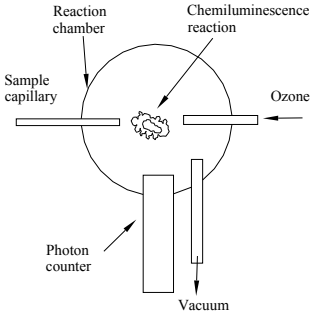

Fig. 3.10 Principle of chemiluminescence

Bosch smoke-gun, on the other hand, works on filtering principle wherein soot particles are collected on a filter medium from a known volume of the exhaust. The filter is evaluated by comparison with standards using photoelectric reflectance method. Both the methods mentioned above are partial flow systems having maximum error of 0.2 BSU, which is the uncertainty in the experiments. The average of three readings was acquired for exhaust smoke data. An example of the filtering type system is a portable Bosch smoke gun shown in Fig. 3.12. A spring-operated sampling pump draws a fixed volume of exhaust gas from the exhaust stream through a controlled density paper filter disc.

Soot particles from the sample are deposited on the filter disc, causing it to darken in proportion to soot particle concentration. A separate 110 V AC or battery-powered photoelectric device measures the light reflected from the darkened filter disc. The readout is calibrated in 0–10 units. Figure 3.13 shows the operating principle of the photoelectric evaluation system. The calibration of the photoelectric readout consists of zero adjustment with the detector exposed to clean filter and full-scale reading with the switched off.

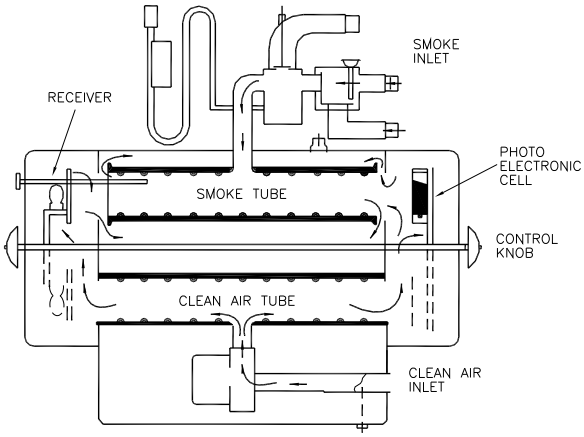

Fig. 3.11 Operating principle opacity meter

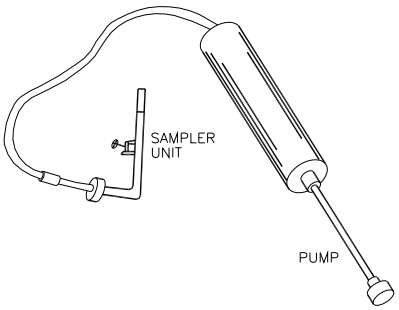

Fig. 3.12 Portable Bosch smoke gun

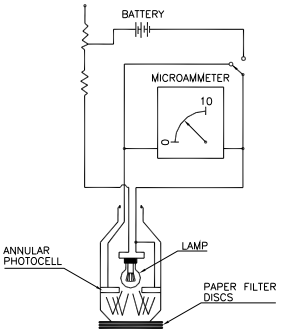

Fig. 3.13 Photoelectric evaluation system

References

Beer JM, Chigier NA (1972) Combustion Aerodynamics. Applied Science Publishers

Bradshaw P, Cebeci T, Whitelaw JH (1981) Eng Calculations for turbulence flow. Academic Press

Chiu WS (1973) The experimental set up for basic diesel spray mixing and combustion studies. Cummins Tech Report doc 3534

Chmela FG, Orthaber GC (1986) Rate of heat release prediction for a direct injection diesel engine based on purely mixing controlled combustion. SAE 99010186

Dent JC (1980) Potential applications of holographic interferometry to engine combustion. Combustion modelling in reciprocating engines, Plenum, New York

Dent JC, Keightley JD, DeBoer CD (1977) Application of interferometry to air fuel measurements. SAE 770825

Lakshminarayanan PA, Dent JC (1983) Interferometric Studies of Vapourising and Combusting Sprays. SAE 830244

Martin MK, Heywood JB (1977) Approximate relationship for the thermodynamic properties of hydrocarbon-air combustion products. Combustion Science and Technology

Matulka RD (1970) The application of holographic interferometry to the determination of asymmetric 3-dimensional density fields in free jet flows. PhD Thesis, US Naval Postgraduate School

Tennent RM (1971) Science Data Book. Oliver and Boyd

Yu RC, Wong VW and Shahed SM (1980) Sources of Hydrocarbon emissions from direct injection diesel engines. SAE 800048

4 Turbulent Structure of the Diesel Spray

Abstract Holographic interferometry has been applied to the study of concentration and temperature distribution in transient vaporising non-burning and burning fuel sprays in a quiescent bomb. Semi-theoretical relations have been obtained in this chapter to describe the axial and radial variations of concentration in the vaporising non-burning spray, and to evaluate penetration of sprays and air entrainment in the free and wall jet regions of non-burning and burning sprays. The movement of the 'tail' of the spray in the post injection period is studied. The data are presented for species concentration and temperature profiles within the burning spray. The equations form the basis for building the phenomenological models of ignition delay, emissions and heat release rate in the next chapters.

Combustion in a diesel engine involves the transient injection of a finely atomised liquid fuel into air at high temperature and pressure. Auto-ignition of these regions and progressive diffusive burning of the remainder of the spray follow rapid vaporisation at the edges of the spray.

The ability to study the processes of vaporisation and combustion in the injected fuel spray to obtain quantitative information on the spatial and temporal distribution of air, fuel vapour, combustion products and temperature is of importance in gaining a better understanding of these basic processes, and in providing data for computer modelling and engine development studies (Shahed *et al.* 1975). Based on the study a full description of the penetration of the spray when it is free, and later when it impinges on the wall and finally detaches from the nozzle tip. The distribution of concentration of fuel vapour in the free and wall jets and description of the liquid core (Lakshminarayanan and Dent 1983) and additionally, the flame structure of a transient burning diesel spray are described.

Vaporising Spray

Free jet region

The free portion of the jet was nearly conical, subtending a half cone angle of approximately 13°, at a virtual source lying upstream of the orifice. To establish the similarity characteristics of the jet vapour concentration profiles, the ratio of concentration at any radial position (for a given axial distance from the jet orifice) to the maximum concentration at the same axial position, was plotted against the radius, non-dimensionalised with respect to the radius at which the concentration has half its maximum value $R_{0.5}$ (Fig. 4.1).

P.A. Lakshminarayanan and Y.V. Aghav, *Modelling Diesel Combustion*, Mechanical Engineering Series, DOI 10.1007/978-90-481-3885-2_4,

The variation of $R_{0.5}$ was plotted against axial distance from the orifice, x (Fig. 4.2). The results show considerable scatter particularly after the termination of injection. To completely describe the jet behaviour we need to know the decay in concentration with axial distance, x. The literature (Steward and Guruz 1977) for steady state jets suggests

$$\frac{1}{C_{f_{\max}}} = const\left(\frac{x}{d_e}\right) \tag{4.1}$$

where d_e is the orifice equivalent diameter and for the non-burning jet is defined as $d_o \times$ [density of injected fuel/density of air in bomb]$^{1/2}$. Equation (4.1) is valid for the region beyond the liquid (potential) core of the jet, which extends from between four and six times (x/d_e) from the nozzle exit plane.

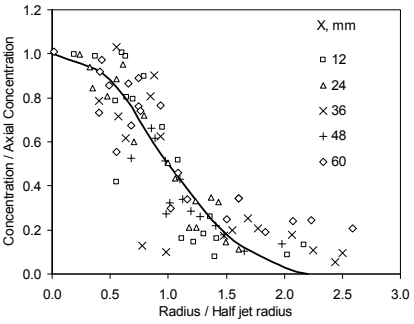

Fig. 4.1 Radial variation of concentration for a typical vaporising free jet (data B)

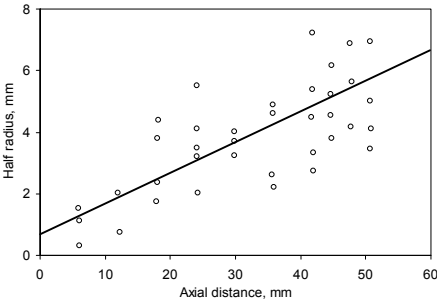

Fig. 4.2 Axial variation of half radius for a typical vaporising jet (data B)

The vaporisation history during the injection process is built up from a sequence of individual interferograms, which represent particular instants in time of the jet's development, as shown in Fig. 4.4. In analysing the variation of C_{fmax} with x/d_e from individual interferograms, it was found as expected that vaporisation and hence C_{fmax} increased progressively with distance, x/d_e from the nozzle orifice. This variation was found to be nearly linear with (x/d_e) and intersected the curve described by equation (4.1) at a value of x/d_e

$$x/d_e = 7.5 \text{ for time } t < t_{inj} \tag{4.2}$$

where t_{inj} = the injection period.

x_o defines the distance from the orifice beyond which the variation of C_{fmax} with axial position, x follows equation (4.1).

When $t > t_{inj}$, injection has ceased, yet a jet like structure is observed (Fig. 4.4). It would be expected that under these conditions, C_{fmax} would be lower than indicated by equation (4.1). In fact analysis of interferograms showed that C_{fmax}

follows a linear variation with (x/d_e) when $t > t\ inj$ and intersects the steady state $C_{f\,max}$ curve (equation (4.1)) at values of (x_o/d_e) progressively larger than 7.5.

A schematic summarizing the probable behaviour of the transient vaporising jet is shown in Fig. 4.3. From Fig. 4.3 the transient evaporating fuel injection process can be considered as the introduction of successive packets of fuel along a steam line coincident with the jet axis. Each packet is made up of a number of elemental sub packets. If it is assumed that the injection period is $5\,\Delta t$ say, then 0, 1, 2 … 5 in Fig. 4.3a represent the distribution of mixture packets injected at times $0, \Delta t, 2\,\Delta t \ldots 5\,\Delta t$. Because of shear and turbulent diffusion, the sub packets and the vaporising droplets and vapour have the distribution from shown in Fig. 4.3a. Packet 4 say, had at $t - \Delta t$, the same state as packet 5 at t. The change in concentration of vapour in packet 4 in the time interval Δt from $t - \Delta t$ to t is due to the combined effects of

- Dilution due to entrained air (B)
- Vaporisation of liquid (C)

The time history of packet 4 between $t - \Delta t$ and t is shown by ABC in Fig. 4.3a. Point 3 on Fig. 4.3a represents the packet with the maximum vapour concentration.

For instants in time greater than the injection period ($t > 5\,\Delta t$) represented schematically in Fig. 4.3b. The jet-like structure is still maintained, turbulent mixing occurs entraining air into the jet like plume, but packets of fuel are not replenished by the nozzle. Therefore, regions near the nozzle tip will be leaner than at the instant injection was complete $(5\,\Delta t)$. Sub packets on the centreline will still move downstream at a faster rate than those near the edges of the plume. Furthermore, no appreciable increase in jet width is observed. Therefore, the concentration profile across the plume near the nozzle tip is likely to be very flat in the central regions as shown in Fig. 4.4.

The concentration at $6\Delta t$ of the central region of the plume at plane MM is $C_{fmax,\,M}$ and is shown in Fig. 4.3b. Figure 4.5 is a plot of the experimental data. Projection of the linear variation of C_{fmax} with x/d_e to a common origin yields the virtual source of the nozzle, at a distance, δ from the exit plane of the orifice. The decrease in C_{fmax} and jet centreline velocity $U_{C.L}$ following the end of injection will be governed by equations having the form of equation (4.1). The variation of x/d_e will follow the penetration relationship derived in reference (Dent 1971), and is given by

$$x_o / d_e \propto \sqrt{\left[\left(\Delta p / \rho_0\right)^{\frac{1}{2}} \frac{\left(t - t_{inj}\right)}{d_e} \right]} \tag{4.3}$$

Figure 4.6 is a plot of experimental data using equation (4.3) with the assumption of constant fuel density (ρ_f). The intercept gives the characteristic value of $x_o/d_e = 7.5$ for the transient vaporising fuel spray during the period of

injection. From the foregoing discussion, the vapour concentration at a particular instant and at any location within the injected spray can be determined as follows.

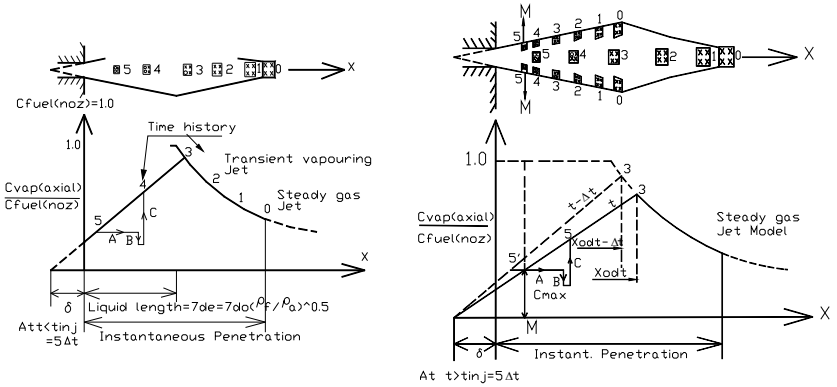

(a) (b)

Fig. 4.3 Scheme of jet detachment and vaporisation

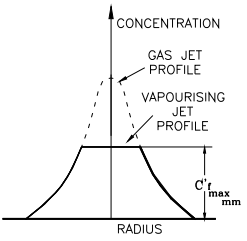

Fig. 4.4 Radial profile of concentration in a vaporising jet

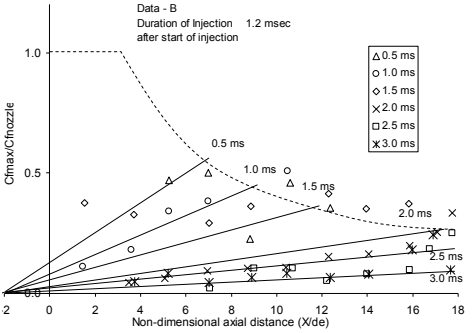

Fig. 4.5 Axial decay of concentration, after end of injection

Equation -4

$$\text{Half Jet Angle } \tan(\textit{cone angle}/2) = 0.22$$

$$\text{Variation of } x_o\text{: } x_e/d_e = 7.5 + 1.71\sqrt{\left[(\Delta p/\rho_l)^{0.5}\frac{(t-t_{inj})}{d_e}\right]}$$

$$\text{Virtual Source, } \delta \text{ is given by } \delta/d_e = 2.3$$

Variation of $C_{f_{\max}}$ (Fig. 4.13)

$$\text{If } \frac{x}{d_e} > \frac{x_0}{d_e},\ C_{f_{\max}}(x) = 5.2\, C_{f_{\max}}(x_0) \quad \left[\frac{d_e}{x+\delta}\right]$$

$$\text{If } \frac{x}{d_e} > \frac{x_0}{d_e},\ C_{f_{\max}}(x) = C_{f_{\max}}(x_0) \quad \left[\frac{x+\delta}{x_0+\delta}\right]$$

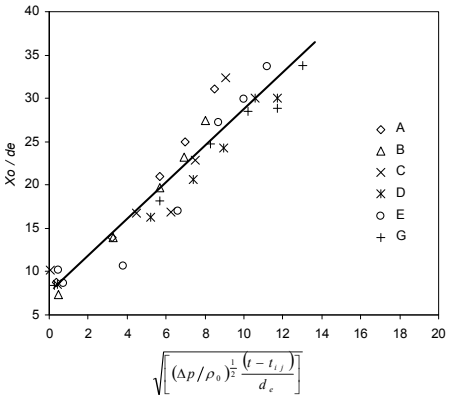

Fig. 4.6 Jet detachment studies

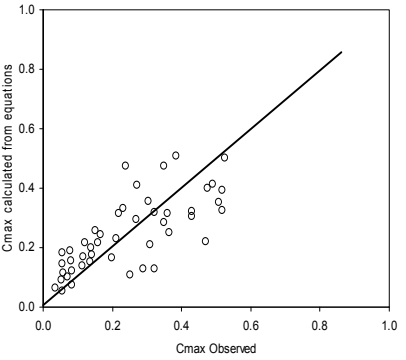

Fig. 4.7 Axial concentration in free jet (data B)

Variation of C_f with radius, r and Axial Distance, x (Fig. 4.14)

$$\text{For } \frac{x}{d_e} > \frac{x_0}{d_e},\ C_f(r,x) = C_{f_{\max}}(x)\ \exp\left(-203\left[\frac{r}{x+\delta}\right]^{2.5}\right) \tag{4.4}$$

$$\text{For } \frac{x}{d_e} > \frac{x_0}{d_e},\ C_{f_{\max}}(r,x) = C_{f_{\max}}(x)\exp\left(-203\left[\frac{r}{x+\delta}\right]^{0.25}\right)$$

$$\text{or } = C'_{f_{\max}} \text{ Which ever is smaller (Fig. 4.4).}$$

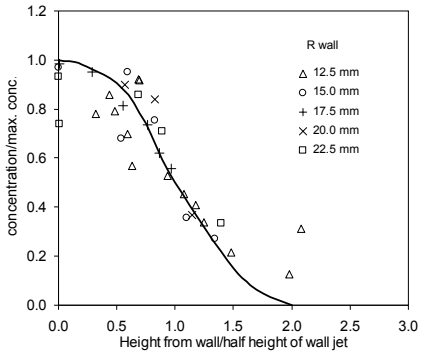

Fig. 4.8 Variation of concentration at any radius of wall jet (data B)

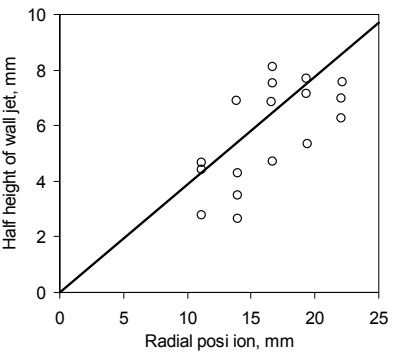

Fig. 4.9 Variation of height of wall jet (data C)

The variation between computed results using the set of equations (4.4) to evaluate C_{fmax} (x) and $C_f(r, x)$, and experimental data are shown in Figs. 4.7, 4.13 and 4.14, respectively.

Wall jet region

Figure 4.15 shows a schematic of the wall jet, and the notation used. Experimental data for the variation of $C_f(y, s)/C_{f\,max}(s)$ with $(y/y_{0.5})$ is shown in Fig. 4.8, where $y_{0.5}$ is the distance at which the vapour concentration is half its maximum value. Figure 4.9 shows the variation of y with thickness (y) of the wall jet, as obtained from experiment. The variation of C_{fmax} with distance, s along the wall was found to follow a hyperbolic relationship approximately (Fig. 4.10).

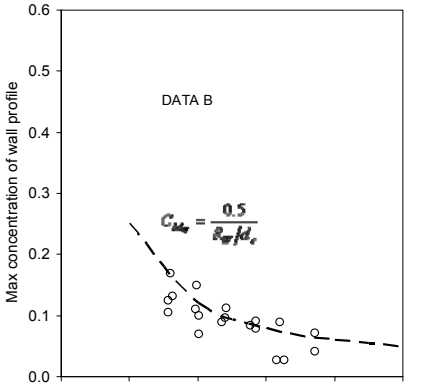

Fig. 4.10 Maximum concentrations in the wall jet along the non-dimensional length along the all

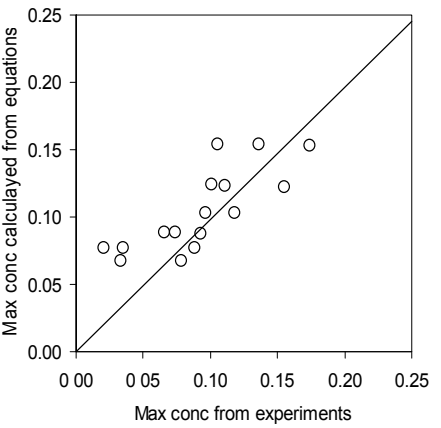

Fig. 4.11 Comparison of maximum concentration calculated using equation (4.8) and experiments for a typical wall jet (data B)

The following relationships were established for the wall jet.

$$\text{For } S > 0.2(x+\delta) \text{ and } (x+\delta) > 0.9(H+\delta)$$

$$C_{f_{w(\max)}} = 0.5\,\frac{d_e}{s} \tag{4.5}$$

$$C_{f_{w,y}} = C_{f_{w(\max)}} \cdot \left[\exp\left(-16.5\left(\frac{y}{s}\right)^{2.9}\right)\right]$$

Figures 4.11 and 4.12 show the comparison between calculated and experimental values of $C_{f_{w(\max)}}$ and $C_{f_{w,y}}$ respectively.

Using equations (4.4) and (4.5) and a modified value of d_e, the values of mixture fraction during combustion were calculated at every point in the jet. Justification for use of equations (4.4) and (4.5) derived from experiments with Pentane, for prediction of mixture fraction of diethyl ether can be made on the basis that the equations are non-dimensional in nature. This is illustrated in Figs. 4.13 and 4.14 where comparison of results obtained with equations (4.4) and (4.5) in this study is plotted with results obtained by Steward and Guruz (1977) for compressed air jets with CO_2 tracer. In the transition region where the jet commences spreading into a wall jet flow (Fig. 4.15) the concentration in the jet can be reasonably described using the expressions derived for a free jet, equation (4.4).

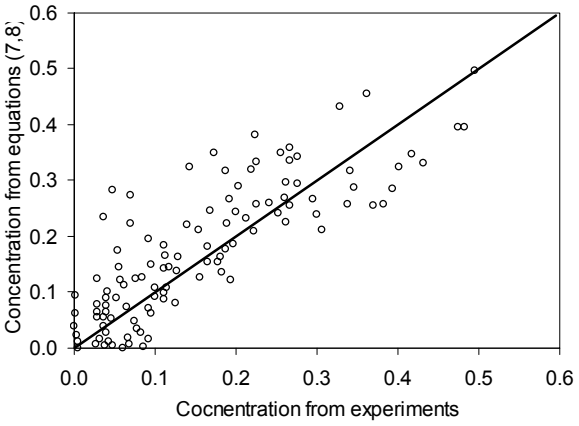

Fig. 4.12 Comparison of calculated concentration of many vaporising jets (free and wall) at many points with the values observed (data B)

On completion of injection, the equations (4.5) slightly overestimate the actual concentrations. With the limited experimental data, an explanation can be provided using a diagram similar to Fig. 4.3b. The point which separates the hyperbolic curve (representing the steady state behaviour of the wall jet) and the straight line (representing the transition developing phase of the wall jet flow), moves continuously away from the stagnation point with time. Extending the argument presented for the case of detaching free jets, the maximum concentration along the radius, *s* (Fig. 4.15) falls approximately on a straight line joining the maximum concentrations at the impingement point and the point separating the steady and transition portions of the wall jet. As the difference between the two values is not large, the assumption that the separating point lies on the radius where the steady wall jet maximum concentration is equal to the concentration at the point of impingement, produced reasonable results, for the present set of conditions.

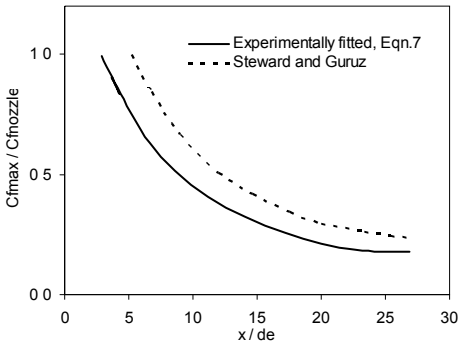

Fig. 4.13 Comparison of axial concentration decay of a transient and a steady jet

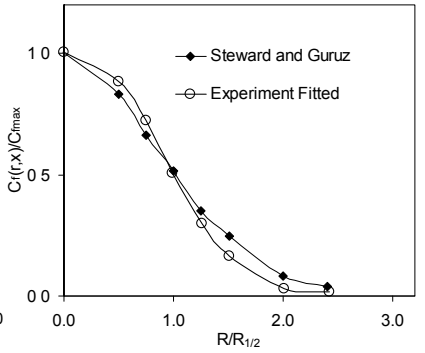

Fig. 4.14 Comparison of radial concentration profiles (fitted from Experiments, Steward and Guruz)

Jet penetration and entrainment of air

The penetration of the jet with time and the rate of air entrainment into it are two important characteristics that need to be known. Comparison of experimental data on jet penetration was made with the relationship obtained by Dent (1971) and the results shown in Fig. 4.16, where agreement is seen to be reasonable. The penetration of the wall jet was investigated in a similar manner, and is plotted against

$$\sqrt{\left[\left(\frac{2\,\Delta p}{\rho_f}\right)^{\frac{1}{2}} d_e t_{imp}\right]} \tag{4.6}$$

Here t_{imp} is the time following jet impingement. The results are shown in Fig. 4.17, from which the wall jet penetration s is

$$s = 0.75 \sqrt{\left[\left(\frac{2\Delta p}{\rho_f} \right)^{\frac{1}{2}} d_e \, t_{imp} \right]} \tag{4.7}$$

For a steady state free jet, the entrainment relationship of Ricou and Spalding (1961) has the form

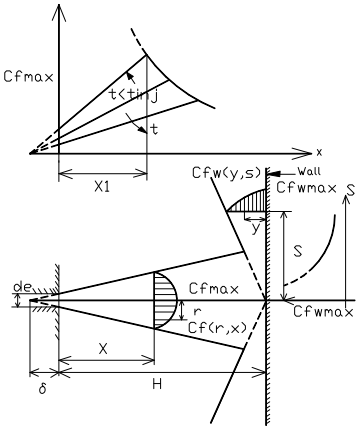

Fig. 4.15 Notations used in the text

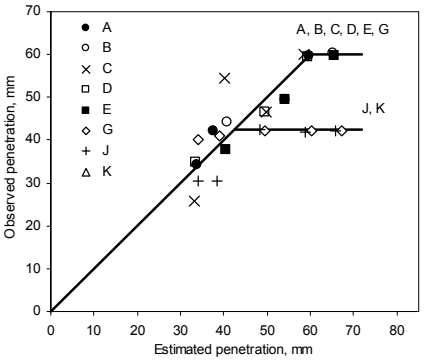

Fig. 4.16 Penetration of free jets

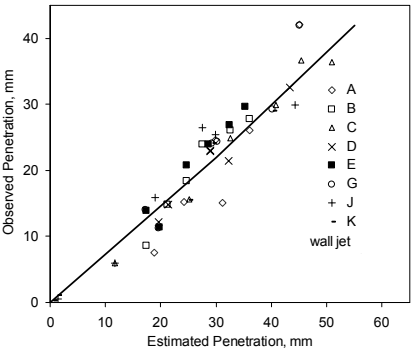

Fig. 4.17 Penetration of wall jets

$$\frac{\dot{m}_a}{\dot{m}_0} = 0.32 \frac{x}{d_e} - 1 \tag{4.8}$$

Here m'_a and m'_o are the rate of air mass entrained into the jet, and the rate of mass flow of the jet fluid through the orifice respectively. Rewriting equation (4.8) as

$$\frac{\dot{m}_a}{\dot{m}_0} = A_f \frac{x}{d_e} - 1 \tag{4.9}$$

and integrating with respect to time, t results in

$$\dot{m}_a = \dot{m}_0 \int_{t_0}^{t} A_f \frac{x}{d_e} - 1 \tag{4.10}$$

Here t_o = time taken by the jet to penetrate a distance equal to the potential core.

From Ricou and Spalding (1961)

$$\frac{dx}{dt} = 4\, U_j \frac{d_e}{x} \tag{4.11}$$

$$\dot{m}_0 = \frac{\pi}{4} d_o^2 \rho_f U_j = \frac{\pi}{4} d_e^2 \rho_a U_j \tag{4.12}$$

$$\dot{m}_a = \frac{\pi}{16} d_e^2 \rho_a \left[\frac{A_f}{3} \left(\frac{x}{d_e} \right)^3 - \frac{1}{2} \left(\frac{x}{d_e} \right)^2 \right]_{x_o(t)}^{x(t)} \tag{4.13}$$

Here $x_o\,(t) = d_e / A_f$ is the distance below which are entrainment is absent.

Substituting the limits and simplifying yields

$$\frac{\dot{m_a}}{\frac{\pi}{16} d_e^3 \rho_a} = \frac{A_f}{3} \left(\frac{x}{d_e} \right)^3 - \frac{1}{2} \left(\frac{x}{d_e} \right)^2 + \frac{1}{6} \left(\frac{1}{A_f} \right)^2 \tag{4.14}$$

A plot of the left-hand term of (4.14) obtained experimentally against the right-hand term calculated for various X and A_f values, is shown in Fig. 4.18. It can be seen that a value of 0.32 for A_f underestimates the experimentally observed entrainment and that a value around 0.5 is reasonable and is close to the value of 0.45 observed by Bremhorst and Watson (1981) in their study of air entrainment into pulsed jets.

Extending the above idea for a wall jet shown in Fig. 4.15, the total rate of air entrainment into the free and wall jets is given by

$$\frac{\dot{m}_a}{\dot{m}_0} = A_f \frac{H}{d_e} + A_w \frac{s}{d_e}, \text{ where } A_f = 0.5 \tag{4.15}$$

Using equation (4.7) in equation (4.15) and integrating, the mass of air in the wall jet portion alone results in

$$m_{a_w} = \frac{\pi}{4z^2} \rho_\infty \left[A_f \, H \, s^2 + \frac{2}{3} A_w \left(s^3 - w^3 \right) \right] \tag{4.16}$$

Here z is the constant of proportionality in equation (4.7) and w is the radius of the free jet at $x = H$. The agreement between computed values of maw with experimental data was obtained for $A_w = 0.95$. This is shown in Fig. 4.19. This value of A_w is close to the value of 0.86 given by Hartel (1962).

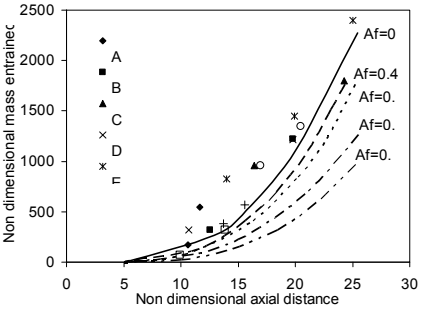

Fig. 4. 18 Air entrainment in a free jet

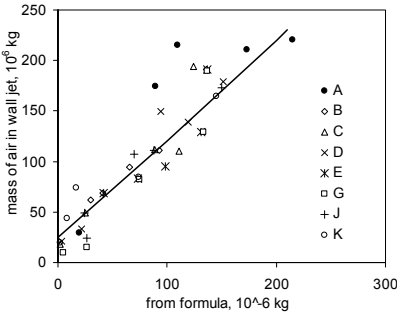

Fig. 4.19 Entrainment of air in a wall jet

Equations (4.5) and (4.7) were compared with wall jet data observed for an impinging steady state jet on a flat surface (Rajaratnam 1976). It was found that wall jet penetration and thickness differed substantially from the data in the penetration rate being nearly half and the half thickness about three times that observed in the above reference (Rajaratnam 1976).

Combusting Sprays

The refractive index at every point in the jet is calculated from the fringe counts using the procedure as by Dent *et al.* (1977) and Dent (1980). The fringe counts were assumed to decrease up to the radius where the refractive index calculated would be such that the temperature of the products of combustion would correspond to the adiabatic flame temperature for the mixture fraction; beyond this point

and up to the axis of the jet the fringe count increases (Fig. 4.20). The refractive index and mixture fraction at any point are used to find the temperature from the chart of T, $n - 1$, Φ (Fig. 3.6), up to the rich limit. Beyond the rich limit, fuel vapour and products of combustion at the rich limit are present. The concentration of the fuel vapour is given by (Appendix I).

$$C_f = \frac{C_{(r,x)} - C_{R\,L}}{1 - C_{R\,L}} \tag{4.17}$$

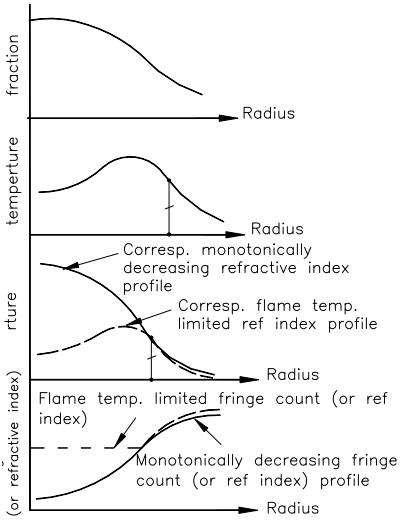

Fig. 4.20 Counting fringes in a burning jet

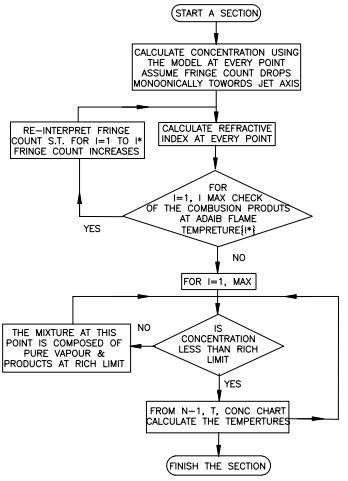

Fig. 4.21 Computational flow chart

Here $C_{R,L.}$ refers to the mixture fraction at rich limit combustion. If the combined Gladstone-Dale constant and average molecular weight of the products of combustion at the rich limit is K_b and M_b respectively (Appendix II), the temperature at any point in the jet can be calculated as

$$T_r = \frac{T_\infty}{M_\infty} \frac{C_f K_f + (1 - C_f) K_b}{\left(K_\infty + \dfrac{n_r - n_\infty}{\rho_\infty}\right)\left(\dfrac{C_f}{M_f} + \dfrac{(1 - C_f)}{M_b}\right)} \tag{4.18}$$

Here ∞, r and f refer to the surroundings, considered point in the jet and fuel vapour. The entire scheme of calculation is summarized in Fig. 4.21.

Figures 4.22–4.24 shows radial variation of temperature at various axial stations from the orifice. Near the nozzle axis the temperature is high, and away from it, the temperature drops. For a time 1.5 ms after the start of injection the

temperatures along the axis of the jet are low and remain so along the whole length of the jet indicating a cool central core region. The temperature increases in the radial direction, reaches a peak and decreases sharply towards the edge of the jet. By 2.5 ms after injection, the central regions of the jet have reached temperatures of the order of the adiabatic flame temperature along the length of the jet. This indicates that strong air entrainment into the tail and central regions must occur. By 3.5 ms, this entrainment appears to have caused a decrease in the temperature of the central regions of the jet from about half the jet length to the tip, the presence of the deflection plate causing a considerable drop in temperature. The tail half of the jet remains at remarkably high temperatures indicating reduction in entrainment.

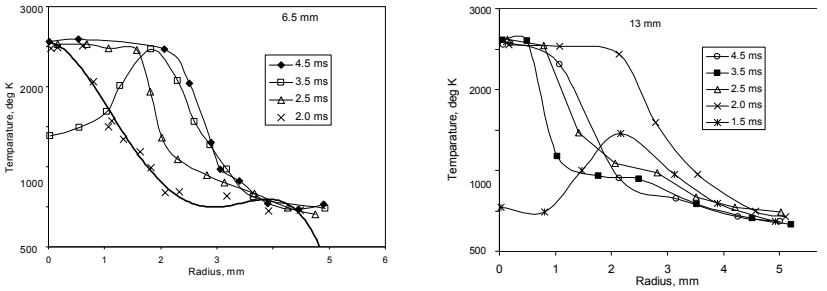

Fig. 4.22 Radial temperature profiles

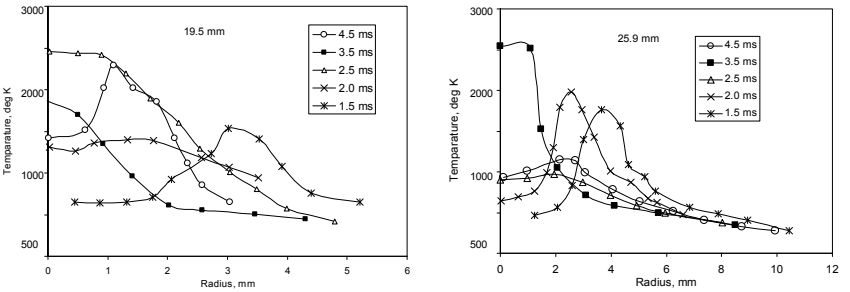

Fig. 4.23 Radial temperature profiles

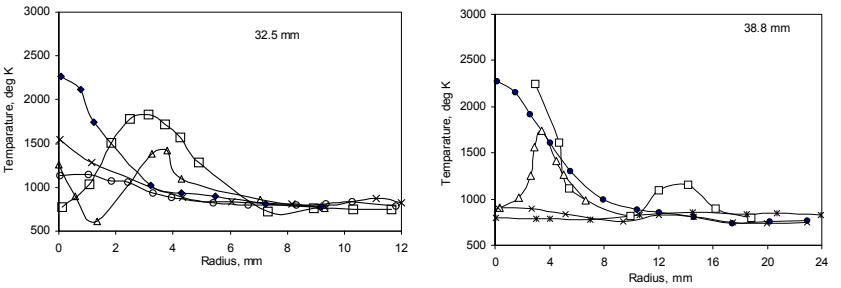

Fig. 4.24 Radial temperature profiles

The concentrations of water vapour, CO_2 and CO vary according to the completion of combustion (Figs. 4.25–4.27). For example, at a distance of 19.5 mm from the nozzle, H_2O and CO_2 increase and then decrease from the periphery to the axis of the jet. The maximum is reached when the mixture fraction is stoichiometric. This peak in the profile disappears at larger intervals of time (e.g. –2.5 ms) due to mixing and entrainment of air. The concentration of oxygen decreases from the periphery towards the axis and is absent near the axis, during the initial period just after the start of combustion. As time progresses, due to further dilution the concentration of oxygen near the axis increases. Very near the wall, the concentrations of H_2O and CO_2 are high for times as large as 4.5 ms, suggesting that combustion is complete. The trends and the values of concentrations of various products and temperatures are similar to those reported by Chigier and Strokin (1974), and Chigier and Apak (1975). Figure 4.27 shows the axial variation of mass-averaged (radial) temperature. Although the peripheral regions of the jet reduce this temperature, a fair idea of vaporisation, combustion and dilution histories can be obtained. These variations of mass averaged temperature and the products of combustion for the whole jet are shown in Fig. 4.28. The notable features are the maximum reached by the temperature and fraction of carbon monoxide and fuel vapour (Fig. 4.29).

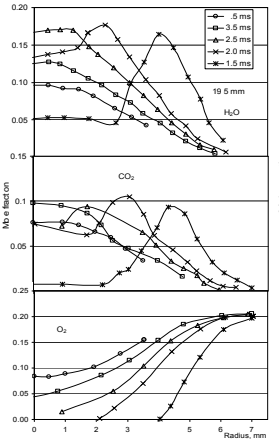

Fig. 4.25 H_2O, CO_2, O_2 at 19.5 mm from the nozzle

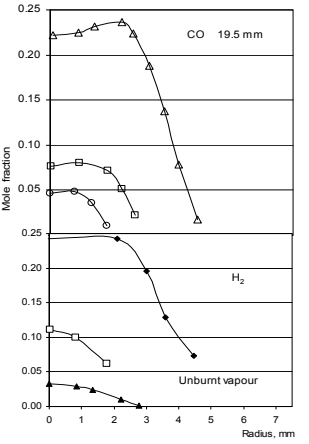

Fig. 4.26 CO, H_2, fuel vapour at 19.5 mm from the nozzle

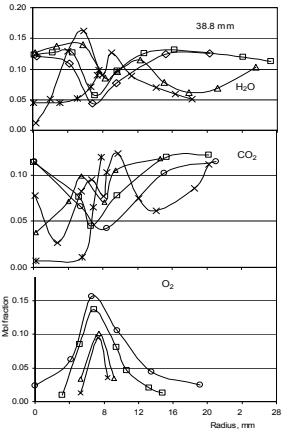

Fig. 4.27 H_2O, CO_2, O_2 at 4 mm from the impingement plane

Finally, the entrainment of air into the free and wall jet were studied in an identical manner to the case of vaporising jets, except for the definition of the equivalent diameter (Beer and Chigier 1972) as given in equation (3.5).

It can be seen in Fig. 4.18 that the entrainment of air in the transient burning jet tends to follow that of a transient vaporising spray. As a check on the calculation procedure, the total amount of fuel vapour at any instant (burned or unburned) in the jet was calculated and was found to give the total amount of fuel injected, at

times (Fig. 4.30) sufficiently long after the end of injection (2 ms). This is similar to the observation made for purely vaporising jets (Fig. 4.31).

Summary of the Model for Vapourising and Combusting Sprays

A holographic interferometric technique has been applied to study the concentration and temperature distributions in transient vaporising and combusting jet sprays with the inherent advantage of mapping the whole field at an instant. Suitable assumptions were made based on the theories of vaporisation and combustion to decouple the effects of temperature and concentration on the interference pattern. While concentration had a dominating effect on the fringe spacing in a vaporising spray, temperature influenced this spacing in a burning spray.

Study of the vaporising jet leads to the description of the radial and axial variations of concentrations of the fuel vapour by simple mathematical functions. It was found that the central regions of the transient vaporising jet are comparable to a steady state jet. At the nozzle, for about six nozzle (equivalent) diameters, the vapour concentration increases monotonically from a virtual source point. The detachment of the jet from the nozzle, at the end of injection was explained by observing the extent of departure from steady state behaviour. Impingement of the jet causes a loss of momentum and growth (thickening) of the wall jet, and as a result slower penetration along the wall.

In the case of a burning jet, it was assumed that the distribution of concentration of fuel vapour would be the same as in a vaporising jet. Assuming equilibrium between reactants and products, the temperature and molar concentrations of species were calculated. From the axis of the jet, a thick envelope of gases where combustion is complete is found. At the core close to the nozzle fuel vapour is present along with some products of incomplete combustion. At the jet boundaries and the jet tip, the products of complete combustion diluted by fresh air are present showing very little heat release. At times sufficiently long after injection, all the fuel is consumed and the temperature is lowered due to dilution by the surroundings.

Holographic interferometry is not devoid of its own difficulties. The post experiment analysis of the fringe count is time consuming. The fringes in a turbulent jet submerged in not so quiescent surroundings are corrupted. The averaging of fringes on either side of the axis of symmetry solved this problem in part. In regions where the fringe density is very high (up to 6 per mm) errors can be introduced in the fringe count. The maximum error in obtaining the fringe count versus radius profile is very much smaller than the error introduced by the thermal noise in the surroundings. This noise is one of the reasons for the deviations in the experimental data from average behaviour (Fig. 4.16); turbulence introduced by the jet causing pockets of concentration is another reason. It is extremely difficult to quantity the

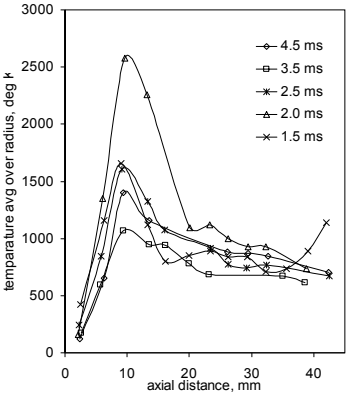

Fig. 4.28 Mass-averaged temperature along axis in a burning jet

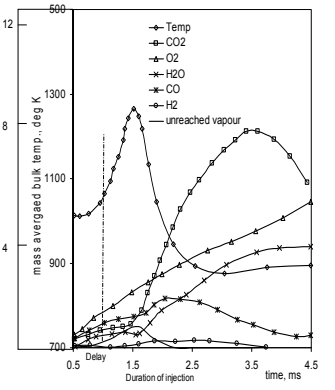

Fig. 4.29 Masses of various components and mass averaged temperature in a transient burning spray

accuracy of the technique in absolute terms with regard to the experimental results presented here. Besides the problems of high fringe density and background thermal noise mentioned above, the fact that vaporisation and combustion 'histories' of the jet are not built up from a single injection event, but rather from a series of injections at the same test condition, results in the inevitable variation between injection events being reflected in the final results. Furthermore, the method of decoupling concentration and temperature effects on refractive index are themselves approximate.

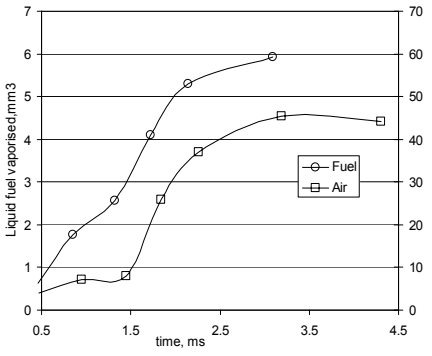

Fig. 4.30 Quantity of fuel vapour and air entrained in a burning jet

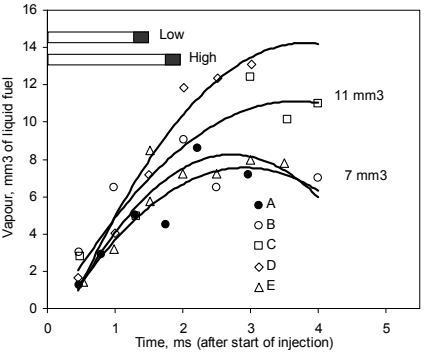

Fig. 4.31 Quantity of fuel vapour in vaporising jet

While being aware of the limitations of the technique as listed above, valuable observations on the spatial variation of concentration distributions within the transient vaporising and burning jet during the injection and post injection periods have been highlighted and described through generalized equations. Similarly, the penetration behaviour of the free and wall jet flow have been described for vaporising burning and non-burning sprays.

Finally, experimental results for the distribution of fuel vapour, air, other equilibrium reaction species and temperature within the burning transient jet have been presented.

Modern View of the Vaporising and Burning Spray

Diesel combustion is a complex, turbulent, three dimensional, a multi-phase process that occurs under conditions of high pressure and temperature. In the absence of detailed measurements within the reacting fuel jet, early attempts to describe diesel combustion were based on studies of steady spray combustion in furnaces and gas turbines. The luminous combustion in a diesel engine is essentially a diffusion flame. Spalding (1979) described this flame as thick and unsteady with instantaneous tattered shape in violent motion. In the brush like portion at periphery, the mixture fraction, f is at stoichiometric proportion on the curve edge, Fig. 4.32. The reaction zone will be a definite volume, enclosed by surfaces on which f_- and f_+ equal to the flammability limits in a turbulent flame.

Subsequently, direct measurements were carried out using flame luminosity detection, interferometry, high-speed backlight, Schlieren, cinematography or sampling probe data to study time histories and spatial distribution of various species (Hiroyasu *et al.* 1980, Aoyagi *et al.* 1980, Matsui *et al.* 1982, Lakshminarayanan and Dent 1983). These experimental works have concluded that soot emissions were elemental carbon that contributed to visible smoke and particulate emissions. Soot concentrations rise rapidly soon after injection starts. High local fuel carbon has also been found in fuel rich cores of high-pressure liquid fuelled turbulent diffusion flames. Pyrolysis of fuel is, therefore, the important source of soot. These high local soot concentrations decrease rapidly as the fuel injection ceases and the rich core mixes to leaner equivalence ratios (Heywood 1988). On the other hand, soot concentrations rise in the spray close to the piston bowl outer radius and at the cylinder wall later that are an order magnitude less, and decay more slowly. Away from the fuel spray core, with increasing distance from centre line, soot concentrations decrease rapidly.

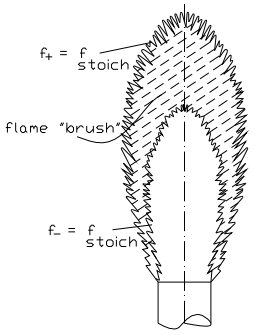

Fig. 4.32 Turbulent flame structure with brush

In the last decade, detailed in situ measurement of the process occurring inside a reacting diesel fuel jet has been carried out by means of advanced laser based diagnostics (Dec 1997). An integrated view of DI diesel combustion was derived from this and other optical data (Dec and Westbrook 1999). The combustion was summarized in a series of idealized schematics that depicted the combustion process (Fig. 4.33). The soot formation starts just downstream of the liquid fuel region and grows in size and volume fraction, as it flows downstream, eventually being oxidized at the diffusion flame. Soot occurs throughout the jet cross section and diffusion flame appears mainly around the jet periphery.

The cause of exhaust smoke and its reduction methods in a small DI diesel engine with a nozzle of small orifice diameter and common rail fuel injection equipment were investigated under high speed and high load conditions using both in-cylinder observations and three-dimensional numerical analysis by Hotta *et al.* (2002). These studies revealed that fuel sprays were easily pushed away by a strong swirl and that the air-fuel mixture immediately flows out to the squish area by a strong reverse squish. Therefore, the air in the cavity is not effectively used. Suppressing the airflow in a cavity using such ideas as enlarging the piston-cavity diameter or reducing the port swirl ratio decreases the excessive outflow of the fuel-air mixture into the squish area, and allows the full use of air in the whole cavity. Hence, exhaust smoke reduces.

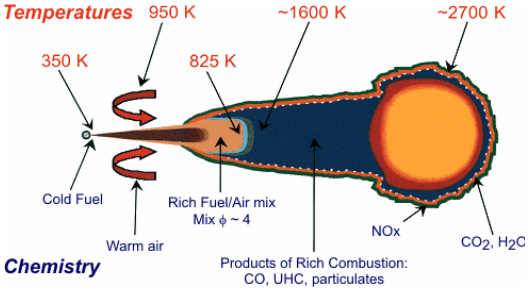

Fig. 4.33 Modern view of a vaporising and burning spray jet

Lyu and Shin (2002) investigated the effect of nozzle characteristics on the performance of a small-bore high-speed DI diesel engine. The volume between needle tip and seat in the nozzle is referred to as the sac. The fuel in this volume contributes to HC emissions. Therefore, Valve-closed-orifice (VCO) type of nozzles was developed wherein the sac is absent. These VCO nozzles resulted into higher smoke due to poorer fuel atomisation than sac type nozzles. They concluded that swirl and spray penetration should be carefully optimised and higher injection pressure is not always advantageous.

Benajes *et al.* (2004) analysed the effect of swirl on combustion and exhaust emissions. They concluded that there is no single optimum value of swirl ratio for the whole operating range of the engine and that matching the level of swirl with other parameters depends on the combustion chamber geometry and injection

characteristics. Nevertheless, the results obtained shed light on the swirl effect on diesel engine combustion and exhaust emissions over a wide range of operating conditions. They observed that NO_x is formed very early in the combustion process and that it depends on the temperature reached during premixed combustion while soot emissions are dependent on oxidation during late combustion phase which is mixing controlled. A theoretical investigation on the effect of combustion chamber geometry and the engine speed on the emissions of soot and NO_x was carried out by de Risi *et al.* (1999). The bowl re-entrance, the spray angle and the injection timing were the critical parameters that had to be optimised. Subsequently new methodologies for design of the combustion chamber shape and the injection strategy were developed aiming at the reduction in emissions without deteriorating engine performance (de Risi *et al.* 2005).

Kurtz and Foster (2004) identified a critical time for mixing in a direct injection diesel engine through the study of increased in-cylinder mixing and its effect on emissions. The results suggested that the fuel injected at the tail end of the fuel injection event had difficulty in mixing and caused large quantities of soot. An innovative method of secondary injection was used to reduce the exhaust emissions by a substantial amount.

References

Aoyagi Y *et al.* (1980) A Gas Sampling Study on the Formation Process of Soot and NO in a DI engine. SAE 800254

Beer JM, Chigier NA (1972) Combustion Aerodynamics. Applied Science Publishers

Benajes J, Molina S, Garcia, JM, and Riesco, JM (2004) The effect of swirl on combustion and exhaust emissions. J Auto Eng, IMechE, 218

Bremhorst K, Watson RD (1981) Velocity field and entrainment of a pulse cored jet. J Fluid Engg, Trans ASME, 103

Chigier NA, Apak G (1975) Interaction of multiple turbulent diffusion flames. Combustion Science and Technology, 10:219–231

Chigier NA, Strokin V (1974) Mixing processes in a turbulent diffusion flame. Combustion Science and Technology, 9:111–118

Dec JE (1997) A conceptual model of D I diesel combustion based on Laser Sheet imaging. SAE 970873

Dec JE, and Westbrook C (1999) Diesel Combustion: An integrated view combining laser diagnostics, chemical kinetics and empirical validation. SAE 1999-01-0509

Dent JC (1971) Basis for comparison of various experimental methods for studying penetration. SAE Transaction 710571

Dent JC (1980) Potential applications of holographic interferometry to engine combustion. Combustion modeling in reciprocating engines, Plenum, New York

Dent JC, Keightley JD, DeBoer CD (1977) Application of interferometry to air fuel measurements. SAE Paper No. 770825

de Risi A, Donabeo, T, and Laforgia, D., 2005, "An Innovative methodology to improve the design and the performance of direct injection diesel engine", International Journal of Engine Research, IMechE, Vol. 5 No 5.

de Risi A, Manieri, D. and Laforgia, D., 1999, "A Theoretical Investigation on the Effects of Combustion Chamber Geometry and Engine Speed on Soot and NOx Emissions", ASME-ICE, Paper No. 99-ICE-207, Vol. 33–1.

Guruz AG, Guruz HK, Osuwan S, Steward R.F. Aerodynamics of a confined burning jet, Combustion Science and Technology, 9:103–110.

Hartel H (1962) Stromongsorgange beim Freien Huberstrahler Luftfahrtechnik, 8

Heywood JB (1988) A text book on Internal Combustion engine fundamentals. McGraw-Hill Int ed

Hiroyasu H, Arai M, Nakanishi K (1980) Soot Formation and Oxidation in Diesel Engines. SAE 800252.

Hotta, Yoshihito, Nakakita, Kiyomi *et al.* (2002) The cause of exhaust smoke and its reduction methods in an HSDI Diesel Engine under high speed and high load conditions. SAE 2002-01-1160

Kurtz, E M and Foster, D E, 2004, "Identifying a critical time for mixing in a direct injection diesel engine through the study of increased in-cylinder mixing and its effect on emissions through study of increased in-cylinder mixing and its effects on emissions", International Journal of Engine Research, IMechE, Vol. 5 No 3.

Lakshminarayanan PA, Dent JC (1983) Interferometric studies of vapourising and combusting sprays. SAE 830244

Lyu, MS and Shin, BS (2002) Study of nozzle characteristics on the performance of a small bore high speed D. I. Engine, Int J Engine Res, IMechE, 3

Matsui Y, Kamimoto T, Matsuoka S (1982) Formation and Oxidation Processes of Soot Particulates in a D. I Diesel Engine – an Experimental Study via the Two Color Method. SAE paper 820464

Rajaratnam N (1976) Turbulent Jets, Elsevier

Ricou FP, Spalding DB (1961) Measurement of entrainment by axisymmetrical turbulent jets. J Fluid Mech, 11: 21–23,

Shahed SM, Chiu WS, Lyn WT (1975) A mathematical model of diesel combustion. Proc. IMechE C94/75

Spalding DB (1979) Combustion and mass transfer, Cox and Wyna Ltd, London.

Steward FR Guruz AG (1977) Aerodynamics of a confined jet with variable density. Combustion Science and Technology, 16:20–45

5 Ignition Delay in a Diesel Engine

Abstract The ignition delay in a diesel engine is defined as the time interval between the start of injection and the start of combustion. This delay period consists of (a) physical delay, wherein atomisation, vaporization and mixing of air fuel occur and (b) of chemical delay attributed to pre-combustion reactions. Physical and chemical delays occur simultaneously. To reduce NO_x, the method adapted in modern engines is to reduce the ignition delay. For predicting heat release in modern engines, therefore, the estimation of ignition delay is no more important. However, the ceiling on NO_x is dipping to such a low level that accurate prediction of ignition delay has become important even if it is small. Ignition delay of diesel sprays is a strong function of ambient temperature and pressure. However, the physical delay has not been modelled satisfactorily in the literature. In this chapter, phenomenological calculations of the cooling of spray surface have shown that the physical parameters and fuel type influence the temperature of the mixture of air and the vapour produced by the first parcel of the injected fuel throughout its life up to ignition. A unique thin-ring like zone on the spray surface is postulated where the preflame reactions have reached a critical level beyond which uncontrolled reactions take place. The time, at which the spray just touches the ring, the ignition is predicted. However, due to turbulence, ignition will take place at only a few points in the neighbourhood of the ring. Detailed consideration of droplet formation, evaporation fuel and preflame reaction has enabled prediction of delay period and location of the ignition accurately within the experimental errors and errors in the input to the calculations.

Ignition delay of a fuel, in the context of diesel engines, is the period from the time the first parcel of fuel enters the chamber to the point when the first flame is observed in the spray. This is different from the combustion performance of the fuel, which influences the efficiency of the engine. The ignition delay of a diesel spray is important from the viewpoint of preparing the fuel before injecting into the engine as well as selecting optimum injection timing. The delay is primarily dependent on the ambient temperature. This has been shown by Wolfer (1950). His correlation showed exponential dependence on temperature as in Arrhenius' equation for rate of reaction. Pischinger, Scheid and Reuter (1987) have experimentally shown the strong influence of the injection parameters like the hole size, injection pressure and types of fuel and hence quality of fuel on the measured delay. The physical parameters mentioned above are normally lumped as physical delay (Thelliez and Ji 1987, Woschni and Anisits 1974). This is either a constant or variable according to the characteristics of the injector and has a form of Wolfer's correlation. Ahmed (1980) and Tsao, Myers and Uyehara (1962) related physical delay to engine operating conditions. Thelliez and Ji (1987)

P.A. Lakshminarayanan and Y.V. Aghav, *Modelling Diesel Combustion*,
Mechanical Engineering Series, DOI 10.1007/978-90-481-3885-2_5,

attempted to incorporate a constant physical delay. It was explained as the time taken for the fuel to reach the length at which ignition occurs. This characteristic length was assumed to depend only on the chamber pressure and temperature at the start of injection contrary to the experimental results (Pischinger *et al.* 1987), which show its dependence on injection parameters as well. This period is about 0.5 ms for the injection systems that are encountered. Andrea and Paschernegg (1969) emphasized the importance of basic research to investigate the physical and chemical complexities involved in igniting and burning hydrocarbon fuels. Since conclusive information was not available, a combination of empirical observations with modified working theories was used to fill the gap in understanding this persistent problem of diesel combustion. An integral of the difference between the temperature of the gases in the engine and the ignition temperature of the fuel over time, from the time of start of injection till the end of ignition delay was found to be nearly a constant irrespective of fuel or engine speed (Andrea and Paschernegg 1969). The present work describes an attempt to incorporate the effects of injection parameters, dimensions of the nozzle orifice, fuel type and ambient conditions into a comprehensive ignition delay model (Chandorkar *et al.* 1988).

Definition and Measurement of Ignition Delay

The definition of ignition delay is the time lag between the start of injection to start of the combustion when air-fuel mixture is ignited. In a diesel engine it can be determined experimentally as the time interval between the start of injection and the start of combustion (Fig. 3.8). Due to vaporization effects, the apparent heat release curve will typically exhibit negative values before combustion for direct injection diesel engines. The start of combustion is taken as the angle value at which rate of apparent heat release changes from negative to positive. The start of injection is defined as crank angle at which the needle of nozzle lifts by 5%. The time difference between the start of injection and start of combustion is called as ignition delay. The Arrhenius type of equation to describe ignition delay,

$$\tau_{id} = a\Phi^{-k^*} P^{-n^*} \exp\left(\frac{E_a}{R_u T_{cyl}}\right) \tag{5.1}$$

Where,

τ_{id} = Ignition delay

Φ = Equivalence ratio

E_a = Activation energy

T_{cyl} = Cylinder charge temperature

R_u = Gas constant

a ,k^* *and* n^* = =Empirical constants

Classical Model for Ignition Delay and Its Extension to Other Fuels

The time taken for visible fire to appear in the premixed zone of spray is a strong function of pressure and temperature in the ambient. In addition, the physical properties such as the Cetane number, viscosity of fuel, nozzle hole size, injected quantity and injection pressure contribute to the delay phenomenon in diesel engines. In the original work of Assanis *et al.* (1999), the measured values of pressure and temperature are necessary to predict ignition delay. If this equation has to be developed as design tool, then it is necessary to predict pressure and temperature precisely for required engine operating condition. Considering pressure and temperature at TDC position will ignore effect of injection timing. Therefore, it is necessary to estimate pressure and temperature at the start of injection by using following equations.

$$T_{cyl} = T_m . \varepsilon_{eff}^{c-1} \tag{5.2}$$

$$P_{cyl} = P_m . \varepsilon_{eff}^{c} \tag{5.3}$$

Where, ε_{eff} = $\frac{V_{disp}}{V_{SOI}}$

Effective compression ratio

c = Polytropic constant

P_{cyl} = Cylinder charge pressure

P_m = Charge pressure at manifold

T_{cyl} = Cylinder charge temperature

T_m = Charge temperature at manifold

V_{disp} = Cylinder volume displaced

V_{soi} = Cylinder volume at start of injection

Here the fact that must be considered is at lower piston speeds achievable pressure and temperature under compression decrease under engine conditions. This is due to higher heat transfer and blow by as more absolute time is available per cycle. Expression developed by Hardenberg and Hase (1979) can be used to describe polytropic exponent.

$$c = k^{+} - \frac{k^{+} - 1}{f.u_p + 1} \tag{5.4}$$

Where, K^+ = Ratio of specific heats, c_p/c_v 1.4
f = Constant 1.1
u_p = Mean piston velocity

In the above correlation of ignition delay, oxygenated fuel is not accounted for. Lahiri *et al.* (1997) introduced fuel to oxygen ratio in place of equivalence ratio. This makes ignition delay a function of the oxygen content in the fuel. The ignition delay increases with addition of alcohols (Huang *et al.* 2004) because alcohols have very low Cetane number. The reduction in ignition delay has been observed with bio-diesel, another oxygen containing fuel described in literature (Szybist *et al.* 2005). The Cetane number of biodiesel is better than that of diesel. Therefore, the Cetane number truly represents the compression ignition quality of fuel. Therefore, this parameter needs to be incorporated while developing a new model for predicting the ignition delay especially with fuels containing oxygen. Here, the correlation developed by Hardenberg and Hase (1979) can be employed.

$$E_A = \frac{B}{CN + 25} \tag{5.5}$$

Where, B = a constant
CN = Cetane number

Watson *et al.* (1980) and Assanis *et al.* (1999) proposed value of $E_a/R_u = 2{,}100$ for diesel D_2. Therefore, the value of constant B needs to be modified from original value 618,840–1,310,000 (Aghav *et al.* 2008) a value inline with observation by Watson *et al.* (1980) and Assanis *et al.* (1999).

Validation of classical model

The time taken for visible fire to appear in the pre-mixed zone of spray is a strong function of pressure and temperature of the ambient. In addition, the physical properties such as Cetane number, viscosity of fuel, nozzle hole-size, injected quantity and injection pressure contribute to the delay phenomenon in diesel engines (Chandorkar *et al.*, 1988). However, for diesel fuels a reasonable estimate of the delay, ID is achieved by Wolfer (1950).

$$ID = 3.45 \exp(2100/T_m) p_m^{-1.02} \tag{5.6}$$

Here T_m and p_m are the mean temperature and pressure of the ambient during ignition delay.

Initially, the prediction model was applied to engine C12. Experimental work was also carried out on the engine with different blends of bio-diesel and exhaust gas recirculation on different engines (A12, C12, E12, and B10) listed in Table 3.2. The conditions at rated power and speed were considered for this study. The comparison of predicted and observed values was encouraging for this engine at

different operating conditions in terms of absolute value as well as trend (Fig. 5.1). Then, the model was applied to other engines namely A12, C12, E12 and B10. The older generation of engines E12 and B12 were also considered for model evaluation. The results and predictions are plotted in Fig. 5.2. The new correlation has better predictability compared to the best model available in literature (Ikegami *et al.* 1986). The newer engine designs have remarkably lesser ignition delay compare to older generation. The predictions with new model are favourable for both old and modern designs with regression coefficient of 0.97 with slope close to one (Fig. 5.2).

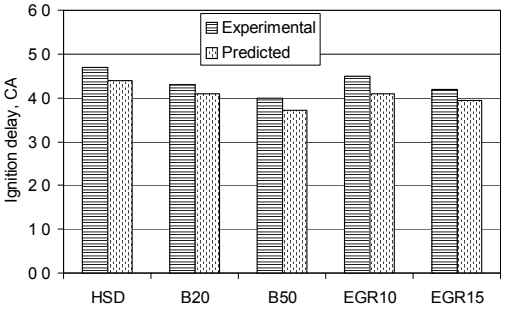

Fig. 5.1 Prediction of ignition delay at rated conditions for engine C12

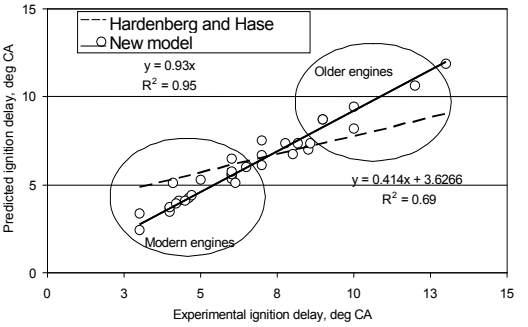

Fig. 5.2 Prediction of ignition delay for A12, C12, E12 and B10 engines

Phenomenological Model of Ignition Delay

Mechanism of ignition delay

The physical preparation of fuel is considered hand-in-and with the chemical reaction. The formation of drops, evaporation and chemical reaction are phenomenologically modelled to explain the total delay. The end of ignition delay period is defined in this model as the state in which very fast rate of exothermic reaction of fuel particles occurs producing a distinct emission of visible light from

the spray surface. The vapour envelope (Andrea and Paschernegg 1969) emanating from the liquid surface depends on its chemical composition and the boiling curve of the fuel. Perceptible ignition will occur with lower fraction of distillation. The group of molecules that ignites early can transfer energy to adjacent and more stable molecules. Oxidation does not occur on intact hydrocarbons but it does on intermediate substances formed during the delay time, such as hydrocarbon radicals and peroxides. Because of non-homogeneity of the fuel air mixture in the spray the local air fuel ratio is extremely high in the areas where vapour emanates from liquid fuel. Initial ignition has the advantage of high oxygen concentration around the fuel. This non-homogeneity persists even after ignition delay.

Spray formation

Diesel fuel as it emerges out of the nozzle orifice is in the shape of a sphere whose diameter is nearly equal to the orifice diameter. Every droplet is assumed to go along a line radiating from an origin at δ (virtual source, see equation (4.4)). Therefore, the problem simplifies to concentrating our attention on the drops inside an annular cone (shown by dotted lines in Fig. 5.3). Subsequently, the drop breaks into smaller droplets due to the combined tearing action of the dense ambient and the instability of large drops. In high-pressure sprays, encountered in diesel engines, the tearing action is very important. This is proportional to the velocity of injection, injection pressure, coefficient of discharge of the orifice and fuel viscosity (Knight 1955, Reitz and Diwaker 1977). According to Knight (1955) the Sauter mean diameter of droplets,

$$SMD = 1.58 \frac{Q^{0.21}}{\Delta P^{0.5}} \upsilon^{0.2} C_D^{0.9} \tag{5.7}$$

Here, SMD = Sauter mean diameter, m
Q = Rate of injection, m /s
Δp = Differential pressure, N/m²
υ = Kinematic viscosity, m²/s
C_D = Coefficient of discharge of the orifice

The SMD given above is characteristic of the whole fuel as soon as it is injected. In reality, there is a typical distribution of drop size decreasing, away from the centre line of the spray. This is calculated as follows. Spalding (1977) gives the distribution of velocity and concentration in a turbulent jet in a quiescent chamber as,

$$\frac{u}{u_{C.L.}} = \frac{1}{\left[1 + 0.414\left(r / r_{\frac{1}{2}}\right)^2\right]^2} \tag{5.8}$$

$$\frac{u}{u_{C.L.}} = \left(\frac{C}{C_{C.L.}}\right)^{0.7} \tag{5.9}$$

Here, *Half radius,* $r_{½}$ = 0.0846 x
r = Radius
x = Axial distance
u = Velocity at (r, x)
C = Mass concentration defined as the ratio of mass of injected substance to the total mass at any (r, x)
Subscript C.L. *indicates* Centre-line value at x.

The velocity of the fuel decreases axially due to loss of momentum to the entrained air. The penetration of fuel along the centre-line (Dent 1971),

$$x = \sqrt{8 u_j d_e t} \tag{5.10}$$

Here, uj = velocity of fuel a t the orifice,
d_e = equivalent diameter of the orifice

The velocity of fuel along the centre-line is obtained by differentiation of equation (5.10) with respect to t. At any other radius, the velocity is obtained by using equation (5.8) and the derivative of equation (5.10) with respect to t.

The volume of the elementary annular cylinder (Fig. 5.3), which contains the first parcel of fuel injected between times 0 and Δt,

$$dV = 2\pi r_a x_a u \, \Delta t d\theta \tag{5.11}$$

This volume increases with time, t, due to air entrainment. The amount of fuel injected into this volume in a time interval, Δt,

$$dm = \rho c \, dV \tag{5.12}$$

Here, ρ = mean density of the fuel, air and products at (r, x)

Substituting equations (5.8) and (5.9) in equation (5.12),

$$\begin{aligned} dm &= function\ of\ \theta\ only = dm(\theta) \\ &= f(\theta)\, d\theta \end{aligned} \tag{5.13}$$

The distribution of mass, $f(\theta)$ with respect to angle, θ, calculated using equations (5.8), (5.9), (5.11) and (5.12), is as shown in Fig. 5.4. The cumulative volume versus drop-size distribution of a diesel spray is as follows (Simmons 1977),

$$W(D) = \exp\left(0.0532\,D - 0.5417\,D^2\right) \tag{5.14}$$

where, D = (Local Sauter mean diameter/Sauter mean dia of the whole spray near orifice)

The volume fraction of fuel with relative diameter in the range D to $D + dD$,

$$dw = \frac{dw}{dD}\,dD \tag{5.15}$$

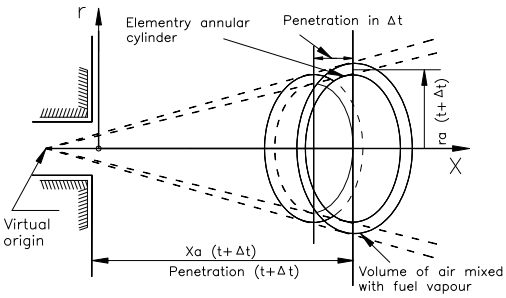

Fig. 5.3 Control volume in the shape of an annular cone

The mass of fuel in this range is,

$$dm = \left[\left(\frac{\pi d_o^2}{4}\right) u_f \rho_f \,\Delta t\right] dW$$

$$dm = K dW \tag{5.16}$$

Here, the first term refers to the total mass of fuel injected in Δt. Equating masses in equations (5.12) and (5.16)

$$f(\theta)\,d\theta = dm(\theta) = K\,dW$$

Integrating, after rearrangement of the equations given above,

$$D = \int_{\theta_{\max}}^{\theta} \frac{f(\theta)\,d\theta}{K\dfrac{dW}{dD}} + D_o \tag{5.17}$$

Here, D_0 is the SMD ratio at the outer envelope of spray and is assumed to be equal to 0.086. The radial distribution of droplet diameter calculated using equation (5.14) is shown in Fig. 5.5. For purposes of calculations, a linear approximation as shown in Fig. 5.5 is helpful. The fuel droplet traces a nearly linear path from the time of formation, often breaking and coalescing with other drops in the neigh-

bourhood. This important phenomenon is however not applicable to the drops on the outer surface of a spray because they are formed first and hence do not interact with other droplets. Break-up of these drops is negligible if the drops are small as in high-pressure sprays. Thus, these droplets on the spray surface can be said to reduce in size only by vaporisation. Evaporation of fuel depends on relative velocity of surrounding medium.

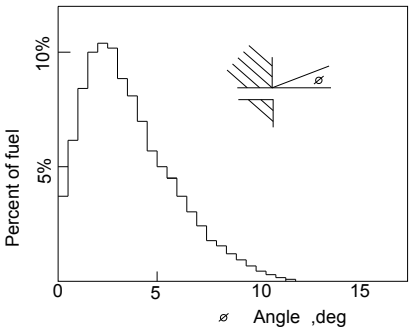

Fig. 5.4 Dispersion of fuel

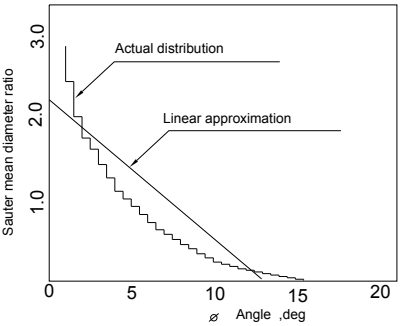

Fig. 5.5 Mean diameter of fuel at different angular positions just after injection

Mass transfer

The relative velocity of drops with respect to the surroundings is 10–20% of the mean velocity at any point (Reitz and Diwaker 1987). The mass transfer from the surface of the liquid drop to the ambient is analogous to the heat transfer. Figure 5.6 schematically shows the evaporation process. From the bulk-surroundings, air flows towards the liquid-surface. This hot air warms up the liquid layer (where concentration of vapour = 1) and evaporation takes place. Since it is not soluble in liquid, the air returns to the bulk flow carrying the fresh vapour along with it. The boundary layer between the bulk and the liquid surface is similar to the heat transfer boundary layer. In general, the bulk flow contains vapour apart from the main constituent, air. However, the mass transfer increases the boundary layer thickness. This effect is equal to ln *(1+B)* where *B* is Spalding's mass transfer number (Appendix III) (Spalding 1977).

Thus, the rate of mass transfer per unit area of the droplet,

$$\frac{dm''}{dt} = Nu\left(\frac{k}{D}\right)\frac{\ln(A+B)}{L'}(T - T_o) \tag{5.18}$$

where, $(T–T_0)$ =Temperature difference between the liquid surface and the bulk a t (r, x)

Nu = Nusselt number

L' = Latent heat + sensible heat t o convert liquid to saturated vapour

Re = Reynolds number of relative flow based on relative velocity
d = Droplet diameter
k = Conductivity of the ambient

The radius of the drop decreases due to evaporation. As the radius reaches zero, mass transfer stops.

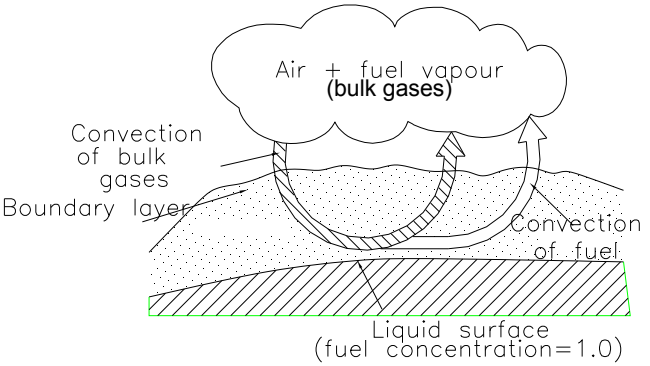

Fig. 5.6 Mechanism of fuel vaporisation from droplet surface

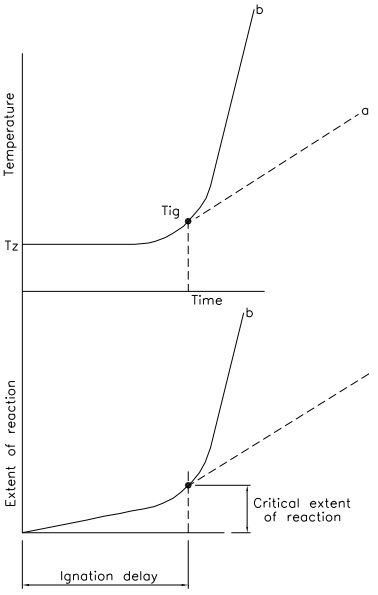

Fig. 5. 7 Schematic representation of temperature and extent of reaction against time

Reactions

The nascent drop as soon as formed starts evaporating and is surrounded by a cloud of vapour-air mixture. The concentration of the fuel vapour, w_{fuel} (kg/m^3) is

the ratio of the mass evaporated (until time = t) from drops injected (during time = 0 to Δt) into the annular conical control volume to the volume of the annular cylinder shown in Fig. 5.3 The length of the cylinder is the penetration of the spray at angle θ from t to t + Δt. The mean radius of the cylinder is $r_a\ (t)$. The concentration, W_{air} of air is similarly defined. It should be noted here that the definition of W_{fuel} is different from that of C_{fuel} given in equation (5.9). The temperature of the mixture is a function of the latent heat of vaporisation, specific heats of vapour and liquid and the temperatures of air and liquid. The temperature, T at $r_a\ (t)$, $x_a\ (t)$ is obtained by solving the heat balance equation,

$$W_{air} C_{p_{air}} \left(T_\infty - T\right) = W_{fuel}\ C_{p_{\text{var}}} \left(T - T_s\right) + L + C_{liq} \left(T_s - T_o\right) \tag{5.19}$$

Here,	W	=	Mass concentration
	C_p	=	Specific heat
	T	=	Temperature
and	L	=	Latent heat of evaporation
subscript	w	=	Ambient
	vap	=	Vapour
	liq	=	Liquid
	s	=	Saturation conditions
and	o	=	Conditions at the liquid surface

Since the injected fuel is sub-cooled during the initial stages of evaporation, the mass transfer number calculations show that the conditions at the liquid surface can be sub-cooled. However, most of the time saturation conditions are reached at the surface.

The evaporated fuel instantly starts reacting according to Arrhenius equation. Assuming a bi-molecular reaction (Spalding 1977), the global rate of change of concentration of fuel,

$$-\left(\frac{dW_{fuel}}{dt}\right) = 0.847 \times 10^9\ W_{fuel}\ W_{air}\ \exp\left(-E_a / RT\right) \tag{5.20}$$

Here,	W_{fuel}	=	Mass concentration of fuel vapour, kg/m^3
	W_{air}	=	Mass concentration of air, kg/m^3
	E_a/R	=	Activation energy/gas constant, K
		=	450 x 104/(CN + 400) (equation 5.24)
	T	=	Temperature of the mixture, K
	CN	=	Cetane number

$$The\ rate\ of\ increase\ of\ mass\ of\ products = -\left(\frac{dW_{fuel}}{dt}\right) dV \tag{5.21}$$

Here dV is the volume of the annular cylinder (Fig. 5.3, equation (5.11)) containing the first parcel of fuel injected. Integrating equation (5.21) from time = 0 to t, the

total mass of products at a desired point in time can be obtained. The mass concentration of products is the ratio of the mass of products in the elementary annular cylinder (Fig. 5.3) obtained by integration, as mentioned above-to the total mass of air, fuel-vapour and products in the elementary annular cylinder. The temperature of the elementary cylinder is proportional to the mass concentration of products. The pre-exponential constant in equation (5.20) is calibrated, such that at the ignition distance and time for arbitrarily selected spray (data for which is given below) the mass concentration of products has a value of 100. Therefore, the unit of mass-concentration is mentioned in the text as arbitrary units.

Spray hole dia	=	0.27 mm
Ambient pressure	=	45 bar
Ambient temperature	=	500ºC
Injection quantity	=	14 mm^3/stroke
Fuel	=	Diesel

Ignition delay

Until the end of the ignition delay period, the increase in concentration of fuel is too small to cause any substantial change in mixture temperature compared to the cooling due to evaporation. This is observed normally in preflame reactions (Fig. 5.7). However, near the end of ignition delay period, the temperature rises rapidly. Curve ‘a’ show the case when the effect of heat release due to preflame reactions is neglected. Curves ‘b’ consider the heat release. It is shown in the figure that until the end of ignition delay it is justified to omit the increase in temperature due to preflame combustion. Practically, at a typical concentration of products, temperature rise is high to cause a high rate of reaction. This typical concentration (100 arbitrary units) according to integral of equation (5.21) is termed as the critical extent of reaction in this chapter.

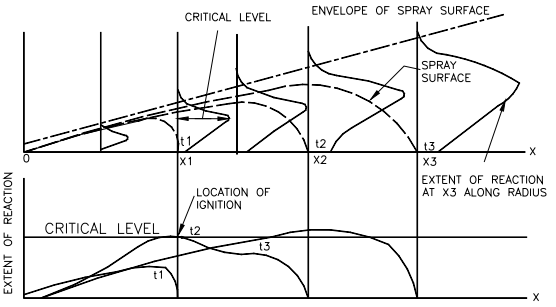

Fig. 5.8 Ignition model

Extent of reaction within the spray

The extent of reaction is defined as the integral over path line of the droplet (on the outer surface of the spray) per unit mass of the air-fuel mixture. It can be seen

that the integral increases monotonically along the path line since the combustion reaction is irreversible. However, the temperatures along the outer path-lines are more and concentration of fuel vapour is less than temperatures along the path-lines close to the centre-line (Fig 5.9). These two contradictory trends result in a definite peak in the plot of extent of reaction against radius. The effect of prolonged stay of fuel on the outer periphery though helps in increasing the integral of equation (5.21); the concentration on the outer periphery is too small to result in higher extent of reaction. In the top half of the Fig. 5.8, the extent of reactions along the radius at different axial distance X_0, X_1, X_2 and X_3 are shown. It takes times, t_1, t_2, and t_3 for the spray to penetrate distances of X_1, X_2 and X_3. The extent of reaction on the outer surface of the transient spray is shown at the bottom of Fig. 5.8.

When the maximum of this extent reaches the critical level at any time, then ignition takes place at that location. Such a critical value will be reached on the spray surface later as well. However, since the ignition has already taken place these locations are irrelevant. It is obvious that this critical value will not be reached before this time because of the monotonic curves along any path-line. For the sane reason, ignition does not take place inside a spray.

Thus, according to this model, the ignition zone is an infinitesimally thin ring on the spray surface. The nature of variation of the extent of reaction, explained now, is a necessary condition to obtain unique ignition delay and location of the ring. Figure 5.9 shows the calculated extent of reaction on the spray surface at different times (1.25, 2, 2.75 ms) after injection for different injector hole sizes for the experiments given in by Pischinger *et al.* (1987). The locii of the maxima are shown by double chain dotted lines. The distance and time at which the locus reaches the critical value (=100 arbitrary units) is the ignition point. It could be seen that with increase in hole-size, ignition delay decreases arid the location of ignition moves towards the nozzle. This phenomenon is discussed in depth later, in another section.

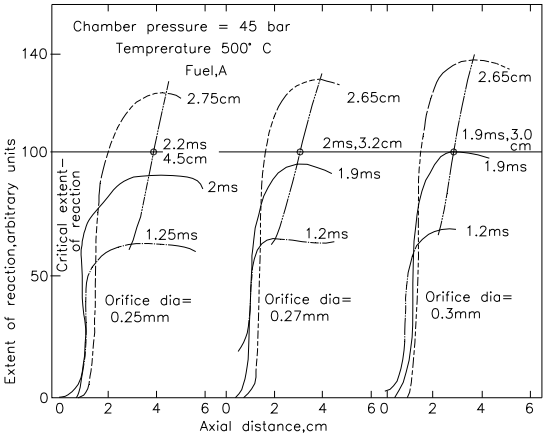

Fig. 5.9 Calculation of ignition model, effect of injector nozzle hole size

Turbulence

Photographic evidence of spray ignition shows that the ignition occurs apparently in small zones at any radius below the surface (Pischinger *et al.* 1987). This can be explained using Fig. 5.10. It shows the Polar plot of extent of reaction at any axial section. The calculations explained earlier in this Paper implicitly assume axisymmetric sprays. In practice, turbulence in sprays causes random fluctuations in the extent of reaction, resulting in critical values at only a few points on the surface, near the thin ring at MM, postulated earlier. The distance of these points from the ring is of the order of turbulence small-scale at the point. The photographic projection of a point on the surface of the spray is however seen as if the ignition point is at a radius less than the maximum. The probable ring zone of ignition is schematically shown in Fig. 5.10.

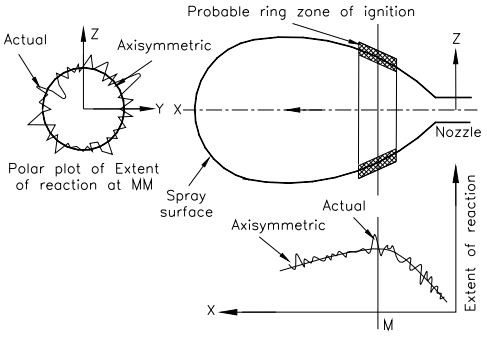

Fig. 5.10 Model of ignition delay

Computations

The mechanism of the ignition delay is easily calculated over the entire spray. The first occurrence of the critical extent of reaction is noted for the estimation of ignition delay and the location of the ignition point.

Validation of the model

Results from highly controlled experiments reported by Pischinger *et al.* (1987) were used to validate the calculations of the effects of injection parameters and ambient on ignition delay. Fuels (Table 5.1) of viscosity Varying from 4 to 60.5 mm^2/s, different boiling ranges and of Cetane numbers were sprayed into a quiescent chamber charged to 45 bar at 450°C, 500°C, 550°C and 600°C. Orifice hole-size was varied from 0.2 to 0.3 mm, keeping injection quantity at 14 mm^3 per stroke and injection duration at 1.8-ms. It was possible by varying injection pressures. Later the quantity of injection was varied from 7 to 28 mm^3 keeping the orifice size fixed at 0.3 mm. Based on the data reported, the mean injection pressure-differential necessary to inject the fuel could be calculated. In general the pressure during injection hole size when injection quantity and is triangular. The mean pressure estimated from the flow is:

$$P_{injection} = \left(\frac{1}{T} \int_{O}^{T} \sqrt{\Delta P} dt \right)^2 + P_{cyl} \tag{5.22}$$

where, P_{cyl} =combustion chamber pressure.

The Sauter mean diameter is dependent more on the arithmetic mean of the injection pressure.

$$P_{average} = \frac{1}{T} \int_{o}^{T} P dt \tag{5.23}$$

Assuming a triangular shape of pressure history and needle closing pressure as equal to 0.8 times needle opening pressure a plot of $P_{injection}$ against $P_{average}$ was made as shown in Fig. 5.11. Thus for any injection condition given in Pischinger *et al.* (1987) an average pressure can be estimated. The results of the model and experiments are compared in Figs. 5.12–5.15.

Effect of orifice size

In Fig. 5.12, the delay is plotted against injector hole size when injection quantity and duration were kept constant at 14 mm^3 and 1.8 ms. with decrease in hole-size atomisation is finer due to high-pressure injection, and hence evaporation of fuel is intense to cool the air-fuel mixture. The low temperature results in very slow rate of conversion of fuel to products of combustion i.e. very slow preflame reaction. Therefore, decrease in hole-size increases the time to reach the critical extent of reaction along the path of drops and hence increase the delay. This effect is pronounced when the hole-size is between 0.2 and 0.27 mm. As the hole-size is increased above 0.27 mm, the injection pressure varies very little. Hence, it does not affect the cooling rate and hence the ignition delay. Longer the delay, longer is the distances over which the rate equation is integrated to reach the critical extent of reaction. This results in the location of ignition occurring far away from the nozzle. Figure 5.13 shows the comparison of computed and experimental distances at which ignition occurred. The trends and values compare well.

Effect of injection quantity

Figure 5.14 shows the influence of injection quantity on the ignition delay. With increase in injection quantity, the injection pressure increases. This results in smaller drop-sizes that evaporate quickly and hence in low temperatures. The rate of preflame reactions decreases. Thus, the critical value of the extent of reaction is reached late to increase the ignition delay. Obviously, the location of ignition also moves farther from the nozzle. Pischinger *et al.* (1987) have explained this differently as a phenomenon due to continued injection at high load, which cools the ignition site. However, in a spray, vapour-air mixture has a high mean velocity compared to the fluctuations. Therefore, the reacting mixture does not stay at a

point and hence it may not be cooled by the fuel that follows it. The method described here is clearly able to predict the observed delay, even though it does not consider the explanation given in Pischinger *et al.* (1987). Figure 5.13 shows that the observed distances of ignition are predicted well.

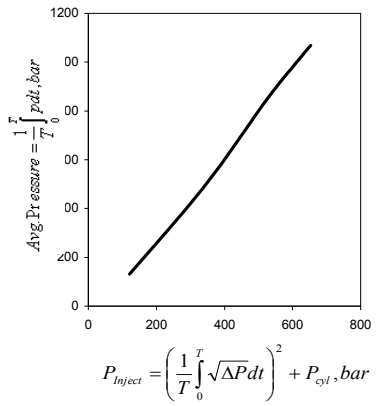

Fig. 5.11 Mean injection pressures for SMD and flow for a triangular injection pressure history

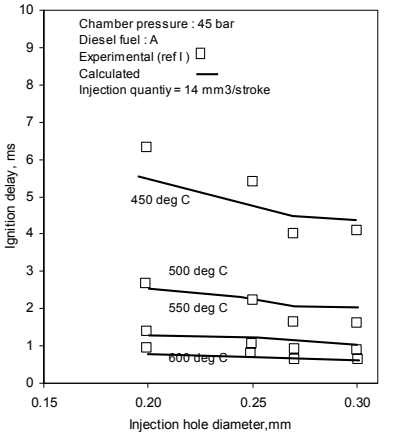

Fig. 5.12 Effect of injection hole diameter on injection delay

Effect of Cetane number

Cetane number of a fuel is determined by the structure of the hydrocarbon (Bailey *et al.* 1986) from the experimental data of Pischinger *et al.* (1987) a correlation similar to that given in Hardenberg and Hase (1979) was observed.

$$\frac{E_a}{R} = \frac{450 \times 10^4}{CN + 400} \tag{5.24}$$

Here, E_a = Activation energy,
R = Gas constant
CN = Cetane number

The effect of Cetane number is given in Fig. 5.15. With decrease in Cetane number from 56 to 39, the increase in activation energy decreases the rate of reaction (equation (5.11)) and hence the integral along the path of droplets. This results in longer delay to obtain the critical level of the extent of reaction. The increase in delay at low temperatures is predicted to be very high as observed experimentally.

Effect of volatility

The vapour pressure of less volatile fuels is very low and the latent heat of vaporisation is high. Hence, these fuels, when sprayed in a chamber, produce very little vapour cloud. In addition, less volatile fuels are thicker or more viscous.

Increased viscosity results in large drop sizes. The net effect is to decrease fuel vapour concentration on the right hand side of equation (5.12). However, due to reduced evaporation the cooling effect is less. Two fuels (Table 5.1) A and G (Pischinger *et al.* 1987) are compared in Fig. 5.16. Even though the fuels are mixtures with definite boiling curves, for simplicity they are assumed to be pure fuels with typical boiling points for a given saturation pressure. The input data are given in Appendix IV and Table 5.1. The trends of calculated delay match with experimental results. Heavier fuel has a higher ignition delay at all temperatures.

Summary

When diesel is injected through an orifice, larger drops are formed near the core and finer droplets at the periphery. Smaller drops evaporate faster and cool the spray zone. However, near the outer periphery of the spray, the concentration of fuel and hence vapour is low to allow slow preflame reaction. At the centre, temperatures are low because fuel concentration is high. In the middle zone, the peak reaction rates are observed. The extent of completion of reaction per unit mass of air-fuel mixture along a path line increases monotonically. This reaches a critical level a t the end of ignition delay along a thin ring-like zone on the surface of the spray. Beyond this level, the reaction is accelerated and spray is covered by premixed flame. In practice due to turbulence, the spray is not axisymmetric. The critical level is reached only at a few points about the thin zone. The time to reach the critical level is a strong function of the cooling rate of the spray, temperature and chemical activation energy of the fuel. The cooling rate is found to be a function of the vaporisation characteristics of the fuel and the injection parameters only. The activation energy is correlated to the reciprocal of Cetane number of the fuel. Thus, the effects of fuel types, injection parameters and ambient conditions on ignition delay could be explained. Increase in injection pressure due to decrease in injector hole-size or due to increase in load, increases the cooling rate and hence slows down the pre-flame reactions. Also, decrease in Cetane number increases the activation energy to decrease the rate of reactions. Decrease in volatility reduces the formation of vapours to decelerate the conversion of fuel to products.

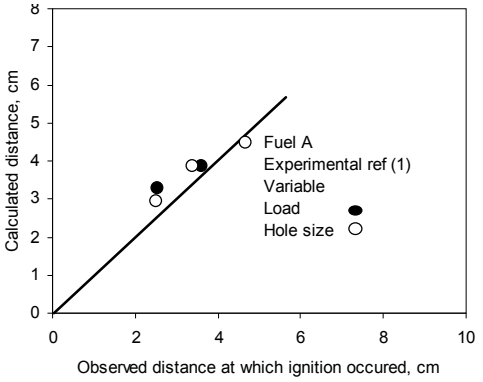

Fig. 5.13 Location of ignition

Table 5.1 Experimental data from Pischinger *et al.* (1987)

Fuel	A	B	B*	G
Cetane number	50.6	39.1	50.6	45
Density at 15 C (kg/m^3)	847	875	875	930
Distillation, 5% recovery (C)	205.5	207.0	207.0	350.0
90% Recovery	341	342	342	450
Kinematic viscosity at 20 C (mm^2/s)	5.0	4.7	4.7	60.5

Note: B* = B + ignition improver

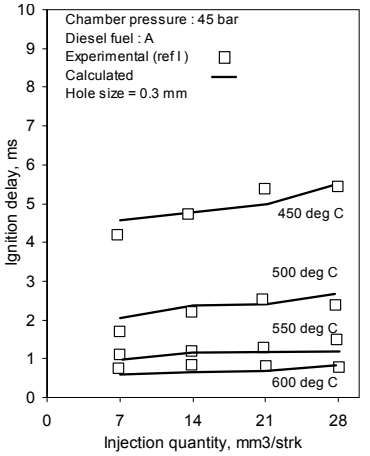

Fig. 5.14 Effect of injection quantity on ignition delay

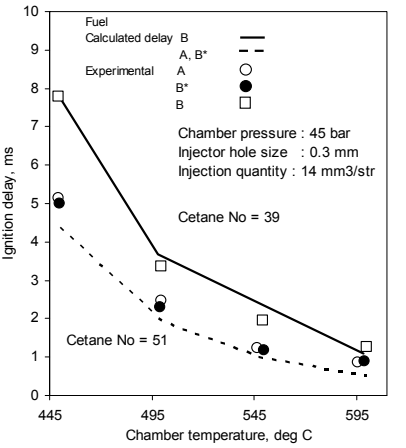

Fig. 5.15 Effect of Cetane number on ignition delay

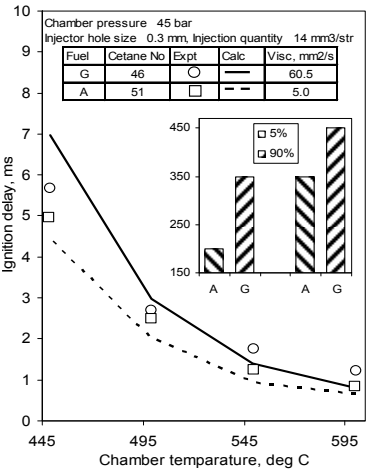

Fig. 5.16 Effect of volatility and viscosity on ignition delay

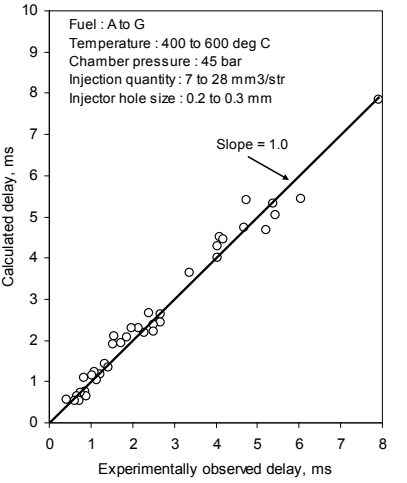

Fig. 5.17 Comparison of predicted and observed ignition delay for different cases and ambient conditions

The ignition delay and location of ignition obtained experimentally compare favourably with the theoretically calculated values to reach the critical level of extent of reaction, for different experimental parameters like hole size and injection quantity for different fuel characteristics like volatility, viscosity and Cetane number and for different ambient conditions like temperature (Fig. 5.17).

References

Aghav YV, Lakshminarayanan PA, Sujeet V, Kumar MN, Kumar C, Babu MKG (2008) Predicting Ignition Delay and HC emission for DI Diesel Engines encompassing oxygenated fuels. SAE International Mobility Conference

Ahmed A (1980) Etude analitique et modelisation correlative de la phase de combustion dans les moteurs allumage par compression surralirmentes, a injection directe, Doctoral Thesis, University Pierre et Marie Curies (Paris VI)

Andrea A, Paschernegg SJ (1969) Ignition Conditions in Diesel Engines, SAE 690253

Assanis DN, Filipi ZS, Fiveland SB, Syrimis M (1999) A Predictive Ignition Delay Correlation Under Steady-State and Transient Operation of a Direct Injection Diesel Engine. ASME-ICE Fall Technical Conference

Bailey BK, Russell JA, Wimer WW, Buckingham JP (1986), Cetane number prediction from proton-type distribution and relative hydrogen population. SAE 861521

Chandorkar SB, Dani AD, Lakshminarayanan PA (1988) Effects of Injection Parameters, Fuel Quality and Ambient on the Ignition Delay and the Location of the Flame Kernel in a Diesel Spray in a Quiescent Chamber. SAE 881227

Dent JC (1971) A basis for comparison of various experimental methods for studying penetration. SAE Transaction 710571

Hardenberg HO, Hase FW (1979) An Empirical Formula for Computing the Pressure Rise Delay of a Fuel From Its Cetane Number and From the Relevant Parameters of Direct-Injection Diesel Engines. SAE 790493

Huang Z, Lu H, Jiang D, Zeng K, Liu B, Zhang J, Wang X (2004) Combustion behaviours of a compression-ignition engine fuelled with diesel/methanol blends under various fuel delivery advance angles Pages 331–341, 95, Bio-resource technology

Ikegami M, Kidoguchi Y, Nishiwaki K (1986) A Multidimensional Model Prediction of Heat Transfer in Non-Fired Engines. SAE 860467

Knight BE (1955) Communication on the performance of a type of swirl atomizer. Proc. I. Mech. E, 169,

Lahiri D., Mehta P, Poola R, Sekar R. (1997) Utilization of Oxygen-Enriched Air in Diesel Engines: Fundamental Considerations. Paper No. 97-ICE-72, New York

Pischinger F, Scheid E and Reuter U (1987) Influences of fuel quality and injection parameters on self ignition of sprays. CIMAC, D-112, Warsaw

Reitz RD, Diwaker R (1987)Structure of High-pressure fuel sprays, SAE 870598

Simmons HC (1977) The correlation of drop-size distribution in fuel nozzle sprays, Part I, drop size volume fraction distribution. J. Eng. Power

Spalding DB (1977) Combustion and Mass transfer. Pergamon Press, Oxford, chapters 4,6,11.

Szybist JP, Boehman AL, Taylor JD, McCormick RL (2005) Evaluation of formulation strategies to eliminate the biodiesel NOx effect, Pages 1109–112, Issue 10, Volume 86, Fuel Processing Technology

Thelliez M, Ji ZM (1987) Reflexion sur la modelisation du delai d' inflammation dans les moteurs dieselm. Entropie, 134

Tsao KC, Myers PS, Uyehara OA (1962) Gas temperature during compression in motored and fired diesel engines. SAE Transactions

Watson N, Pilley AD, Marzouk M (1980) A Combustion Correlation for Diesel Engine Simulation. SAE Paper No. 800029
Woschni G, Anisits F (1974), Experimental investigation and mathematical representation of rate of heat release in diesel engines dependent upon engine operating conditions, SAE 740086
Wolfer HH (1950), Ignition lag in diesel engines, Translation Royal Aircraft Est, 358

6 Heat Transfer

Abstract The empirical correlations estimate the surface-averaged heat transfer coefficient in terms of the bulk gas temperature and a surface-averaged or total heat flux. The investigations have revealed that during the combustion period, the wall heat flux is locally substantial in space and time, due to the transient nature of the flame propagation. During combustion, the heat flux increases rapidly after spray impingement on the wall. A phenomenological model is proposed to predict the convective heat transfer from the spray to the wall. The analogy of Woschni is applied for the spray impinging on combustion chamber. This heat transfer has strong impact on NO_x formation and combustion-chamber design.

A large surface area of the combustion chamber is exposed to gases in later part of the combustion and heat transfer. Therefore, the heat transfer rate must be estimated accurately enough, while experimentally obtaining the heat release rate during this period.

Heat Transfer Across the Walls

Hohenberg's correlation (1979) for the instantaneous heat transfer considers truly the conditions present in a DI diesel engine. This correlation is based on extensive experiments done on DI diesel engines. The instantaneous heat transfer across the walls for engines A12 to D12 mentioned in Table 3.2 is estimated using the following equation.

$$h_c = \frac{130 P_{cyl}^{\ 0.8} \cdot \left(u_p + 1.4\right)^{0.8}}{V_{inst}^{\ 0.06} \cdot T_{cyl}^{\ 0.4}} \tag{6.1}$$

where, h_c = Heat transfer coefficient
u_p = Piston velocity
V_{inst} = Instantaneous cylinder volume
T_{cyl} = Temperature of the Cylinder charge

The cycle-averaged heat transfer coefficient for individual surfaces can be used in the network of resistances to iteratively obtain different surface temperatures of the combustion chamber enabling precise estimation of instantaneous heat transfer (Gajendra Babu and Murthy 1976).

$$\frac{dQ_{ht}}{d\theta} = h_c A_s \left(T_{cyl} - T_w\right) \cdot \left(\frac{1}{6N}\right) \tag{6.1}$$

where, A_s = Instantaneous surface area
T_w = Wall temperature

P.A. Lakshminarayanan and Y.V. Aghav, *Modelling Diesel Combustion*, Mechanical Engineering Series, DOI 10.1007/978-90-481-3885-2_6,

Heat Transfer Coefficient at the Wall Where the Spray Impinges

An analogy between the in-cylinder flow and the steady state turbulent flow through a circular tube is used by Woschni (1967) to estimate heat transfer coefficient. The spray properties and wall impingement were predicted by earlier work of authors (Aghav *et al.* 2005, 2007, Lakshminarayanan *et al.* 2002). The analogy adopted by Woschni (1967) is applied for the spray impinging on combustion chamber.

$$h_c = C^* L^{-0.2} P_{cyl}^{\ 0.8} u_{wall}^{0.8} T_m^{-0.35} \tag{6.2}$$

Where, h_c = Heat transfer coefficient
C^* = A constant
L = Characteristic length, wall spray diameter, mean diameter of ring
P_{cyl} = Cylinder pressure, bar
u_{wall} = Wall spray velocity, m/s
T_m = Mean temperature of outer and inner boundaries of circular regions

The wall jet portion of the engine spray is divided into five annular rings (Fig. 6.1). The annular divisions grow every time step as per wall spray growth. For every division, the mean spray temperature, area and heat flux are predicted and finally integrated to get the heat flux.

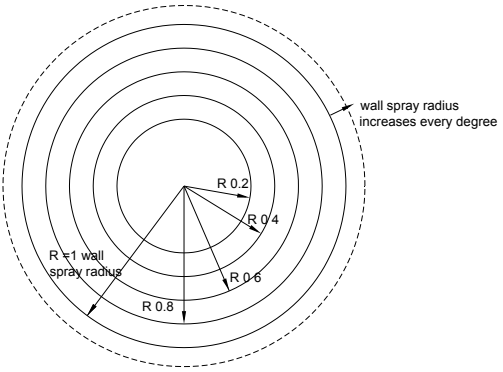

Fig. 6.1 Section of wall spray divided in annular rings

$$h_{f_{ring}} = h_c \left(T_m - T_p \right) \tag{6.3}$$

$$h_{t_{ring}} = \sum h_{f_{ring}} A_{ring} \tag{6.4}$$

Where, $h_{f\ ring}$ = Average heat flux for an annular division
T_p = Piston temperature, K

$h_{t\ ring}$ = Average heat transfer for a annual division

A_{ring} = Area of a annular division

The mixing controlled combustion model proposed by Lakshminarayanan *et al.* (2002) with introduction of wall impingement is employed for prediction of heat release. The rate of burning is proportional to the available fuel and the rate of entrainment of air. The temperatures and equivalence ratios in wall spray are also corrected by ratio of net heat release to gross heat release rate.

$$t_{corr} = \left(\frac{\frac{dQ}{d\theta} - \frac{dh_t}{d\theta}}{\frac{dQ}{d\theta}} \right) t \tag{6.5}$$

$$\Phi_{corr} = \left(\frac{\frac{dQ}{d\theta} - \frac{dh_t}{d\theta}}{\frac{dQ}{d\theta}} \right) \Phi \tag{6.7}$$

where, $\frac{dQ}{d\theta}$ = Rate of heat release

$\frac{dh_t}{d\theta}$ = Rate of heat transfer

Heat Transfer from Spray to the Wall

A phenomenology for heat transfer arising out of interactions between spray and combustion cavity is developed during modelling for NO_x model. The CFD study and measurements for a heavy-duty engine described in reference (Nishiwaki 1998) were considered for model validation. The details of the engine as well as the assumed data are given in Table 6.1.

Initially the geometric spray properties like penetration and impingement. is predicted. Then physical properties like vapour concentration are predicted for different annular zones of the spray (Chapter 4). Finally, after impingement, the convective heat transfer is considered and heat fluxes from different divisions of wall spray are predicted.

The heat flux predicted by new model is compared with CFD results at spray and wall interaction section (Fig. 6.2). This shows the new model predicts slightly higher radius as well as heat flux, but overall trend matches with CFD results. Then average heat flux at different crank angle position is compared for predictions with new model, CFD and experimental value (Fig. 6.3). Predictions with new model are done with different number of divisions to study the model sensitivity. With ten annular divisions, the predicted values match CFD results. The predictions with CFD and new model are similar however; both are higher than experimental values especially during initial period after impingement. The reason

could be numerical approach followed by the simulation models and errors in instruments to measure sudden rise in temperature.

Table 6.1 Details of engine, A6 for heat transfer study

Bore × stroke, mm	130 × 150 mm
Connecting rod length	273 mm
Compression ratio	17.25
Boost pressure	2.85 bar
Boost temperature	315 K
Engine speed	1,420 rpm
Nozzle	8 hole
Fuel mass injected	80.38 g
Start of injection	351.2 CA
Spray cone angle	150 (assumed)
Duration of injection	27 CA (assumed)

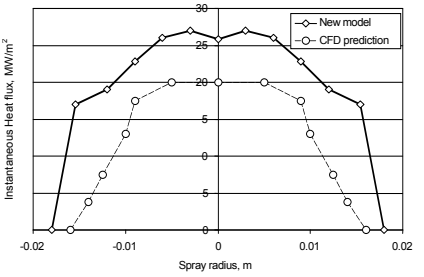

Fig. 6.2 Heat flux profiles along spray cross section at piston wall

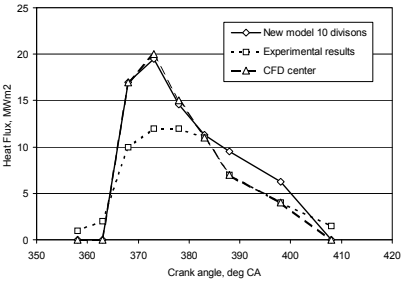

Fig. 6.3 Heat flux data at various crank positions

References

Aghav YV, Lakshminarayanan PA, Babu MKG, Azimuddin and Dani AD (2007) Validating newly evolved smoke model at widely varying operating conditions of DI diesel engine. GTP-06-1096, ASME Journal of Engineering for Gas Turbines and Power

Aghav YV, Lakshminarayanan PA, Babu, MKG, Nayak, NS, and Dani, AD (2005) Phenomenology of Smoke from Direct Injection Diesel Engines. Paper No. 1350, Proceedings of ICEF2005, ASME

Gajendra Babu MK, Murthy BS (1976) Simulation and evaluation of Exhaust and Intake system of a 4-stroke spark ignition Engine SAE 760763

Hohenberg GF (1979) Advanced approaches for heat transfer calculations" SAE 790825

Lakshminarayanan PA, Aghav YV, Dani AD, Mehta PS (2002), Accurate prediction of the rate of heat release in a modern direct injection diesel engine. Journal of Automobile Engineering, IMechE, 216

Nishiwaki K (1998) Modelling Engine Heat Transfer and Flame-Wall Interaction. In Proc. COMODIA 98, pp. 35–44

Woschni G (1967) A Universally Applicable Equation for the Instantaneous Heat Transfer Coefficient in the Internal Combustion Engine. SAE 670931

7 Heat Release in Indirect Injection Engines

Abstract The rate of heat release in an in direct injection engine is modelled on the lines of the observed rate in a direct injection engine. The premixed burning is assumed to take place only in the prechamber. The diffusion burning was modelled to be proportional to the modelled rate of air entrainment and available fuel. The diffusion burning is stopped in the auxiliary chamber, once all the air in it is consumed. Comparison of experimental data with the results of simulation over a wide range of speed and load was encouraging. Different engine parameters were varied and their effects on engine performance are discussed.

High-speed indirect injection (IDI) engines produce less nitric oxides and particulate emissions than similar automotive direct injection (DI) engines. In addition, high speed DI engines requires high-pressure fuel injection equipment, which is expensive and fine nozzle orifices, which are difficult to maintain. On the other hand, IDI engines are less fuel efficient due to large pumping losses in the auxiliary chamber. The disadvantages of DI engines have caused a revival of interest in improving the fuel economy of IDI engines (Scott 1985, Lakshminarayanan and Nagpurkar 1986). Effect of changes in the geometry and assembly parameters on the engine performance could be studied if a simple representative model is available. The combustion model is an important Part of this. In this paper, an attempt is made to describe the combustion process in the two chambers of an IDI engine.

A wealth of literature is available on modelling of IDI engines (Bowden *et al.* 1969, Brandstetter 1980, Miyamoto *et al.* 1985, Mansouri *et al.* 1982, Terada 1981). Most of them fall in the category of incomplete models (Borman 1980), which require certain parameters empirically adjusted for the specific system being modelled. Complete which require only fundamental data or correlations of a general nature and not specific to the system being modelled are not available. Of the former type, quasi-dimensional and zero-dimensional models are popular. The model discussed in the present work is zero dimensional and of incomplete type.

Bowden *et al.* (1969) synthesized the heat release rate from the fuel injection pressure diagram. The magnitude of heat release in the auxiliary-chamber was modelled to depend on the total amount of injected fuel and on the ratio of the volume of this chamber to the total clearance volume. The portion of the fuel injected early was assumed to burn in the auxiliary chamber. An element of fuel was assumed to burn according to two laws in the shape of triangles (Austen and Lyn 1962), exclusively in one of the two chambers. The heat release in the main chamber was modelled delayed by 10º crank angles. Brandstetter (1980) has reported calculations for a spark ignition IDI engine. In this model, two Wiebe's constants were used for the two chambers (Wiebe 1956). During combustion, fuel exchange was allowed to take place through the connecting throat. The fuel was

P.A. Lakshminarayanan and Y.V. Aghav, *Modelling Diesel Combustion*, Mechanical Engineering Series, DOI 10.1007/978-90-481-3885-2_7,

assumed to have memory of the chamber in which it was before combustion and hence of the Wiebe's constant. In addition, the combustion in the main chamber was assumed delayed by a definite crank angular time after it started in the prechamber. Miyamoto *et al.* (1985) used a single Wiebe's function. There was no distinction between the temperature and pressures in the two chambers. The total heat release due to premixed combustion was found to be 88% of energy injected during the ignition delay. The combustion duration was correlated to the total fuel that would burn diffusively. Smoke was found to be dependent on this duration. Mansouri *et al.* (1982) used a stochastic mixing approach during the combustion and expansion processes to describe non-uniform distribution of fuel air ratio in an IDI engine. Most of the discussions were written at 1,500 rpm. About 3% reduction in the efficiency was calculated for 70% reduction in the effective area of the throat. The difference between the pressures in the two chambers was small as the speed was very low. Terada (1981) neglected the pressure difference between the two chambers. The experimentally obtained heat release rates and the time difference between the start of combustion in the two chambers were input to a thermodynamic simulation program to calculate the temperatures and the formation of nitric oxides.

Description of the Phenomenological Model

The experimental heat release rates in the two chambers of the IDI engine under study (RET7, Table 3.2) were analysed and it was found that they were similar to that shown in Terada (1981). The rate in the prechamber was very high in the beginning and was tapering off later. The heat release starts later in the main chamber and is comparatively slower. The ignition delay was slightly lower than that was observed in a DI engine of equivalent geometry. Based on these observations a model, which is closely related to a DI engine combustion heat release, was developed. The main features of the present model are (Lakshminarayanan and Nagpurkar 1986):

- It clearly shows the difference in pressures and temperatures in the two chambers and hence is useful in calculating emissions.
- It does not assume a definite crank angular delay between the start of combustion in the two chambers.
- Combustion in the prechamber is completely stopped after all the air is utilized.
- It reacts well with the changes in injected fuel and speed.
- It is zero dimensional and simple to apply.

Combustion model

Let us consider the fuel injected in the form of a transient spray into an infinite surrounding after the ignition delay is over (Fig. 7.1). The air is entrained in the spray to vaporise the liquid fuel and mix with the vapour. The rate of chemical re-

action is very high, compared with the rate at which the fuel mixes with air (Plee and Ahmad 1983). Thus, the rate of burning is controlled by the rate of diffusion of air or the mixing rate. Figure 7.2 shows the rate of formation of vapour-air mixture. If the fuel available for diffused burning is known,

$$Rate\ of\ burning = Available\ fuel \times Rate\ of\ mixing\ with\ air \tag{7.1}$$

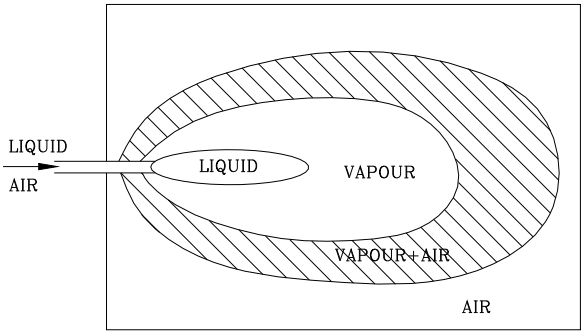

Fig. 7.1 A typical vaporising spray

Figure 7.3 shows the amount of air entrained by a transient spray and the rate of fuel injected. In the case of a diesel engine, the surrounding is finite and the maximum air is limited. The time scale in the diagram is non-dimensionalised with respect to combustion duration for convenience. Any fuel that mixed with air during ignition delay is termed premixed fuel and it burns at a rate determined mostly by the chemical kinetics and engine turbulence. In Fig. 7.3, the rate of diffusion of air is plotted. The fuel available for burning decreases because of burning itself. Applying equation (7.1), the rate of diffusion burning could be obtained. For DI engines, Watson *et al.* (1980) have shown that the two rates of burning discussed above could be written as below. The second equation is the well-known Wiebe law of burning (1956).

$$\dot{m}_p(\tau) = \beta m_f C_{P_1} C_{P_2} \tau^{C_{P_1}-1} \times \left(1 - \tau^{C_{P_1}}\right)^{C_{P_2}-1} \tag{7.2}$$

$$\dot{m}_d(\tau) = (1-\beta) m_f C_{d_1} C_{d_2} \tau^{C_{d_2}-1} \times \exp\left(-C_{d_1} \tau^{C_{d_2}}\right) \tag{7.3}$$

Here,

β	=	The amount of fuel mixed with air during the delay.
C_{P1}	=	A constant dependent on the delay period.
C_{P2}	=	*Nearly constant (=5000) for all engines*
C_{D1}, C_{D2}	=	Constants describing rate of diffused combustion

$\dot{m}_P(\tau) = \frac{dm_P}{d\tau}$ = Rate of burning of premixed fuel

$\dot{m}_d(\tau) = \frac{dm_d}{d\tau}$ = Rate of diffusion burning

τ = Time, non-dimensionalised with respect to nominal Combustion duration.

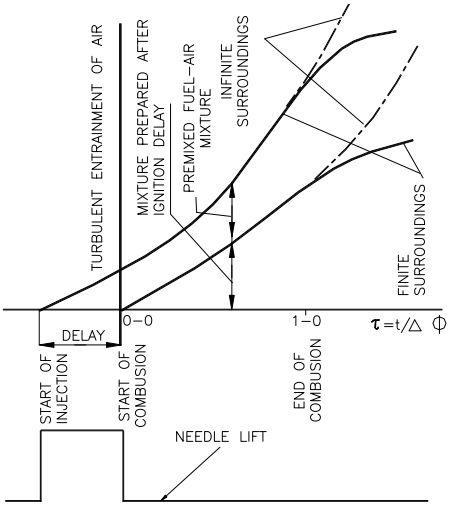

Fig. 7.2 Rate of formation of vapour–air mixture

Equation (7.3) could be explained using Figs. 7.2 and 7.3. Integrating (7.3) we get,

$$m_d(\tau) = (1-\beta)\ m_f \left(1 - \exp\left(-C_{d_1}\tau^{C_{d_2}}\right)\right) \tag{7.4}$$

Substituting $m_{d_u}(\tau) = (1-\beta)\, m_f \exp\left(-C_{d_1}\tau^{C_{d_2}}\right)$ in equation (7.3) we get

I II

$$m_d(\tau) = \left(m_{d_u}(\tau)\right)\left(C_{d_1} C_{d_2} \tau^{C_{d_2}-1}\right) \tag{7.5}$$

Here, $m_d(\tau)$ = Fuel quantity that would bum diffusively after τ

The I term on the right refers to fuel available for diffusion burning and the II term describes the rate of air entrained into the spray, or mixedness. An equation similar to (7.5) could be derived from Viebe function also. Thus, equations (7.5) and (7.1) have the same meaning. This idea was extended to an IDI engine (RET7,

Table 3.2). In this type of engines, let us assume, for convenience, that all the fuel is injected within the delay period. Figure 7.4a shows the rates of diffusion burning in both the main and auxiliary chambers. The size of the auxiliary chamber limits the rate of entrainment of air. Thus, only part of the available fuel is burnt in the pre-chamber and the rest flows to the main chamber along with burned gases in the form of a torch. Line a represents the fuel available in the main chamber if there is no burning in the auxiliary chamber. The amount of fuel increases due to the piston action. Line b will be the case if there is piston movement and there is burning in the auxiliary chamber only. If burning takes place in both the chambers, the available fuel is represented by line c. Using equation (7.1) the rate of diffusion burning could be obtained. The fuel and air premixed during the delay period burns at a rate determined by kinetics and turbulence only. Since it occurs very fast, we model it as a phenomenon happening only in the auxiliary chamber. Figure 7.4b shows the net burning rates in the two chambers derived from this model. Swirl chamber engines are over swirled at high speeds and low swirled at lower speeds (Scott 1985). Therefore, the preparation rate during the delay period decreases with speed. The mixing of fuel and air in the two chambers, their conversion to products and the exchange of gases between the two chambers are schematically shown in Fig. 7.5.

The equation for the model could be written as

$$\text{Rate of appearance of unprepared fuel in a chamber, } x = \frac{dm_{ux}}{d\tau}$$

$$= c\frac{dm_{ux}}{d\tau} - \frac{dm_{dx}}{d\tau} \tag{7.6}$$

Here, x =I refers to auxiliary chamber

=II refers to main chamber

$\frac{dm_x}{d\tau}$ = Rate of transport of gases to chamber from the adjoining chamber.

C = Concentration of fuel in the chamber from which the above transport takes place

$\frac{dm_{dx}}{d\tau}$ = Rate of diffusive burning in chamber X

The flow rate is given by the equation for flow through an orifice.

$$\frac{dm_x}{dt} = f\left(T_1, P_1, P_2, A, D_c\right) \tag{7.7}$$

Here, T_1, P_1 = Upstream temperature and pressure

P_2 = Downstream pressure,

A = Geometrical area

D_c = Discharge coefficient of the orifice

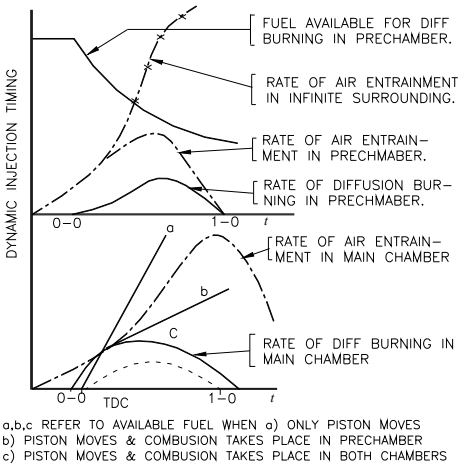

Fig. 7.3 Rate of diffusion burning

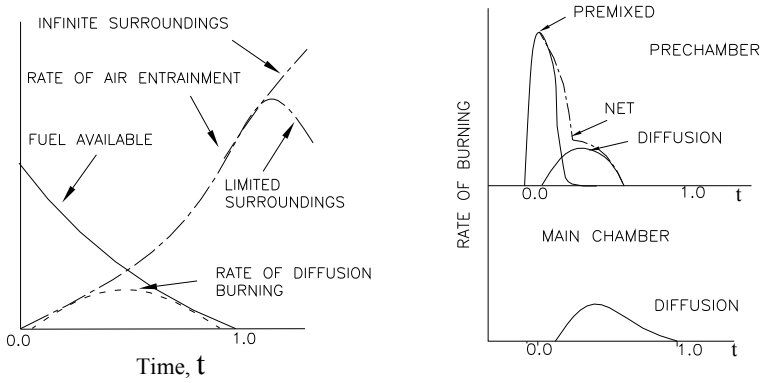

(a) (b)

Fig. 7.4 Rates of burning in an IDI engine

$$Rate\ of\ diffused\ burning = \frac{dm_{dx}}{d\tau} = m_{ux} g(\tau) \tag{7.8}$$

Here,

$$\begin{aligned} g(\tau) &= Rate\ of\ mixing \\ &= C_{d_1} C_{d_2} \tau^{C_{d_2}-1} \end{aligned} \tag{7.9}$$

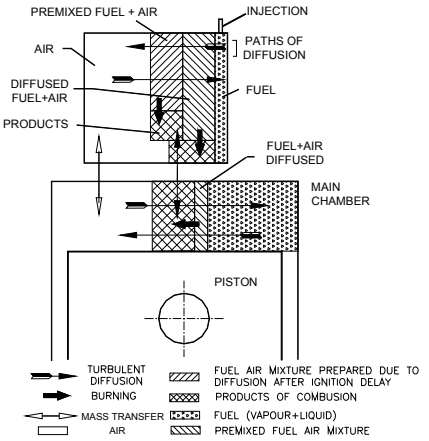

Fig. 7.5 Schematic of combustion model

$$Rate\ of\ burning\ of\ \ premixed\ \ fuel = \frac{dm_{P_I}}{d\tau}$$

$$= (1-\beta)\, m_f\ C_{P_1}\ C_{P_2}\ \tau^{C_{p_1}-1}$$

$$= \left(1-\tau^{C_{p_1}}\right)^{C_{p_2}-1} \tag{7.10}$$

Here, m_f = Total injected fuel.
Premixed fuel fraction,

$$\beta = 1 - q\ \lambda^m\ \delta^{\,n_N p} \tag{7.11}$$

where, λ = Relative air fuel ratio
δ = Ignition delay in milliseconds
N = engine speed, rev/min
q, m, n, p = Constants for a given engine

The ignition delay expressed in an equation similar to Wolfer (1938) is given by

$$\delta = A\ P_I^r\ \exp\left(E/(R_u T_I)\right) \tag{7.12}$$

Here T_I, P_I = Prechamber temperature, K, pressure, bar respectively

A, E	=	Arrhenius pre-exponent and pseudo activation energy
R_u	=	Gas constant

Heat transfer
The heat transfer coefficient in the two chambers was assumed the same and calculated using Woschni's formula (1961) (equations (6.3) and (17.32)).

Gas exchange model
The gas exchange process was modelled (Brandstetter 1980) as simple filling and emptying of the engine cylinder (Fig. 7.6).

Friction power
Millington and Hartles (1968) give two different formulae for calculating friction power for DI and IDI engines. The extra pumping loss encountered by the flow between the auxiliary and main chambers is the reason for the difference. Since, in the present model the indicated work is calculated using the pressure in the main chamber, the formula given for DI engine is applicable.

$$fmep\ (bar) = A + B\,U_p + C\,C_m^2 \tag{7.13}$$

$$A = 0.06898(compression\ ratio = 4)$$
$$B = 0.02897$$
$$C = 4.008 \times 10^{-3}$$
$$U_p = crank\ speed\ (revolution/s)$$
$$C_m = mean\ \ piston\ speed, ms^{-1}$$

Calculation procedure
Applying first law of thermodynamics, the models mentioned above were solved to obtain the state of gases in the two chambers. Fourth order Runge-Kutta method was used to solve all the first order ordinary differential equations. Step sizes of 5°, 0.1° and 1° were used during gas exchange, ignition delay and combustion respectively to avoid instabilities in the results.

Experimental Technique

The steady state parameters were measured using conventional techniques. The measurement of differential pressure however, needed some care. The two piezoelectric transducers, whose sensitivities are close to each other, were calibrated using a calibrating unit where hydraulic pressure was created by placing accurate weights on a standard piston. The electrical charge-amplifiers were set according to the calibration constants obtained above. The outputs of the two amplifiers were fed to a Subtracting amplifier, to obtain the difference. Since the pressure difference

during the gas exchange is very small, the nearly horizontal line during this period was taken as the zero reference.

Results and Discussions

The parameters C_{P1}, C_{P2}, C_{D1}, C_{D2} in equations (7.2), (7.3) and (7.11) were correlated to the relative air fuel ratio (λ), delay (δ ms), and speed (Watson *et al*. 1980) for the engine under consideration.

$$C_{P_1} = 3 + 3.90 \times 10^{-4} \left(\delta N\right)^{1\,05}$$

$$C_{P_2} = 5000$$

$$C_{d_1} = 13.9 \left(\lambda\right)^{0\,64}$$

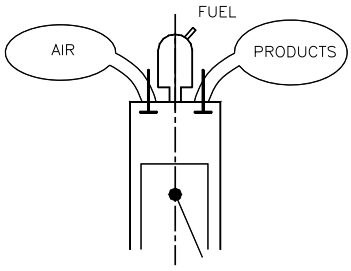

Fig. 7.6 Gas exchange model

$$C_{d_2} = 1.14\, C_{d_1}^{\;0\,26}$$

$$C_{d_2} = 1 - 5.5\lambda^{-0\,293} \left(\delta N\right)^{-0\,25}$$

The other constants in equations (7.11) and (7.12) are:

$q = 5.5$	$r = -1.19$
$m = -0.293$	$A = 2.58 \times 10^{-4}$
$n = -0.25$	$R_u = 8.32$ kJ/kmol K
$p = -0.25$	$E = 38{,}689$ kJ/kmol

Using these parameters, simulation of 1/4, 3/4 and full loads at 1,500, 2,000, 2,500, 3,000 and 3,500 rpm was made, the base condition of this was full load at

2,500 rpm. Comparison of transient absolute pressures and differential pressures obtained experimentally and by calculations is shown in Fig, 7.7. In general, the comparison is favourable. At very low loads, the model predicts slightly earlier pressure rise in the swirl chamber. This is because the effect of low loads on delay was not taken into account. At 2,000 rpm, the experimental pressure-difference is higher than the predicted value. It was observed during experiments that the pressure in the swirl chamber was cyclically varying as in the case of spark ignition (SI) engines. The origins of these variations may be similar to those in an SI engine. It was also observed that at high speeds and high loads the differential pressure was a clear smooth curve, superimposed by high frequency fluctuations. Similar disturbances were noticed by Mansouri *et al.* (1982) at 1,500 rpm. It was also observed that these disturbances increased with speed and load. These may be due to the vortices produced at the sharp edges of the throat, resonating in the swirl chamber cavity. The pressure in swirl chamber is low during compression stroke due to throttling. Then the pressure rises quickly due to the heat released by premixed burning. At some loads and speeds, a second peak in the differential pressure could be observed. This is due to diffusion burning in the swirl chamber.

Figures 7.8–7.11 show some parameters at base condition. Flow through the throat is shown in Fig. 7.8. The concentration of unprepared fuel in the two chambers is shown in Fig. 7.9. Only a part of the fuel is completely burned in the prechamber and the rest flows to the main chamber. Figure 7.10 shows the heat release rate in the two chambers. They are similar to the results reported by Terada (1981) and as discussed in Section 2.1. The time lag in starting of combustion in the main chamber could be clearly seen.

The mean temperatures in the two chambers are shown in Fig. 7.10. In Fig. 7.11, smoke is correlated with the duration of diffusion combustion defined as the time between 5% and 95% of the net heat release in the main chamber (Miyamoto *et al.* 1985). Two data points, which were far away from the mean curve, were omitted. In this graph, a wide range of speed and load is covered.

Figures 7.12–7.15 show results of some parametric studies made using the combustion model. In Fig. 7.12, the sensitivity of the model to changes in the value of nominal combustion-duration (input to the model) is shown. The peak pressures and exhaust temperature are affected more by this parameter. The change in indicated mean effective pressure (i m.e.p.) is small. Figure 7.13 shows the effect of change in volume of prechamber keeping the compression ratio constant. With increase in volume, the mean gas temperature during injection increases as the heat transfer and throttling losses decrease. Consequently, the delay decreases. However, if the volume is very high, the burned gases at high pressure are throttled during expansion and the i m.e.p decreases. Therefore, there is a clear optimum volume of the swirl chamber.

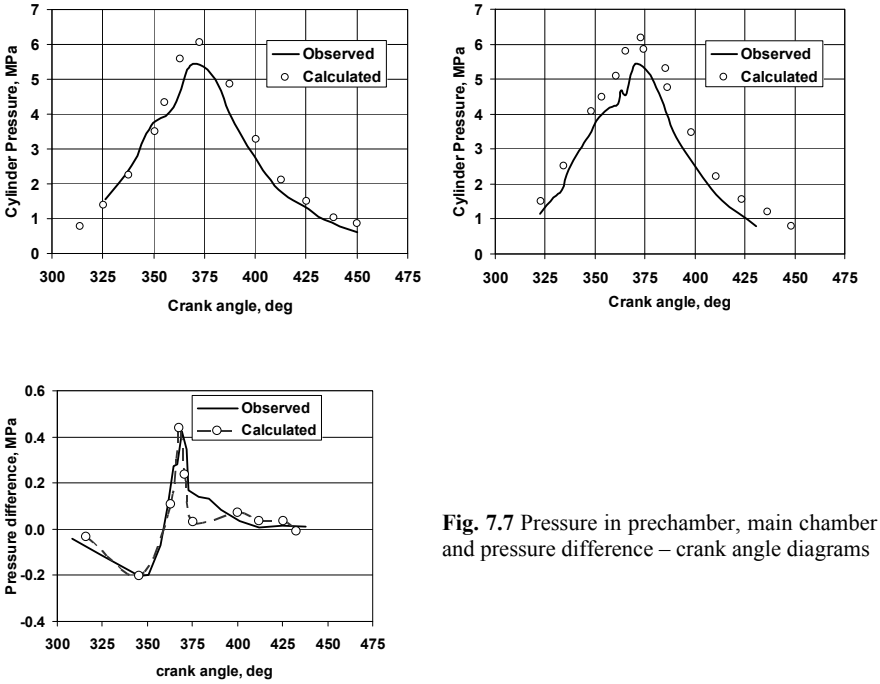

Fig. 7.7 Pressure in prechamber, main chamber and pressure difference – crank angle diagrams

Peak pressures in the two chambers are affected very little. In Fig. 7.14 the effect of change in fuel, timing is shown. The peak pressure increases with negligible change in i m.e.p. as the timing is changed. This is due to the complementary roles of both throttling and heat transfer. This tolerance to timing is helpful in designing a simple mechanism for advancing the timing with speed. The duration of combustion in the main chamber and the temperature of the exhaust gases decrease as expected. Figure 7.15 shows the effect of insulation on the engine performance. The full lines show the engine behaviour for constant dynamic injection timing. The flow pattern and hence the convective heat transfer coefficient is affected very little when the engine is insulated. However, since the wall temperatures are nearly constant, heating of the gases during the intake stroke reduces the volumetric efficiency. This increases the duration of diffusion burning as the overall air-fuel ratio reduces, leading to lesser i.m.e.p. Since the average gas temperatures are higher, the ignition delay decreases with increased insulation. Consequently, the premixed burning is less.

The maximum pressures in the two chambers decrease and the imep is affected very little if for a given insulation the timing was changed (dashed lines in Fig. 7.15) to obtain constant start of combustion. Figure 7.16 shows the engine behaviour if the swirl chamber alone was insulated. The trends are the same as in case of complete insulation. The effect of compression ratio keeping the ratio of volumes of prechamber to main chamber constant is shown in Fig. 7.17. Since the expansion

ratio increases, there is an increase in i.m.e.p. Optimisation of throat area and timing would lead to further increase in i m.e.p. The effect of changing the throat area is shown in Fig. 7.18. With increase in throat-area from 0.5 to 1.5 times the base-value there is a 10% increase in indicated mean effective pressure mainly due to reduced throttling (Scott 1985, Mansouri *et al.* 1982). This study assumed that the rate of air entrainment was unaffected by the change in throat area.

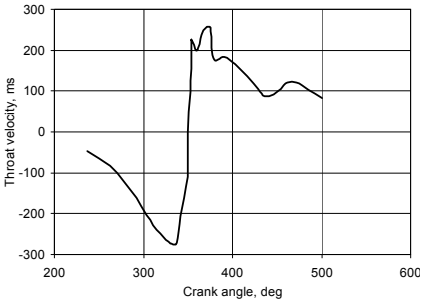

Fig. 7.8 Flow velocity through throat

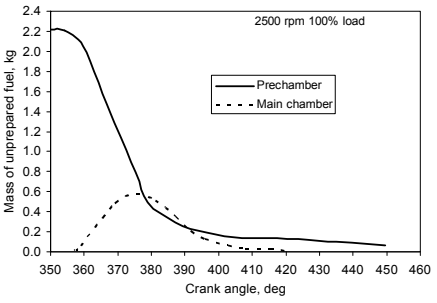

Fig. 7.9 Mass of unprepared fuel

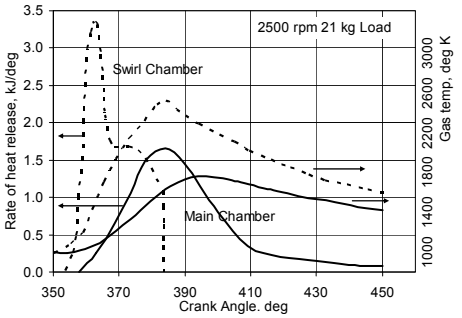

Fig. 7.10 Heat release rates in the swirl chamber and the main combustion chamber

Conclusions

1. A physical explanation was provided for the available heat release correlations for DI engines.
2. One such correlation (Watson *et al*. 1980) was extended to IDI engines. It was written as: Rate of diffusion burning = Rate of air entrainment × available fuel for diffusive burning (Scott 1985).
3. Constants in the correlation were tuned using experimental data over wide ranges of speed and load. Swirl chamber pressure and the differential pressure were predicted reasonably well.
4. Smoke was correlated with duration of diffusion burning in the main chamber.

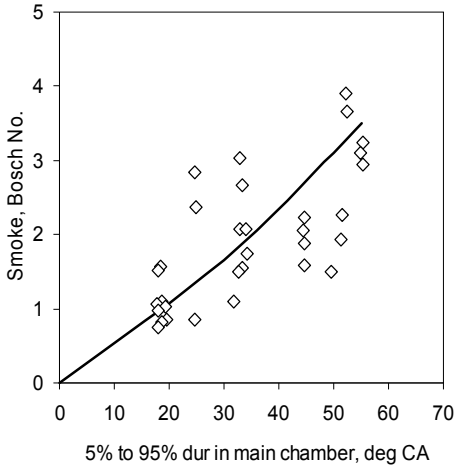

Fig. 7.11 Correlation of smoke and diffusion combustion duration

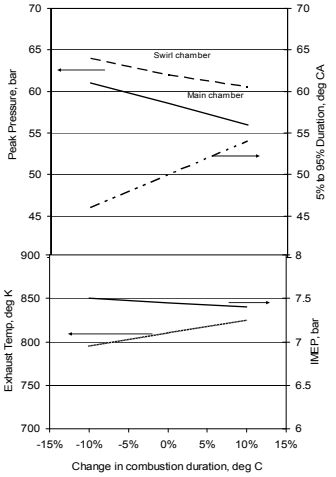

Fig. 7.12 Effect of change of combustion duration on engine performance

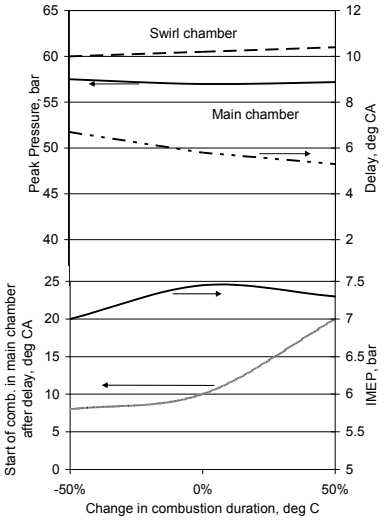

Fig. 7.13 Effect of change of swirl chamber volume on engine performance

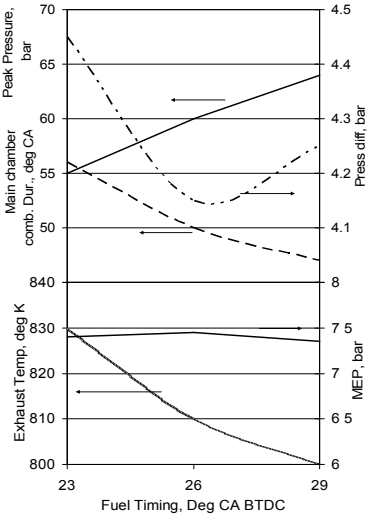

Fig. 7.14 Effect of change of fuel timing on engine performance

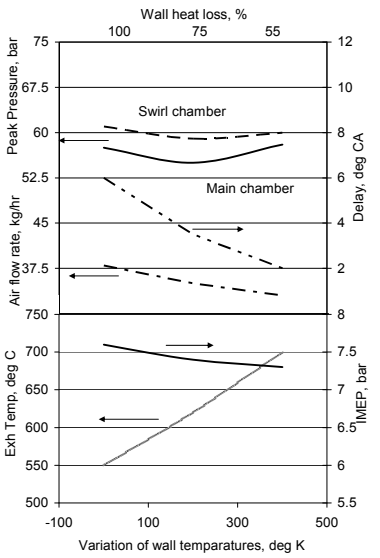

Fig. 7.15 Effect of insulation on engine performance

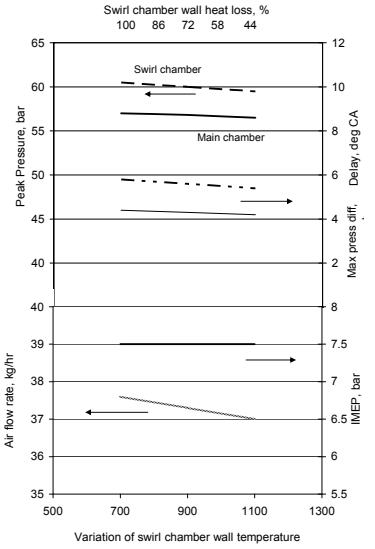

Fig. 7.16 Effect of insulation of swirl chamber on engine performance

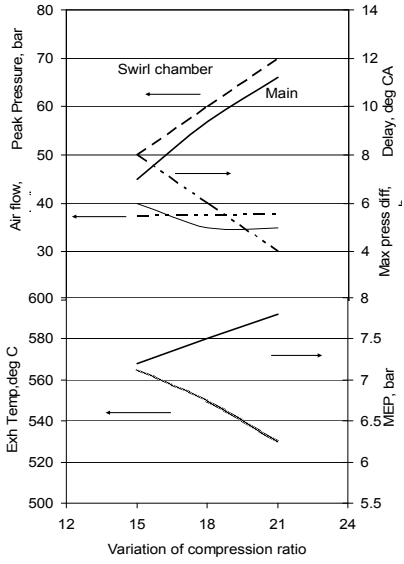

Fig. 7.17 Effect of variation of compression ratio on engine performance

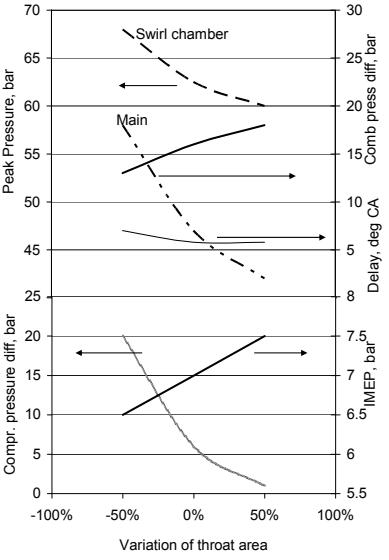

Fig. 7.18 Effect of variation of throat area on engine performance

5. Parametric studies were made to describe the effect of changes in volume of the swirl chamber, throat area, heat transfer, compression ratio, fuel timing and

duration of combustion. In general, the results reflected the observed trends in a real engine.

6. Bmep, temperature, heat transfer and air flow obtained by integration over the cycle are predicted to an accuracy of about 5% over entire speed load range. Measured values of instantaneous pressures in the two chambers are within 7% of predicted results above 50% full load. At lower loads, the predicted pressures are higher.

References

Austen AEW, Lyn WT (1962), The application of heat release analysis to engine combustion study, CIMAC, Copenhagen

Borrnan GL (1980) Modelling flame propagation and heat release in engines. Combustion modelling in Reciprocating Engines, Ed. Mattavi JN, Amann CA, Plenum, New York

Bowden CM, Samaga BS, Lyn WT (1969) Rate of heat release in high speed induction ignition engines, Proc. Swirl chamber wall heat loss Main chamber variation of swirl chamber wall temperature – IMechE 1969-70 184 1. Part 3

Brandstetter WR (1980) Modelling of a stratified charge engine with an unscavenged prechamber, Combustion modelling in reciprocating engines, Ed. Mattavi JN, Amann CA, Plenum, New York

Lakshminarayanan PA, Nagpurkar UP (1986) Rate of heat release for divided combustion chamber. SAE 860084

Mansouri SH, Heywood JB, Radhakrishnan K (1982) Undivided chamber engine Part I: A cycle simulation, which predicts and emissions. SAE 820273, Detroit, February

Millington BW, Hartles ER (1968) Frictional losses in diesel engines, SAE 680590

Miyamoto N, Cnikahisa T, Murayama, Sawyer TR (1985) Description of diesel engine rate of combustion and performance using Vibe's functions. SAE 850107

Plee SL, Ahmad T (1983) Relative roles of premixed and diffusion burning in diesel combustion, SAE 831733

Scott J (1985) Giving the IDI diesel a fresh start, SAE 850452

Terada K (1981) Ermittlung der Gastemperaturen in beiden Brennraumen eines viirbelkammer dieselmotors. Motortechnische Zeitschrift (MTZ), 42

Watson N, Pilley AD, Marzouk M (1980) A combustion correlation for diesel engine simulation, SAE 800029

Wiebe I (1956) Halbempirische Formel fur die Verbrennungsgeschwindigkeit. Verlag der Akademie der Wissenschaften der UdsSR, Moscow

Wolfer HH (1938) Ignition lag in diesel engines, VDI-Forschungsheft No. 392

Woschni G (1961) A universally applicable equation for the instantaneous heat transfer co efficient in the internal combustion engine SAE 675931

8 Mixing Correlations for Smoke and Fuel Consumption of Direct Injection Engines

Abstract The mixing of fuel with air in a diesel engine strongly dictates the specific fuel consumption and exhaust smoke. Many experimental studies reported the optimum swirl for a given diesel engine at a given operating condition. However, the attempts to correlate the relative penetration, or cross wind velocity or the ratio of total momentum of fuel and air, or the angular speed of sprays at a characteristic time resulted in only partial success in the past. This chapter introduces the concept of useful air. The ratio of momentum of the useful air to the total momentum of injected fuel near TDC at the end of ignition delay period is found to bear a universal relationship with the indicated efficiency and dry soot emissions in case of combustion chambers supported by air swirl. The concept is enhanced when the injected quantity is small, by considering spray detachment from the nozzle tip and the swirling cloud of fuel vapour near the walls of combustion chamber. The correlation was validated for different combustion chamber designs of engine bores from 75 to 110 mm, running at rated speeds from 1,200 to 2,500 rpm. The proposed correlation of momentum ratio has universal application for different fuelling, operating speeds, and combustion chamber shapes and bores when the combustion is intensely supported by air swirl.

The Adaptation of diesel fuel to direct injection engine necessitates the understanding of mixing of fuel with air. All direct injection (DI) diesel engines are generically the same with the following features to achieve optimum mixing of fuel. (a) High pressure injection of diesel fuel through fine nozzle holes, (b) momentum incorporated to air during the inlet stroke by the inlet port, and (c) a bowl in piston which amplifies the inlet-swirl and contains majority of combustion. A variety of synergistic designs of these three processes has been successful. Before self-ignition of fuel, the reaction rate is slow and found to be dependent on rates of turbulent mixing and chemical reactions (Chandorkar *et al.* 1988). At the end of the delay period the concentration of products of combustion reaches a critical level to initiate uncontrolled premixed combustion. Subsequently, diffusion controlled main combustion takes place. The rate of combustion in this period is exactly equal to the rate at which air is mixed with fuel. In the pockets where ignition occurs, the fuel and air are mixed in stoichiometric proportion. If the delay period to form the critical concentration of precursors is zero, then no fuel could be mixed leaner than stoichiometric burning. In this case, there would be no hydrocarbon emission. However, since the delay is finite, there could be pockets diluted by air to proportions less than lean flammability limit, before auto-ignition occurs in several pockets. Thus, this fuel does not burn and contributes to emission. Dent (1980) correlated the emission of aldehydes and soot with mixing rate calculated

P.A. Lakshminarayanan and Y.V. Aghav, *Modelling Diesel Combustion*,
Mechanical Engineering Series, DOI 10.1007/978-90-481-3885-2_8,

from a mixing parameter, Taylor's microscale. Morris and Dent (1976), and Bassoli, Bodritti and Cornetti (1985) correlated fuel consumption and soot emission with the ratio of the total air momentum at TDC to the total momentum of injected fuel with some success. Ball (1980) related the performance to the ratio of penetration of fuel spray at the end of ignition delay to the penetration up to impingement against the wall. Timoney (1985) correlated the engine performance with the crosswind velocity. Wakuri *et al.* (1985) have attempted to correlate the angular spray dispersion with the engine behaviour. Ishida, Kihara and Furubayashi (1985) reported improvement in performance proportional to a K-factor, defined as the ratio of the piston cavity volume to the total volume at TDC including the piston land and groove crevices. Munro (1979), and McLean, Bremfoerder and Hamelink (1986) have reported performance and emissions benefits as the piston top land is reduced. In this paper, an attempt is made to explain the indicated behaviour and emissions of all the direct injection diesel engines. Kuo, Henningsen and Wu (1988a) thoroughly evaluated the correlations mentioned above. They had presented detailed experimental and calculated data on three types of cavities namely re-entrant type (R) and two shallow cavities (S1, S2) (Fig. 8.1). The data consisted of injection duration, injection velocity, total momentum of air, total momentum of fuel injected, distribution of radial velocity in the piston cavity, amount of air inhaled and quantity of injected fuel. All the experiments were designed to study the effects of variation in speed, and air-fuel ratio and shapes of piston bowl on the indicated specific fuel consumption (ISFC) and dry Soot in the exhaust. After evaluating the correlations of the data mentioned above, they concluded that although the correlations seem to have potential in specific cases as interpretive tools, the lack of generality limited their usefulness for the design engineer (Kuo *et al.* 1988a). In this chapter, the performance and emissions were successfully related to the characteristic ratio of the momenta of air useful to combustion and the injected fuel (Dani *et al.* 1990).

Characteristic Parameter for Air Fuel Mixing in a Cross Flow

A correlation between ISFC and the product of swirl number of air flow (Appendix V) at the end of the inlet stroke, as measured in a steady flow rig according to von Thien (1965), and the number of spray orifices was developed by the authors for engines A8, D8, F8, G8, H8, K8, N8, C9, C10 (Table 3.2). When the product attains a value between 10 and 12, the ISFC is the minimum (Fig. 8.2). This relationship is akin to the work of Wakuri *et al.* (1985) but does not indicate the type and shape of combustion chamber and injection parameters except the number of spray orifices. At higher engine speeds the injection velocity increases to improve the atomisation of fuel and hence combustion efficiency. Therefore at higher speeds the ISFC for the same swirl number and the number of sprays is lesser. Abramovitch (1963), Ramsey and Goldstein (1971) and Kamotani and Greber

(1972) studied the trajectory of steady gas jets in a uniform cross flow. The ratio of jet momentum fluxes of air and fuel was the major correlating parameter. Morris and Dent (1976) encountered difficulty in using this parameter and hence considered the measured air fuel ratio inside the gas jet to correct the parameter. The correlation implied that it is applicable to combustion chamber supported by swirl and the effect of fuelling on the air fuel-mixing rate is to be considered. In this chapter, the dilution of fuel is appropriately taken into account as only the air, which is taking part in main combustion, is considered. In a transient jet, the flux of fuel is not continuous. Over fuelling and under fuelling could be considered by the integrated momentum of injected fuel. Instead of the ratio of momentum fluxes considered by Abramovitch (1963) the ratio of the momentum of air useful to combustion and the integrated momentum of injected fuel is considered along the lines of Bassoli *et al.* (1985), at a characteristic instant in time.

The concept of useful air

Air, which is available during the main period of combustion for mixing with fuel, is termed useful. Its description involved understanding of air volumes, spray pattern and transients after injection is completed (Dani *et al.* 1990).

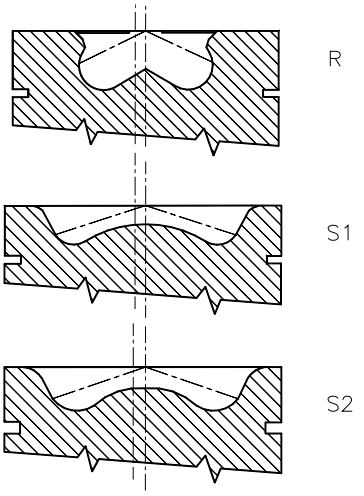

Fig. 8.1 Three piston cavities used for evaluating air-fuel momentum correlations (Kuo *et al.* 1988a)

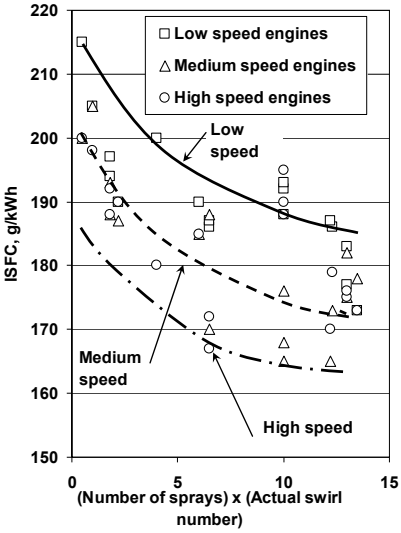

Fig. 8.2 Correlation of product of number of sprays

The engine size

There are two cases to be distinguished. (1) When the bumping (squish) clearance above the squish area is small and (2) when the clearance is very large, of the order of the depth of the bowl in piston. Figure 8.3 shows these two cases schematically.

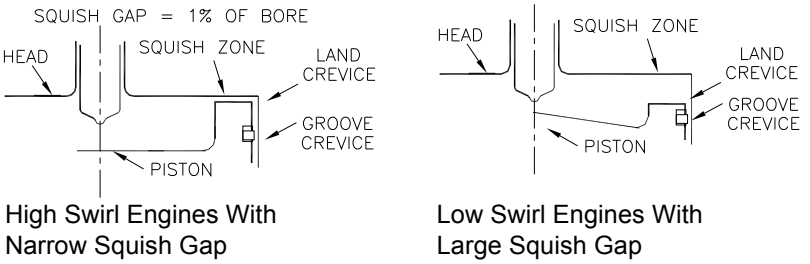

Fig. 8.3 Effect of engine size on useful air

Case (1): Small squish clearance: In engines of bore less than 120 mm the air swirl at BDC is high (swirl number 1.5–3.5) and is further enhanced at TDC due to the reduction in moment of inertia of the air. The sprays are designed to remain within the cavity during substantial period of combustion. Therefore, the air in the squish gap remains fairly in an unmixed state with the fuel. Thus, the air in this gap is not useful.

Case (2): Large squish clearance: In large engines of bore greater than 120 mm the swirl level is low (swirl number less than 1.5) and the bowl in piston is shallow. In addition, the squish clearance is of the order of the bowl depth. Hence, about a third of spray is designed to penetrate up to the cylinder wall. The air above the squish gap is useful as the fuel mixes with it during the period of combustion. In both the cases, the zone of air in the piston land and ring groove crevices remains unavailable and hence not useful (Munro 1979, McLean *et al.* 1986). The concept of unavailability of air in squish gap in small engines is very closely related to the K-factor (Ishida *et al.* 1985).

Potential core of the spray

In the potential core of a turbulent jet, the concentration of fuel (Lakshminarayanan and Dent 1983) is very high. Downstream of this core intense mixing with the air entrained due to shear flow takes place. In the case of liquid sprays, even when the chamber is above critical pressure and temperature of the fuel, the liquid core is observed within the potential core to slightly increase the unmixed length of the potential core. The length of the potential and liquid core (Lakshminarayanan and Dent 1983) is given in 8.1 as

$$l = 7.5\, d_e \tag{8.1}$$

Here, d_e = equivalent spray orifice diameter

$$= d\sqrt{\frac{\rho_f}{\rho_a}}$$

D = geometrical diameter of the orifice

ρ_f = density of the fuel

ρ = density of air

Figure 8.4a and b show the liquid core in different cases. The volume of air in the zone defined by the radius, corresponding to the length of the liquid core is unavailable for combustion, in large or small engines.

Characteristic time

When the fuel enters the combustion chamber and mixes with air during the ignition delay period, the mixtures that are too lean or too rich to burn (equivalence ratio outside the range of 0.5–3) give the trend of variation of HC emission (Henningsen 1984). In addition, the penetration is important from the viewpoint of understanding HC emissions and ISFC (Kuo *et al*. 1988b). The end of ignition delay period is the characteristic time at which all the parameters of the correlation are evaluated. At or about the maximum engine load, the fuel spray penetrates almost up to the wall of the piston bowl or the cylinder wall at the end of the ignition delay depending upon design of the cavity and the size of the engine bore. Figure 8.4a shows this case. However, at part loads the penetration at the characteristic time falls short of the distance to the wall of the combustion chamber. The air in the zone between the spray tip and the combustion chamber wall remains unavailable for combustion Fig. 8.4b shows schematically the part load cases.

Spray detachment

At the end of injection, the spray detaches from the nozzle. The detached zone still contains traces of fuel and the mixture in it is too lean to burn effectively. Figure 8.4c shows the spray detachment schematically at the end of delay period. The penetration of the detached portion of the jet is calculated using equation (4.7) as shown in Fig. 8.3. The air in the radius corresponding to the detachment is not useful for effective combustion.

In all cases shown in Fig. 8.4a–d the air in the annular ring of radial width A is useful. Therefore, the proportion of useful air is less than that given by the K-factor, by the amount corresponding to the initial thick spray or detached tip and the non-penetrated distance.

Calculation of momentum of injected fuel

The integration of instantaneous product of injected fuel quantity and the fuel velocity at nozzle tip gives the total momentum of injected fuel. However, measurement of the instantaneous fuel flow and the velocity is tedious in commercial engines. Assuming the coefficient of discharge, C_d as 0.8 and coefficient of velocity, C_v as 0.9 the momentum could be calculated from the pressure-time diagram measured at the inlet to the injector. For a quick estimate the average pressure determined by the area under the diagram during the injection period may be used. The average velocity calculated using the average pressure mentioned above, however, results in higher estimate of average velocity because of the non-linear relationship,

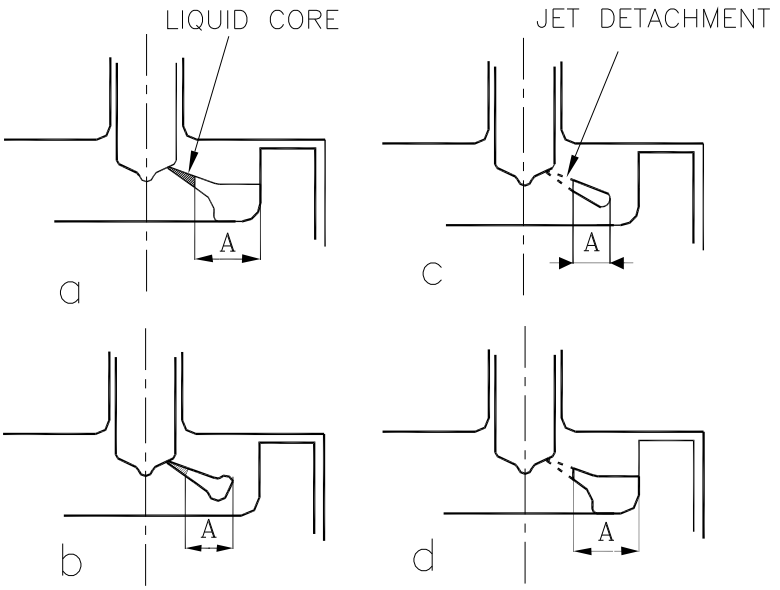

Fig. 8.4 Schematic of fuel spray showing positions of liquid core and detachment

$$velocity \propto \sqrt{pressure\ difference} \tag{8.2}$$

The estimate is correct only when the pressure difference is constant during needle open period. Assuming a parabolic variation of pressure from needle opening pressure to needle closing pressure, the average pressure that will yield correct average velocity could be obtained. In Fig. 8.5, average is shown along the y-axis and the correct pressure for velocity calculation is read along the x-axis. By using this help-graph for any average nozzle pressure, average velocity could be easily calculated. The total momentum of the injected fuel could then be calculated as the product of fuel mass injected per cycle and the average velocity. The penetration of the spray at the end of ignition delay is appropriately calculated using the average velocity at the nozzle tip during this period. The penetration,

$$x = \min\left(C_d \sqrt{8\, u_j d_e\, t},\, B\right) \tag{8.3}$$

Here, u_j = Fuel velocity at the nozzle tip
d_e = Equivalent orifice diameter
t = Time from the start of injection and
B = Distance from nozzle to the bowl

There are special cases when the injected quantity is so low that the spray detachment calculated from equation (8.2) is larger than the bowl radius, B at the characteristic time. Near the wall, the fuel collects like a cloud (Whitehouse and

Way 1969) and swirls along the wall (Fig. 8.4d). A reasonable estimate for the maximum detachment is assumed as 70% of the bowl radius which means that the thickness of the cloud is about twice the radial distance from the point of maximum velocity to the wall (Fig. 8.6).

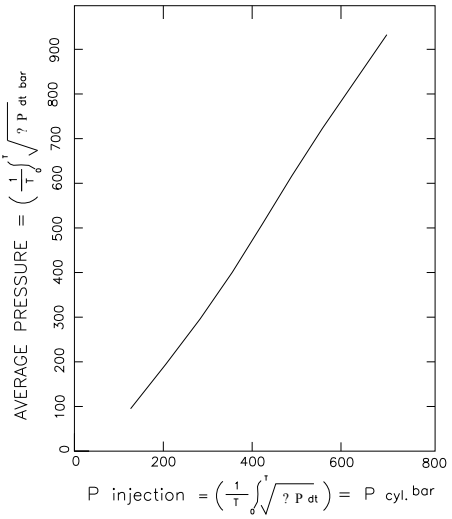

Fig. 8.5 Relationship between average pressure and corrected injection pressure

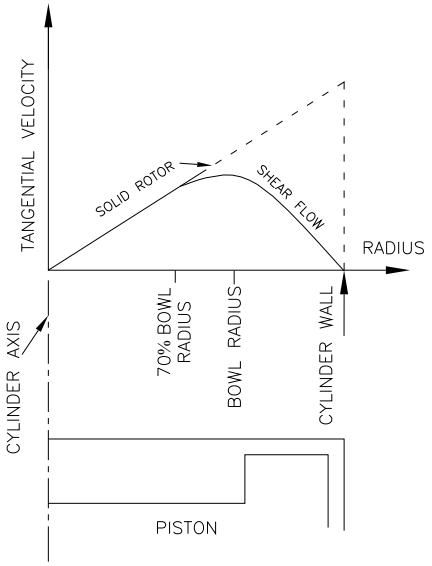

Fig. 8.6 Variation of tangential velocity of air in radial direction

Calculation of momentum of useful air

At TDC the tangential velocity of the air in the cup and squish gap is as shown in Fig. 8.6. The linear variation of velocity suggests strong solid-body rotation above the cylinder axis. Due to the wall drag, the velocity falls off close to the wall. The linear relationship is assumed valid in the squish gap also. The total air momentum in the annular ring of radial width A as shown in Fig. 8.4 could be calculated from the velocity profile. Results of thorough analytical flow calculations using finite difference techniques are given in Kuo *et al.* (1988a) for different types of combustion chambers (R, S1 and S2).

In case such calculations are not possible, a reasonable estimation of the air momentum could be made by assuming,

- Solid body rotation of air during piston travel from BDC to TDC
- Air density as a function of compression ratio with respect to inlet valve closing time
- End of ignition close to TDC
- The total angular momentum is retarded by about 25% during compression stroke, due to friction in the squish gap
- The spray reaches the walls of the piston bowl by the end of ignition delay period
- The velocity profile in general is as shown in Fig. 8.6 (Borgnakke *et al.* 1981). Using this profile and assuming the momentum loss due to friction the angular momentum could be easily calculated

Characteristic mixing parameter of an engine

The ratio of the momentum of air useful to combustion at TDC as explained above to the integrated momentum of fuel is defined as the parameter characteristic of the engine design and operating conditions. This factor will cover the principles envisaged by various investigators in the following manner (Table 8.1):

Table 8.1 Introduction of different facts in a single correlation

Feature	Figure showing the concept of useful air	Reference
Momentum ratio and crosswind velocity	Fig. 8.4a–d	Morris and Dent (1976), Bassoli *et al.* (1985), Timoney (1985)
Penetration at the end of ignition delay	Fig. 8.4a–d	Ball (1980)
Swirling angle	Fig. 8.4d	Wakuri (1985)
K-factor	Fig. 8.3a, b	Ishida *et al.* (1985)
Exclusion of dead volumes	Fig. 8.3a, b	Ishida *et al.* (1985), Munro (1979), McLean *et al.* (1986)

Since the principle direction of air, movement is tangential and that of the fuel is radial, the crosswind velocity concept is in the calculation of momentum of air.

The basis of the present work is improved definition of the ratio of the momentum of air to the momentum of injected fuel. Depending upon the ignition delay, the outer radius of the typical annular volume changes. The outer radius is nearly equal to the penetration of fuel in a swirling flow. For medium size engines, as already described, we are excluding squish volume and hence K-factor is considered. Since the land and groove crevices are not considered the dead volumes are excluded. The swirling angle is dependent on the strength with which airflow deflects fuel spray. This is dependent on the momentum ratio. Thus, the new definition of momentum ratio in this paper seems to cover wide-ranging observations and concepts of previous workers.

The indicated performance is not only a function of fuel air mixing and hence rate of burning but also a function of the heat transfer, especially about compression TDC. Therefore, while attempting to derive universal relationship of the performance and emissions with fuel air mixing the factor of engine surface to volume ratio (proportional to engine bore) must be kept in mind. Since the heat transfer at TDC is fairly well understood, it may not be difficult to incorporate this effect while estimating ISFC. However, the authors have refrained from doing this for reasons of brevity and hence assumed that for the popular bores in the range of 70–125 mm the heat transfer phenomenon is similar. The combustion behaviour of the direct injection open chamber diesel engine with swirl-supported combustion was found strongly related to the characteristic parameter. This was validated over a wide range of diesel engines.

Validation of the Mixing Parameter

Input data for the validation of the correlation

For a part of the validation of this correlation, the data given by Kuo *et al.* (1988a) for chamber shapes (Engines R1, S1, S2 in Table 3.2) shown in Fig. 8.1 were extensively used. The engine data are given in the following table.

Bore × stroke	88 × 85.5 mm
Fuel injection system	Rotary pump, 5 holes × 0.22 mm, 150 spray angle, 33.9 MPa opening pressure

Instead of the value of fuel momentum given in Kuo *et al.* (1988a), the momentum calculated by the product of mean fuel velocity and the injected quantity given in Kuo *et al.* (1988a), was used. Assuming a coefficient of discharge of the orifice in the nozzle as 0.8, the average injection pressure difference is calculated from the published injection velocity (Kuo *et al.* 1988a). This pressure difference was used in equation (8.2) to calculate the detachment at the end of ignition delay. Results of these calculations are tabulated in Appendix VI.

The correlation worked even when the air and fuel momenta are obtained by simplified calculations assuming solid body rotation with a 25% loss in momentum during compression stroke. The authors collected extensive data on four of the engines. The types of combustion chambers and operating speeds are mentioned in the following table.

Engine type	Bore, stroke (mm)	Speed (rpm)	Piston cavity
A8	75, 76	2,200	toroid Fig. 8.7 A8
B8	100, 120	1,500, 2,000, 2,300	toroid Fig. 8.7 B8
C8	110, 116	1,200, 1,500, 1,800, 2,000	hemisphere Fig 8.7 C8
D8	100, 110	1,200,1,600,1,800, 2,000	toroid Fig. 8.7 D8

Results

Figure 8.8 shows the major exhaust soot exhaust indicated carbon (EIC defined as dry soot emitted per unit of energy produced at the engine shaft, g/kWh) of combustion chambers R, S1 and S2 plotted against the characteristic ratio of the momentum of useful air to the total momentum of fuel. There is a unique optimum range of the characteristic ratio for both re-entrant and shallow type piston bowls. Therefore, independent of the shape of piston cavity and air-fuel ratio, the spray pattern can be matched with the piston bowl by designing the proper dimensions.

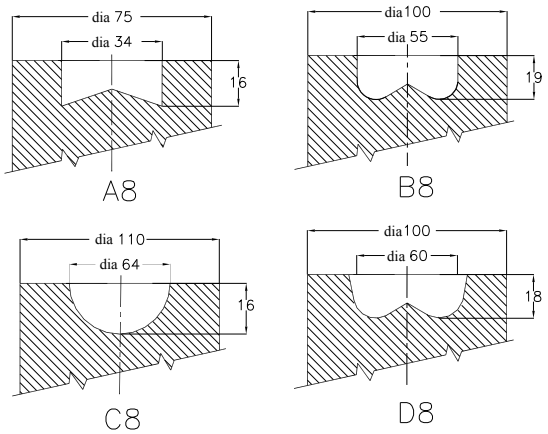

Fig. 8.7 Types of piston cavities used for correlation validation A8, B8, C8, and D8

This is in contrast with the conclusion of Bassoli *et al.* (1985) and Kuo *et al.* (1988a) where the optimum range varied with the piston cavity shape lacking in generality, as the parameter identified by them did not capture the exactly the air fuel mixing phenomenon and the factors affected them. Above a certain value of

momentum ratio, excessive mixing causes too much of dilution resulting in poor quality lean burning. When the air momentum is less, rich burning causes excessive emission of carbon. Carbon emission increases at a lesser rate when the mixing parameter is above the optimum range than when it is below the optimum.

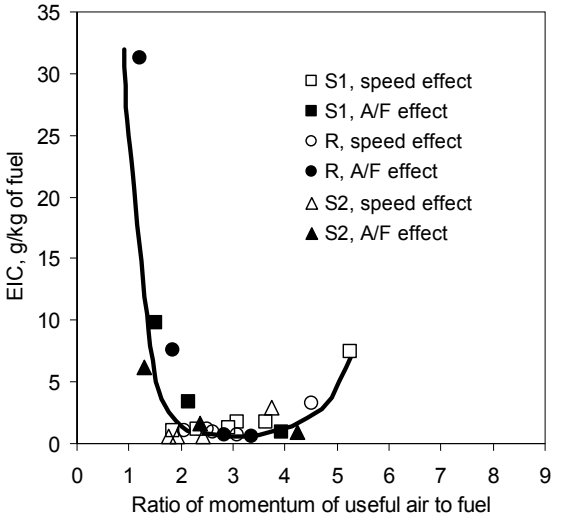

Fig. 8.8 Measured exhaust soot (exhaust indicated carbon) as a function of ratio of momentum of useful air to total fuel momentum

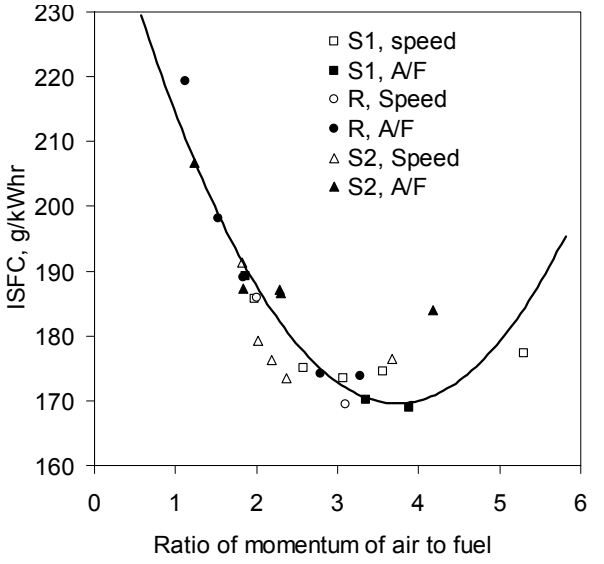

Fig. 8.9 Indicated specific fuel consumption as a function of characteristic mixing parameter

Similarly, Fig. 8.9 shows the effect of the characteristic mixing parameter on the indicated specific fuel consumption (ISFC) of chambers R, S1 and S2. A thick line shows the relationship. There is a definite optimum range of the characteristic ratio for ISFC as well. Nevertheless, this range is narrower than that for EIC. In addition, it lies within the optimum range for EIC.

The data of engines A8, B8, C8 and D8 covered wide ranges of operating speed, bore sizes and spray arrangement. The shapes of the piston cavities were hemispherical and toroidal type. Thus, the most popular range, of direct injection diesel engines was considered. The ratio of the momentum of useful air to the fuel momentum is calculated using the simplified method, as explained earlier. The indicated performance, the estimated air momentum at TDC from the steady flow rig data, total momentum of the injected fuel consumption and other data of these engines are tabulated in Appendix VII. In Fig. 8.10, the indicated specific fuel consumption is plotted against the characteristic mixing parameter. For comparison, the relationship in Fig. 8.9 is transcribed as a thick line in Fig. 8.10. The correlations of engines A8, B8, C8 and D8 could be seen to coincide with the relationship observed for types R, S1 and S2 in Fig. 8.1.

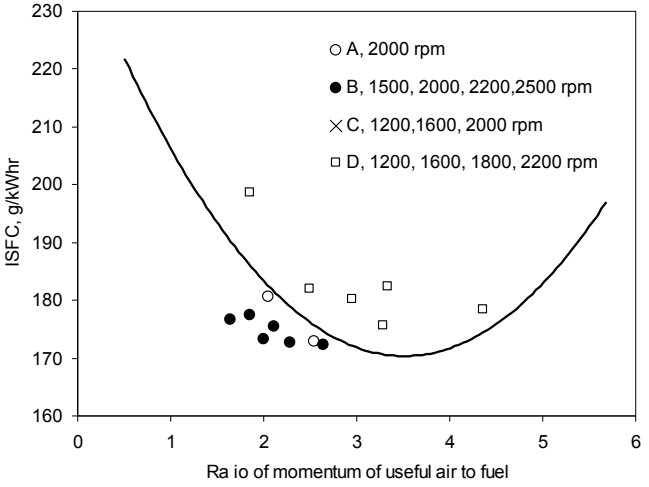

Fig. 8.10 Indicated specific fuel consumption as a function of characteristic mixing parameter

The carbon emissions of engines A8, B8, C8 and D8 were measured using Bosch smoke meter in Bosch smoke number. The smoke values were converted to carbon particulate concentration using the correlation of Hardenberg and Albrecht (1987). Figure 8.11 shows the correlation curve transcribed from Fig. 8.8 against the backdrop of the exhaust carbon of the commercial engines namely A8, B8, C8 and D8. The favourable comparison of the correlations shown in Figs. 8.8–8.11 with measured data of fuel consumption performance and smoke emissions of various commercial and experimental diesel engines validates the universality of

the correlation. The optimum range of mixing parameter for the performance and emission is irrespective of the shape of the piston cavity, type of engine, size and speed for all direct injection diesel engines.

Conclusion

After study and evaluation of various mixing correlations, a new concept of useful air was introduced. This is the air in the annular zone, where the fuel spray excluding liquid core is present at the end of ignition delay period. The ratio of the momentum of the useful air to the total momentum on the total injected fuel is defined as the characteristic parameter. The mixing parameter is found strongly correlated with the indicated performance and dry soot emissions of direct injection engines. The correlation has been validated by using seven types of combustion chambers in pistons of size from 75 to 110 mm running at speeds from 2,500 to 1,200 rpm and at wide ranging air to fuel ratios.

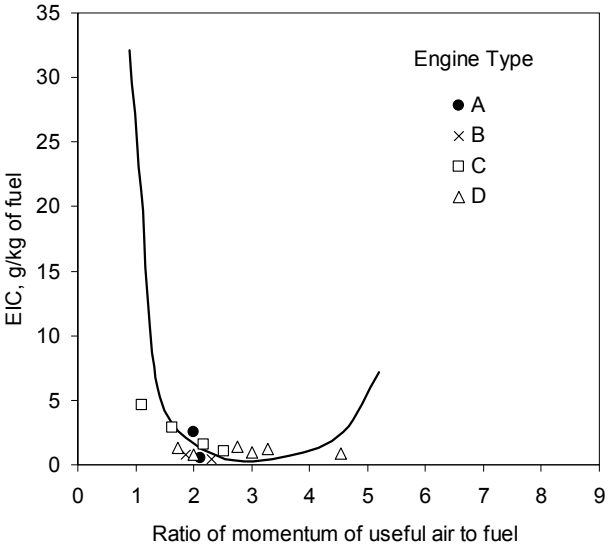

Fig. 8.11 Exhaust soot (exhaust indicated carbon) as a function of mixing parameter

References

Abramovitch GN (1963) The theory of Turbulent Jets. MIT Press

Ball WF (1980) A practical approach to the combustion modelling of direct injection diesel engine. Conference on recent progress in automobile engine and emissions, La Sociéte' des 1' automobile, Paris, April 2–3

Bassoli C, Bodritti G, Cornetti GM (1985) Optimum air motion and spray formation for D.I. Diesel. SAE Paper 850501

Borgnakke C, Davis GC, Tabaczynski RJ (1981) Prediction of in-cylinder swirl velocity and turbulence intensity for an open chamber cup in piston. SAE 810224

Chandorkar SB, Dani AD, Lakshminarayanan PA (1988) Effects of injection parameters, fuel quality and ambient on the ignition delay and the location of the flame kernel in a diesel spray in a quiescent chamber. SAE Transactions, SAE 881227

Dani AD, Nagpurkar UP, Lakshminarayanan PA (1990) Universal Mixing Correlations for the Performance and Emission of Open Chamber Diesel Combustion Supported by Air Swirl. SAE 900446

Dent JC (1980) Turbulent mixing rate - its effect on smoke and hydrocarbon emission from diesel engines. SAE 800092, Diesel combustion and emissions, SAE Proceedings, P-86

Hardenberg H, Albrecht H (1987) Limits of soot determination from optical measurements (in German) Motoren Techniche Zeitschrift, MTZ, 48, 2

Henningsen, S (1984) Hydrocarbon emission from the ignition delay period in a D.I. diesel engine. SAE Transactions, 93, Sec.6, pp 28–40

Ishida, Kihara, Furubayashi (1985) Development of Direct Injection diesel engines. SAE 850068

Kamotani Y, Greber I (1972) Experiments on turbulent jet in a cross flow. AIAA J., 10, No. 11,

Kuo TW, Henningsen S, Wu KJ (1988a) Evaluation of four mixing correlations for performance and soot emission characteristic of a small open chamber diesel engine. SAE 880599

Kuo TW, Wu KJ, Henningsen (1988b) Effects of fuel over-penetration and over-mixing during ignition delay period on hydrocarbon emissions from a small open chamber diesel engine. Proc. of International symposium on basic processes in I.C. engines III, ASME

Lakshminarayanan PA, Dent JC (1983) Interferometric studies of evaporating and combusting diesel sprays. SAE Transactions, SAE830244

McLean DH, Bremfoerder FW, Hamelink JC (1986) Development of headland ring and piston for a four stroke direct injection diesel engine. SAE 860164

Morris CJ, Dent JC (1976) The simulation of air-fuel mixing in high swirl open chamber diesel engines", Proc. I. Mech. E., 190, 47/76

Munro R (1979) Some diesel piston features in design analysis and experiment. SAE 790858, Diesel engine thermal cooling, SP-449

Ramsey JW, Goldstein RJ (1971) Interaction of a heated jet with a deflecting stream, J Heat Transfer, ASME, Sec. C, 93, No. 4

Timoney DJ (1985) A simple technique for predicting optimum fuel air mixing conditions in a direct injection diesel engine with swirl, SAE paper 851543

von Thien (1965) Entwicklungsarbeiten an Ventilkanalen von Viertakt Dieselmotoren. Osterreichen Ingenieur Zeitschrift, Heft 9, Jg 8, Springer

Wakuri V, Ono S, Takasaki K (1985) Influences of air swirl on fuel spray combustion in a marine diesel engine. International symposium on flows in I.C. engines, ASME, FED. 28, pp 47–55

Whitehouse ND, and Way RJB (1969–1970) Rate of heat release in diesel engines and its correlation with fuel injection data. Diesel Engine Combustion, The IMechE Proc. 184, part 3J

9 Heat Release in Direct Injection Engines

Abstract An accurate model for the heat release rate in a modern DI diesel engine is newly evolved from the known mixing controlled combustion model. In this chapter, the combustion rate is precisely described by relating the mixing rate to the turbulent energy created at the exit of the nozzle as a function of the injection velocity and by considering the dissipation of energy in free air and along the wall. The complete absence of tuning constants distinguishes the model from the other zero-dimensional or pseudo multi-dimensional models, at the same time retaining the simplicity. Successful prediction of the history of heat release in engines widely varying in bores, rated speeds and types of aspiration, at all operating conditions validated the model. The earlier model has explained correctly the effect of kinetic energy of fuel injection. However, it considered only the spray in the air and the accuracy of prediction was only about 65%. In most of the engines of bore less than 130 mm, wall jet plays a very important role. By considering the wall jet in detail, the heat release has been explained to accuracy better than 95%. This was proved for a variety of engines. The bores range from 85 to 280 mm.

Early DI Diesel Engines operated at relatively low compression ratios and low injection pressures. They, hence, demanded very advanced injection timings in commensurate with the large ignition delay. Such a design was the result of the available technology and lack of norms for noise and emissions.

During the ignition delay period in the beginning of combustion, up to about 20% of the injected fuel is prepared to stoichiometric proportion. Due to high flame speed, the prepared mixture burns at high temperature to produce nitric oxides and explosive noise characteristic of a diesel engine. This troublesome period of combustion is kinetically controlled. On the other hand, the rest of the fuel burns as and when the mixture is prepared because the delay is absent with hot gases and radicals available in the vicinity, remnant of the fuel burnt earlier. This second part is diffusive and the rate of combustion of the majority of fuel is controlled by the physical mixing processes in the spray.

With the advent of new norms, reduction in ignition delay held the key to solving emission and noise problems. Higher temperature at the beginning of injection by increased compression ratio reduced the delay period so substantially that the delay could be ignored. Higher injection pressures and higher turbulence were introduced to improve the mixing rate and hence to maintain the combustion duration within a reasonable limit, in spite of the loss of fast burning premixed combustion regime.

P.A. Lakshminarayanan and Y.V. Aghav, *Modelling Diesel Combustion*,
Mechanical Engineering Series, DOI 10.1007/978-90-481-3885-2_9,

Heat Release Rate in Diesel Engines

Single dimensional models

Probably, Austen and Lyn's work (1960) is the earliest in identifying the strong relationship between the injection rate and the heat release rate. The rate of injection diagram was subdivided into elemental fuel packets emitted in the form of rectangular pulses. Each pulse is converted to heat according to an exponentially decaying function. The convolution integral of the heat release from individual packets summed neatly to the net heat release rate (see Fig. 2.2). However, application of this elegant idea was fraught with complexity, as the decay constants for elemental heat-release rates were not available for a general engine. Therefore, the global heat release rate function of Wiebe (1970) ruled the world of diesel engine simulation for many years. The function has two engine-dependent constants to be tuned for a given engine type. The function could not explain the effect of speed and load easily. Further, it could not reflect the effects of the shape of the combustion chamber and the fuel injection rate on the history of heat release. The engine simulation was carried out using this function with a vast data bank of tuneable constants. Since a single Wiebe function could not predict the rate of early premixed burning, Watson *et al.* (1980) introduced the concept of double Wiebe function. This needed more number of constants adjusted for a given engine type. While such algebraic functions were easy to compute, very complex multidimensional models were proposed at the other end of the spectrum.

Multidimensional models

Shahed *et al.* (1973), Dent and Mehta (1981), and Hiroyasu *et al.* (1983) found that the understanding of the spray structure offered the clue to heat release rate. Essentially, they were detailed two-dimensional description of axisymmetrical sprays. The mixing of the fuel with the ambient air entrained due to high shear velocity of the jet was studied. A stoichiometric switch was devised that will completely burn the fuel in an element when the fuel air mixture is chemically correct. Depending upon the coarseness of the division of spray for calculations, a highly fluctuating heat release rate was obtained. Smoothening of the curves was resorted to match with the experimental data.

The three-dimensional simulation of the injection, mixing and burning (Gosman *et al.* 1985, Cartillieri and Johns 1983) describes in full various phenomena in the engine. The chamber is divided into finite volumes with moving boundaries. In principle, the airflow past the valves, the break-up of fuel into tiny droplets, vaporisation and combustion up to formation of pollutants could be studied. Nevertheless, the volume of computation is too prohibitive to carry out many parametric studies. Though the trends could be obtained, the sub-models must be validated thoroughly by experiments for using the output for design work. The three dimensional models were of immense use to appreciate the inner mechanism of diesel

sprays, but very difficult to comprehend during the full simulation of a diesel engine.

Mixing controlled combustion

In simplicity, avoidance of engine dependant tuning constants and easy application, the work of Chmela and Orthaber (1999) was an innovation. The burn rate is described strictly proportional to the mixing rate which in turn is determined by the average turbulent kinetic energy of the sprays. In turn, the turbulent energy decays at any time proportional to the energy itself. The work predicted the trend of heat release successfully if there was little impingement of sprays on the piston. However, the calculated and experimental courses of heat release fell apart after the spray reached the walls. The deviation in the character of calculated heat release was obvious in engines of capacities less than 2 L and at more than half load. The majority of diesel engines belong to this category. An attempt has been made in the present work to enhance this model by encompassing the phenomena at the wall and the instantaneous injection rate derived from the indicated performance of fuel injection equipment (Lakshminarayanan *et al.* 2002).

Rate of mixing and burning in a fuel spray

Let us consider the fuel injected in the form of a transient spray into an infinite surrounding (Fig. 9.1). The air in the ambient entrains in the spray due to the turbulent shear between the ambient air and the fuel emanating from the nozzle at high velocity.

This figure shows the diffusion of air in the fuel spray to prepare a thin mantle of fuel to stoichiometric proportions somewhere in the middle of the spray. The simplest description for a burning spray is the model where products of combustion exist outside this mantle and fuel rich mixture remains unburned inside it (Fig. 9.2). When compared with the slow mixing rate of fuel with the air, the rate of chemical reaction is too large to determine the rate of combustion. Thus, the availability of fuel in chemically correct proportion by turbulent mixing determines the burn rate and not the speed of reaction.

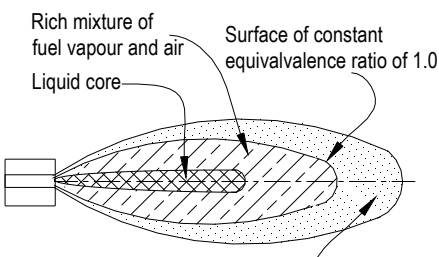

Fig. 9.1 Vaporising spray

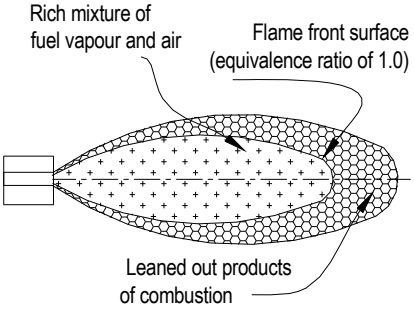

Fig. 9.2 Combusting spray

Lakshminarayanan and Nagpurkar (1986), and later Chmela and Orthaber (1999) have shown that the rate of burning is proportional to the available fuel and the rate of entrainment of air (see Chapter 7).

Rate of burning ∝ Rate of air entrainment × Fuel available

$$\frac{dQ}{d\theta} = C_{\mathrm{mod}el} f_1(fuel \cdot availability) f_2(mixing) \tag{9.1}$$

Here, $\frac{dQ}{d\theta}$ = Rate of heat release
C_{model} = A model constant = 1,000 kJ/kg/deg
f_1 *and* f_2 = Functions

The same conclusion could be arrived at from the well-known empirical relation for burning by Wiebe (1970) as well.

Analogy of rate of mixing controlled combustion with Wiebe function

The cumulative fuel burnt, m_b at any time, t is given by an exponential Wiebe function, equation (9.2), where m_f is the total injected fuel.

$$m_b = m_f \left(1 - e^{-at^b}\right) \tag{9.2}$$

The deceleration of combustion with time is emphasised by the exponent t_b. Differentiating equation (9.2) on either side, we obtain the rate of burning, equation (9.3).

$$\frac{dm_b}{dt} = \left(m_f . e^{-at^b}\right) \quad \left(abt^{b-1}\right) \tag{9.3}$$

$$\frac{dm_b}{dt} = \left(factor_1\right) \quad \left(factor_2\right)$$

Where, m_b = Cumulative mass of fuel burnt
m_f = Cumulative mass of fuel injected
$\frac{dm_b}{dt}$ = Rate of burning
a and b = Engine specific constants

The first factor on the right hand side of equation (9.3) corresponds to the fuel remaining un-burnt and the second represents the rate of mixing due to entrainment of air. In Fig. 9.3, these two terms are shown graphically. By converting the fuel spray in Fig. 9.1 to a simple two-dimensional cone, we can transform the penetration distance to time co-ordinate as shown in Fig. 9.3. The rate of entrainment increases

and the available fuel decreases with time or analogously with the penetration distance. The simple product of these two curves is in the form of a hump representing the rate of diffusive burning of a diesel spray as shown in the lower part of Fig. 9.3.

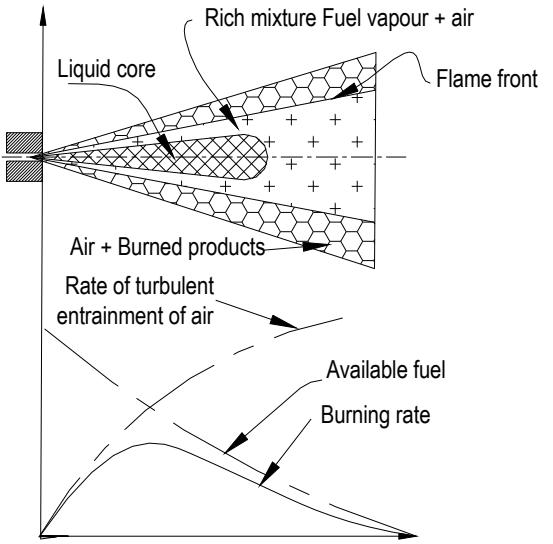

Fig. 9.3 Rate of mixing, available fuel and combustion rate

Model for Mixing Controlled Combustion

Regimes of combustion in a modern DI diesel engine

The rate of heat release of diffusive combustion in a modern DI diesel engine has three characteristic regimes of combustion (Fig. 9.4). In the first, the early stage of combustion starts almost along with the beginning of injection of fuel. Here, the rate of rise of the heat release rate is at its highest in its entire history and proportional to the turbulent kinetic energy produced at the nozzle as very little time has elapsed for any substantial decay of the energy. In the second distinctive part, the combusting spray has impinged on piston wall (Fig. 9.5). There is a sudden loss of kinetic energy to slow-down the rate of mixing and hence combustion. The spray continues to burn at nearly constant rate until the injection is on.

In the third regime after the injection ends, the combustion rate decays asymptotically as fresh energy input to turbulence in the fuel spray has stopped. The fuel continues to burn until too little diesel is left to burn. The mixing rates in the three regimes could be quantified by using the turbulent kinetic energy of the spray.

Two factors affecting heat release rate

Available fuel factor, f_1

At any instant, the fuel available for burning is the portion of the fuel so far still left un-burnt.

Available fuel = cumulative fuel injected – fuel burnt

$$f_1(fuel.availability) = m_f - \frac{Q}{LCV} \tag{9.4}$$

Here, m_f = Cumulative mass of fuel injected
Q = Cumulative heat release
LCV = Lower calorific value of fuel

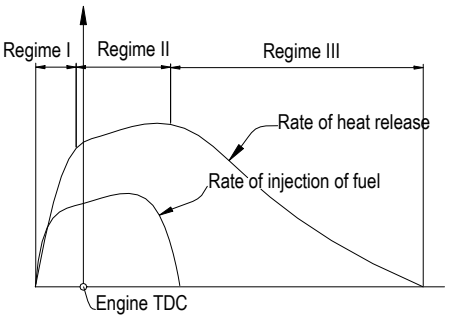

Fig. 9.4 Three regimes of diffusive combustion of a modern diesel engine

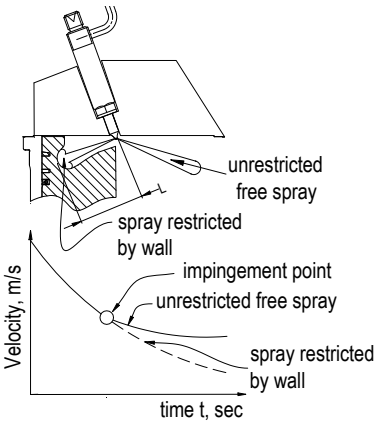

Fig. 9.5 Loss of velocity after impact against the wall, due to finite size of the combustion chamber

Mixing rate factor, f_2

The rate of mixing of fuel vapour and air depends on local density of turbulent kinetic energy. Three sources of kinetic energy are there in a diesel engine namely, swirl, squish and injection velocity of fuel (Fig. 9.6). The contribution of each source to total kinetic energy for a typical modern engine was summarised by Chmela and Orthaber (1999), for example, as in Table 9.1. Since the major portion of kinetic energy comes from the injection of fuel, other sources of kinetic energy are neglected. A part of this kinetic energy is converted into turbulence that is responsible for mixing process.

Table 9.1 Contribution of different sources to turbulent kinetic energy of the spray (Chmela and Orthaber 1999)

Source	Contribution to total kinetic energy (%)
Swirl flow	2.0
Squish flow	1.5
Fuel injection	96.5

k-ε theory

In zero dimensional combustion models, it is not easy to apply the Magnussen's *k-ε* theory of turbulent burning (Magnussen and Hjertager 1976), where the ratio of kinetic energy to dissipation rate, k/ε determines the rate of mixing and hence the rate of burning. Chmela and Orthaber (1999) postulated a modified turbulent mixing rate, which is akin to the k-ε model.

Modified k-ε model

The rate parameter for the combustion controlled by mixing, k/ε is substituted by the ratio of turbulence intensity to a distance characteristic of the transport of momentum in the combustion chamber of volume, V.

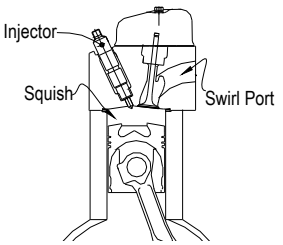

Fig. 9.6 Sources of kinetic energy

$$\text{Turbulence Intensity} \propto \sqrt{k} \text{ and}$$

$$\text{Mixing distance for momentum transport} \propto \sqrt[3]{V}$$

$$\textit{Mixing parameter} \propto \frac{\sqrt{k}}{\sqrt[3]{V}}$$

Even at low turbulence level, the combustion rate will not become zero in engine conditions. Hence, it was proposed that the mixing rate is an exponential function of the mixing parameter.

$$f_2(mixing) = e^{C_{rate}\frac{\sqrt{k}}{\sqrt[3]{V}}} \tag{9.5}$$

Where, C_{rate} = Constant for mixing rate = 0.002 s
k = Density of turbulent kinetic energy
V = Instantaneous cylinder volume

Input rate and dissipation rate of turbulent kinetic energy of fuel spray

At any instant, the spray contains an unburned fraction, f and correspondingly a burned fraction of *(1-f)*, of the cumulative fuel injected until then, m_f (Fig. 9.7a).

Figure 9.7b shows the rate of turbulent energy input, $\frac{dE_i}{d\theta}$ and its dissipation rate, $\frac{dE_{diss}}{d\theta}$ depicted as energy exchanges across the control surface enveloping the injected fuel and the air mixed with it, where θ is the crank angle in degree. The energy balance is given by the differential equation (9.6).

$$\frac{dE_u}{d\theta} = \frac{dE_i}{d\theta} - \frac{dE_{diss}}{d\theta} \tag{9.6}$$

Where, E_u = Total turbulent kinetic energy of fuel jet at a given crank angle instant, θ

$\frac{dE_{diss}}{d\theta}$ = Rate of energy dissipation across the control surface

C_{diss} = Dissipation constant = 0.01 s^{-1}

Energy input

The kinetic energy created by the injection at high velocity degenerates to random turbulence determined by the conversion efficiency C_{turb}. The value of C_{turb} is 0.2 for all the direct injection studies in this work. The injection velocity of an elemental mass dm_f is v. Then the input turbulent energy to the spray would be given by equation (9.7).

$$dE_i = C_{turb}\frac{1}{2}dm_f v^2 \tag{9.7}$$

We can rewrite the equation as follows

$$\frac{dE_i}{d\theta} = C_{turb}18\rho_f\left(\frac{n}{C_d A_n}\right)^2\left(\frac{1}{\rho_f}\frac{dm_f}{d\theta}\right)^3 \tag{9.8}$$

Here, $\frac{dE_i}{d\theta}$ = Rate of generation of kinetic energy of fuel jet into cylinder

C_{turb} = Efficiency of conversion of kinetic energy to turbulence energy in free jet = 0.2

n = Engine speed

ρ_f = Density of fuel

C_d = Coefficient of discharge of the nozzle

A_n = Area of nozzle holes

$\frac{1}{\rho_f}\frac{dm_f}{d\theta}$ = Volumetric injection rate of fuel

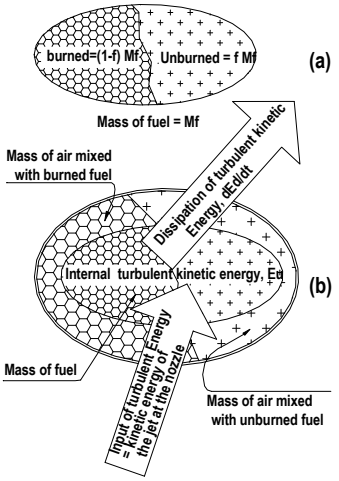

Fig. 9.7 (a) Burned and unburned fuel. (b) Air mixed with fuel and flow of turbulent kinetic energy across the control surface of the spray and its decay

Calculation of fuel injection rate

The rate of injection can be obtained by simulation of the fuel injection equipment. Alternatively, it can be obtained from experimental data if available, as in case of engines studied in the present work. The instantaneous flow area around the needle seat obtained from the measured needle lift and the total area of the spray-holes are considered as two orifices in series. The rate of fuel injection at any instant is calculated using the effective area, A_n of flow through the two orifices, and the measured pressures at the injector entry, p_f and in the cylinder p_c. A flow coefficient, C_d of 0.8 is reasonable for the spray holes (see Appendix IX).

The instantaneous injection rate,

$$\frac{dm_f}{d\theta} = c_d\ \rho_f\ A_n \sqrt{\frac{2\left(p_f - p_c\right)}{\rho_f}} \tag{9.9}$$

In the present work, the heat release rate is modelled as a strong function of the rate of fuel injection (Lakshminarayanan *et al.* 2002). Therefore, the accuracy of estimation of the fuel injection rate is important, especially in the first regime of combustion.

Energy dissipation

With passage of time, the turbulent kinetic energy of the spray dissipates to heat as the size of eddies reduces to a level too low to maintain the turbulent kinetic energy. The rate of loss $\frac{dE_{diss}}{d\theta}$ is proportional to the internal turbulent energy of the spray, Eu at the given instant. It could be treated as transfer of energy across the control surface (Fig. 9.7b).

$$\frac{dE_{diss}}{d\theta} = -\frac{C_{diss}}{6n} E_u \tag{9.10}$$

Where, E_u = Total turbulence energy of fuel jet at the instant

$\frac{dE_{diss}}{d\theta}$ = Rate of energy dissipation across the control surface

C_{diss} = Dissipation constant = 0.01 s^{-1}

The turbulent internal energy specific per unit mass of mixture determines the combustion rate. The total mass of the air in the fuel air mixture is estimated as follows. Here,

Air mass = air fuel ratio in the burning part of the mixture × fuel injected so far

= Air excess ratio for diffusion combustion × stoichiometric air fuel ratio × fuel mass

$= \lambda_{diff} AFR_{stoich} m_f$

m_f = Cumulative mass of fuel injected, $\int_0^t \frac{dm_f}{dt} dt$

λ_{diff} = Air excess ratio for diffusion burning = 1.4

AFR_{stoich} = Air fuel ratio for the stoichiometric combustion of diesel

Density of turbulent energy

At any instant during combustion, the density of turbulent kinetic energy is obtained by dividing the total turbulent energy of the spray by the total mass of the air fuel mixture in the spray.

$$k = \frac{E_u}{m_f (1 + \lambda_{diff} \ AFR_{stoich})} \tag{9.11}$$

The turbulent intensity characterised by the root mean square of the deviation of velocity from the mean can be expressed proportional to the square root of the density of the kinetic energy.

Modelling three regimes of heat release rate

The first regime of burning dependent on turbulence energy in free jet: During this early period, the spray is in the free air (Fig. 9.5). The increase in mass of the spray due to air entrainment allows the rate of penetration of the spray to decelerate with time (Lakshminarayanan and Dent 1983), equation (9.12).

$$s = \sqrt{8\, C_d\, U_j\, d_e\, t}\left(\frac{T_o}{T}\right)^{\frac{1}{4}} \tag{9.12}$$

Where, s = Penetration of spray
U_j = Velocity of fuel jet at the exit of the nozzle
d_e = Equivalent diameter of orifice
t = Time after start of injection
T_o = Reference temperature, 294 K
T_{surr} = Surrounding temperature
C_d = Coefficient of discharge of the nozzle

Differentiating equation (9.12), we obtain the velocity of penetration of the free jet in the air, V_{free}.

$$V_{free} = \sqrt{8\, C_d\, U_j\, d_e}\,\frac{1}{2\sqrt{t}}\left(\frac{T_o}{T_{surr}}\right)^{\frac{1}{4}} \tag{9.13}$$

During this period, the combustion accelerates at the highest rate in its entire history with increasing turbulence intensity due to continuous input of kinetic energy from the injected fuel. In addition, the efficiency of transformation of normal kinetic energy to turbulence, C_{turb} is also high at 0.2, as the spray has not yet reached the wall to lose momentum to the wall, equations (9.6) and (9.7). Considering the rate of dissipation of energy, the turbulence energy at any instant can be calculated to predict the rate of combustion by integrating the differential equation (9.6).

The second regime of combustion: It is influenced by the energy in the wall jet and input of energy from the spray. In engines of smaller bore sizes, combustion decelerates after the spray reaches the wall at a distance, L from the injector tip (Fig. 9.5). It starts at a time when $L=s$ in equation (9.12). During this intermediate

period of combustion, there is a continuous loss of momentum to the wall. The growth of the spray, V_{wall}, along the wall is sluggish (Lakshminarayanan and Dent 1983). Here, the effect of temperature of surrounding air is taken into account as in equation (9.13).

$$V_{wall} = 0.75\sqrt{U_j d_e}\,\frac{1}{2\sqrt{t}}\left(\frac{T_o}{T_{surr}}\right)^{\frac{1}{4}} \tag{9.14}$$

In other words, the kinetic energy input to the portion of the fuel in the wall jet is less by a factor, C_{wall} given by the ratio of the kinetic energy of the spray along the wall and the free spray.

$$C_{wall} = \left(\frac{V_{wall}}{V_{free}}\right)^2 \tag{9.15}$$

Hence, the right hand side of the equation (9.8) is moderated by multiplying by the factor C_{wall} to obtain the energy input to the wall jet. Since the total turbulent energy in the fuel is nearly equal to that contained in the static conical portion of the spray in the air from the injector the wall, the energy in the spray is approximately static and so is the rate of heat release. With increasing volume of the wall jet, the energy density drops slightly and hence the mixing rate or the combustion velocity.

The third decaying part of combustion

With no more fresh input of energy to the spray after the end of injection, the average turbulence intensity of the spray degenerates monotonically, according to the differential equations (9.6) and (9.10). The exponential term in equation (9.5) for the rate of combustion reflects the pattern of decaying heat release rate.

Steps to calculate heat release rate using the new model

Step 1: Prediction of impingement and loss in kinetic energy

In the first step of calculations, the instance of wall impingement and loss in velocity is computed by using average injection pressure, nozzle hole size, compression ratio and impingement distance by using equation (9.12), when the penetration of spray s equal to impingement distance L. If injection duration is more than the time for impingement, then instantaneous velocities of unrestricted and restricted sprays are calculated using equations (9.13) and (9.14). The ratio of these velocities gives C_{wall} at different times after impingement.

Step 2: Computation of factors of rate of heat release
In the second step of calculations, the two factors affecting rate of heat release are calculated at an interval of one degree of crank angle. The first factor of available fuel is calculated from cumulative mass of fuel injected and cumulative heat release using equation (9.4). The second factor of mixing rate is computed from the injection trace, the cylinder volume and the nozzle details using equation (9.5). The useful kinetic energy is calculated by using equations (9.6), (9.8) and (9.10), considering the effect of wall impingement.

Step 3: Resultant rate of heat release
The product of two factors along with the model constant, C_{model} gives rate of heat release at different time intervals.

Experimental Validation

Engines under study
Five direct injection diesel engines differing widely in swept volumes, rated speeds, methods of aspiration and injection systems were selected for validation studies. The engine details are summarized in Tables 9.2 and 3.2. The results of engine E9 are from Chmela and Orthaber (1999). The shapes of cavities for engines A9, B9, C9 and D9 are shown in Fig. 9.8.

Heat release rate from the experiments

The net heat release is calculated applying the first law of thermodynamics (Heywood 1988) to the pressure crank angle diagram. The instantaneous heat transfer rate across the walls to the cooling medium is added to the net rate to obtain the gross heat release rate.

The heat release rate for engine-E9 is straight available in the literature without any need to process the experimental pressure diagram.

Net heat release rate

Engines A9, B9 and C9
The indicated pressure diagrams and the injection traces were collected in the computer during the experiment. From the pressure diagram and the engine bore and stroke, the rate of net heat release was calculated by using the first law of thermodynamics with the help of the internal computer resident in the *AVL Indiskop*. The calculation of net rate of heat release does not consider the heat transfer across the walls of the combustion chamber.

Engine D9
The available indicated pressure diagrams were manually digitised after smoothening by two-points moving average method. First law of thermodynamics was used to calculated net heat release rate (Heywood 1988).

Estimation of heat transfer across the walls

Large surface area is exposed to gases in later part of the combustion and hence for heat transfer. Therefore, the heat transfer rate must be estimated accurately enough, while obtaining the heat release rate during this period, experimentally. Hohenberg's correlation (1979) for the instantaneous heat transfer considers truly the conditions present in a DI diesel engine. This correlation is based on extensive experiments done on a DI diesel engine. The instantaneous heat transfer across the walls for engines A9 to D9 was estimated using the following equation.

$$h_c = \frac{130 p_c^{\,0.8} \cdot \left(v_p + 1.4\right)^{0.8}}{V^{0.06} \cdot T_g^{\,0.4}} \tag{9.16}$$

Here, h_c = Heat transfer coefficient
v_p = Piston velocity
V = Instantaneous cylinder volume
T_g = Cylinder charge temperature

The cyclic-averaged heat transfer coefficient for individual surfaces can be used in the network of heat resistances to iteratively obtain different surface temperatures of the combustion chamber enabling precise estimation of the instantaneous heat transfer (Gajendra Babu and Murthy 1976).

$$\frac{dQ_{ht}}{d\theta} = h_c A_s \left(T_g - T_w\right) \cdot \left(\frac{1}{6n}\right) \tag{9.17}$$

Here, A_s = Instantaneous surface area
T_w = Wall temperature

Results

Parametric studies of Engine A9
The naturally aspirated Engine-A9 was selected for detailed study to validate the new model for different operating parameters of load and speed. The swept volume

per cylinder is about 1 L and it was rated at 2,700 rpm and 80 hp. The experimental data were collected at six different points (Table 9.3). The main inputs to the calculation are the injection trace shown in Fig. 9.4, impingement distance of 32.5 mm computed from the geometry of the combustion chamber and the conditions in the chamber at the start of injection (Table 9.2).

Table 9.2 Details of engines studied

Engine	A9	B9	C9	D9	E9 (Chmela and Orthaber 1999)
Bore (mm)	105	105	175	280	124
Stroke (mm)	120	120	220	320	165
Compression ratio	18:1	18:1	14.5:1	11:1	18:1
Number of valves	2	2	2	4	4
Swirl number	2.1	2.1	1.0	0.8	1.8
Impingement distance, L (mm)	32.5	36	70	120	55[a]
Aspiration	NA	T	TA	TA	TA[a]
Boost ratio	1	1.8	2.5	4	2.5[a]
Fuel pump	Rotary	Inline	Individual	Individual	Common-rail
Injection pressure (bar)	800	600	800	700	800[a]
Injected qty (mm^3/str)	55	75	600	3,200	255
Number of holes in the injector × hole size	5 × 0.2	5 × 0.24	8 × 0.33	8 × 0.55	8 × 0.24[a]
Speed (rpm)	2,700	2,500	1,500	750	1,000
Bmep (bar)	7	10	17	24.5	22
Cavity dia (mm)	60	62	130	220	100[a]

TA – turbocharged and after-cooled; T – turbocharged; NA – naturally aspirated
[a]Data assumed for computation

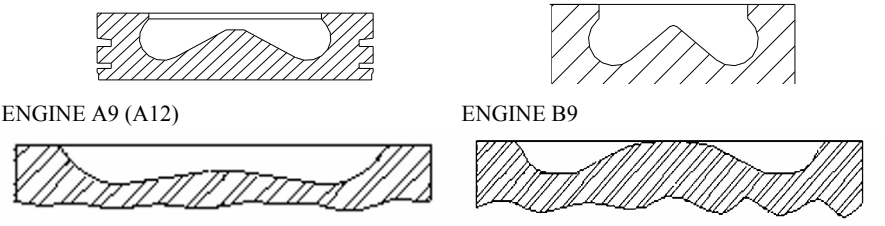

Fig. 9.8 Engine cavities studied

Table 9.3 Data points of engine A9

Data point	Speed (rpm)	Load		Injection pressure (bar)	Fuelling (mm^3/str)
		(Nm)	(%)		
1	2,700	55	100	800	54
2	2,700	41	75	800	43
3	2,700	28	50	800	34
4	2,700	14	25	800	26
5	1,400	67	100	600	63
6	750	0	0	400	7

Table 9.4 Data points of other engines B9, C9, D9 and E9

Engine	Speed (rpm)	Load (Nm)	%	Injection pressure (bar)	Fuelling (mm^3/str)
B9	2,500	65	100	600	75
C9	1,500	700	100	700	480
D9	750	3,750	100	800	3,200
E9	1,000	350	100	800	255

Base data at rated 100% load and 2,700 rpm

At 2,700 rpm, and 100% load, the spray reached the wall at about 9° after start of injection (Fig. 9.9). This can be obtained from the equation (9.12) for spray penetration. The velocities of penetration of the spray tip along the wall and if it were unrestricted can be seen in Fig. 9.10. The instantaneous ratio of the square of the two velocities is used in calculating C_{wall} and the kinetic energy in the spray along the wall.

Next, the entire heat release history is calculated in steps of 1° crank angle. The rate of injection is calculated using the needle lift, the instantaneous geometric area of flow and the flow coefficient of the nozzle (Fig. 9.11). Using equations (9.4) and (9.5), the available fuel and the mixing rate are calculated. The two factors are shown in arbitrary units in Fig. 9.12. After the impingement on the wall the conversion efficiency of kinetic energy to turbulence sharply drops. After the end of injection, the degeneration of turbulence without any fresh addition of energy dictates the heat release rate. The calculated heat release rate is shown in Fig. 9.13 with the experimentally obtained burn rate in the backdrop. A very satisfactory comparison between the experiment and the present model could be seen. In addition, the results from the earlier successful mixing controlled combustion model (Chmela and Orthaber 1999) are also superimposed for comparison. The deviation from the experiment is obvious beyond the point of impingement against the wall.

Other loads and speeds

Similarly, rate of heat release (ROHR) was calculated for 75%, 50% and 25% load at 2,700 rpm (see Figs. 9.14–9.16). The instance of impingement was approximately the same at all loads for the given engine speed. At 1,400 rpm, the wall impingement

occurred at about 8° after start of injection, which is reflected in ROHR curve in Fig. 9.17. At 750 rpm and low idle, there was no impingement (see Fig. 9.18). In the background, for every case the burn rate obtained experimentally and that calculated using the earlier mixing controlled combustion (MCC) model (Chmela and Orthaber 1999) are shown for comparison.

Study of Engine-B9

The Engine-B9 was turbocharged version of Engine-A9 with a compression ratio of 17.0. Here, the comparison between the experiment and model is still better because the ignition delay is lesser than in the case of the naturally aspirated version (Fig. 9.19). As the impingement is not taken into account, the earlier mixing controlled model over-estimates the heat release rate and hence thermal efficiency.

Engine-C9 and Engine-D9

Engine-C9 and Engine-D9 are of bores 175 and 280 mm respectively running at high brake mean-effective pressure of 17 and 24.5. The engines are rated at 1,500 and 750 rpm; however, the corresponding piston speeds are of state of art. Again, the effectiveness of the new mixing controlled model is demonstrated in the Figs. 9.20 and 9.21.

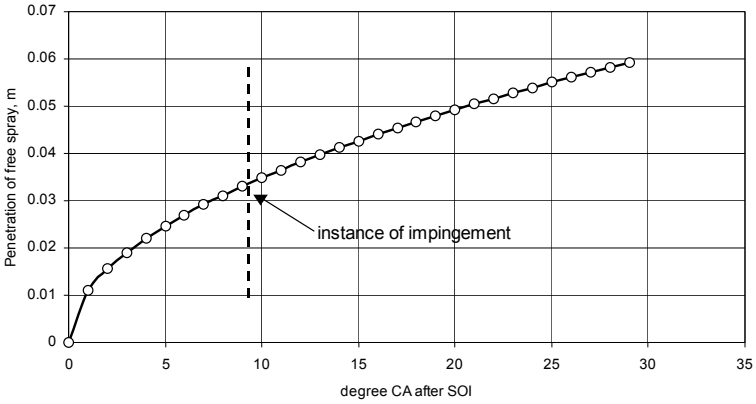

Fig. 9.9 Spray penetration in free air – Engine A9, 2,700 rpm and 100% load

Engine-E9

The engine-E9 (Chmela and Orthaber 1999) was studied at the rated conditions of the engine, namely, 1,000 rpm and 22 bar using the new model and that presented in the same reference. Since the dimensions of the combustion cavity were not explicitly available, a probable impingement distance was obtained from data on engines of similar bores (Fig. 9.22). The experimentally obtained heat release rate compared more favourably with the new model than the known models. The observation is similar to cases of other engines.

Discussions

To appreciate the accuracy of the models a typical data of 100% load and 2,700 rpm for engine-A9 is studied in Fig. 9.23. The deviation of the heat release predicted using the present and the earlier models from the measured is plotted. The deviation is significantly less in the case of the present work after the wall impingement. The relatively low error in the third regime of combustion in the present work validated the accuracy of the dissipation model proposed by Chmela and Orthaber (1999) for turbulent energy (equation (9.10)). This was not obvious in his work as it was camouflaged, unfortunately, by the large error integrated during the second part of combustion.

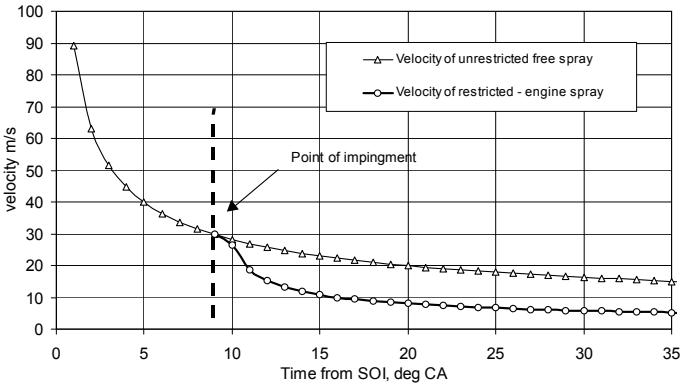

Fig. 9.10 Spray penetration velocities in free air and along the wall – Engine A9, 2,700 rpm and 100% load

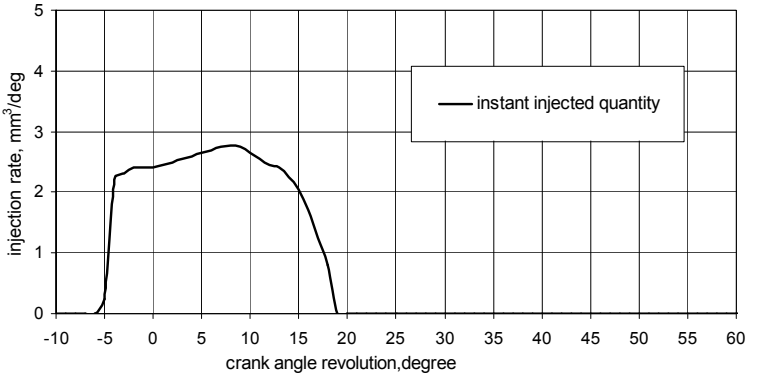

Fig. 9.11 Rate of injection derived from the needle lift diagram, instantaneous geometric flow area and the flow coefficient of the nozzle holes

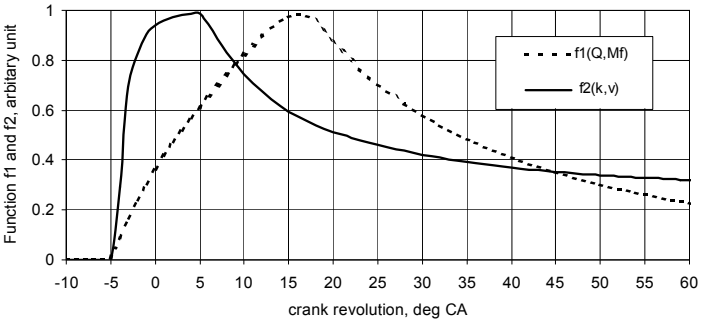

Fig. 9.12 Mixing rate, f2 and available fuel, f1 – Engine A9, 2,700 rpm and 100% load

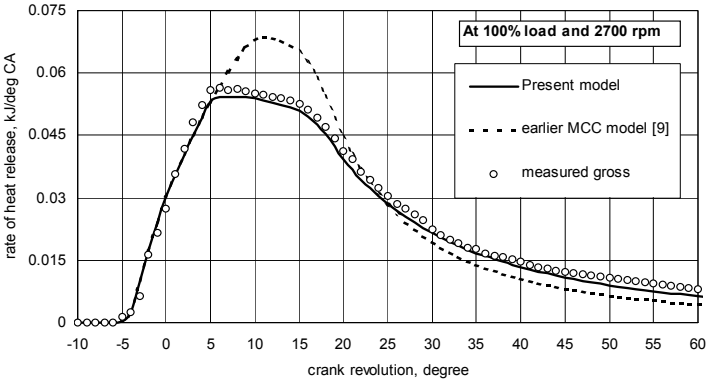

Fig. 9.13 ROHR, Engine A9, 100% load, 2,700 rpm

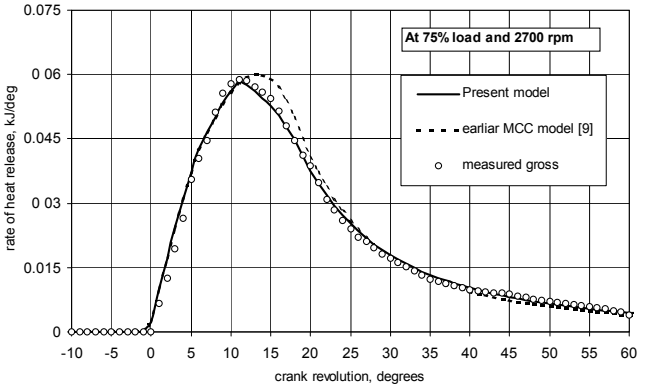

Fig. 9.14 ROHR, Engine A9, 75% load, 2,700 rpm

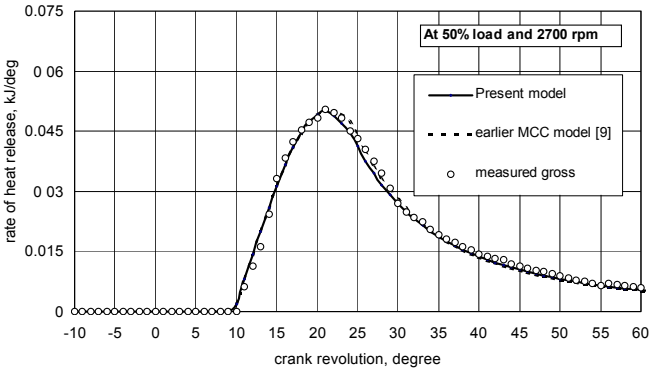

Fig. 9.15 ROHR, Engine A9, 50% load, 2,700 rpm

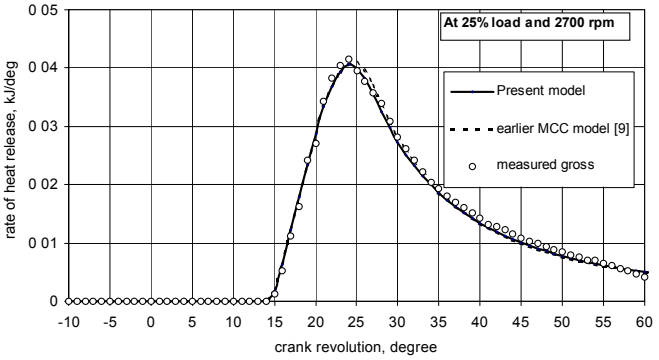

Fig. 9.16 ROHR, Engine A9, 25% load, 2,700 rpm

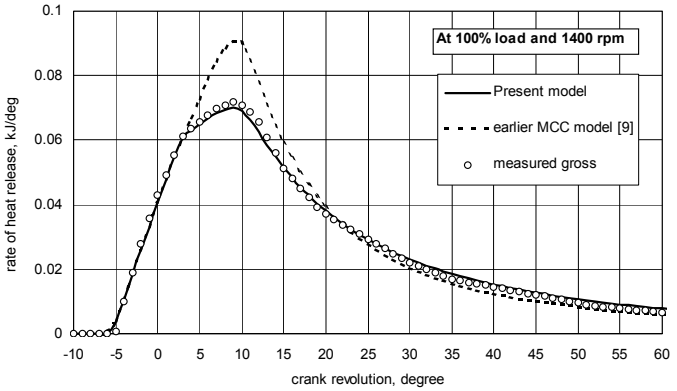

Fig. 9.17 ROHR, Engine A9, 100% load, 1,400 rpm

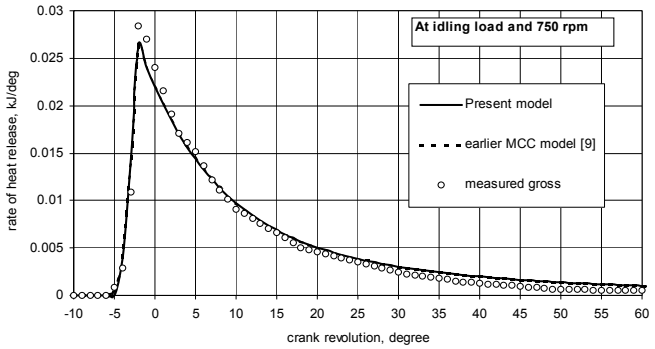

Fig. 9.18 ROHR, Engine A9, idling load, 750 rpm

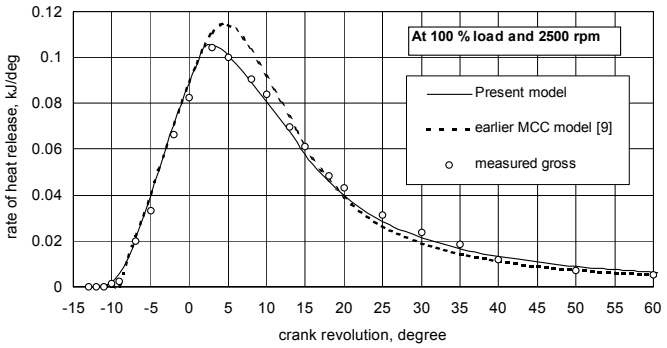

Fig. 9.19 ROHR, Engine B9, 100% load, 2,500 rpm

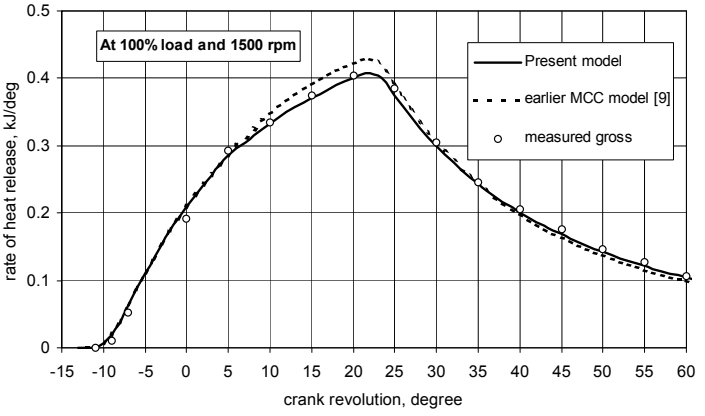

Fig. 9.20 ROHR, Engine C9, 100% load, 1,500 rpm

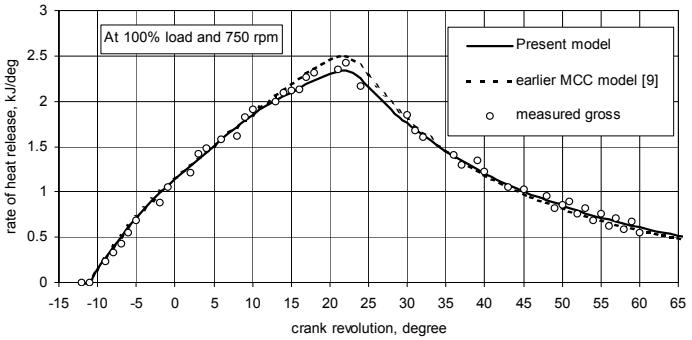

Fig. 9.21 ROHR, Engine D9, 100% load, 750 rpm

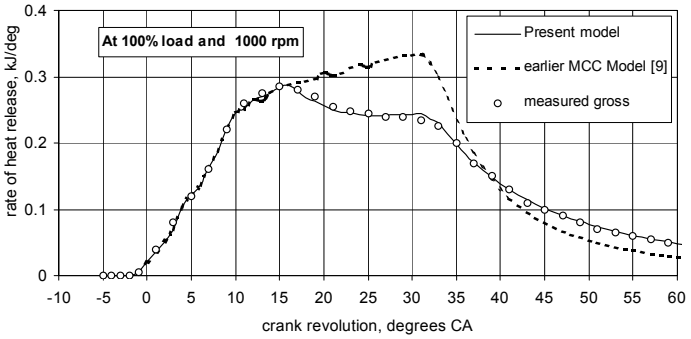

Fig. 9.22 ROHR, Engine E9, 100% load, 1,000 rpm (Chmela and Orthaber 1999)

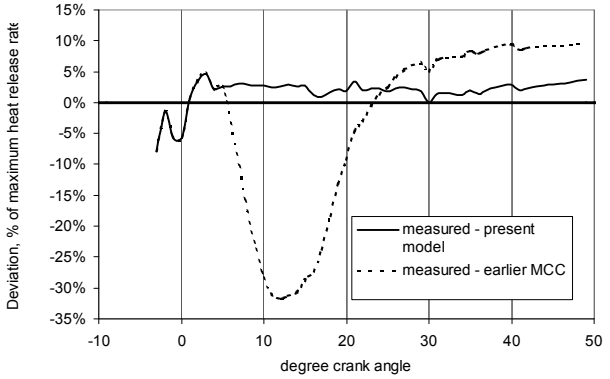

Fig. 9.23 Deviation of the models from the measured heat release for Engine-A9 at 100% load and 2,700 rpm

To study the overall accuracy, the root mean square (RMS) deviation is evaluated. It is obtained at 1° crank interval during the 5–95% of cumulative heat release, by calculating the square of the deviation of the predicted rates from the measured. Then, the square root of the sum of squares is divided by the maximum of the measured heat release, to obtain the percentage RMS of the deviation. Table 9.5 compares for the five different engines at various operating conditions. The overall accuracy of the new model stands out in comparison at 1.5%. The new model has improved prediction substantially for engines with smaller bore sizes and at loads higher than 25%. The deviation is relatively five times better than the best available mixing controlled combustion model, as shown in Table 9.5.

Chemical kinetics may not be fast enough at cold starting conditions. Further, during transient conditions, the characteristic air excess-ratio may be less than 1.4. This is so because the injected quantity exceeds the steady state requirements or in case of turbocharged engines, the familiar turbo-lag does not allow the air in commensurate with the injected fuel. In such cases, the predicted and actual heat release rate histories may diverge. Except these operating conditions on the fringe, the new model is probably the first satisfactory tool for design work and predicting the engine performance accurately at different speeds and loads in steady state.

Table 9.5 Accuracy of prediction of heat release rates using the new model

Engine	Speed (rpm)	Load (%)	Deviation (%)	
			Present model	MCC model (Chmela and Orthaber 1999)
A9	2,700	100	2.1	14.5
	2,700	75	1.0	5.3
	2,700	50	1.2	2.5
	2,700	25	1.5	1.6
	1,400	100	1.5	9.8
	750	0	1.4	1.4
B9	2,500	100	1.3	6.2
C9	1,500	100	1.5	2.8
D9	750	100	1.8	3.0
E9	1,000	100	1.5	16.0
Average			1.5	6.4

Summary

Emissions of Nitric Oxides and noise are primarily attributed to the combustion of fuel premixed during the ignition delay. To reduce the delay and hence solve the twin problems, high compression ratio is designed in modern diesel engines. The kinetically controlled premixed combustion is almost absent in these engines and most of the combustion is diffusive. The diffusive heat release rate in diesel engines is proportional to the fuel not yet burned and the turbulent mixing rate. Turbulence is generated in the spray by the shear velocity at the exit of the nozzle and

its decay rate is a linear function of the kinetic energy of the spray. The mixing length is postulated as a function of the volume of the combustion chamber. The mixing rate is an exponential function of the ratio of turbulence intensity to the mixing length. To predict heat release rate, the study of mixing rate in free air is enough, if the injected quantity is sufficiently low to avoid wall impingement. However, at higher loads, the drop in turbulent energy due to collision against the walls of the combustion chamber must be necessarily considered in order not to overestimate the thermal efficiency. The new model enhances of the known mixing controlled combustion model. Since it considers the wall impingement, it is a single dimensional model with the simplicity and ease of application of a zero dimensional model. The new model was thoroughly validated as a valuable tool by comparing the predicted heat release rates with the measured in five engines of widely varying bore sizes. The accuracy was demonstrated at different conditions of loads and speeds in steady state.

References

Austen AEW and Lyn WT (1960) Relation between fuel injection and heat release in a direct injection engine and the nature of the combustion process. Proceedings of the Institute of Mechanical Engineers

Cartillieri W and Johns RJR (1983) Multidimensional Modeling of Engine Processes: Progress and Prospects. Fifteenth CIMAC Congress, Paris

Chmela FG and Orthaber GC (1999) Rate of heat release prediction for a direct injection diesel engine based on purely mixing controlled combustion. SAE 99010186

Dent JC and Mehta PS (1981) Phenomenological combustion model for a quiescent chamber diesel engine. SAE 811235

Gajendra Babu MK and Murthy BS (1976) Simulation and evaluation of Exhaust and Intake system of a 4-stroke spark ignition Engine. SAE 760 763

Gosman AD, Tsui YY, Watkins AP (1985) Calculation of Unsteady Three-dimensional Flow in a Model Motored reciprocating Engine and Comparison with Experiment. Fifth International Turbulent Shear Flow Meeting, Cornell University

Heywood JB (1988) A text book on Internal Combustion engine fundamentals. McGraw-Hill International edition

Hiroyasu H *et al.* (1983) Development and use of a spray combustion modelling to predict diesel engine efficiency and pollutant emissions. Bulletin of JSME 26 No. 214

Hohenberg GH (1979) Advance approach for heat transfer calculation. SAE 790825

Lakshminarayanan PA, Aghav YV, Dani AD Mehta PS (2002) Accurate prediction of the rate of heat release in a modern direct injection diesel engine. IMechE, 216, J Automobile

Lakshminarayanan PA and Dent JC (1983) Interferometric studies of vapourising and combusting sprays. SAE 830244

Lakshminarayanan PA, Nagpurkar UP (1986) Rate of heat release for divided combustion chamber. SAE 860084

Magnussen BF and Hjertager BH (1976) On mathematical modelling of turbulent combustion with special emphasis on soot formation and combustion. International symposium on combustion

Shahed SM, Chiu WS, and Yumlu VS (1973) A preliminary model for the formation of nitric oxides in DI diesel engine and its application in parametric studies. SAE 730083

Watson N, Pilley AD, Marzauk M (1980) A combustion correlation for diesel engine simulation. SAE 800029

Wiebe IT (1970) Brennverlauf und Kreisprozeb von Verbrennungsmotoren. VEB Verlag Technik, Berlin

10 Hydrocarbons from DI Diesel Engines

Abstract Hydrocarbon (HC) emissions from direct injection (DI) diesel engines are mainly due to fuel injected and mixed beyond lean combustion limit during ignition delay and fuel effusing from the nozzle sac at low pressure. The concept has been developed to provide an elegant model to predict the HC emissions considering slow burning. The model has been validated by collecting data on HC and pressures in cylinder and in fuel injection system from the experimental engines which are naturally aspirated, turbocharged or turbocharged with intercooling. New universal coefficients for the correlation of HC with operating parameters were obtained.

HC emissions from diesel engines are due to several factors. The fuel leaned beyond flammability limits (Greeves *et al.* 1977), bulk quenching during expansion, fuel effusing from nozzle sac after completion of injection (Yu *et al.* 1980) are the most important reasons. Only under extreme operating conditions like long idling or cold starting, wall-wetting, cyclic misfire and local under-mixing influence the HC (Dent and Lakshminarayanan 1983). On the other hand, in spark ignition engines, the emission of HC (Dent and Lakshminarayanan 1983) is mainly due to quenching near the cylinder walls and crevices like adsorption and desorption by oil film on the cylinder walls, and quenching. The detailed work of Yu *et al.* (1980) on diesel engines dealt with design parameters that have decisive influence on the HC. HC formation was studied by looking at the structure of spray, in an engine of bore of 140 mm. Except for the effect of engine speed, influence of all the operating parameters was satisfactorily explained. The temporal factor due to speed was not having any effect in the model as opposed to the experimental results because reaction of over-mixed fuel was not considered. Ikegami *et al.* (1983) carried out a schematic study of particulate and hydrocarbon from a direct injection diesel engine by sampling from a mini dilution tunnel. HC concentrations were found affected by ignition delay or by temperature in the engine cylinder. Nakayama *et al.* (1994) studied the effects of valve timings and valve lift systems on HC in cold start condition on an engine of bore 85 mm. Tsunemoto *et al.* (1992) studied the effects of combustion and injection systems on HC and particulate emissions on an engine of bore 102 mm. Parametric studies were made by varying aspect ratio of piston cavity, swirl at TDC, start of injection and excess air fuel ratio. HC emissions were found invariant for swirl and the shapes of the cavity if they were optimised for smoke and fuel consumption. A good empirical correlation was arrived at between the particulate matter and Bosch smoke number. Dent (1980) considered the influence of mixing scale of the shear flow generated by the spray, on HC emissions. All the above work showed that for the usual operating conditions of speed and load, HC emission from a reasonably optimised engine

P.A. Lakshminarayanan and Y.V. Aghav, *Modelling Diesel Combustion*, Mechanical Engineering Series, DOI 10.1007/978-90-481-3885-2_10,

depends on the fuel injected and over-mixed during ignition delay. The fuel evaporating from the sac (Greeves *et al.* 1977) after injection and reacting slowly during expansion stroke adds to the HC emissions.

In this chapter, a phenomenological model is successfully made for HC emissions from direct injection diesel engines. The unburned HC was correlated with the over-mixed fuel during the ignition delay and the fuel effusing from the sac that undergoes slow burning in the expansion stroke (Fig. 10.1). The over-mixed fuel is calculated from the measured instantaneous pressures in the nozzle and in the cylinder in conjunction with the effective flow area derived from the measured needle lift. Slow reaction of the over-leaned fuel was considered during the characteristic time of ignition delay. The ratio of observed raw HC emissions in the exhaust to the total quantity of fuel injected is defined as the Exhaust Indicated Hydrocarbons, EIHC or specific Hydrocarbon, SHC.

Injection characteristics and the indicated diagrams

Engines A10 to G10 in Table 3.2 were fully instrumented for needle lift, pressures in the injection line and in cylinder. Table 3.2 explains the details of FIE used on the engine. To cover a wide range of engines in the study of HC emissions, the engine used by Yu *et al.* (1980) was also studied using the integrated parameters such as ignition delay, nozzle hole-size and injected quantity. In Table 3.2 and Appendix XV, it is mentioned as engine H10. Figure 3.8 shows typical traces of line pressure, cylinder pressure, needle lift and apparent heat release of the turbocharged engine, B10 at 90% load. All the engines from A10 to G10 were of modern type designed for low emissions of NO_x and hydrocarbons. The compression ratio was relatively higher to enable injection delayed with respect to the previous generation of engines to which engine G10 belongs. The decrease in ignition delay

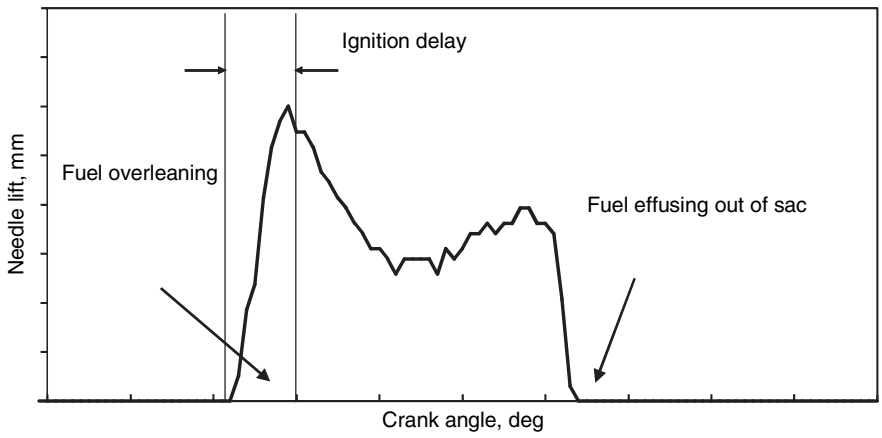

Fig. 10.1 Phenomenology of HC formation.

in such engines resulted in lower premixed burning fraction and hence the sharp first peak is missing in the heat release diagrams (Chmela *et al.* 1999). Further, to filter out the fluctuations in pressure due to physical effects in the cylinder, and the duct leading the pressure to the transducer, a moderate smoothening of the pressure diagram is optionally carried out using the moving average software in the AVL Indiskop. However, since the smoothening was done over duration of 2° crank angle the missing of first peak is more due to higher compression ratio and delayed fuel injection than due to smoothening.

HC Model

In the theoretical approach of Yu *et al.* (1980), the effects of fuel-air mixing are isolated from the effect of injection system characteristics, misfire, and other sources. The contribution to hydrocarbon emissions from fuel-air mixing is calculated using a transient spray model. The spray structure in different types of engines (A10–G10, Table 3.2) was found similar during the small period of ignition delay and hence they could be represented by simple numbers.

Spray structure

The spray mixing model and spray characteristics are determined by equations of spray penetration and growth of spray-width. A schematic behaviour of the transient vaporising spray is shown in Fig. 4.3 before detachment of the spray and after detachment (Lakshminarayanan and Dent 1983). The transient evaporating process can be considered as the introduction of successive packets of fuel along many streamlines radiating from a virtual origin of the spray located inside the nozzle at a distance from the mouth.

Ignition delay

Theoretical estimation

Ignition delay (*ID*) is the time lag between the start of injection to the ignition. The time taken for visible fire to appear in the pre-mixed zone of spray is a strong function of pressure and temperature of the ambient. In addition, the physical properties such as Cetane number, viscosity of fuel, nozzle hole size, injected quantity and injection pressure contribute to the delay phenomenon in diesel engines (Chandorkar *et al.* 1988). However, for diesel fuels a reasonable estimate of the delay, ID is achieved by Wolfer (Watson and Pilley 1980).

$$ID = 3.45 \exp\left(2100/T_m\right) p_m^{-1\,02} \tag{10.1}$$

Here T_m and p_m are the mean temperature and pressure of the ambient during ignition delay

Experimental estimation

Alternatively, the delay could be measured using the experimental pressure and needle lift traces (Fig. 3.8). Using the first law of thermodynamics, the apparent heat release rate could be calculated from the pressure crank-angle diagram. The ignition delay is measured as the time from the point of needle-lift to the start of heat release. However, the measurement noise does not allow us to pick the two points clearly from experimental data. Therefore, as the needle opening is assumed to be at a threshold of 10% of the maximum lift and the time when 5% of cumulative heat release is reached is considered the start of burning. The ignition delay of engines A10 to G10 was satisfactorily predicted using equation (10.1) and the results matched with the delay obtained from the pressure and needle lift traces.

Fuel injected during delay

The flow area of the nozzle holes, A, is calculated using the series of resistances namely, the gap between the needle seat, seat in the needle and spray holes by treating them as a series of orifices. A flow coefficient, C_d of 0.8 is reasonable for the spray holes. The instantaneous injection rate, dq/dt is given by the pressures before the nozzle, p_2 and in the cylinder, p_1 and instantaneous flow area (see Appendix IX).

$$dq/dt = C_f \rho_f A \sqrt{\frac{2(p_2 - p_1)}{\rho_f}} \tag{10.2}$$

Here, ρ_f = density of fuel.

Since the value of p_1 and p_2 change during the delay period, their mean values are considered in the equation. The amount of fuel injected during the delay period of combustion process, Q_{del} is obtained from the delay period and the rate of injection.

$$Q_{del} = ID \frac{dq}{dt} \tag{10.3}$$

Over-leaned fuel air mixture

Considering the structure of the nascent spray during the ignition delay, the fuel-air mixture beyond the lean combustion limit of relative air-fuel ratio, ΦL will not burn efficiently, as it is over-leaned. It will be emitted as unburned HC by the engine. The value of ΦL lies between 3.0 and 5.0, for most of the operating and injection parameters (Yu *et al.* 1980). In the present work, a lean limit of 5.0 is used. The concentration profiles along the axis and radius of conical spray is self-preserving except for the rich core containing liquid spray (Lakshminarayanan and Dent 1983). The zone of lean fuel-air mixture lies on the periphery of the cone and hence the simplified laws of similarity for concentration profiles are valid. Hence,

in principle, with the help of equations (4.1)–(4.5) it is possible to estimate the fuel mass leaned beyond the flammability limit, ΦL. The equations (4.1)–(4.5) and those given in the reference ((Lakshminarayanan and Dent 1983) allow calculation of over-leaned fuel at the end of ignition. The fuel integrated over the spray volume using equation (10.6) is not finite. Therefore, the over-leaned fuel is calculated as the difference between the fuel injected during the delay using equation (10.9) and that integrated from zero radius to the radius of Φ_L.

Over-leaning factor

The detailed calculations of a number of cases given in Appendix XVI for various engines showed that the over-leaned fuel could be expressed as a fraction of the fuel injected during the delay period and that the fraction is a constant. The value of the fraction was roughly equal to 0.01, if either the delay or the injected quantity during the delay is not large and dealt with in detail later in the chapter. The fraction is defined as the over-leaning factor.

Fuel effusing the injector sac

The liquid fuel remaining in the sac after the needle closed is at a pressure equal to that in the engine cylinder. However, the heat transferred from the hot combustion gases to the sac vaporises a part of the fuel components. The vapour comes through the holes at velocities too low to mix sufficiently with air and burn in the short period available during the expansion. The residue remains in the sac to be injected normally in the next cycle. The actual formation of hydrocarbons from the fuel in the sac is a function of the time and the rate at which the fuel discharges from the sac volume (Greeves *et al.* 1977). Therefore, the hydrocarbon emission, *HCv* due to sac volume is

$$HCv = V_s \ \rho_f \ y \tag{10.4}$$

Here, y refers to the yield or the fraction of fuel evaporated from the sac of volume, V_s *and* ρ_f is the density of fuel.

Other sources of hydrocarbons

The engine coolant temperature and lubricating oil could influence hydrocarbon emissions as well. However, in the present model, the engine is considered warmed up sufficiently so that the two factors have negligible effect on HC emissions.

Formation of unburned hydrocarbons

After the ignition delay, the combustible mixture of air and fuel within limits of combustion burns explosively to form equilibrium combustion products. The fuel beyond the lean limit of combustion burns slowly or partially decomposes to lighter fractions, or recombines to heavier hydrocarbon molecules resulting in exhaust hydrocarbons. This phenomenon is modelled according to a global slow burning rate.

Global slow burning rate

The diesel combustion is heterogeneous in nature, where the fuel evaporates and, the burned and unburned gases mix during expansion. Hence, many processes contribute to hydrocarbon emissions from a diesel engine. Greeves *et al.* (1977) and Yu *et al.* (1980) explain the phenomenon of bulk quenching as a physical process, related to the incomplete combustion of the combustible mixture due to volume expansion. The leaned out fuel finds it difficult to support a propagating flame in the expansion stroke, as the reaction rate is very slow by virtue of low concentration of fuel. In the present work, quenching is modelled using a global slow rate of reaction.

$$Diesel + 18\ Air \rightarrow \text{Pr}oducts\ of\ combustion \tag{10.5}$$

$$Mean\ reaction\ rate = A\, C_a^n C_f^m \exp(\frac{E}{RT}) \tag{10.6}$$

Where, A = 150–210
Ca = Mean concentration of air in the lean zone-1, approximately
C_f = Mean Concentration of fuel leaned out and effused from the sac
n = 18
m = 1
E/R = 2,100 K

The equation for slow reaction is validated for the Ignition delay period in an earlier work of Chandorkar *et al.* (1988). The dilution of the leaned out fuel after a characteristic period will be too low even to continue the slow reaction. The typical period scales with the delay period. The quantity of slow burnt fuel is given by the mean reaction rate and a characteristic ignition delay.

$$Slow\ burnt\ \ fuel = Reaction\ rate \times Ignition\ delay \tag{10.7}$$

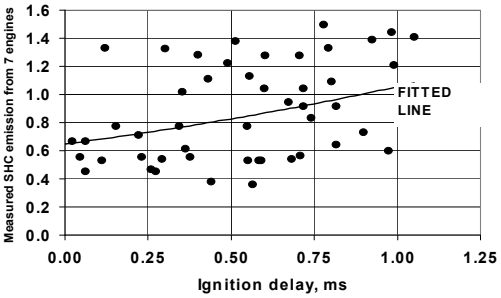

Fig. 10.2 Correlation of exhaust indicated hydrocarbon with ignition delay

Predicting HC in the Exhaust

Relating HC to ignition delay

The measured Specific HC is plotted against the ignition delay as given by Greeves *et al.* (1977) (Fig. 10.2). Their correlation seems to be valid for a given engine and at one condition of speed and load. For a wide variety of engines and operating conditions, the correlation coefficient is as low as 0.3.

Relationship of HC emissions and sac volume

Figure 10.3 shows (Greeves *et al.* 1977) the effect of sac volume alone on HC at a particular condition of load and speed for the engine studied. The negative intercept on the horizontal axis corresponds to the volume of holes. The yield value could be estimated as 0.21.

On the other hand, insignificant correlation was found between the observed mass of HC emissions and the sac volume for various engines at different operating conditions (Fig. 10.4).

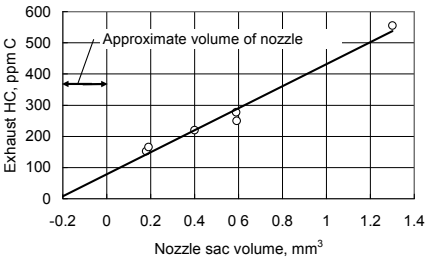

Fig. 10.3 Effect of nozzle sac volume on HC concentrations and yield (Greeves *et al.* 1977)

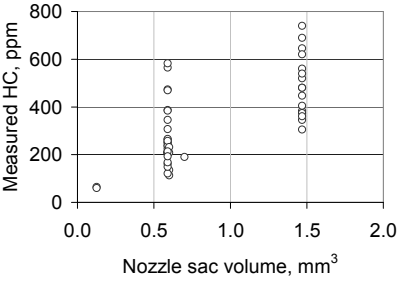

Fig. 10.4 Effect of nozzle sac volume on HC for many engines

HC and fuel injected during delay

As a first step, the observed HC was plotted against the ratio of fuel injected during ignition delay to the total fuel injected in Fig. 10.5, without considering the emissions from the sac. The regression coefficient was 0.93 showing the important effect of the quantity of fuel injected during ignition delay, Q_{del} on HC emissions from a diesel engine. The straight-line relationship in a semi-log plot showed that with increasing amount of fuel injected during delay, the emissions increased exponentially (Fig. 10.5). Figure 10.6 shows a good non-linear relationship in a Cartesian coordinate system. However, the fuel injected during the delay period is many times higher than the observed HC emissions. Further, the exponential relationship suggests that more time is available for the fuel to lean out when the delay increases. Therefore, considering an over-leaning factor and the effect of sac volume will improve the correlation quantitatively.

$$HC/m_f = 0.0012 \ \exp\left(2.86 \frac{Q_{del}}{\text{total fuel injected}}\right) \tag{10.8}$$

Specific HC in the exhaust

Specific HC in the exhaust is defined as the ratio of HC emissions in the exhaust to the quantity of fuel injected during delay. Thus, the Specific HC could be modelled using the expression given below.

$$EIHC \text{ in exhaust} \propto [(\text{fuel injected during delay from equation } (9) \times \text{fuel over leaning factor} + \text{sac volume} \times \text{yield}) - \text{slow burnt fuel from equation } (13))] / m_f = m_{cal} / m_f \quad (10.9)$$

Phenomenological model

The relationships with important parameters, namely the sac volume and fuel injected during the delay suggest that the correlation will not predict HC, if the two parameters are considered individually. The over-leaning factor and the unburnt fuel yielded by the sac volume when incorporated, lead to a phenomenological model. The suitable yield from the sac was found to be 12%.

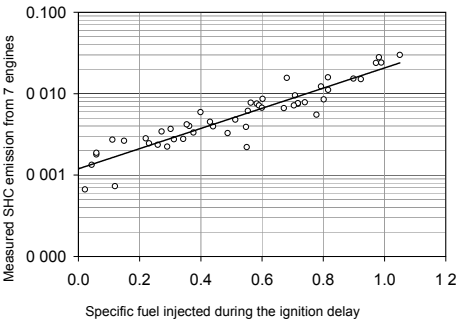

Fig. 10.5 Semi-log plot of specific mass of fuel injected during the ignition delay and HC

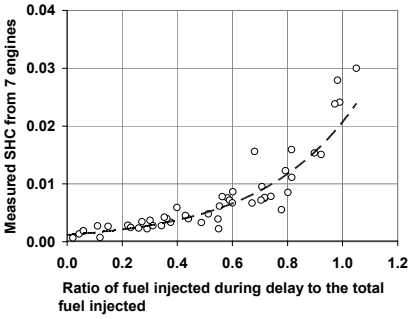

Fig. 10.6 Specific fuel injected during the ignition delay period

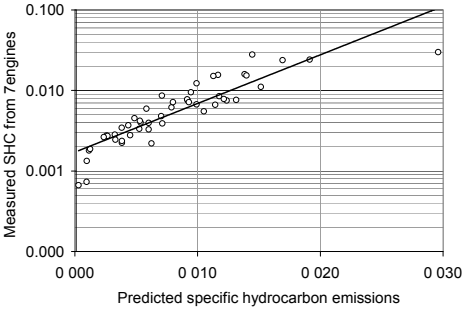

Fig. 10.7 Semi-log plot of specific mass of fuel and HC considering sac and an over-leaning factor was 0.008

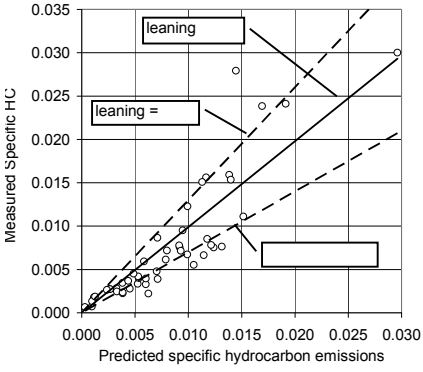

Fig. 10.8 Specific mass HC considering over-leaning and sac

An average over-leaning factor of 0.008 could be obtained from the thick jet structure of a diesel spray given in equations (4.1)–(4.5), during the ignition delay period. The measured Specific HC was plotted against the EIHC calculated using this factor in equation (10.9) on a semi-log paper in Fig. 10.7 and on a linear graph paper in Fig. 10.8. Here, the coefficient of the fit was better than 0.9 validating the proposed model for predicting HC emissions, quantitatively.

Discussions

The fuel injected during the ignition delay is cold and is dispersed into various packets of different air fuel ratios. The fuel leaned beyond an air excess ratio of 5.0 exits the engine as unburned hydrocarbon emissions. By studying the spray structure, the over-mixed fuel is estimated to lie between 0.007 and 0.011 of the fuel injected during the delay period in direct injection diesel engines (Fig. 10.8). The lower value of leaning factor is valid when the ignition delay is relatively less. The HC emissions are augmented by fuel effusing from the sac. The yield from the sac is about 0.12. The over-leaned fuel-air mixture burns slowly along with the fuel leaked from the sac during a characteristic period. The reaction rate could be described by Arrhenius type relationship. The ignition delay correlation (equation (5.1)) was applied to predict ignition delay. On engine C10, detailed experiments were carried out with oxygenated fuels and exhaust gas recirculation, EGR at rated conditions. The predictions were in agreement with observed values (Fig. 10.9).

Then, similar prediction methodology was applied to different engines widely varying in dimensions, methods of aspiration and rated speeds. Older version of engine E10 and B10 were also considered for model evaluation where larger amount of HC was observed. The satisfactory comparison of predicted and experimental values of HC emission under different operating conditions proved validity of new correlation (Fig. 10.10).

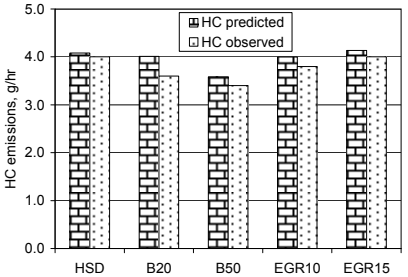

Fig. 10.9 Prediction of HC emissions at rated conditions for engine C10

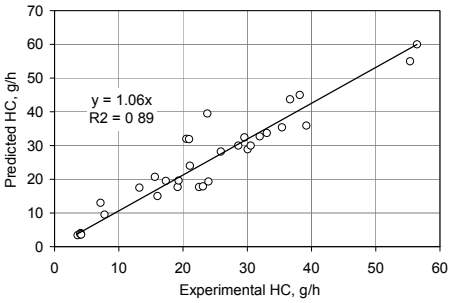

Fig. 10.10 Prediction of HC emissions for many engines

Summary
A strong relationship of HC exists with the sum of leaned-out fuel during the ignition delay and fuel yielded by the sac. Detailed consideration of over-leaning factor enables prediction of exhaust indicated HC for any DI diesel engine over a wide range of speeds and loads irrespective of the nature of aspiration, after reasonable warm up of the engine. The model considers the chemical effect of fuel on HC emissions indirectly in the ignition delay term.

References

Chandorkar SB, Dani AD and Lakshminarayanan PA (1988) Effects of injection parameters, fuel quality and ambient on the ignition delay and the location of the flame Kernel in a diesel spray in a quiescent chamber. SAE 881227

Chmela FG and Orthaber GC (1999) Rate of heat release prediction for a direct injection diesel engine based on purely mixing controlled combustion. SAE 99010186

Dent JC (1980) Turbulent mixing rate- its effect on smoke and hydrocarbon emissions from diesel engines. SAE800092

Dent JC, Lakshminarayanan PA (1983) A model for Absorption and Desorption of fuel vapour by Cylinder Lubricating Oil films and its contribution to Hydrocarbon Emissions. SAE 830652

Greeves G, Khan IM, Wang CTH, Fenne I (1977) Origins of Hydrocarbon emissions from diesel engines. SAE 770259

Heywood JB (1988) A text book on Internal Combustion engine fundamentals. McGraw-Hill International editions

Ikegami M, Xin-he Li, Nakayama Y, Keimiwa (1983) Trend and origins of Particulate and Hydrocarbon emission from direct injection diesel engine. SAE 831290

Lakshminarayanan PA, Dent JC (1983) Interferometric studies of vapourising and combusting sprays. SAE 830244

Nakayama Y, Maruya T, Oikawa T, Fujiwara M, Kawamata M (1994) Reduction of HC emission from VTEC engine during cold start condition. SAE 940481

Tsunemoto H, Ishitani H, Konno A (1992) The increase of HC emissions from a direct injection diesel engine during long idling operation. SAE 922227

Watson N, Pilley AD (1980) A Combustion correlation for diesel engine simulation SAE 800029

Yu RC, Wong VW and Shahed SM (1980) Sources of Hydrocarbon emissions from direct injection diesel engines. SAE 800048

11 Hydrocarbon Emissions from Spark Ignition Engines

Abstract To contrast the phenomenon of HC formation in a Diesel and a spark ignition engine, a chapter is included on the latter. The absorption and desorption of fuel by cylinder lubricating oil films has been modelled using principles of mass transfer in this Chapter. *Henry's* Law for a dilute solution of fuel in oil is used to relate gas to liquid phase fuel concentrations. Mass transfer conductances in gas and liquid phases are considered, the former via use of *Reynolds's* Analogy to engine heat transfer data, the latter through assuming molecular diffusion through an effective penetration depth of the oil film. Oxidation of desorbed fuel is assumed complete if the mean of burned gas and lubricating oil film temperatures is greater than 100 K. Below this value, the desorbed fuel is considered to contribute to hydrocarbon emissions. Comparison with engine test data corroborates the absorption/desorption hypothesis. The model indicates the equal importance of gas and liquid phase conductance.

The literature of unburned hydrocarbon emissions (HC) from spark ignition (SI) engines is comprehensively cited by Lavoie and Blumberg (1980). The HC emissions phenomenon is different from that in a Diesel engine, where it is generated by the fuel over-leaned at the surface of the sprays and by the fuel effusing from the nozzle sac. Four sources of unburned hydrocarbon generation have been identified for SI engines.

- Quenching of the propagating flame at cold wall surfaces in the combustion space
- Unburned fuel air mixture trapped in the piston top land and ring crevices
- Gas phase quenching when the engine is operating under extreme conditions of stoichiometry
- Absorption/desorption processes by cylinder lubricating oil films and deposits, which is identified as one of the major phenomenon.

Daniel (1957) identified the existence of cylinder quench layers and their relationship with engine stoichiometry, and showed a correlation with quench layer thickness established from burner studies. Daniel concluded that the observed quench distances were of the right order of magnitude to account for HC emissions. An extensive sampling valve study by Daniel (1967) identified the major engine operating variables controlling HC emissions. From his measurements, Daniel also concluded that post quench mixing and oxidation of the quench mass was taking place during the expansion and exhaust strokes of the engine cycle.

Lavoie and Blumberg (1980), and Lavoie, Lorusso and Adamczyk (1980) based on the observations of Daniel, considered a model for diffusion and oxidation of

P.A. Lakshminarayanan and Y.V. Aghav, *Modelling Diesel Combustion*, Mechanical Engineering Series, DOI 10.1007/978-90-481-3885-2_11,

the quench mass in the turbulent thermal boundary layer separating the cylinder wall from the burned gas region formed behind the propagation flame front. The model indicated that oxidation of the diffused HC was rapid and any remaining wall quenched HC was in low temperature regions of the thermal boundary layer (below about 1,100 K).

An in cylinder sampling valve study by Lorusso *et al.* (1981) indicated rapid and extensive burn-up of quench layer hydrocarbons, upper limit calculations showing that less than 10% of exhaust HC originate from the quench mass. Recent fundamental experimental studies by Blint and Bechtel (1982) corroborate the findings of Lorusso *et al.* (1981).

Unburned mixture trapped in the piston top land and ring crevices during the compression and combustion phases of the engine cycle, and which later in the expansion process expand into the combustion space, is known to be a major contributor to exhaust hydrocarbons (Lavoie and Blumberg 1980, Wentworth 1968).

Gas phase quenching when chemical reaction rates are low compared with turbulent mixing rates will occur under extremely unfavourable engine stoichiometry (Hamamoto *et al.* 1976) and excessive combustion chamber turbulence (Chigashi *et al.* 1971).

Unburned fuel adborpiton/desorption processes by lubricating oil films contributing to exhaust HC emissions have been identified by Kaiser *et al.* (1980, 1982) from bomb and engine studies. Support for this mechanism has been provided by the modelling study of Carrier *et al.* (1981) which has shown the variation of HC emissions with engine speed and cooling water temperature to follow observed experimental trends more closely than the comprehensive model of Lavoie-and co-workers (Lavoie and Blumberg 1980, Lavoie *et al.*1980).

From the foregoing discussion the major sources of HC emission from homogeneous spark ignited engines operating under normal conditions are those due to crevice volumes and absorption/desorption of unburned fuel by lubricating oil films and deposits.

A model for HC emission based upon a consideration of the contribution from crevice volumes, and the cyclic absorption/desorption phenomenon due to the lubricating oil film is presented in this chapter (Dent and Lakshminarayanan 1983). The absorption/desorption process is considered to be controlled by both gas and liquid phase conductances, unlike Carrier *et al.* (1981) who consider the liquid (lubricating oil film) phase to be controlling. The model is compared with the extensive experimental data of Lavoie and Blumberg (1980) obtained in a low turbulence engine with a disc shaped combustion chamber geometry. The effects of engine speed, load, equivalence ratio, exhaust gas circulation (EGR) and spark timing are compared with experiment. Parametric studies to investigate the effects of compression ratio, lubricating oil film thickness and cylinder charge turbulence are also presented and discussed.

Description of the Engine Model

- The engine model is considered in three sub-sections:
- Breathing
- Combustion
- HC emissions

Breathing

Detailed dynamics of flow through the engine (Lakshminarayanan *et al.* 1979a–d, 2002) can be considered for evaluating breathing by the engine. However, for most of the model based controls of modern engines a filling and emptying model is used. Here, the engine intake is considered a pipe with two resistances – the carburettor and the intake valve. Ahead of the carburettor resistance, a plenum at ambient conditions is assumed. The engine exhaust flow is considered through a resistance – the exhaust valve – into a plenum, which is at exhaust manifold pressure and temperature. Figure 11.1 shows a schematic of the induction exhaust configuration.

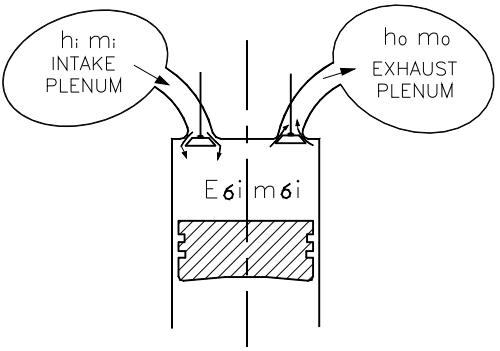

Fig. 11.1 Schematic diagram of engine and surroundings

The flow across the valves and throttle are quasi-steady and depend on effective flow areas and discharge coefficients, which have been taken from Sherman and Blumberg (1977). The model is of the 'filling and emptying' type without wave action effects – energy and mass conservation about an open system are applied. EGR is considered a diluent present in the air with composition of the exhaust gases. Considering the instantaneous cylinder volume as the system control volume (σ) energy and mass conservation equations can be written as:

$$dE_\sigma = \sum_{all\ i} h_i\, d_{m_i} + \delta Q - \delta W \tag{11.1}$$

$$dm_\sigma = \sum_{all\ i} dm_i \tag{11.2}$$

E_σ and m_σ are the instantaneous internal energy and mass of the cylinder contents, m_i and h_i are mass and specific enthalpy of specie i, (fuel, air or burned gas) entering or leaving the control volume. Q and *w* are heat and work transfer.

$$dm_i = f_i\ dm_V = f_i \rho_V\ C_d\ A_V\ U_V.dt \tag{11.3}$$

Here, f_i is the mass fraction of specie *i,* P_v the density, A_v the flow area and U_v the velocity at the valve and C_d the coefficient of discharge. U_v is a function of the pressure drop across the valve and upstream pressure.

Back flow into the induction system is accounted for in the following manner. The inlet valve closes after bottom dead centre hence a quantity of the cylinder charge is forced back into the inlet port-induction manifold as the piston moves towards TDC on the compression stroke, this mass is assumed to reside as a plug in the inlet tract. Late in the exhaust stroke of the inlet tract, plug flow is again considered, and no mixing with the plug of induction charge residing in the inlet tract is assumed. As the next induction stroke commences, these two plugs of burned gas and fresh charge, are drawn into the engine cylinder. The computation scheme keeps track of these plugs for use in the energy and mass conservations equations (11.1) and (11.2).

Combustion

The air fuel mixture induced into the cylinder mixes with the residual fraction with EGR the effective residual increases. The gaseous mixture is compressed, heat transfer with the cylinder walls being calculated from Woschni's correlation (Woschni 1967).

Following the ignition process, the burned and unburned gases in the cylinder are considered separated by a thin flame front. Heat transfer to the cylinder walls is considered independently from these two zones using Woschni's correlation. The ignition delay is an input parameter to the computation, the data being taken from reference (Lavoie and Blumberg 1980). A cosine burning 'law' (Lavoie and Blumberg 1980) is used for calculation of the mass-burning rate. The burned mass fraction a at any crank angle during the burn period is defined by:

$$\alpha = 0.5\left[1 - \cos\left\{\frac{\pi}{1.16}\,\frac{(\vartheta - \vartheta_{0.05})}{(\vartheta_{0.95} - \vartheta_{0.05})}\right\}\right] \tag{11.4}$$

Here, θ is crank angle and subscripts 0.05 and 0.95 refer to the position when 5% and 95% of the charge has been burned.

Use of the Cosine Burning 'Law' in preference to the phenomenological models described in references (Hires *et al.* 1978, Dent and Lakshminarayan 1980)

enables comparison of the results obtained with the HC emission model developed here with that presented by Lavoie and Blumberg (1980).

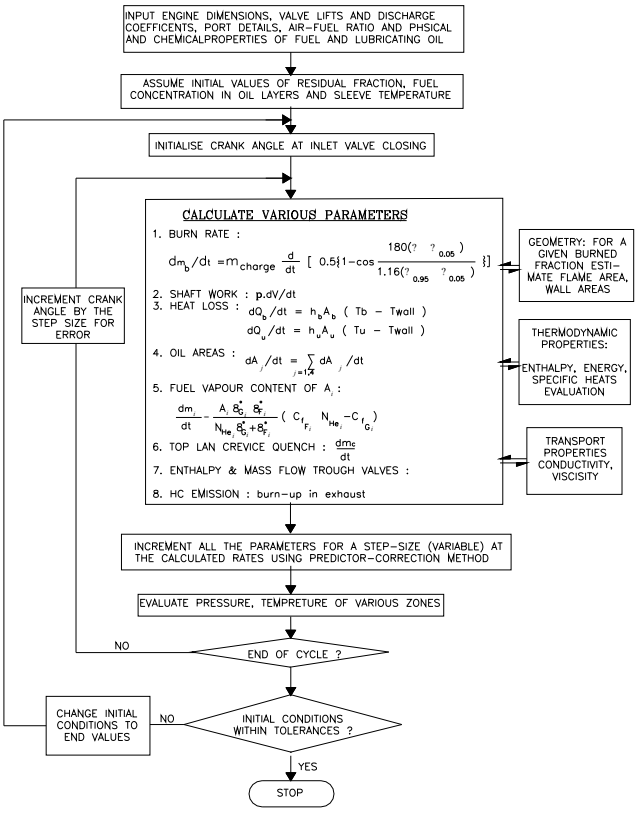

Fig. 11.2 Model

During the combustion process the contributions of unburned mixture and burned products to total internal energy E and volume V are:

$$m_b\, e_b + m_u\, e_u = E \tag{11.5}$$

$$m_b v_b + m_u v_u = V \tag{11.6}$$

Here, e and v are specific internal energy and volume and suffices u and b refer to unburned mixture and burned products. The set of equations (11.1) (11.2) (11.4) (11.5) and (11.6) are used in the evaluation of cylinder pressure and burned and

unburned gas temperatures. A schematic of the solution procedure is shown in Fig. 11.2.

HC emissions

The piston motion exposes the cylinder liner and oil film to the charge gases at various times during the engine cycle. The lubricating oil film is assumed to be of a uniform thickness on the liner surface, and its total area can be considered as made up of four regions.

Region (1) in contact with unburned gases

Region (2) that was in contact with unburned gases and is presently covered by the piston

Region (3) in contact with burned gases

Region (4) that was in contact with the burned gases and is presently covered by the piston

The sum of the areas of these four regions is invariant, but individual areas increase or decrease at the expense of its neighbours. This is summarized schematically in Figs. 11.3 and 11.4.

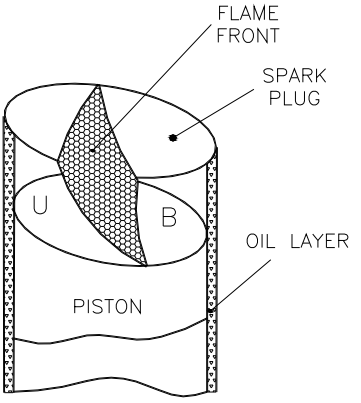

Fig. 11.3 Schematic diagram of oil layers, flame front, unburned zone (U) and burned gas zone (B)

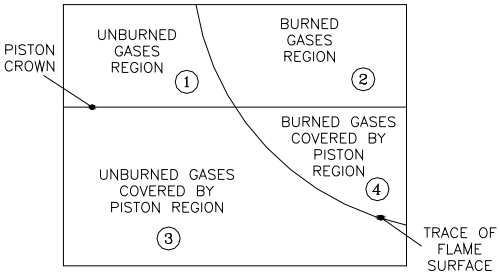

Fig. 11.4 Schematic of oil regions participating in absorption and desorption

The following mechanism is considered to apply for the transfer phenomenon of fuel vapour between the gas and liquid (oil film) phases.

Between the bulk gas state (*C*) (charge condition at any instant) and the oil film gas phase interface (*S*), vapour transport is by convective mass transfer through the burned and unburned gas turbulent boundary layers.

Henry's Law is assumed to hold for the absorption of the vapour by the oil film, and the partial pressure of the fuel vapour (P_{fs}) in the gas phase adjacent to the interface S state is related to the mole fraction of the fuel dissolved in the oil film (n_{fL}) by the Henry Constant (H_C) where:

$$H_C = \frac{P_{f_s}}{n_{f_L}} \tag{11.7}$$

A *Henry* Number N_{Hc} is defined (17) as:

$$m_b v_b + m_u v_u = V \tag{11.8}$$

Here, m_{fs} and m_{fL} are the mass fractions of fuel vapour in the gas phase and dissolved into the oil layer respectively. Equations (11.7) and (11.8) are combined to yield.

$$N_{HC} = \left(\frac{H_c}{P_{tol}}\right)\left(\frac{M_o}{\overline{M}}\right) \tag{11.9}$$

Here, P_{tot} is the total instantaneous cylinder pressure and M_O and $\overline{M}$ are the molecular weights of oil and the charge gas mixture – here assumed air. The evaluation of the Henry Constant for the oil film is discussed in Appendix XI.

The transfer of the dissolved fuel across the oil film is assumed to occur by molecular diffusion. A linear concentration gradient in the oil film is assumed. To accommodate the effects of engine speed on the diffusion process, a penetration depth (δ) is assumed over which the concentration gradient will be effective. This procedure is similar to that adopted in transient heat conduction (Kreith 1960) where, for fast transients a finite body can be assumed to be semi-infinite in behaviour. From Kreith (1960) the penetration depth can be expressed as

$$\delta = \sqrt{\frac{\pi D}{N}} \tag{11.10}$$

Here D is the molecular diffusion coefficient for the oil film and N is engine speed. Figure 11.5 shows a schematic of the ideas discussed above. For a dilute mixture of fuel in air the convective mass flux ($\dot{m}''$) across the gas phase boundary layer can be expressed as (Spalding 1963)

$$\dot{m}'' = g_G^* \left(m_{f_G} - m_{f_s}\right) \tag{11.11}$$

Here g_G* is the gas phase mass transfer conductance and is evaluated in Appendix XII, m_{fg} and m_{fs} are the mass concentrations of fuel vapour in the bulk gas state (G) and on the gas side of the interface (S). Across the penetration depth, $\dot{m}''$ can be written as

$$\dot{m}'' = g_F^* \left(m_{f_L} - m_{f_F} \right) \tag{11.12}$$

Here,

g_F^* =Liquid phase mass transfer conductance (and is evaluated in Appendix XII)

m_{fL} and m_{fF} = Mass concentrations of the dissolved fuel on the liquid side of the interface (L), and in the bulk of the oil film (F)

Equating (11.11) and (11.12) and using equation (11.8) along with algebraic re-arrangement and the definition of $\dot{m}''$ in equation (11.12) results in

$$\dot{m}'' = \frac{g_G^* \, g_F^*}{N_{Hc} \, g_G^* + g_F^*} \left[m_{f_G} - m_{f_F} \, N_{Hc} \right] \tag{11.13}$$

The desorption results in a change of sign in $\dot{m}''$ equations (11.11)–(11.13). The mass transfer flux ($\dot{m}''$) from equation (11.13) multiplied by the surface areas of the cylinder liner in contact with unburned or burned gases gives the rate of absorption of desorption of fuel vapour by the oil film.

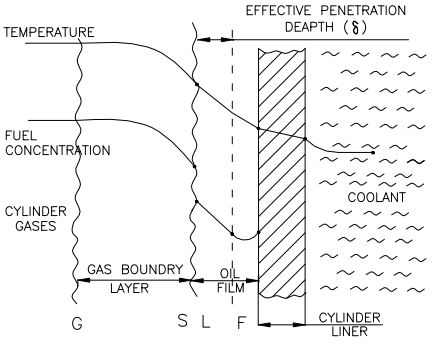

Fig. 11.5 Temperature and concentration gradients within the engine

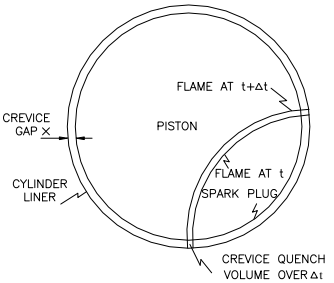

Fig. 11.6 Interaction of flame and top land crevice

As pointed out earlier, the dissolved fuel content of the four regions considered will change due to mass transfer and also because of changes in regional surface areas due to flame propagation and piston movement (see Figs. 11.3 and 11.4). This is expressed mathematically for the region i as:

$$\frac{dm_i}{dt} = \dot{m}'' A_i + \rho_o Z_o \sum_{\substack{j=1,4 \\ i \neq j}} m_{f_{F_i}} \frac{dA_{i,j}}{dt} \tag{11.14}$$

Here, dm_i/dt = Rate of change of the fuel content of I

A = Surface area of the region

ρ_o *and* Z_o = Density and thickness of the oil layer respectively,
m_{fFi} = Mass fraction of fuel in oil in the region 1
dA_{ij}/dt = Rate of change in area of the region (i) due to changes in the boundaries of adjacent regions.

Complete oxidation of desorbed fuel into the burned gases was assumed if the arithmetic mean of the burned gas and oil film temperature is above 1,100 K. At lower temperatures the desorbed fuel is integrated and considered to contribute to HC omitted during blow down, justification for this is given in Appendix XIII.

The contribution of ring crevice to HC emission

As the propagating flame front passes over the piston crown fuel air mixture is trapped in the top land crevice where it is assumed to region unreacted. Considering the flame propagate on over the time interval Δt (Fig. 11.6) the hatched crevice volume v traps the unreacted fuel air mixture. The mass of gas (m_c) trapped is determined by the prevailing pressure P in a cylinder and the temperature of the walls T_w and can be expressed as:

$$dm_c / dt = \left[\frac{P}{R T_w}\right]\left[\frac{dv}{dt}\right] \qquad (11.15)$$

The crevice volume, V is calculated from the crevice gap x, which is here assumed to be constant. In actual conditions, however, the gap varies with piston material, construction details and its temperature under varying conditions of operation. m_c is assumed to undergo no reaction in the cylinder and contributes to the total HC emission at the exhaust valve. It is assumed that the crevice mass discharged is in proportion to the mass of burned gas discharged over any time interval.

Oxidation of HC during exhaust

The hydrocarbons emitted from the engine are assumed to be uniformly mixed with the products of combustion and any remaining air in the cylinder. The process of exhaust flow, oxidation of the emitted HC, and heat transfer to the port follow Lavoie and Blumberg (1980). However at exhaust valve closure the exhausted gases are assumed to continue flowing through the exhaust port and pipe at a progressively diminishing velocity. This requires a change in the flow regime from turbulent to laminar and an appropriate change in the friction factor for use with the Reynolds analogy relationship.

Solution procedure

The submodels – breathing, combustion and HC emissions – are used in a thermodynamic cycle simulation program (Ferguson *et al.* 1976) to evaluate HC emission behaviour of the engine. Transport and thermodynamic properties of unburned mixture and burned products are available from the various subroutines of the simulation program. The rate of change of heat loss, work output, combustion, relevant surface areas, fuel vapour absorbed and desorbed from the oil film, crevice

mass trapped, and inducted and exhausted masses from the cylinder, are used in an interactive integration scheme of the predictor corrector type which is part of the cycle simulation program. The complete computation scheme is shown in Fig. 11.2.

Initially, the oil film contains no absorbed fuel, and during the desorption process not all the fuel vapour is desorbed. Hence, there is a progressive accumulation of fuel in the oil film, until a steady mean concentration is reached, with further absorption and description occurring about the mean. It was found that the number of engine cycles to reach this mean value was dependent on wall temperature, engine speed and oil film thickness. With the range of these parameters investigated here it was found that when wall temperature is low, or engine speed high or oil film thickness large, about ten cycles were necessary to achieve the steady value, while at the other extreme of these parameters steady oil film concentration was achieved within two cycles. This point will be dealt with further in the discussion of results.

Comparison of the Model Prediction with Engine Experiments

The results obtained with the model described were compared against the experimental data of Lavoie and Blumberg (1980) and Lavoie *et al.* (1980) obtained on a CFR engine. The engine details and operating conditions are given in reference (Lavoie *et al.* 1980) where engine speed, load, equivalence ratio, EGR and timing were varied relative to a baseline condition, which is listed here in Table 11.1.

Table 11.1 Basic engine-operating parameters

Base point engine conditions	Ref (Lavoie and Blumberg 1980)
RPM	1,250
IMEP	380 kPa (55 psi)
A/F	16.0 ($\Phi = 0.9$)
Compression ratio	7.1 (8.65 for EGR runs)
Spark timing	MBT (35 BTC)
EGR	0%
Burning interval	(–14 , 34)
ISFC	240 g/kW-h (0.395 lb/hp-h)

The effects of compression ratio and wall temperature were evaluated against the data of reference (Lavoie *et al.* 1980). The effects of turbulence of intake charge were evaluated using the model and the operating conditions of references (Lavoie and Blumberg 1980, Lavoie *et al.* 1980) over a range of engine speed. Direct comparison with experimental data was not possible. The gas exchange and combustion submodels were tested for accuracy against mass flow data provided by Lavoie (1975) and IMEP data of Lavoie and Blumberg (1980). At their worst

computed airflow was within 2% and IMEP within 8% of the experimental values. The deviation in IMEP could be due to the use of Woschni's equations (Woschni 1967) for heat transfer, which was not modified in any way for the present study.

Figure 11.7 shows the variation of HC (fuel vapour) in the oil layer with crank angle for the first cycle of the computation at the engine baseline condition. The mass of HC will be zero initially and then will follow a trend similar to cylinder pressure as it then increases and decreases to a value of approximately 0.2 mg at the end 720° CA. The trend with cylinder pressure is to be expected because absorption and desorption are related directly to the Henry Constant (equation (11.7)) and the mass transfer conductance g_G* (equation (11.11)). Because of the finite engine cycle time there will be fuel remaining within the oil layer at the end of the engine cycle (720° CA), the quantity depending on engine speed and oil film thickness (wall temperature variation). The quantity of fuel remaining in the oil film at the end of the first cycle will provide the initial condition for the second cycle where once again there will be a residual of fuel at the end of the cycle and hence there is a build up of fuel mass in the oil film until a steady level is reached about which there is a periodic variation due to absorption and desorption.

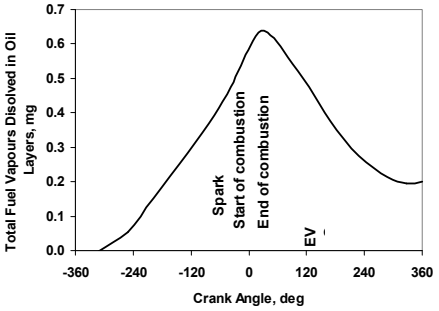

Fig. 11.7 Fuel content of oil layers variation with crank angle

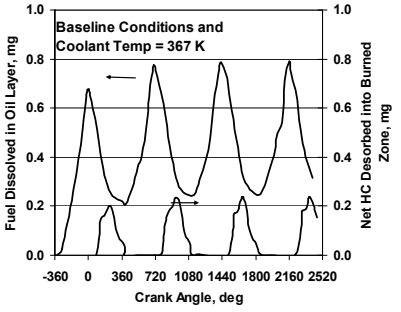

Fig. 11.8 Stabilisation of fuel quantity in oil layers at 367 K coolant temperature

This point is emphasised in Figs. 11.8 and 11.9, where variation mass desorbed with crank angle and cycle number is also shown. It will be seen from Fig. 11.8 that the net HC absorbed into the burned gas commences about 90° ATDC on the expansion stroke, and increases rapidly as the expansion proceeds. This is due to three factors. The boundary layer film temperatures are below 1,100 K (see Fig. A.9), therefore oxidation of the desorbed HC is negligible. Secondly, the surface area for desorption increases as the expansion proceeds, and thirdly the decrease in cylinder pressure during expansion cause an increase in the Henry Number N_{Hc}, which from equation (11.13) results in an increased desorption rate $\dot{m}''$. A further increase in the desorbed mass of hydrocarbons occurs following exhaust valve opening for the three reasons just discussed above. During the exhaust stroke beyond the bottom dead centre the desorbed hydrocarbons decrease because of the reducing surface area for desorption. The decrease in cylinder pressure with inlet valve opening reduces this trend for a moment, but admission of fresh charge

increases the concentration of fuel vapour mfG (equation (11.13)). This coupled with minimal desorption areas around TDC causes desorption of hydrocarbons to fall rapidly to zero. It should be noted that in all comparisons with experimental data the results for absorption and desorption were considered after the steady state value had been reached.

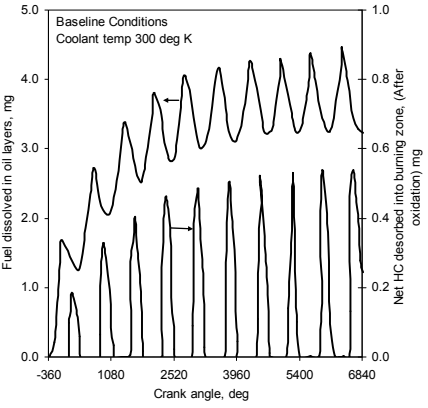

Fig. 11.9 Stabilisation of fuel quantity in oil layers at 300 K coolant temperature

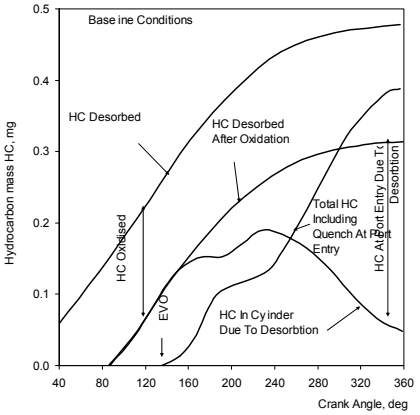

Fig. 11.10 Variation of integrated hydrocarbons with crank angle

Figure 11.10 shows the variation with crank angle in integrated HC (fuel) desorbed before oxidation – curve (A) – the integrated desorbed HC remaining after in cylinder oxidation – curve (B) – and the integrated desorbed HC remaining in the cylinder after exhaust valve opening – curve (C). It should be noted that oxidation of the desorbed HC ceases after about 80° ATDC because the gas temperature has fallen below 1,100 K, hence the constant difference between curves (A) and (B). The difference between curves (B) and (C) is the integrated mass of HC desorbed which is discharged to the exhaust port along with the appropriate integrated mass of the crevice contribution, this is shown as curve (D).

Figure 11.11 shows the variation in exhaust HC concentration and gas velocity at the exhaust port with crank angle. The HC concentration follows the exhaust velocity, as the velocity drops after the blow-down period, the HC concentration falls due to the fact that the crevice mass flow rate discharged in the exhaust flow is proportional to the mass flow rate of burned gases exhausted. Following blow down, the HC concentration follows the exhaust flow until valve closure.

Effect of engine speed

Figure 11.12 considers the effect of engine speed on HC emission, where the agreement with experimental data is good. The computed ring crevice contribution is approximately constant. This follows from the condition of the test where engine stoichiometry and IMEP were held constant. The decrease in HC omitted with speed will be due to the reduced engine cycle time allowing lower absorption and desorption to occur, higher cylinder wall temperatures at the higher speeds result

in reduced oil film thickness due to reduced viscosity and also an increase in the Henry's constant which reduces the fuel vapour absorbed, It should be noted that while the change in mean wall temperature over the speed range is small (approximately 16 K), Henry's constant varies by a factor of 2 (see Appendix XI).

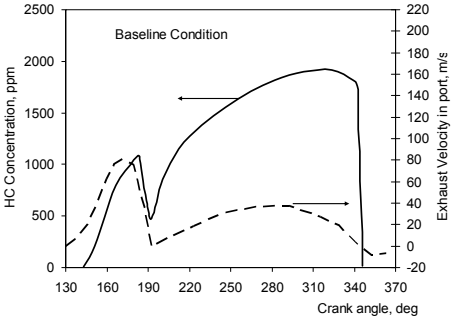

Fig. 11.11 Variation in the HC emission at the exhaust port with crank angle

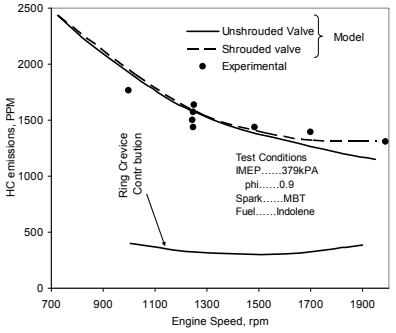

Fig. 11.12 Effect of engine speed on HC emissions

Effect of IMEP

Figure 11.13 shows the effect of load (IMEP) on exhaust HC at fixed engine speed, equivalence ratio and MBT timing. The crevice contribution to exhaust HC is again approximately constant in accordance with Lavoie *et al.* (1981). The decrease in the desorbed HC mass fraction (ppm) emitted with increase in engine load is due to increased wall temperature – from 400 to 455 K –- as the load is increased from 240 to 655 kPa, and the increased post desorption oxidation due to higher burned gas temperatures with increasing load.

Effects of equivalence ratio and timing

The effects of equivalence ratio at base line operating condition are shown in Fig. 11.14, while Fig. 11.15 shows the effect of spark retard to produce a 10% fuel economy penalty (ISFC). Increasing equivalence ratio (Φ) increases the concentration of fuel vapour in the bulk gas state m_{FG}, which will increase the absorption and hence desorption from the oil layer. In addition, the higher cylinder pressures with increasing Φ will promote higher absorption. The crevice mass contribution will increase progressively with increase in Φ.

Retarded timing (Fig. 11.15) will produce a reduced level of HC emission compared with Fig. 11.15 due to lower cylinder peak pressures producing lower fuel absorption, and higher expansion temperatures resulting in higher HC oxidation. The increase in HC emission when $\Phi < 0.7$ can be attributed to higher cyclic variability because of the low compression ratio (7.1:1) and quiescent nature of the combustion chambering of the CFR engine. This point is corroborated by the lower scatter of experimental data for the retarded timing (Fig. 11.15) where higher temperatures at ignition would contribute to better ignition of the lean mixture.

Effect of EGR

Figure 11.16 shows the effect of EGR at fixed engine speed, load, equivalence ratio, and MBT timing, but with engine compression ratio increased to 8.65:1. The comparison with experimental data is not adequate, prediction indicating a small increase in exhaust HC with increasing EGR. The absorption desorption mechanism contributes a decreasing amount of HC with increase in EGR due to reduced cylinder pressure levels, while the small decrease in wall temperature – 8 K – as the EGR increases causes an increase in HC absorption and desorption. The lower burned gas temperatures with increasing EGR result in a lower oxidation rate. The model described here does not account for wall quenching. However, wall quenching as indicated by Lavoie and Blumberg (1980) is likely to be a major contribution to HC emissions with increasing EGR. The wall quenching is as important as bulk gas quenching and cyclic variability due to poor combustion.

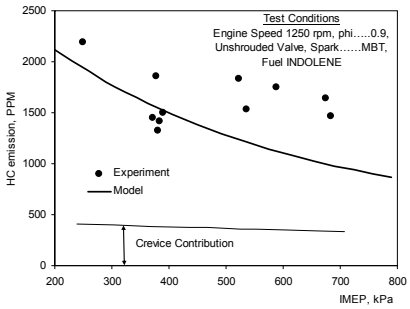

Fig. 11.13 Effect of IMEP

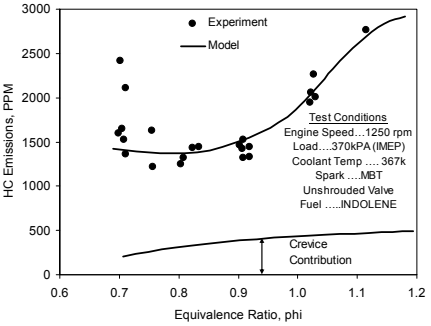

Fig. 11.14 Effect of equivalence ratio

Effect of indicated specific fuel consumption

Figure 11.17 shows the variation of HC emission with Indicated Specific Fuel Consumption (ISFC), the experimental data were obtained at constant equivalence ratio, speed, IMEP and compression ratio of 6.92. The ISFC variation was achieved by spark retardation. The agreement shown in Fig. 11.17 between prediction and experiment is fair. The decrease in the crevice contribution with increasing ISFC follows directly from the reduced cylinder pressure levels as ISFC increases with spark retard. This reduction of cylinder pressure also results in a small HC contribution from the absorption desorption mechanism. Finally, oxidation of the desorbed HC will increase with spark retard. It should be emphasized that the oil film thickness on which the foregoing computations were made was assumed to be a constant 5 μm at the baseline condition (Table 11.1) this appeared to be a reasonable mean between maximum and minimum values computed for the top ring cylinder bore oil film thickness for a petrol engine (Allen *et al.* 1975), and gave a reasonable level of HC emission when compared with the baseline experimental data. The oil film thickness was considered to vary in proportion with the square root of the oil film kinematic viscosity (Schlichting 1955). Hence, from the

baseline conditions, variation in oil film thickness could be computed with changes in engine variables that altered the cylinder wall temperature. The procedure used for wall temperature evaluation is given in Appendix XIV.

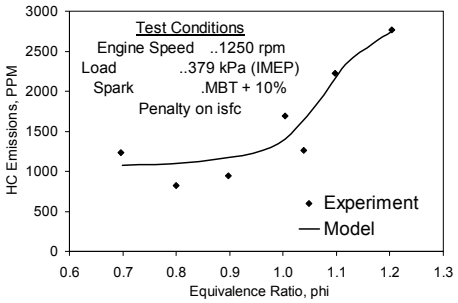

Fig. 11.15 Effect of spark retard

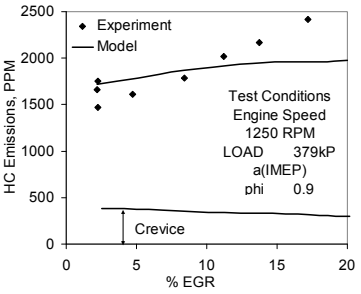

Fig. 11.16 Effect of EGR

In making the comparison with the engine data of Lavoie *et al.* (1980) it should be noted that the CFR engine used in the test reported by Lavoie and Blumberg (1980) was modified in several ways: a masked inlet valve was used to create higher in cylinder air motion, the ring pack was altered to give better oil control and less blowby, and the exhaust port was longer. The tests by Lavoie *et al.* (1980) were run on isooctane rather than the Indolene-clear used by Lavoie and Blumberg (1980). The variation of the ignition timing and $\theta_{0\,05}$ and $\theta_{0\,95}$ with compression ratio were provided by Lavoie (1982) for use in the comparison with the data of Lavoie *et al.* (1980). To accommodate the better oil control with the new ring pack, model predictions for the data used from the above reference were made with a baseline oil film thickness of 2 μm, which appears to be reasonable for current engine practice.

Effect of compression ratio and the temperature of the combustion chamber walls
Figure 11.18 shows the variation of HC emission with compression ratio while Fig. 11.19 shows HC variation with change in wall temperature. In both the figures, agreement between predictions with the 2-μm film thickness and experiment appears reasonable. The crevice contribution increases with compression ratio (Fig. 11.18) because of the increased cylinder pressure, this will also increase the HC contribution from the absorption/desorption mechanism. The HC oxidation level will fall with increase in compression ratio because the IMEP has been maintained constant during the test, and therefore expansion pressures and temperatures will be reduced.

Effect of oil film thickness
The effects of variation in wall temperature on HC emission shown in Fig. 11.19 are essentially due to the variation in the Henry Constant and oil viscosity variation with temperature. The crevice mass contribution to HC emission decreases with increasing wall temperature due to reduced gas density in the crevice gap. The result of a parametric study of the effect of oil film thickness on HC emission is

shown in Fig. 11.20, for the baseline condition. The emission of HC levels off at oil film thickness greater than about 5 μm, indicating that under operating conditions where the lubricating oil film thickness is greater than about 5 μm the effective penetration depth is the controlling thickness.

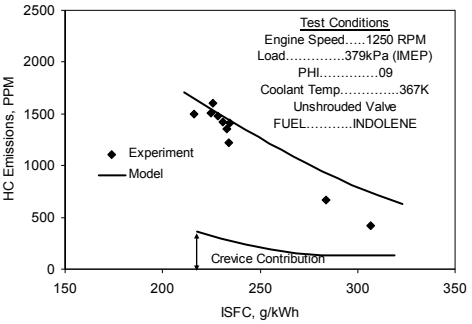

Fig. 11.17 Effect of spark timing

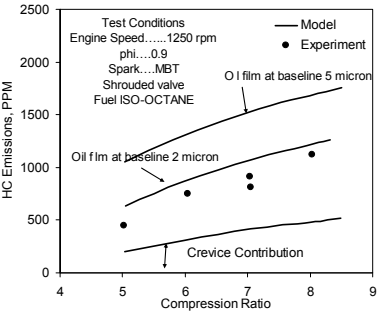

Fig. 11.18 Effect of compression ratio

Effect of increased gas motion

The effect of increased gas motion with a masked valve on HC emission cannot be assessed from the results of references (Lavoie *et al.* 1980, Lavoie and Blumberg 1980), because of the significant differences between the two test situations mentioned above. However, assuming a 5 μm baseline oil film thickness and using the ignition and burn angle data from references (Lavoie *et al.* 1980, Lavoie 1982), a prediction of the HC emission variation with engine speed using a masked valve is shown plotted in Fig. 11.12 for comparison with the unmasked valve predictions based on reference (Lavoie and Blumberg 1980). It will be seen that the differences in HC emission predicted are negligible with increased charge turbulence in the speed range 750–1,250 rpm, however at 1,900 rpm a small increase is noted.

To comply with the test conditions of references (Lavoie *et al.* 1980, Lavoie and Blumberg 1980) the load (IMEP) was maintained constant over the speed range of the tests conducted with each valve type. Because of the retarded timing of the high turbulence masked valve tests, cylinder pressure levels are lower than the post ignition pressures of the unmasked case at the same crank position. However following ignition the faster combustion obtained with the masked valve results in a faster rate of pressure rise and peak pressure than with the unmasked valve (Fig. 11.21).

There effects appear to balance each other in relation to the fuel absorption process. The differences in the expansion phase of the pressure diagrams obtained with the combustion model are not significant and therefore the oxidation temperatures are not significantly different. The relative effects of gas phase and oil layer conductances g_G* and g_F* and the Henry Number N_{Hc} over the engine cycle can be assessed from equation (11.13). The magnitude of the parameter $g_G^* N_{Hc} / g_F^*$ indicates whether the gas phase (g_G*) or the oil film (g_F*) controls the absorption and desorption processes.

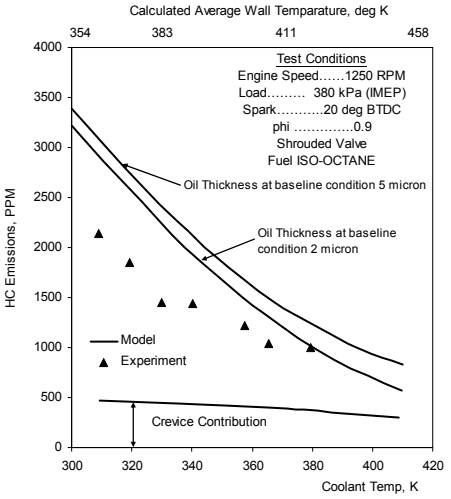

Fig. 11.19 Effect of coolant temperature on HC emissions

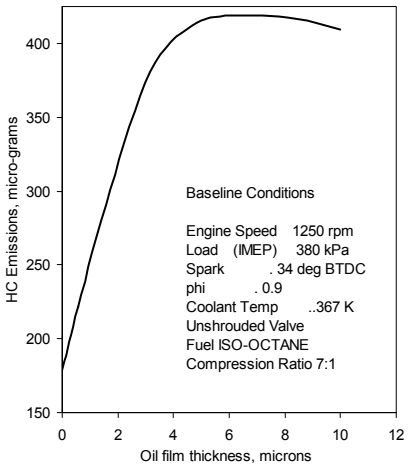

Fig. 11.20 Effect of oil thickness on HC emissions

When $g_G^* N_{Hc} / g_F^*$ is large equation (11.13) reduces to the following equation and the oil film controls.

$$\dot{m}'' = g_F^* \left(\frac{m_{m_G}}{N_{Hc}} - m_{f_F} \right) \tag{11.16}$$

Furthermore, if N_{Hc} is itself large the process of absorption will be negligible as $m_{fG} / N_{Hc} \rightarrow 0$. Conversely, when $g_G^* N_{Hc} / g_F^*$ is small, equation (11.13) reduces to the following equation and the gas phase controls.

$$\dot{m}'' = g_G^* \left(m_{f_F} - m_{f_F} N_{Hc} \right) \tag{11.17}$$

Figure 11.22 shows the variation of $N_{Hc}\, g_G^*/g_F^*$ over the engine cycle for the baseline condition and a 5 μm oil film thickness. It will be seen that over most of the engine cycle the gas and oil film conductances play an equally important role, however around TDC the effect of the oil film becomes dominant, but this will be reduced considerably if the oil film thickness is considered to be 2 μm.

The use of Woschni's correlation for the evaluation of the convective heat transfer coefficient h and hence g_G^* by the Reynolds Analogy is a limitation in evaluating the effects of intake turbulence. In Woschni's correlation, effects of changes in motion of air and turbulence will only be seen during the combustion phase of the engine cycle through their influence on the pressure diagram. Therefore, during the induction and compression periods of the engine cycle where

intake charge motion plays an important role on the process of fuel absorption into the lubricating oil film, a modification to the constant, C1 in the velocity term of Woschni's correlation would appear necessary to account for change in valve geometry. This problem needs to be addressed before firm conclusions can be drawn as to the effects of intake charge turbulence on HC emission. See equations (6.3) and (17.32).

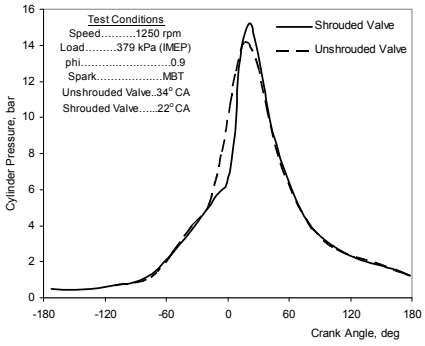

Fig. 11.21 Cylinder pressure diagram computed for shrouded and unshrouded valves

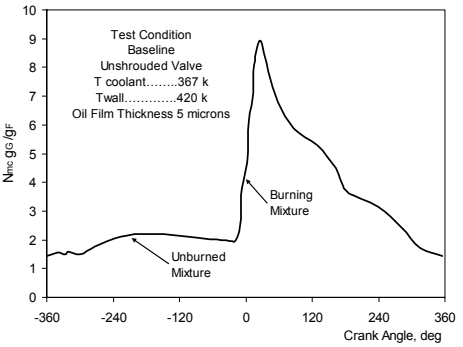

Fig. 11.22 Variation of mass transfer conductance parameter with crank angle

Conclusions

A model for fuel absorption and desorption by engine cylinder lubricating oil films has been presented which in general is in accord with engine experiments over a wide range of operating variables apart from EGR, where it is considered that factors such as bulk quenching and poor combustion resulting in higher cyclic variability will contribute to the higher value of exhaust hydrocarbons observed experimentally with increasing EGR.

The effects of engine geometry have not been investigated here, but it is clear from simulation studies (Lakshminarayanan and Dent 1982) that changes in combustion chamber geometry including spark plug location will result in changes in the burned and unburned gas areas in contact with cylinder wall surfaces; which will result in differing fuel absorption and desorption levels.

The effect of induction generated flow and turbulence on HC absorption during the induction and compression strokes of the engine needs further study.

Although precise information was not available for the lubricating oil film thickness and the Henry Constant for the fuel oil film combination, it can be concluded that the minimum oil thickness compatible with adequate cylinder lubrication and an oil structure such that its Henry Constant is large will contribute to reduced HC emission.

References

Allen *et al.* DG (1975) Prediction of Piston Ring Cylinder Bore Oil Film Thickness in Two Particular Engines and Correlation with Experimental Evidence. IMechE Conference on Piston Ring Scuffing, London

Blint RJ, Bechtel JH (1982) Hydrocarbon Combustion near a Cooled Wall. SAE 820063.

Carrier G, Fendell F, Feldman P (1981) Cyclic Absorption / Desorption of Gas in a Liquid Wall Film. Combust. Sci. Technol., 25

Chigashi S, Hamamoto Y, Kizima A (1971) Effects of Turbulence on Flame Propagation in a Closed Vessel. Bull JSME, 14

Daniel WA (1957) Flame Quenching at the Walls of an Internal Combustion Engine. 6th International Combustion Engine

Daniel WA (1967) Engine Variable Effects on Exhaust Hydrocarbon Composition (A Single Cylinder Engine Study with Propane as the Fuel). SAE 670124, SAE Transactions 76

Dent JC, Lakshminarayanan PA (1980) Lean Burn Spark Ignition Engine combustion Modelling and Experiments. Symposium on Research in Internal Combustion Engines in UK Universities and Polytechnics, Kings College, London

Dent JC, Lakshminarayanan PA (1983) A Model for Adsorption and Desorption of Fuel Vapour by Cylinder Lubricating Oil Films and its Contribution to Hydrocarbon Emissions, SAE 830652

Ferguson CR, Keck JC, Oforah O (1976) A Theoretical Investigation on the Effects of Mixture and Flow Non-uniformities on Spark Ignition Engine Combustion. US Dept of Transportation, Interim Report, June

Hamamoto YH, Wakisaka T, Chigashi (1976) Limits of Flame Propagation in Spark Ignition Engines Behaviour of Flames and Exhaust Emissions. 16th FISITA Congress, Tokyo

Hires SD, Tabaczynski R, Novak JM (1978) The Prediction of Ignition Delay and Combustion Intervals for a Homogeneous Charge Spark Ignition Engine. SAE 78032, SAE Transactions 87

Kaiser EW, Adamczyk AA, Lavoie GA (1980) The Effect of Oil Layers on the Hydrocarbon Emissions Generated During Closed Vessel Combustion. 18th International Symposium on Combustion

Kaiser EW, Lorusso JA, Lavoie GA, Adamczyk AA (1982) The Effect of Oil Layers on the Hydrocarbon Emissions from Spark Ignited Engines. Combust. Sci. Technol., 28

Kreith F (1960) Principles of Heat Transfer. International Textbook Co., Scranton

Lakshminarayanan PA and Dent JC (1982) Generalised Procedure for Flame and Combustion Chamber Surface Determination in Spark Ignition Engines. SAE Paper 821223

Lakshminarayanan PA, Janakiraman PA, Gajendra Babu MK and Murthy BS (1979a) An Ultrasonic flow meter for measurement of Gas Velocity and Temperature in intake and exhaust of an Internal Combustion Engine. SAE Transactions, 790689

Lakshminarayanan PA, Janakiraman PA, Gajendra Babu MK and Murthy BS (1979b) New Instrumentation Technique for the study of unsteady Gas Exchange Process in engine Manifolds, Spring Meeting, Central States Section, The Combustion Institute, Apr 9–10, Columbus, Indiana

Lakshminarayanan PA, Janakiraman PA, Gajendra Babu MK, Murthy BS (1979c) Measurement of pulsating temperature and velocity in an internal combustion engine using an ultrasonic flow meter. Journal of Physics, E: Scientific Instruments 12, 1053–1058

Lakshminarayanan PA, Janakiraman PA, Gajendra Babu MK, Murthy BS (1979d) Prediction of Gas Exchange Processes in a Single Cylinder Internal Combustion Engine. SAE 790359

Lakshminarayanan PA, Nayak N, Dingre SV, Dani AD (2002) Predicting Hydrocarbon Emissions From Direct Injection Diesel Engine ASME paper

Lavoie GA (1982) Personal Communication

Lavoie GA, Lorusso JA, Adamczyk AA (1980) Hydrocarbon Emissions Modelling for Spark Ignition Engines. Symposium on Combustion Modelling in Reciprocating Engines, General Motors Research Laboratories, Nov 1978. Plenum Press, London

Lavoie GA, Blumberg PN (1980) A Fundamental Model for Predicting Fuel Consumption NO and HC Emissions of the conventional Spark Ignition Engine. Combust. Sci. Technol., 21
Lorusso JA, Kaiser EW, Lavoie GA (1981) Quench Layer Contribution to Exhaust Hydrocarbons from a Spark Ignited Engine. Combust. Sci. Technol., 25
Schlichting H (1955) Boundary Layer Theory. Pergamon Press, London
Sherman RH and Blumberg PN (1977) The Influence of Induction and Exhaust Processes on Emission and Fuel Consumption in the Spark Ignited Engine. SAE 770880, SAE Transactions 86
Spalding DB (1963) Convective Mass Transfer. Edward Arnold, London
Wentworth JT (1968) Piston and Ring Variables Affect Exhaust Hydrocarbon Emissions. SAE 680109, SAE Transactions 77
Woschni G (1967) A Universally Applicable Equation for the Instantaneous Heat Transfer Coefficient in the Internal Combustion Engine. SAE 670931, SAE Transactions 76

12 Smoke from DI Diesel Engines

Abstract Although DI Diesel engines are becoming popular because of their fuel economy as well as low exhaust emissions, they emit higher amount of visible exhaust termed as smoke. The characterization of this smoke has remained a challenge in engine development and modelling work. A new phenomenological model is explained in this chapter encompasses the spray and the wall interaction by a simple geometrical consideration. A dimensionless factor was introduced to take care of the nozzle hole manufactured by hydro-erosion (HE) as well as the conical shape of the nozzle hole (k-Factor) in case of valve-closed-orifice type of nozzles. The smoke emitted from the wall spray formed after wall impingement is the major contributor to the total smoke at higher loads. As the fuel spray impinges upon the walls of the combustion chamber, its velocity decreases. This low-velocity jet contributes to the higher rate of the smoke production. Therefore, the combustion bowl geometry along with injection parameters plays a significant role in the smoke emissions. While considering the smoke, interestingly the chemical kinetics, which is very fast compared to the mixing phenomenon in the spray entraining the surrounding air, is dropped. In addition, the thesis considers the mixing at the wall in detail. The latter enables explanation of sudden rise in the rate of increase in smoke at about 50% load for many types of engines at different speeds. Therefore, smoke, the result of incomplete combustion (chemistry) has been treated by ignoring the fast chemistry, as the slow physical mixing seems to be controlling. Though it appears paradoxical, it is the truth. There are mainly two types of smokes from a DI diesel engine, cold and hot smoke. Cold smoke is white in appearance under direct illumination, consisting of a mixture of fuel and lubricating oil particles in an un-burned or partly burned state. This form of smoke is sometimes referred to as liquid smoke or fog. Hot smoke is black in appearance, consisting of solid particles of carbon from otherwise complete combustion of fuel. This form of smoke is often referred as hot or solid smoke. In the present work, the study is focused on black smoke coming out of diesel engine under hot conditions.

Khan *et al.* (1973) first presented a model for the prediction of soot related to engine operating condition. Hiroyasu and Kadota (1976) proposed a two-step semi empirical model and applied it to the multi-packet combustion model. Later on, the model was extended up to a simple three-dimensional model (Nishida and Hiroyasu 1989). However, this model lacked generality and required adjustment of a number of constants.

Fusco *et al.* (1994) developed a phenomenological soot model consisting of an eight-step mechanism. They proposed that either pyrolysis of fuel could result in soot precursor radicals or growth species with possibilities of oxidation at

P.A. Lakshminarayanan and Y.V. Aghav, *Modelling Diesel Combustion*, Mechanical Engineering Series, DOI 10.1007/978-90-481-3885-2_12,

intermediate stages. Although this model is more detailed, it requires tuning of as much as 21 empirical parameters.

Magnussen *et al.* (1976) carried out experimental investigation on steady state free diffusion flames and developed combustion model based on k-ε model for turbulence. Special attention was given to soot formation and combustion in turbulent flames and it was concluded that soot was formed and contained in the turbulent eddies within the flame and that the burn up of the soot was related to the dissipation of turbulence. Dec and Tree (2001) investigated interactions of combusting fuel jet free in air and at the wall in a diesel engine using laser diagnostics. They found that soot deposition on the wall and blow-off are not the major contributors to engine-out soot emissions. In this view, Dent's work (1980) was unique. The importance of turbulent energy dissipation rate on smoke in diesel engines was identified quantitatively. The turbulent mixing rate was correlated with smoke for a quiescent chamber diesel engine.

There is a principal mathematical problem in the modelling of the engine-out soot emissions by using formation and oxidation methodology (Stiesch 2003). Usually, at least 90% and often 99% of the formed soot becomes oxidized with a minute fraction remaining in the exhaust gas. Since the soot mass in the exhaust is the very small difference between two nearly equal quantities i.e. between formation and oxidation, a significant error will result if only a small deviation in either the production or the formation rate.

In this chapter, the applicability of Dent's correlation (1980) to explain mixing controlled diesel combustion is explored. Finally, a model (Aghav *et al.* 2005, 2007a) that clearly distinguishes the free jet and wall jet regimes of a diesel-engine spray and their turbulence structure is developed to explain the smoke. This model avoids the mathematical difficulty of finding the difference between two large and nearly equal integrals.

Phenomenon of Soot Formation

In a conceptual sketch of a steady open turbulent flame, all the fuel injected go through vaporization process during ignition delay and then is converted into soot, Fig. 12.1. The simplest description for a burning spray is the model where the products of combustion exist outside a thin mantle of flame and the fuel-rich mixture remains unburned inside it. Many flamelets are formed at the peripheral mantle of the combusting spray.

Most of this soot will be oxidized at the surface of flame depending on the level of turbulence. The average size of a flamelet could be equated to the Taylor's microscale, ℓ_m. This scale defines the size of the mixing field. However, some of the soot escapes through the gaps that are scaled by viscosity and the high frequency components of turbulence between these eddies. The Kolmogorov length scale, η describes the gap between adjacent flamelets. This description is also applicable to

the fuel spray in an engine; however, the wall impingement needs to be considered, as it results in loss of turbulent kinetic energy that is necessary for oxidation. Most of this soot will then be oxidized at the periphery of the spray. The soot escaping can be estimated by calculating flow through the holes scaled by the Kolmogorov length scale during a characteristic time as follows (Aghav *et al.* 2005).

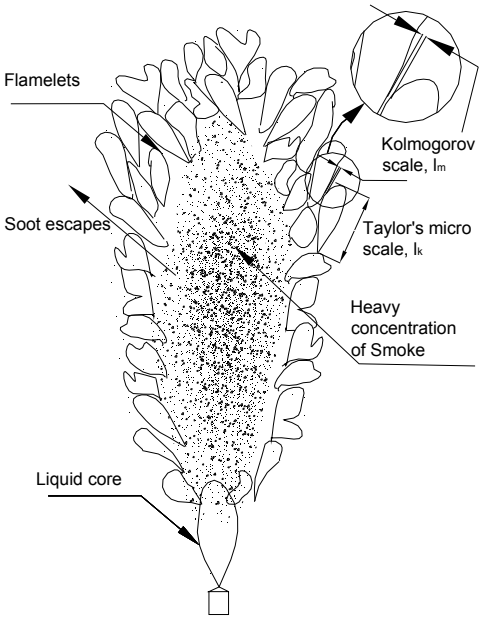

Fig. 12.1 Conceptual cross section of turbulent flame indicating the soot path

$$Soot = \left(\frac{u_{inj} A_h n_h A_s \, t_{int} \rho_s}{V_{air}} \right) \tag{12.1}$$

Where,

$Soot$ = Soot in mg/m^3

A_h = Area of holes for the escape of soot, function of Kolmogorov scale,η $\pi \, \ell_m \eta$

n_h = Number of soot holes per unit surface area

A_s = Surface area of the spray

t_{int} = Time scale for integration of smoke passing through holes of size given by Kolmogorov scale

u_{inj} = Average velocity of sprays, $\dfrac{m_f}{C_d A_o n_o t_{dur}}$

A_0 = Effective area of nozzle hole, $\dfrac{\pi d_o^2 \left(1 + N_f\right)}{4}$

N_f = Nozzle feature, %HE or KF e.g. 10%, 15%, etc.

The nozzles holes are defined as some base orifice size with %HE. The sample calculation is given in the Appendices IX and X

d_o = Diameter of the basic nozzle hole

t_{dur} = Injection duration

V_{air} = Volume of air sucked in per cycle

ρ_s = Density of soot, 2,000 kg/m^3

The features of the nozzle hole namely hydro-erosion, HE and k-Factor, KF used in the above equations are explained in the Appendices IX and X (Kampmann 1996).

Smoke is modelled to form instantaneously inside the spray, as the chemical reaction rates are too high compared to the physical rate of diffusion of the smoke at the peripheral surface of the spray. The phenomenological model, therefore, neglects chemical reaction and emphasizes the physical phenomenon.

In turbulent sprays, the liquid droplets are not only decelerated and deformed by the gas phase, but an additional dispersion and some diffusion of the liquid phase can be observed that is caused by the turbulent eddies in the gas flow. On an average, the random orientation of the turbulent velocity fluctuations leads to a quicker, more homogenous dispersion of the liquid droplets than in a laminar gas flow. At the same time, the momentum transfer between gas and liquid moderates the turbulent level within the gas phase. In turbulent sprays, typically a particle is assumed to interact with an eddy for a period taken as the eddy-life time, t_{int} (Stiesch 2003). This period is also considered as the time scale of integration.

$$t_{\text{int}} = \frac{C^{3/4}}{\sqrt{\frac{2}{3}}} \frac{k}{\varepsilon} \tag{12.2}$$

Where, Cu = Stiesch (2003) constant = 0.09

ε = Turbulent kinetic energy dissipation rate

$k = \left(\dfrac{3}{2} u_{inj}^2\right)$ = Turbulent kinetic energy

Though the above equation is only true for an isotropic flow, which is not the case at the spray envelope, for brevity it is assumed uniform all over the surface by considering a mean time, t_{int}. It is hypothesized as the mean time scale for the two types of spray e.g. free and wall sprays and the favourable comparison presented later validates such a bold assumption.

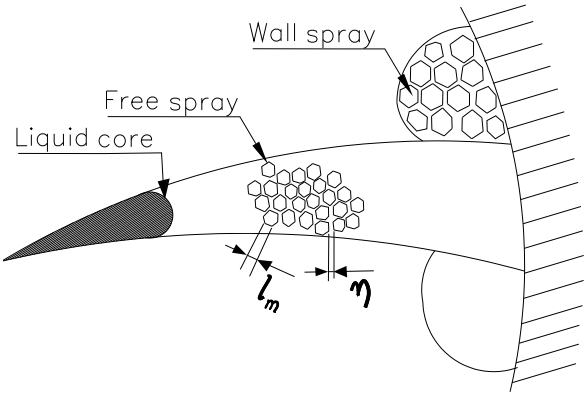

Fig. 12.2 Free jet fuel spray and subsequent wall jet under engine conditions

Application to Engine Conditions

To derive the concept equation (12.1), a steady open non-growing turbulent flame is considered. For simplicity, there is no liquid or wall jet considered (Fig. 12.1). Therefore, only the time scale of integration, tint is considered. However, in case of the engine sprays, there are a liquid phase, a free growing spray and a growing wall jet, which are happening one after another (Fig. 12.2). Initially, the free spray would grow up to wall with a conical shape. Then, the spray penetrates along a flat wall and it is modeled to spread equally in all radial directions. The tip of the spray would form a surface of a right circular cylinder. This model simplifies the complicated combustion cavity wall to a flat plate perpendicular to the spray axis. The liquid phase is not considered to be contributing to soot. The free growing spray is considered as a frustum of cone up to the wall impingement on the wall. The soot is estimated within integration limits of t_{liq} to t_{imp}. The following equation considers growing surface area of this free spray as time marches until wall impingement occurs.

$$Soot_{free} = \int_{t_{liq}}^{t_{imp}} u_{inj} A_h n_{h_{free}} \rho_s dt \tag{12.3}$$

If wall impingement occurs then soot is estimated from the free spray as well as the wall jet. During this period, the wall jet grows along the wall, while the free portion of the jet remains static as a cone up to the wall. The portion of the smoke from the free spray is modelled as a frustum of static cone.

$$Soot_{freestate} = \int_{t_{imp}}^{t_{imp}+t_{int}} u_{inj} A_h n_{h_{free}} \rho_s dt \tag{12.4}$$

The soot emitted from the growing wall spray can be estimated as below.

$$Soot_{wall} = \int_{t_{imp}}^{t_{imp}+t_{int}} u_{wall} A_h n_{h_{wall}} \rho_s dt \tag{12.5}$$

The duration of integration, t_{int} used in equations (12.4) and (12.5), is explained earlier in equation (12.2). After soot escapes from spray boundaries, no burnout of soot is considered to take place. Finally, the soot emitted from the free and wall portions of all the sprays are summed up to arrive at total soot in mg/m^3 by using the following equation.

$$Soot_{all} = \frac{(Soot_{free} + Soot_{freestat} + Soot_{wall})n_o}{V_{air}} \tag{12.6}$$

Where,

A_h = Area of soot hole

$n_{h_{free}}$ = Number of smoke holes for free portion

$$= \left(\frac{A_{s_{con}}}{A_{s_\ell}} \right)$$

$A_{s_{con}}$ = Surface area of spray considering cone

A_{s_ℓ} = Area of Taylor microscale

$n_{h_{wall}}$ = Number of smoke holes for wall portion

$$= \left(\frac{A_{s_{ci}}}{A_{s_\ell}} \right)$$

$A_{s_{cir}}$ = Circular surface area of spray at the wall

t_{liq} = Time for which spray is liquid

t_{free} = Time for which spray is free

t_{imp} = Time at which impingement starts

A_{sw} = Surface area of wall spray

u_{wall} $= 0.75\sqrt{\frac{u_{inj}\ d_e}{t_{imp}}} =$ Velocity of wall jet

d_e = Equivalent diameter of spray hole

The total soot estimated is converted to Bosch Smoke Unit (BSU) by using the MIRA correlation (1965), because BSU of smoke is selected for comparison with the experimental data for validation. The main inputs are the maximum injection pressure, the engine airflow, the geometry of the nozzle spray and the cavity shape. The impingement parameters are estimated using the geometry and the equations of spray: penetrations (Aghav *et al.* 2005, Lakshminarayanan *et al.* 2002).

Correlating smoke: phenomenon with spray characteristics

The important engine parameters needed for smoke calculation are collected from the experimental engine under different load and speed conditions, Table 3.2 for engines A9, B10, C12 … P12. Most of the data are related to the fuel injection system and combustion cavity (Fig. 12.3). At all these test points, smoke data are collected for the analysis.

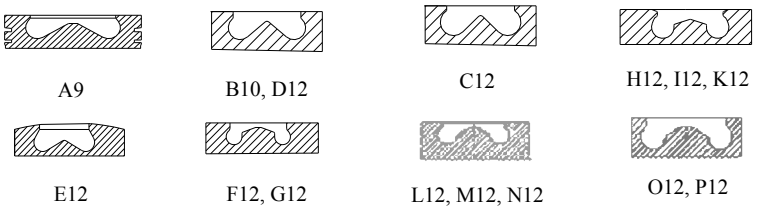

Fig.12.3 Combustion chambers

Concept of turbulent dissipation rate turbulent mixing and smoke

The turbulent energy dissipation rate ε can itself be used to define length, time and velocity scales associated with the small-scale dissipative structure of turbulent motion. *Kolmogorov* defined this smallest time scale of turbulence as

$$\tau = \left(\frac{\nu}{\varepsilon}\right)^{\frac{1}{2}} \tag{12.7}$$

Where,

τ = *Kolmogorov* time scale
ν = Kinematic viscosity of air
ε = Turbulent kinetic energy

Dent (1980) evaluated these scales in the context of quiescent chamber engine. The turbulent energy dissipation can be expressed as

$$\varepsilon = \frac{\gamma P_{inj} 6N}{\rho_f \theta_{ip}} \tag{12.8}$$

The overall dissipative mixing rate can be written as follows.

$$\frac{1}{\tau} = \left(\frac{C}{v^{0.5}}\right)\left[\frac{N}{\theta_{ip}}\right]^{1.5}\left[\frac{Q}{nd_o^2}\right] \tag{12.9}$$

where,

P_{inj} = Injection pressure

$$= const\left(\frac{6NQ}{\theta_{ip} n d_o^2}\right)^2$$

N = Engine speed, rpm

n = Number of spray holes

d_O = Spray hole diameter, m

θ_{ip} = Duration of injection, deg CA

Q = Injected quantity per stroke

ρ_f = Fuel density

When this concept is applied was applied for a smaller sized experimental engine C12 then the results showed two distinct regimes (Fig. 12.4). The two regimes could be identified as spray with and without wall impingement. Wall impingement of spray results in slower combustion rate due to loss of turbulent kinetic energy (Assanis *et al.* 1999).

To study the role of wall impingement, a factor, degree of impingement, is defined as

$$deg_{imp} = \left(1 - \frac{t_{imp}}{t_{dur}}\right) \times 100 \tag{12.10}$$

Where, deg_{imp}= Degree of impingement

t_{imp}= Time at which impingement starts

t_{dur}= Duration of injection

When impingement starts, the degree of impingement is 0%. There is no impingement when this value is negative and there is impingement when this value becomes positive. The estimation of impingement time is explained in detail in the Appendix VIII. Smoke values were plotted against degree of impingement for the smoke data of the experimental engine with bore less than 125 mm (see Fig. 12.5). This graph shows two distinct zones and relations. Before impingement starts, there is a linear correlation between smoke values and degree of impingement. This correlation becomes parabolic once impingement starts. This graph signifies a large contribution of impingement to the smoke emitted through exhaust. Therefore, it is necessary to incorporate this phenomenon during development of new model for better predictions.

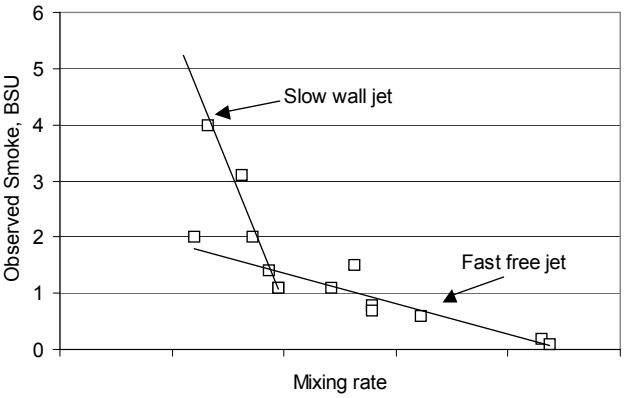

Fig. 12.4 Exhaust smoke against mixing rate

At all the experimental points, the smoke values were predicted using the new model that considers the effective turbulent energy at the spray surface for burning of smoke generated inside the spray. The main inputs are the maximum injection pressure, the engine airflow, the geometry of the nozzle spray and the cavity shape. The impingement parameters are estimated using the geometry and the equations of spray penetrations (Lakshminarayanan *et al.* 2002, Lakshminarayanan and Dent 1983).

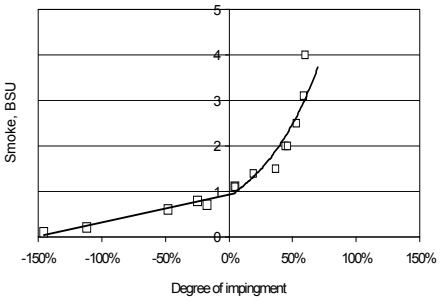

Fig. 12.5 Smoke values at different loads against degree of impingement, Engine C12

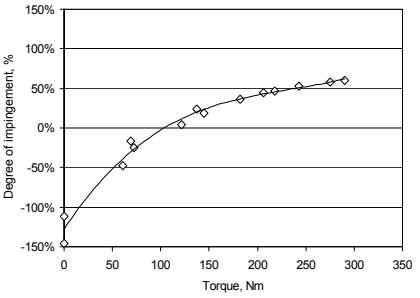

Fig. 12.6 Predicted and observed smoke, Engine C12

Then, the duration of integration is evaluated using the density of turbulent energy supplied by the fuel sprays (Stiech 2003). The fuel sprays were divided into free and wall jets and the smoke is evaluated from these jets separately and added together to obtain the total smoke in the exhaust. The results of the model highlighted that above brake torque of 100 Nm, the spray impingement was predominant for the experimental engine at all the speeds (Fig. 12.6). The predicted results are summarised in Table 12.1.

Table 12.1 Predicted results, Engine C12

Data point	Impingement time	Degree of impingement	Smoke, BSU		
	Deg CA	%	Free portion	Wall portion	Total
1	10.78	53	0.5	1.5	2.1
2	11.4	37	0.6	0.4	1
3	13.69	4	0.8	0	0.8
4	14.22	–48	0.5	0	0.5
5	14.81	–146	0.1	0	0.1
6	7.83	58	0.6	2.5	3.1
7	8.51	44	0.6	0.8	1.5
8	9.11	24	0.7	0.2	0.8
9	9.25	–17	0.7	0	0.7
10	9.4	–112	0.1	0	0.1
11	6.37	60	0.6	2.9	3.5
12	7.27	46	0.7	1.1	1.8
13	7.34	19	0.7	0.1	0.8
14	7.34	–24	0.6	0	0.6

In Fig. 12.7, the observed as well as predicted smoke values for all the data points are plotted against brake torque. Although the predicted values are slightly lower than observed, both the curves indicate similar trend rising along torque. The study using the new phenomenological smoke model indicated favourable comparison over a wide range of smoke values with regression coefficient of 0.98 with slope near to one for one engine (Fig. 12.8).

Then the remaining engines were considered for model application. The investigations were limited to the operating conditions of the engines with single injection and no exhaust gas recirculation. Parameters related to the engine performance and fuel injection system were collected simultaneously along with the smoke. In Fig. 12.9, the observed smoke was plotted against the speed, for engines of variable speed applications. Here, rising trend of smoke is indicated as speed reduces. These engines are sufficiently fuelled at lower speeds to derive higher torque at lower speeds, hence are working at lower air-fuel ratios. Similarly, at a constant engine speed, as the load increases, the smoke increases (Fig. 12.10). The slope of the curve changes at about 50% load.

The increase in smoke with increase in load is seen to be less significant when the engine runs at high speed, compared to the drop in smoke at the same load, when the engine runs at a low speeds. This can be attributed to the higher air-fuel ratio and turbulence level at higher speeds. The correlation of smoke with method of aspiration and brake mean effective pressure met with little success (Fig. 12.11).

The smoke reduces as the injection pressures and air-fuel ratio increase; however, the correlation is not satisfactory (Figs. 12.12 and 12.13).

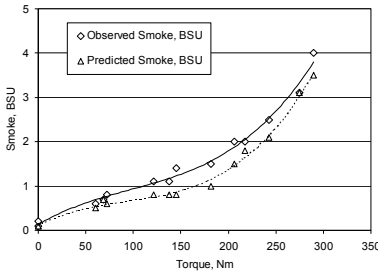

Fig. 12.7 Smoke versus torque, Engine C12

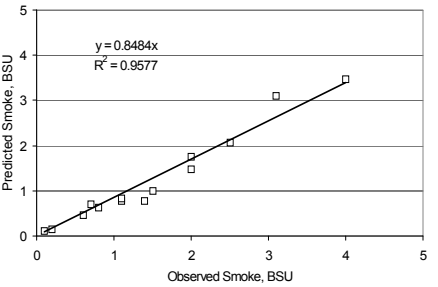

Fig. 12.8 Predicted versus observed smoke, Engine C12

To evaluate the effect of impingement, the observed smoke was plotted against the degree of impingement, Fig. 12.14, where the degree of impingement is defined as the ratio of time after wall impingement to the total duration of injection. There is no impingement when this value is negative and there is impingement when this value becomes positive as explained earlier in this chapter. The smoke increases as the impingement increases. The effect of the wall-jet on the smoke emission due to abrupt loss of turbulence at the wall, therefore, seems to be more important than that of injection pressure or air-fuel ratio. The wall effect was given less importance in phenomenological models for smoke, published earlier (Dent and Mehta 1981, Hiroyasu *et al.* 1983). Beyond 50% load, wall impingement is the important parameter in heavy duty DI diesel engines. Therefore, the new model presented earlier in this paper, which considers these two effects namely wall effect and turbulence effect, has better prediction capability.

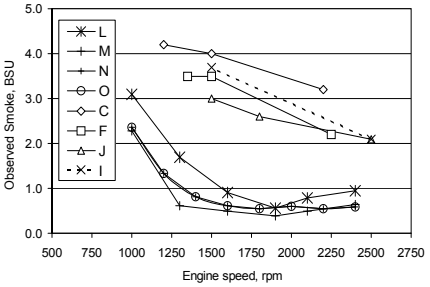

Fig. 12.9 Observed smoke along full throttle for different engines

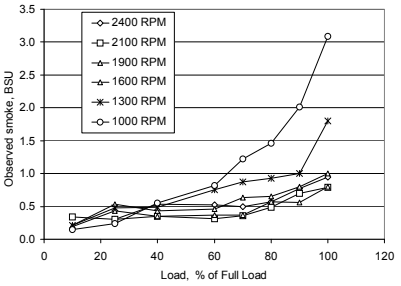

Fig. 12.10 Observed smoke at part loads at different speeds, Engine L12

Steady state conditions

Initially, the model was applied at full throttle condition of the engines of variable speed application. The predicted and observed smoke values of these engines were plotted against speed (Figs. 12.15 and 12.16). For the engine types I12, B10, F12 and L12 the predictions at full load follow both the magnitude and trend of the observed values. In case of engines M12, N12 and O12, the model slightly over-

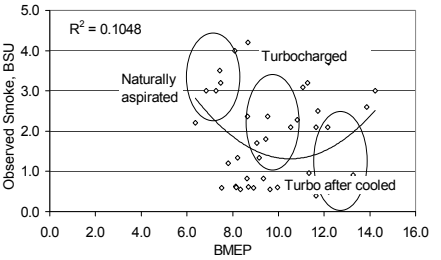

Fig. 12.11 Brake mean effective pressure and smoke

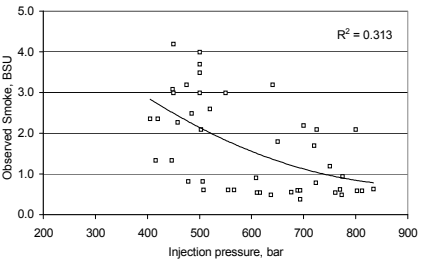

Fig. 12.12 Injection pressure and smoke

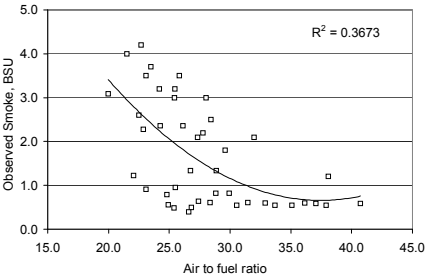

Fig. 12.13 Air to fuel ratio and smoke

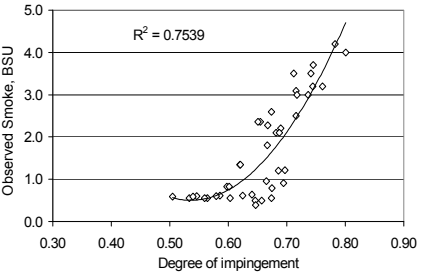

Fig. 12.14 Degree of impingement and observed smoke

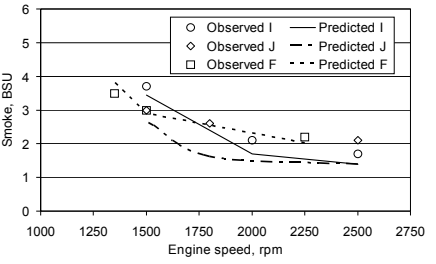

Fig. 12.15 Predicted and observed smoke, full throttle of engines I12, B10 and F12

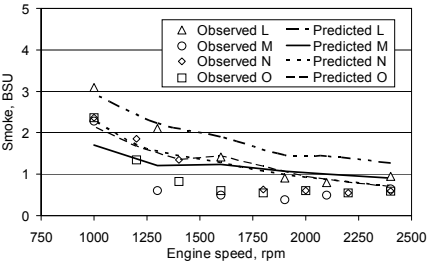

Fig. 12.16 Predicted and observed smoke, full throttle of engines L12, M12, N12, O12

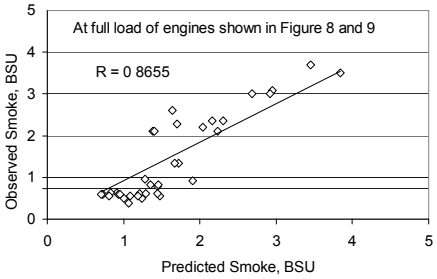

Fig. 12.17 Predicted and observed smoke, full load of I12, B10, F12, L12, M12, N12 and O12

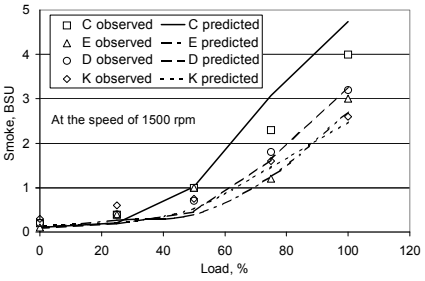

Fig. 12.18 Predicted and observed smoke, part loads of C12, E12, D12 and K12

predicts the smoke. The observed smoke was compared with predicted smoke, at all the data points of above engines in Fig. 12.17. Although there are some deviations, the overall regression coefficient is 0.87 for these points. These slight discrepancies are dealt with later in the discussion section. With increase in engine speed, the turbulence increases on the spray boundaries both in free spray and at the wall due to higher injection pressure of mechanical cam-driven injection equipment. This causes more complete burnout of smoke and hence the smoke decreases with increase in speed. The comparison of experiment and prediction is encouraging.

Then, the model was applied for typical part load conditions of engines at constant speed of 1,500 rpm. The predicted smoke values plotted against load is in close agreement with observed values (Fig. 12.18). The departure of the rate of increase in smoke with load at 50% load is correctly predicted. The rate at which the smoke increases with load is very small initially corresponding to when the spray is free and increases at a high rate after the spray impinges on the wall at higher loads. The smoke was also modelled at part throttle i.e., part load conditions for the engines of variable speed applications. The predicted values for each data point were compared favourably against the experimentally observed values (Fig. 12.19). The same trend of smoke at all speeds for different engine operating condition could be seen in Figs 12.20–12.24.

Finally, the predicted values of smoke were compared with all the observed values at different speeds and loads (Fig. 12.25). The observed regression coefficient is 0.89 with a slope of 0.88 represented by thick line. This study using the new smoke model indicated satisfactory comparison over a wide range of smoke values.

While the correlation between the observed smoke and the calculated smoke is good for a wide variety of engines, some deviations could be observed at full load for the on-road engines, M12, N12 and O12. These points are enclosed in ellipses. If these specific few points are considered as outliers, then the slope becomes close to 1.0 with regression coefficient tending to 0.95 represented by the dashed

line in Fig. 12.25. The possible causes for the deviation of computed smoke from the observed smoke values might be the lack of consideration of the reverse squish

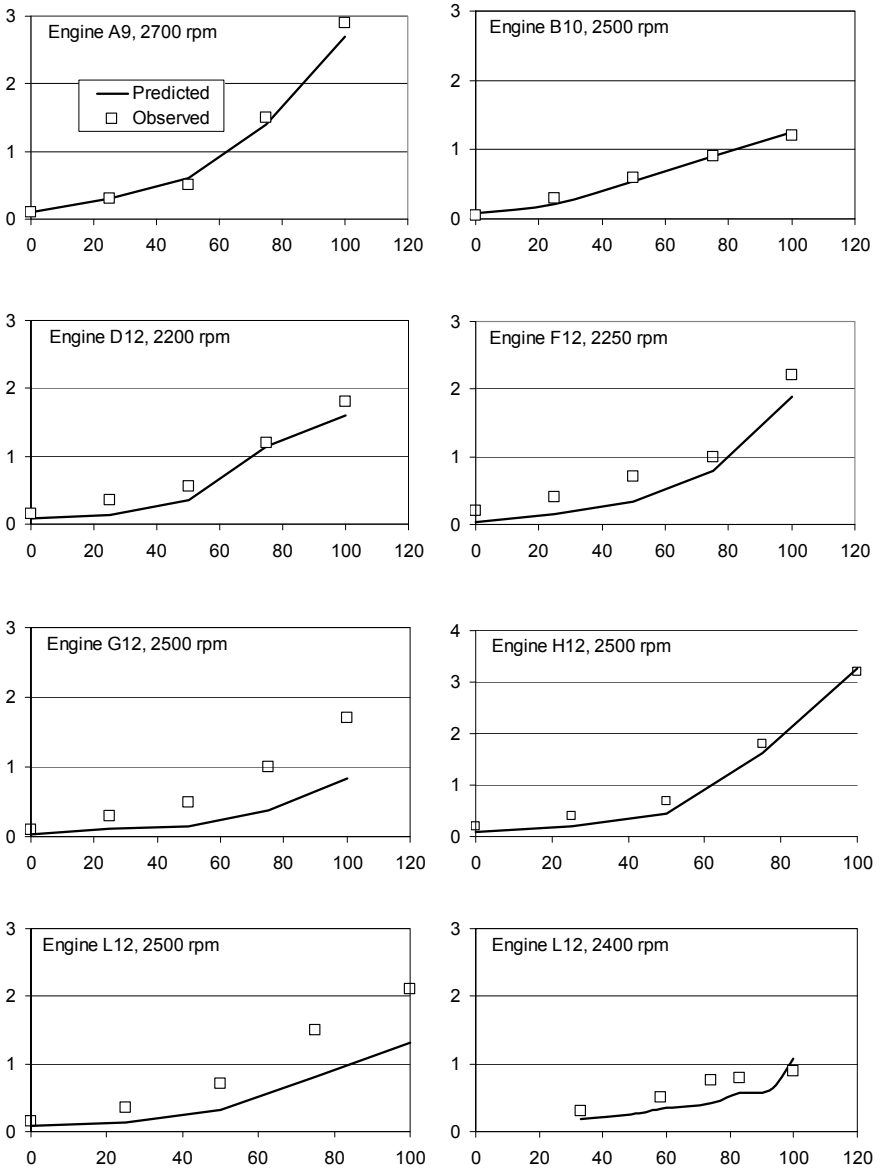

Fig. 12.19 Predicted (□) and observed (—) smoke versus % load for various engines at rated speed

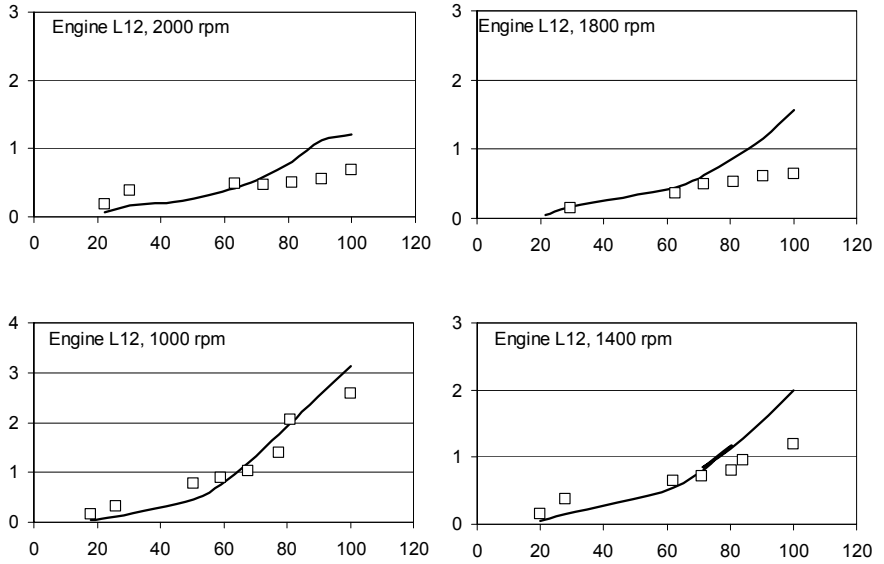

Fig. 12.20 Predicted (□) and observed (—) smoke versus % load for engine L12 at part loads

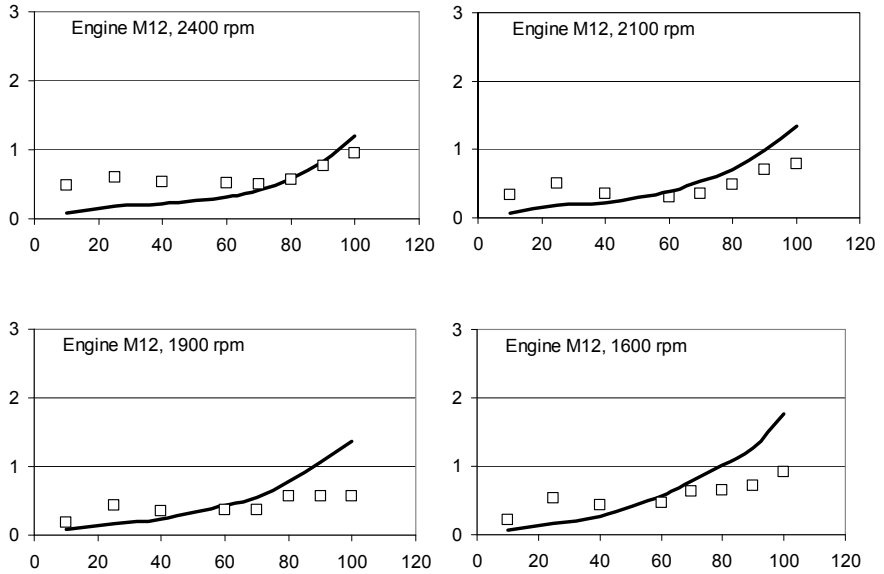

Fig. 12. 21 Predicted (□) and observed (—) smoke versus % load for engine M12 at part loads

and the complete profile of the cavity where spray impinges. The injector offset with respect to the cavity is also not considered which might change the degree of impingement and hence, the soot produced at the wall. In addition, the simplified model of a flat wall perpendicular to the spray axis is a reason for the differences observed between the experiment and the model. Thus, better understanding of the Kolmogorov scales at the wall will improve prediction capability of the model. The agreement between the experimental results and the theoretical results without any tuning of model-constants that are engine-specific makes the model a potentially useful tool for predicting the smoke emissions (Figs. 12.15–12.25).

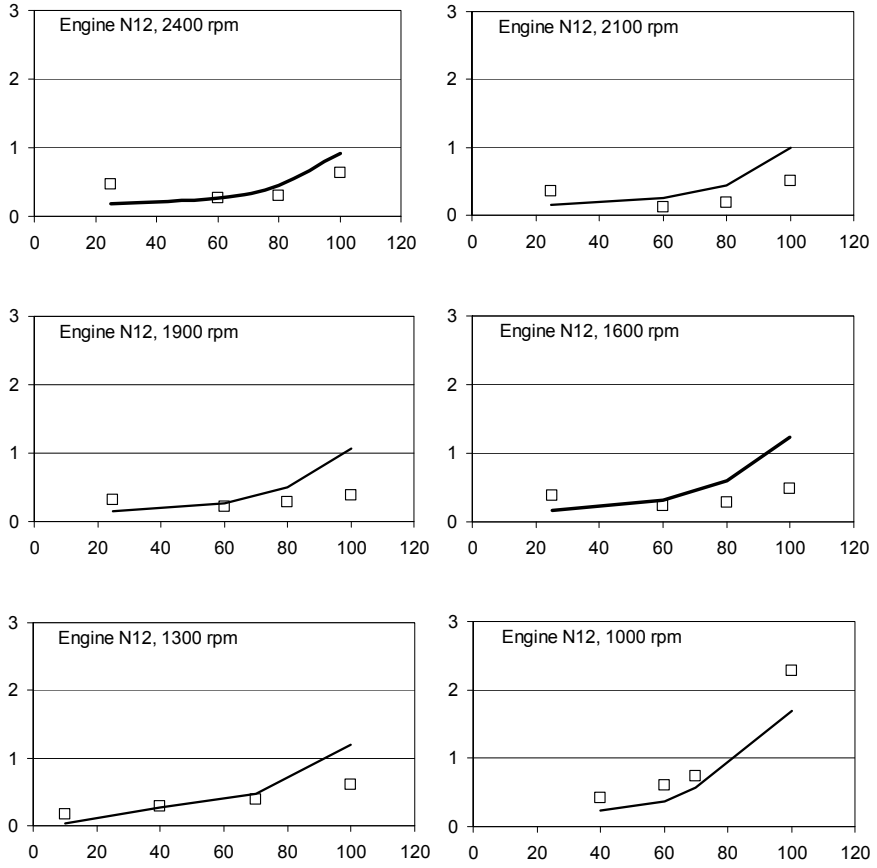

Fig. 12.22 Predicted (□) and observed (—) smoke versus % load for engine N12 at part loads

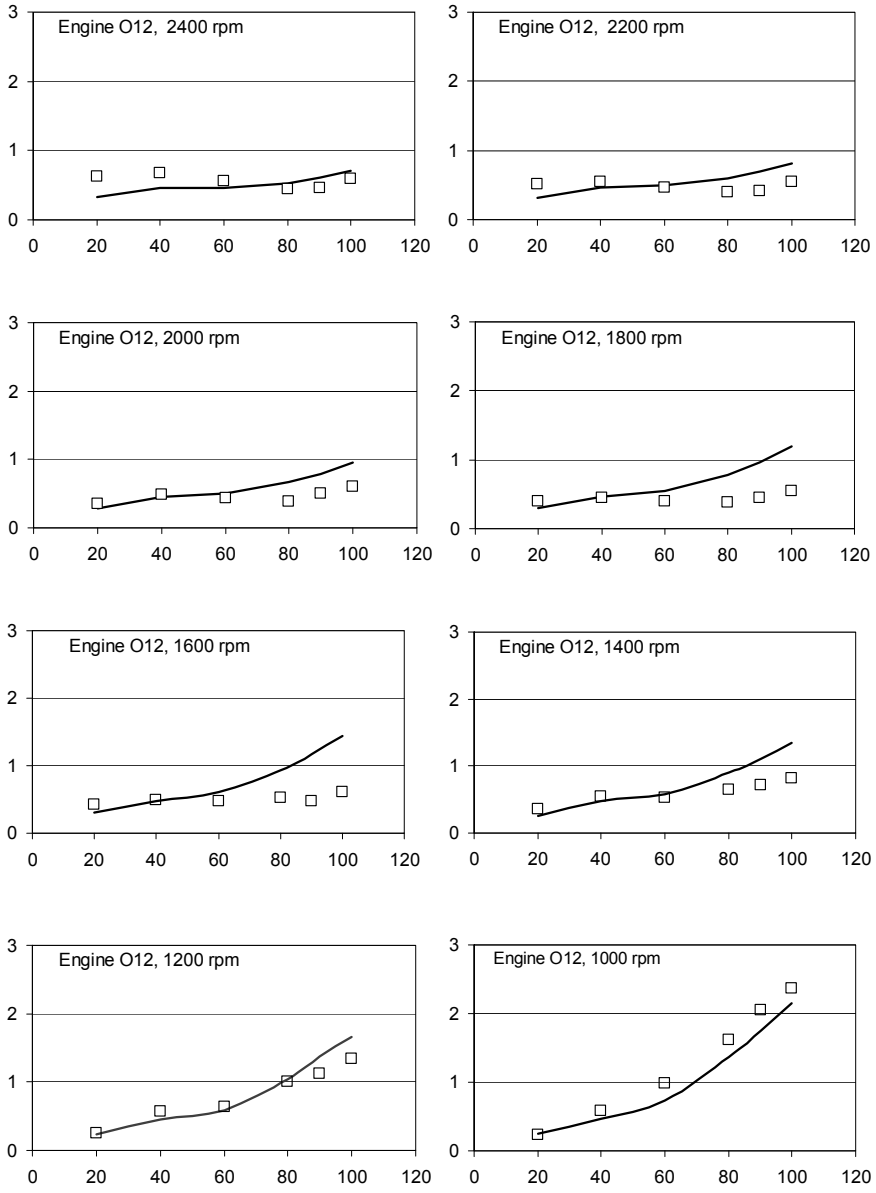

Fig. 12.23 Predicted (□) and observed (—) smoke versus % load for engine O12 at part loads

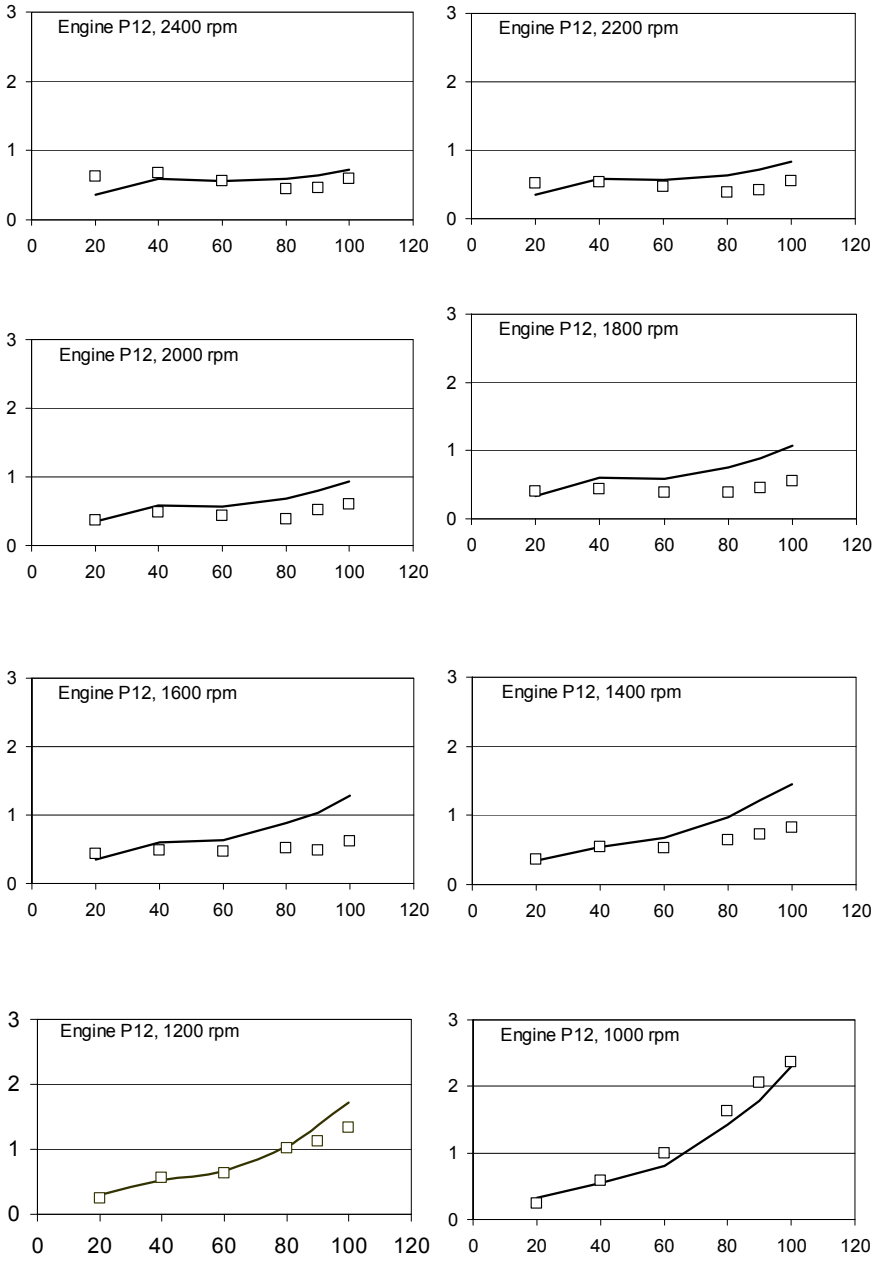

Fig. 12.24 Predicted (□) and observed (—) smoke versus % load for engine P12 at part loads

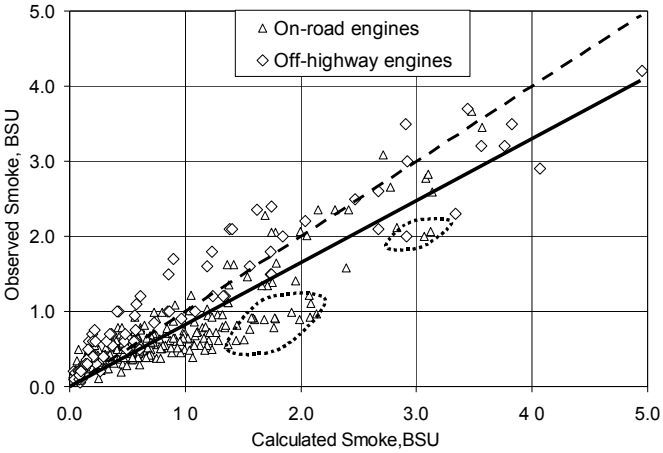

Fig. 12.25 Predicted and observed smoke for all engines (Table 4.1)

The comparison of the experimental data over the entire engine performance map at different loads and speeds is satisfactory, even though for some engines the differences are large. The previous phenomenological models found it difficult to predict even with many empirical constants adjusted for every given engine the following.

- The sudden change in the rate of increase in the smoke with increase in load at 50% load
- Gradual decrease with increase in speed

In the present attempt, no empirical constant to be fine-tuned for a given engine is used. The model rightly predicts the increase in smoke with load, due to the loss of turbulence at the wall and hence higher Kolmogorov scale that allows escape of smoke unburnt through the spray periphery. In addition, it shows the decrease in smoke with speed, due to better turbulence i.e., lower Kolmogorov scale at higher injection pressure at higher speeds in a jerk-type injection system. There are, however some limitations to the soot model in terms of the understanding pulsed injection, effect of squish and fuel type.

Benchmarking with well known smoke model

Explain the boost model here. Compared to the extremely complex 3-D models or the phenomenological soot model based on mixing-controlled combustion used in advanced software like AVL-Boost (2005), the present model focuses on the main physical phenomenon at the surface of the spray for a brief period of the life of the eddies. Figure 12.26 shows the comparison of observed smoke with the predicted smoke using this software and using the model described in this paper. The prediction of the trend of smoke behaviour by the present model with respect to load, especially above 50% load is more favourable than AVL-Boost. The present model could be extended to multi-jet and multiple injection common rail system,

which enhances the turbulence many times at the surface area of fuel sprat. By modelling the turbulence scale, it will be possible to predict lower smoke when such a fuel injection system is used.

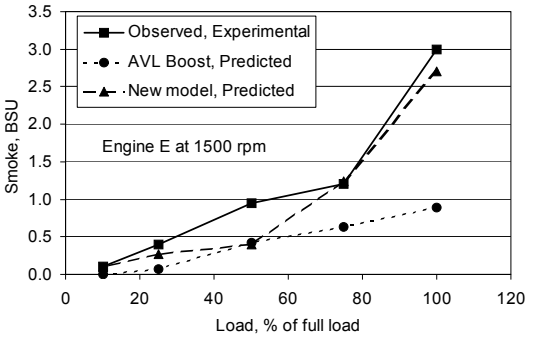

Fig. 12.26 Comparison of new model, AVL BOOST and experimental data, engine E12

Transient conditions

As compared to steady state working of diesel engine, the smoke emitted is more during the unsteady or transient operation mode i.e. free acceleration, full load acceleration etc. This is because of lack of sufficient air for the complete combustion of higher quantity of diesel injected to accelerate. In rapid acceleration, the engine speed increases after a time lag and remains a constant. This time delay is observed for smoke opacity also. A transient cycle could be considered as a sequence of quasi-stationary process with regards to particle formation since the combustion and injection characteristic times are short compared with the time scale for the change in engine conditions at transient running. Hence, the validity of the correlations at stationery conditions could be extrapolated to transient cycles.

A "free acceleration" test is specified in few emission standards (Ministry of Road Transport, India, 2004) where the accelerator pressed from low idle to high idle position and maximum smoke is recorded. Such a standard is evolved in such countries because the road infrastructure for the dense diesel vehicle traffic asks for frequent change of gears and engagement of clutch, leading to free acceleration of engines. A turbocharged engine was considered for this study as they suffer from higher smoke during free acceleration. The results of steady state and free acceleration were plotted against speed (Fig. 12.27). This shows that air-fuel ratio during free acceleration goes below steady state operation during certain range, which results in higher smoke values. They new model (Aghav *et al.* 2007a, b, Hulwan *et al.* 2007) was applied to certain points of low air fuel ratio (AFR) to predict the maximum smoke value. The predictions at specific points are in close agreement with experimental results (Fig. 12.28). The maximum values as well as the trend of smoke during transient condition are predicted satisfactorily with new model.

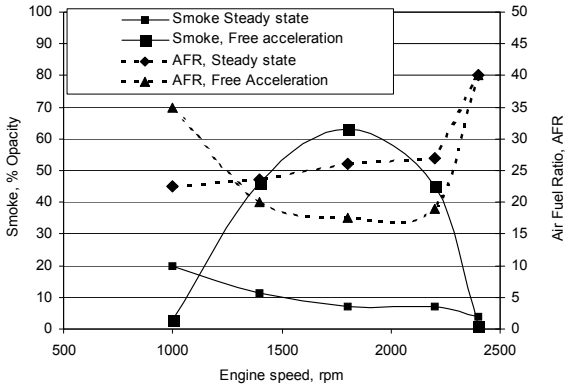

Fig. 12.27 Comparison of steady state and free acceleration smoke and AFR at various speeds, Engine B10

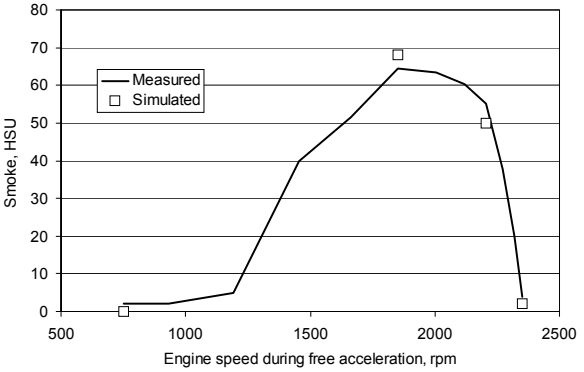

Fig. 12.28 Prediction for free acceleration smoke

References

Aghav YV, Lakshminarayanan PA, Babu MKG, Azimuddin, Dani AD (2007a) Validating newly evolved smoke model at widely varying operating conditions of DI diesel engine, GTP-06-1096, ASME Journal of Engineering for Gas Turbines and Power

Aghav YV, Sujeet V, Kumar MN, Thatte V, Babu MKG (2007b) Simulation of Turbocharged DI Diesel Engine during free Acceleration using AVL Boost. AVL Users International Conference, Graz

Aghav, YV, Lakshminarayanan, PA, Babu, MKG, Nayak, NS, and Dani, AD (2005), Phenomenology of Smoke from Direct Injection Diesel Engines. Paper No. 1350, Proceedings of ICEF2005, ASME

Assanis DN, Filipi ZS, Fiveland SB Syrimis M (1999) A Predictive Ignition Delay Correlation under Steady State and Transient Operation of a Direct Injection Diesel Engine. ASME-ICE Fall Technical Conference

AVL Boost 4.1 Users Guide (2005)

Dec JE, Tree, Dale R (2001) Diffusion-Flame/Wall Interactions in a Heavy-Duty DI Diesel Engine. SAE 2001-01-1295

Dent JC (1980) Turbulent mixing rate – Its effect on smoke and hydrocarbon emissions from Diesel Engines. SAE 800092

Dent JC, Mehta PS (1981) Phenomenological combustion model for a quiescent chamber diesel engine. SAE paper 811235

Fusco A, Knox-Kelecy AL, and Foster DE (1994) Application of a Phenomenological Soot Model to Diesel Engine Combustion. Third International Symposium COMODIA

Hulwan DB, Joshi SV, Aghav YV (2007) Smoke Prediction for Turbocharged DI Diesel Engine during free Acceleration. International Review of Mechanical Engineering, 1, N3, May

Hiroyasu H *et al.* (1983) Development and use of a spray combustion modeling to predict diesel engine efficiency and pollutant emissions. Bulletin of JSME, 26 No. 214

Hiroyasu, Kadota (1976) Models for Combustion and Formation of Nitric Oxide and Soot in Direct Injection Diesel Engines. SAE 760129

Kampmann, S, Dittus, B, Mattes, P, and Kirner, M (1996) The influence of hydrogrinding at VCO nozzles on the mixture preparation in a DI diesel engine. SAE 960867

Khan IM, Greeves G, Wang CHT (1973) Factors Affecting Smoke and Gaseous Emissions From Direct Injection Engines and a Method of Calculation, SAE 730169

Lakshminarayanan PA Dent JC (1983) Interferometric studies of vapourising and combusting sprays. SAE paper 830244

Lakshminarayanan PA, Aghav YV, Dani AD, Mehta PS (2002) Accurate prediction of the rate of heat release in a modern direct injection diesel engine. IMechE, 216, Journal of Automobile

Lyu M S, Shin BS (2002) Study of Nozzle Characteristics on the Performance of a Small Bore High Speed D. I. Engine. Int. J. Engine Research IMechE, 3 2

Ministry of Road Transport, India (2004) Free acceleration test, MoRTH/CMVR/TAP 115/116

Nishida K and Hiroyasu H (1989) Simplified three-dimensional modeling of mixture formation and combustion in a D.I. diesel engine. SAE paper 890269

Stiesch G (2003) Modelling engine spray and combustion processes, Springer

The Measurement of Diesel Exhaust Smoke (1965) Motor Industry Research Association MIRA Report

Users Guide, AVL Boost 4.1, 2005

13 Oxides of Nitrogen from Direct Injection Diesel Engines

Abstract Many models for prediction of emissions and combustion based on phenomenology of spray combustion for DI diesel engines are available in literature. All of them utilized empirical heat transfer correlation, which are mass averaged. Experimental observations from modern diesel engines of heavy-duty application showed that NO_x formation suppresses at higher loads although favourable conditions exists. A new phenomenological model for NO_x emission is developed based on mixing controlled combustion incorporating localized wall heat transfer. In this work, a phenomenological model for heat transfer from wall spray is also proposed which is employed along-with heat release model to account for effect of localized heat transfer. A simple geometrical relation is employed for the spray-wall interaction and subsequent turbulence structure for spray developed earlier by the authors. This model is one-dimensional and does not need any engine specific tuning. The newly evolved NO_x model takes into consideration all the engine operating parameters viz. engine speed, fuel injection pressure, intake air pressure, temperature and swirl number etc. The effects of Exhaust Gas Recirculation and Biodiesel on NO_x formation are also incorporated in this model. The new model was validated by conducting experimental investigations on six-engines at different operating conditions with widely varying features.

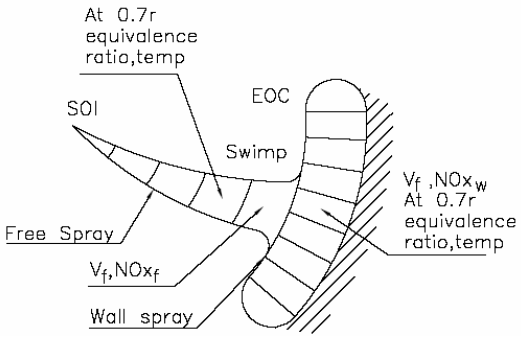

Fig. 13.1 Conceptual sketch of spray for NOx estimation

Most of the combustion takes place in diffusive mode in modern DI diesel engines. In present work, the concept of mixing controlled combustion model is applied to NO_x formation. NO_x is formed at the spray envelope only, and integrated over combustion duration and averaged over entire cylinder volume. The spray wall interaction is also observed especially at higher loads. The engine

P.A. Lakshminarayanan and Y.V. Aghav, *Modelling Diesel Combustion*, Mechanical Engineering Series, DOI 10.1007/978-90-481-3885-2_13,

spray is divided in a liquid core, a free growing spray and a growing wall jet (Fig. 13.1). The NO_x estimation is made for one spray on volume basis and multiplied by number of sprays to arrive at integrated value. The concept equation for NO_x formation is as follows:

$$NOx_{cycle} = \frac{\left(\int_{SOC}^{EOC} \sum_{i=1}^{i=n} V_{spray} NOx \right) \frac{N_o}{\rho_f} \left(\frac{dm_f}{d\theta} \right) t_{dur}}{V_{cyl}} \tag{13.1}$$

Here,

NOx_{cycle} = Cycle averaged NOx, ppm
V_{spray} = Spray volume
N_o = Number of holes
SOC =Start of combustion for each volume
EOC = End of combustion for each volume
$\frac{dm_f / d\theta}{\rho_f}$ = Rate of injection, mm^3/deg
t_{dur} = Combustion duration, sec
$\sum_{i=1}^{i=n}$ = Summation of n volumes of spray

At low to medium loads only free spray is formed. The volume of the free spray is split into five conical regions of equal length.

$$NOx_{free} = \frac{\left(\int_{SOI}^{EOC} \sum_{i=1}^{i=5} V_{free} \; NO_{x\,fi} \right) \frac{N_o}{\rho_f} \frac{dm_f}{d\theta} t_{dur}}{V_{cyl}} \tag{13.2}$$

Here,
SOI = start of injection
EOC = End of combustion

At higher load, the interaction of the spray with the wall is observed. The wall spray formed after impingement is also divided in five volumes of annular cylinders (Fig. 13.1).

$$NOx_{wall} = \frac{\left(\int_{SOI}^{EOC} \sum_{i=1}^{i=5} V_{wall} NO_{x\,wi} \right) \frac{N_o}{\rho_f} \frac{dm_f}{d\theta} t_{dur}}{V_{cyl}} \tag{13.3}$$

Here,

V_{free} = Sectional volume of wall spray volume

V_{wall} = Sectional volume of wall spray

SWI = Start of wall impingement

Finally, the NO_x formed in free and wall sprays are summed up to arrive at cycle NO_x.

$$NO_{x\,cycle} = \left(NO_{x\,free} + NO_{x\,wall}\right) \tag{13.4}$$

The equivalence ratio and flame temperature are estimated at 0.7 times radius as a representative for the different volumes of free and wall spray. The NOx in every volume is predicted as a function of equivalence ratio, Φ and flame temperature (Fig. 13.2) (Uyehara 1980).

$$NO_x = f(\Phi, t_{flame}) \tag{13.5}$$

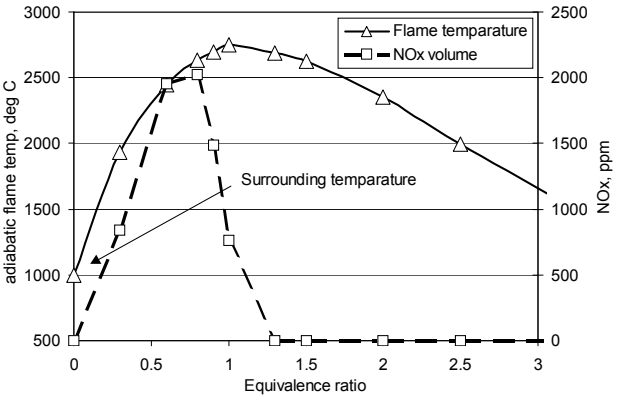

Fig. 13.2 Behaviour of NOx and flame temperature

The interactions between the spray and the wall are instrumental in rapid convective heat transfer. This heat transfer is also considered for estimation of NO_x by correcting temperature in different zones. Estimation of spray properties and heat transfer is described in Appendices VIII and XV. In engine environment, the fuel spray is dynamic and interaction with the wall can be observed especially at higher loads. Therefore, the fuel spray is divided in three sections: (a) the liquid core, (b) free spray, and (c) wall jet after impingement upon wall. The various phases of spray development are schematically shown in Fig. 13.3. Early phase the free spray grows until the wall of combustion chamber. Subsequently, it remains static and the wall jet develops. As soon as the injection ends, the tail of the spray starts moving and slowly the burnout of spray occurs.

Before detachment

In Fig. 3.10, notations of the free axisymmetric spray (Lakshminarayanan and Dent 1983) are shown, with profiles of concentration along the axis and radius. The virtual source of the evaporating jet is inside the orifice at a distance δ from the nozzle tip. Along the axis, the concentrations of fuel vapour decreases hyperbolically, Fig. 3.10, from the virtual origin where S is the distance from the mouth of the nozzle.

$$C_f(x) = 5.2\, C_{f_{noz}} \left[\frac{d_e}{S + \delta} \right] \tag{13.6}$$

Experiments have shown that the vapour concentration increases linearly from the virtual origin to a fixed position, S_{liq}, until the jet detaches. The distance can be considered as the length of the liquid core in the spray.

At any radius,

$$C_f(r,x) = C_{f_x} \exp\left\{ -203 \left[\frac{r_s}{S + \delta} \right]^{2.5} \right\} \tag{13.7}$$

$$\Phi = 14.7 \frac{C_f(r,x)}{1 - C_f(r,x)} \tag{13.8}$$

Along the radius, the distribution of the vapour concentration is Gaussian. However, near the core of the spray, the concentration is limited to the maximum vapour concentration described above (Fig. 3.10). Along the wall-spray the following correlation is employed

$$C_{f_{wall}} = 0.5 \frac{d_e}{S_{wall}} \tag{13.9}$$

$$\Phi = 14.7 \frac{C_{f_{wall}}}{1 - C_{f_{wall}}} \tag{13.10}$$

Where,

C_{f_x} = Vapour concentration along axis of free spray

δ = Virtual source, 2.3 d_e

S_{liq} = Liquid core, 7 d_e

$C_{f_{noz}}$ = Vapour concentration at nozzle

$C_{f_{(r,v)}}$ = Vapour concentration at any position in free spray

Φ = Equivalence ratio, the ratio of chemically correct (stoichiometric) fuel-air ratio to actual fuel-air ratio

r_s = Radius of spray

$C_{f_{wall}}$ = Vapour concentration along wall spray

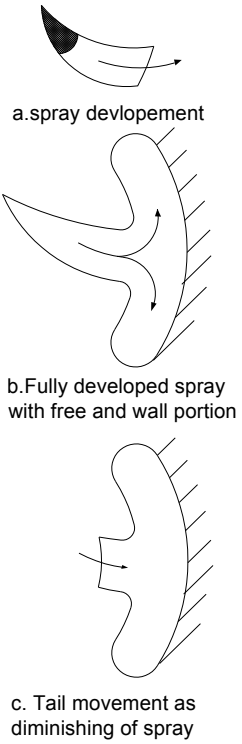

Fig. 13.3 Main events during development of engine spray

After detachment

After end of injection, the tail of spray also penetrates similar to the tip of the jet, however slowly. The jet-like structure is still maintained, and turbulent mixing occurs entraining air into the jet like plume, but packets of fuel are not replenished by the nozzle. Therefore, regions near the nozzle tip will be leaner than at the instant injection was complete. Sub-packets on the centreline will still move downstream at a faster rate than those near the edges of the plume. Furthermore, no appreciable increase in jet width was observed (Lakshminarayanan and Dent 1983).

Phenomenon of Heat Transfer

The convective mode of heat transfer plays a dominant role in modern DI diesel engines. The localized effect of this heat transfer was considered on NOx formation. The wall spray formed after the impingement of spray was considered instrumental in rapid convective heat transfer. The convective heat transfer rate can be described by Newton's law of cooling as:

$$Q_{wall} = h_c A_s (T_{cyl} - T_{wall}) \tag{13.11}$$

Here, Q_{wall} = Heat transfer to wall
h_c = Heat transfer coefficient
A_s = Surface area
T_{cyl} = Cylinder gas temperature
T_{wall} = Piston wall temperature

Exhaust Gas Recirculation (EGR)

To cope with today's stringent emission norms, various techniques are being employed by the engine manufacturers to reduce the emissions from engines. EGR is the most popular method of reducing NO_x emissions. The principle of this method is reduction of oxygen available for combustion by introduction of certain quantity of exhaust gas into the engine intake air. Reduced oxygen content results in lowering the peak flame temperature and hence reduced NO_x formation..

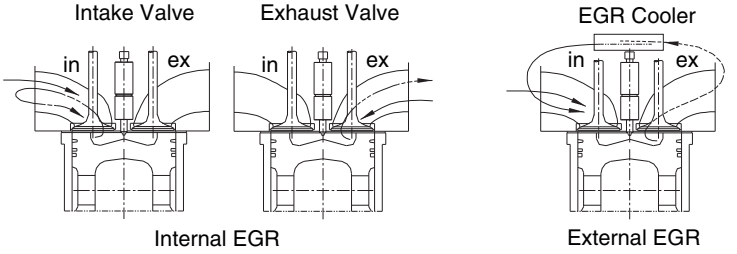

Fig. 13.4 Different EGR admission methods

There are mainly two admission methods for EGR admission (1) internally of the engine and (2) externally by means of piping (Fig. 13.4). Either opening the intake can do the internal EGR during the exhaust stroke or opening the exhaust valve during intake stroke. The external EGR can be done by tapping the fraction of exhaust gas through the exhaust pipe and recirculation into the intake manifold. The precise control over amount of EGR can be possible through the external EGR. Predictability of NO_x by the model is improved by taking into consideration

the EGR effect. The EGR is defined by volumetric percentage of total engine flow i.e. incoming air plus fuel flow. The airflow will be reduced by the same percentage as that of exhaust flow re-circulated. This effect is taken into consideration by introducing the correction for spray volume available for NO_x formation in free as well as wall spray, equations (13.14) and (13.15).

$$\%EGR = \left(1 - \frac{engine\ air\ \ flow\ with\ EGR}{engine\ air\ \ flow\ without\ EGR}\right) \times 100 \tag{13.12}$$

Free portion spray,

$$V_{free\ corrected} = V_{free}\left[1 - \frac{EGR}{100}\right] \tag{13.13}$$

Wall spray,

$$V_{wall\ corrected} = V_{free}\left[1 - \frac{EGR}{100}\right] \tag{13.14}$$

The flame temperature is also corrected using following correlation.

$$T_{flame corrected} = T_{flame}\left[1 - \frac{EGR}{100}\right] \tag{13.15}$$

Here,

V_{free} = Free spray volume
V_{free_corr} = Corrected free spray volume
V_{wall} = Wall spray volume
$V_{wall\text{-}corr}$ = Corrected wall spray volume
T_{flame} = Flame temperature
$T_{fllame\ corrected}$ = Corrected flame temperature
EGR = % of exhaust gas recirculated

Corrected spray volumes and temperatures are employed for NO_x predictions as in equations (13.14) and (13.15).

Phenomenology of Oxides of Nitrogen

As a case study, first data point of the engine C12 (Table 3.2) is discussed here. The spray properties were estimated considering injection pressure, spray-hole

geometry and needle lift diagrams. The injection starts at 10° before top dead centre and wall impingement occurs at about 13° after start of injection and 3° after top dead centre. The estimations of penetration of free spray and wall jet against crank angle are shown in the Fig. 13.5 in the graphical form.

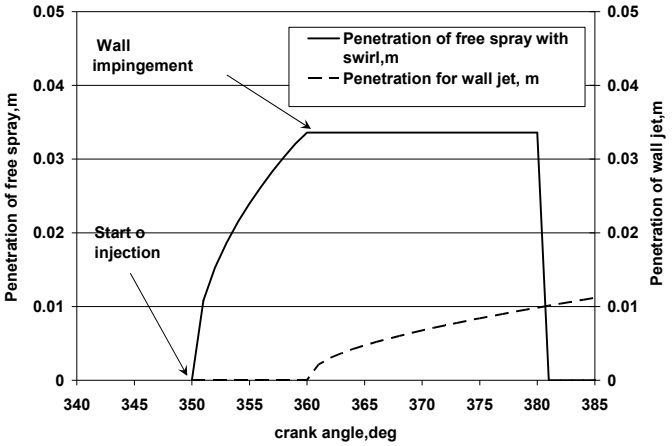

Fig. 13.5 Spray behaviour under engine environment

The heat release pattern was predicted based on mixing controlled combustion considering wall impingement. Then the wall heat transfer is estimated considering convection between wall spray and piston (Fig. 13.6). Finally, the NO_x emissions were predicted for free spray and wall jet portion for every crank angle using equations. The effect of heat transfer is also considered for wall jet. Then the NO_x from wall and free portions is summed up to arrive at final value. Then cumulative summation is considered as NO_x emission in the exhaust until the combustion is over (Fig. 13.7).

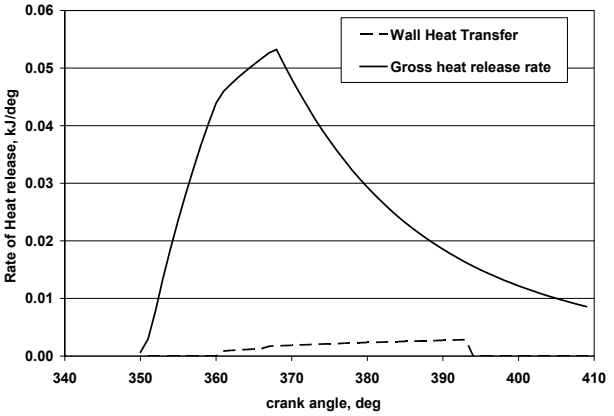

Fig. 13.6 Heat release and heat transfer

The experimental and predicted results for all the data points of engine C12 (Table 3.2) are given in Table 13.1. Predictions of NOx against observations with and without heat transfer are plotted in Fig. 13.8. Consideration of heat transfer improved model predictability. The prediction and observations are plotted against percentage load for different speeds namely rated, maximum torque and minimum operating speed. The trends along speed and load match with experimental observations satisfactorily (Fig. 13.9).

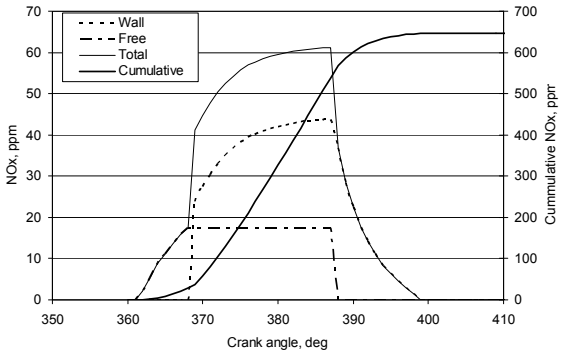

Fig. 13.7 NOx estimation in different portions of spray

Table 13.1 Effect of heat transfer on NOx prediction, Engine C12

Data point	Torque	Engine speed	Injection pressure	Injected quantity	Observed NO_x	Estimated NOx with heat transfer	Estimated NO_x without heat transfer
	(Nm)	(rpm)	(bar)	(mm^3/str)	(ppm)	(ppm)	(ppm)
1	242.5	2,200	640	57.0	769	690	762
2	181.9	2,200	560	42.8	634	528	583
3	121.3	2,200	350	29.0	369	362	415
4	275.0	1,500	500	65.0	1,073	840	883
5	206.3	1,500	400	47.3	892	658	710
6	137.5	1,500	330	35.0	584	473	505
7	290.0	1,200	450	64.0	1,254	886	926
8	217.5	1,200	310	48.0	999	636	671

Effect of EGR

Experiments were conducted with different EGR proportions on engine C12 (Table 3.2) at 1,500 rpm (Table 13.2). NOx measurement was carried out on the engine C12 at 75% load. Exhaust gas recirculation (Deshmukh *et al.* 2007, 2008) is generally not recommended at 100% load as it results in reduction of air-fuel

ratio to such a low value that the smoke emissions cross acceptable limits (Fig. 13.10). In first part, NO_x measurement was done without circulation of the exhaust gas into engine intake air. In the second part, exhaust gas was introduced into the intake air in different percentages by means of different sizes of orifices and measurement was carried out for certain EGR percentages.

Then the newly developed model was applied to validate the NOx predictability of the model with EGR effect. Measured and predicted values of NOx emissions were plotted against EGR proportions in Fig. 13.11. This plot indicated close agreement of predictions with observations for EGR application also.

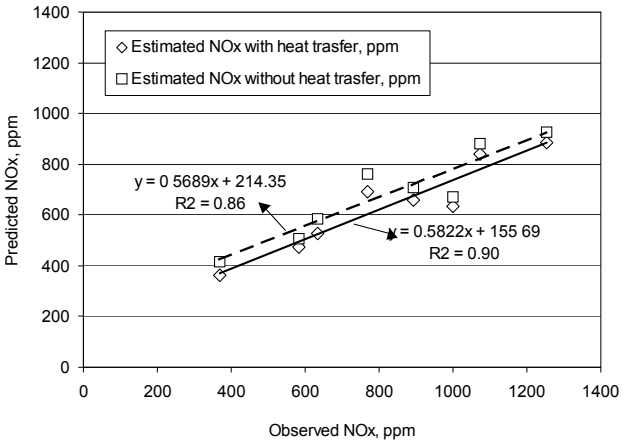

Fig. 13.8 Effect of heat transfer on NOx prediction, Engine C12

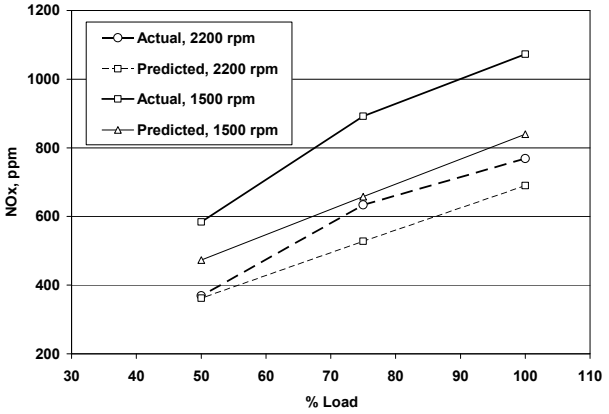

Fig. 13.9 NOx trend lines at different speeds, Engine C12

The experimental and predicted values of NO_x for engine C12 (Table 3.2) agree satisfactorily (Table 13.2). Consideration of wall heat transfer effect has improved the NO_x predictability of the model substantially. Inclusion of EGR effect further enhances the capabilities of the model. The predicted NO_x follows the same trend of the measured with different EGR percentages (Fig. 13.11). The model showed reduction in temperature inside the engine cylinder and hence NO_x on application of EGR as expected. Finally, the model was applied to the eleven engines namely L8, A9, B9, A10, B10, C12, D12, F12, H12, I12 and K12 described in Table 3.2 at rated and maximum torque speeds. The predicted values for all the 39 data points were plotted against observations (Fig. 13.12). The new model marginally under-estimates NO_x at lower operating speeds where higher NO_x was generated. This could be due to non-consideration of premixed phase. Even though the diffusion phase alone was considered for NO_x estimation, the correlation is satisfactory with regression coefficient of 0.89 for all the data points.

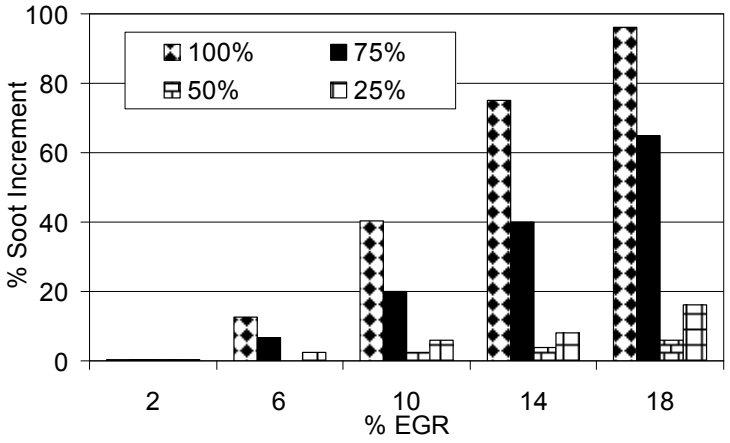

Fig. 13.10 Effect of EGR on soot, Engine C12

Effect of oxygen in the fuel

Experiments were conducted with different proportions of bio-diesel blend on engine C12 at 1,500 rpm. NO_x measurement as well as indicator diagrams were collected simultaneously (Deshmukh *et al.* 2008). The main observation with addition of Biodiesel, NO_x emissions increased as well as injection timing as well as start of combustion advanced. Then this data was used as input for NO_x model and predictions were made. The predictions followed the trend similar to observations (Fig. 13.13). The advancing effect and higher duration of injection are responsible for the increase in NO_x emissions with bio-diesel.

Table 13.2 Effect of EGR, Engine C12

Speed	Load	Injection pressure	Injection duration	Fuelling	EGR	Observed NOx	Estimated NOx with heat transfer
(rpm)	(%)	(bar)	(deg)	(mm^3/str)	(%)	(ppm)	(ppm)
1,500	75	500	19	48.5	0	652	614
1,500	75	500	19	48.5	9	553	544
1,500	75	500	19	48.5	12	519	528
1,500	75	500	19	48.5	15	504	509
1,500	75	500	19	48.5	18	436	474

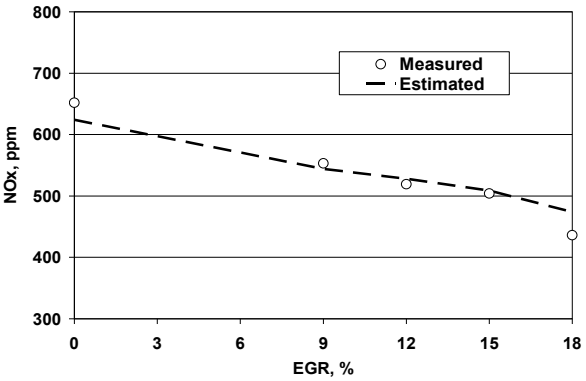

Fig. 13.11 Comparison of predicted and observed values of NOx for different EGR percentages, Engine B12

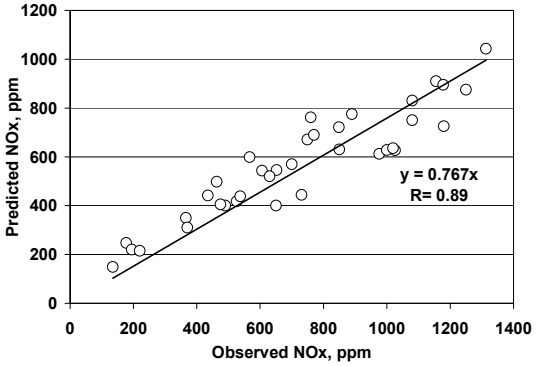

Fig. 13.12 Comparison of predictions and observed values for six-different engines

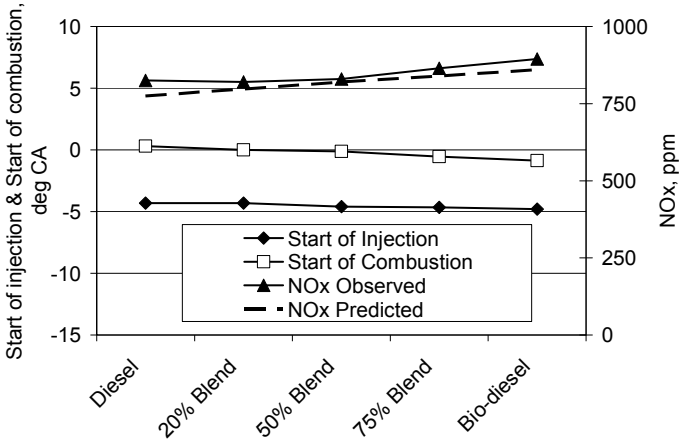

Fig. 13.13 Effect of biodiesel addition on start of injection, combustion and NOx

References

Deshmukh BS, Aghav YV, Gokhale NP, Kumar MN, Ramesh A, Babu MKG (2008) An innovative EGR admission concept for heavy duty Diesel Engine. SAE International Mobility Conference

Deshmukh BS, Aghav YV, Gokhale NP, Kumar MN, Ramesh A (2007) EGR mal-distribution Analysis for DI Diesel Engines using AVL Boost. AVL users International Conference, Graz

Lakshminarayanan PA Dent JC (1983) Interferometric studies of vapourising and combusting sprays. SAE 830244

Uyehara OA (1980) Effect of Burning Zone A/F, Fuel H/C on Soot Formation and Thermal Efficiency. SAE 800093

14 Particulate Matter from Direct Injection Diesel Engines

Particulate matter is a significant source of pollution from diesel engines and occurs when fuel burns in air deficit atmosphere, which is typical of diesel combustion with heterogeneous combustion. Particulate matter forms as a result of thermal cracking of fuel molecules under air deficiency. This leads to division of oxygen under acetylene and through polymerization to carbon rich macromolecules, which then agglomerate into the final particulates (Pischinger and Baker 2003). Diesel particulate matter is therefore a complex mixture of organic and inorganic compounds in solid and liquid phases (Johnson *et al.* 1994). The mathematical modelling of particulate matter is always concentrated around soot because of its complex nature. Experimental investigations on PM emissions from used engines indicate that PM emissions are higher during transient phases of test cycle as compared to cold start or cruise phase (Shah *et al.* 2004). Few experimental investigations indicate a reduction in PM emissions up to 27% from engines using biodiesel in place of diesel on account on higher reactivity of soot formed from biodiesel (John *et al.* 2003). Norton *et al.* (1998) have studied Fischer Tropsch catalytic conversion process for diesel fuel and its impact on engine out emissions. The study indicates about 24% reduction in PM emissions from engine using diesel that has undergone Fischer Tropsch transformation. Different studies have been carried out to establish contributions of soot, unburnt HC from fuel and lubricating oil (Cartillieri and Trittari 1984, Cartillieri and Wachter 1987, Cartillieri and Herzog 1988).

Most of the analytical correlations consider only soot and very few unburnt HC to estimate particulate matter. However, they do not account for contributions from lubricating oil and sulphur. An attempt has been made in this work to describe contributions of the different sources to arrive at total PM value.

Phenomenology of Particulate Matter (PM)

The PM collected on a filter is separated with an extraction solvent into two fractions. One fraction is the insoluble organic fraction (IOF) made up of a solid carbon material (soot) and sulphates that cannot be dissolved by an organic solution. The other fraction can be dissolved by an organic solution and is called the soluble organic fraction (SOF), which has been adsorbed by the soot or condensed onto the filter. It is composed of unburned fuel and lubricating oil and their thermally synthesized components. Figure 14.1 depicts the different constitutes of PM. In the present work, models for predicting soot and HC have been developed which do not need engine depending constants. Additionally SOF

P.A. Lakshminarayanan and Y.V. Aghav, *Modelling Diesel Combustion*,
Mechanical Engineering Series, DOI 10.1007/978-90-481-3885-2_14,

fraction from oil is predicted based on lubricating oil consumption tests and PM analysis. The correction to PM for different fuel sulphur levels is mentioned is ECE standards (Dieselnet 2008). This correction factor was extrapolated to estimate contribution of sulphates. The contributions are termed as yield in following equations.

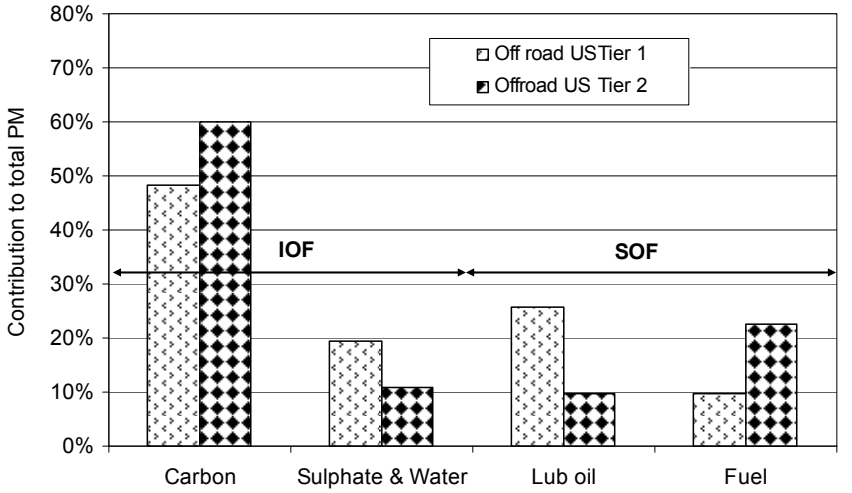

Fig. 14.1 Constituents of particulate matter at different emission norms

$$PM = IOF + SOF \tag{14.1}$$

$$PM = soot + sulphate + SOF_{loil} + SOF_f$$

Where,

PM = Particulate matter

IOF = Insoluble oil fraction

$Soot$ = Soot, estimated by equation (3.26)

Alternatively following equation can be used to convert observed values of filter smoke number, FSN are available.

$$= \frac{4.95 \times FSN^{(0.38 \times FSN)}}{405} \times Exh\_Flow, m^3/hr$$

Sulphate = Sulphate from fuel, $Fuel\_Flow \bullet sulphur\_content \bullet yield$

SOF_{loil} = SOF from lubricating oil, $LOC \bullet yield$

LOC = Lubricating oil consumption

SOF_f = SOF from fuel born HC, $HC \bullet yield$

$yield$ = Contribution to particulate matter

Validation of Correlation

The particulate matter is generally measured over 5-mode, 8-mode or 13-mode test cycle depending on application (Dieselnet 2008). Different weighting factors are applied and the sample is collected on single filter to get the final cycle averaged value. The same methodology was applied for the estimation of PM. For every mode estimates were made, weighting factors were applied and finally summed up to get the final cycle averaged value. The comparison of such results is done with the observed values for engines E12 and C12 (Table 3.2). These engines are of constant speed application where 5-mode cycle was applicable and the comparison of results was satisfactory. Figure 14.2 indicates the values obtained experimentally and predicted for both the engines.

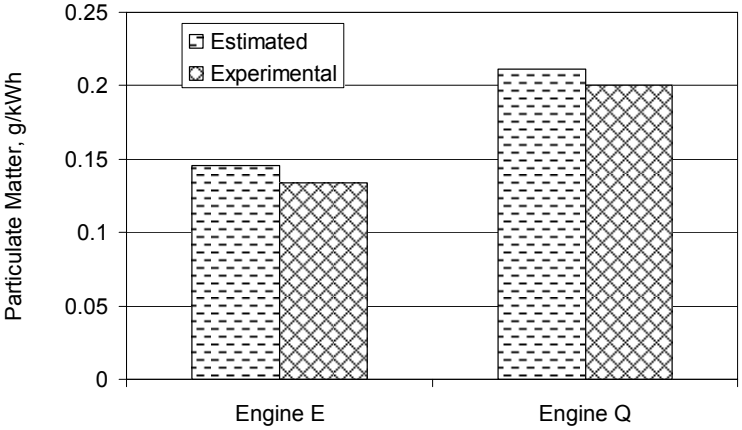

Fig. 14.2 Comparison of estimated and observed PM

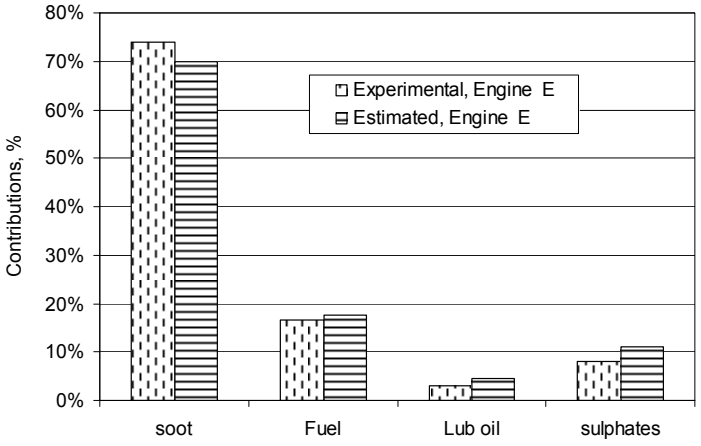

Fig. 14.3 Comparison of estimated and observed constitutes, Engine E12

Since the overall values agreed, analysis of contribution of each constituent was done for these engines (Figs. 14.3 and 14.4). This analysis showed that the new model accurately predicts not only overall value but also contributions of each of constituents effectively.

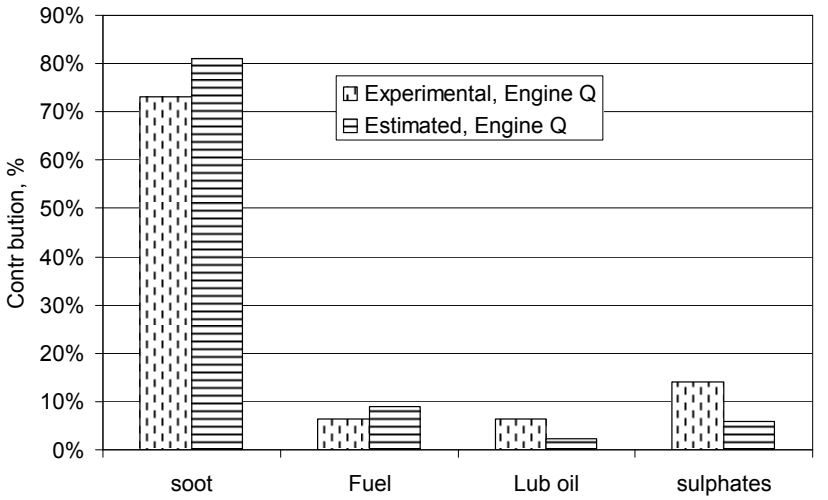

Fig. 14.4 Comparison of estimated and observed constitutes, Engine C12

Different experiments are conducted to collect the required data. The important results obtained from the experiments are compared with the predictions with new phenomenological model. The satisfactory comparison validated the applicability of the new model for combustion and emissions as a development tool.

References

Cartillieri W, Herzog PL (1988) Swirl supported of quiescent combustion for 1990's heavy duty DI diesel engines – An analysis. SAE 880342

Cartillieri W, Trittari P (1984) Particulate Analysis of light duty diesel engines [IDI and DI] with particular reference to lubricating oil particulate fraction. SAE 840418

Cartillieri W, Wachter WF (1987) Status report on preliminary survey of strategies to meet US-1991 HD diesel emission standards without exhaust gas after treatment SAE 870342 http://www.dieselnet.com/standards/ referred in 2008

John M. E. Storey, John F. Thomas, Samuel A. Lewis, Sr., Thang Q. Dam, K. Dean Edwards, Gerald L. DeVault, Dominic J. Retrossa (2003) Particulate Matter and Aldehyde Emissions From Idling Heavy-Duty Diesel Trucks, SAE 2003-01-0289

Johnson JH, Bagley ST, Gratz LD, Leddy DG (1994) A review of diesel particulate control technology and emission effects. SAE 940233

Paul Norton, Keith Vertin and Brent Bailey, Nigel N. Clark and Donald W. Lyons, Stephen Goguen and James Eberhardt (1998) Emissions from Trucks using Fischer-Tropsch Diesel Fuel, SAE technical series Paper no. 982526

Prof. Dr. S. Pischinger, Dr. H. Backer (2003) Internal Combustion Engines – Volume II

Sandip D. Shah, David R. Cocker, J. Wayne Miller, and Joseph M. Norbeck (2004) Emission Rates of Particulate Matter and Elemental and Organic Carbon from In-Use Diesel Engines, Environ. Sci. Technol.

15 Multi-dimensional Modelling of Diesel Combustion: Review

Yu Shi and Rolf D Reitz

Engine Research Center, University of Wisconsin-Madison

Abstract With the exponentially increasing computational power of modern computers, multi-dimensional Computational Fluid Dynamics (CFD) has found more and more applications in diesel engine research, design and development since its initiation in the late 1970s. Enhanced understandings of the physical processes of diesel combustion and correspondingly improved numerical models and methods have both driven simulations using multi-dimensional CFD tools from qualitative description towards quantitative prediction. To numerically resolve the complex physics of diesel combustion requires modelling of turbulent flows, high-pressure spray development, as well as combustion chemistry and relevant mechanism of pollutants formation. This chapter reviews the basic approach of multi-dimensional CFD modelling of diesel combustion, and focus is placed on the description of advanced turbulence, spray, and combustion models, and the introduction of popular CFD codes for engine simulations. In addition, recent efforts for reducing the computational expense of multi-dimensional CFD modelling are also discussed.

Fundamental concepts of fluid dynamics were substantially established in 1800s and more complex turbulent flows were intensively investigated in 1900s. Models help to mathematically reveal the physics of fluid flows, and with the increasing complexity of studied problems numerical solutions are often needed instead of analytical ones. This leads to an important branch of fluid dynamics, Computational Fluid Dynamics (CFD). Improved CFD techniques and the exponentially increasing computational power of modern computers during the twentieth and twenty-first centuries have had a great impact on applying the sciences of fluid mechanics to design problems in engineering practice. Consequently, multi-dimensional CFD has found more and more applications in diesel engine research, design and development since its initiation in the late 1970s. Compared to phenomenological models, multi-dimensional CFD models provide more detailed physical information about the gas exchange processes, in-cylinder flow structures, spray development, as well as combustion chemistry and pollutant formation in diesel engines.

The first part of this chapter reviews the basic approach that is used in CFD modelling of diesel engines, including the basic assumptions, equations, and numerical methods. This is followed by a description of advanced turbulence, spray and evaporation, and combustion models of in-cylinder phenomena. Detailed

P.A. Lakshminarayanan and Y.V. Aghav, *Modelling Diesel Combustion*, Mechanical Engineering Series, DOI 10.1007/978-90-481-3885-2_15,

discussion of the historical evolution and mathematical derivation of these models is beyond the scope of the present review. Instead, focus is placed on their applicable ranges, advantages and disadvantages. The reader is encouraged to refer the relevant literature cited for each model. Recent efforts for reducing the computational expense of multi-dimensional CFD modelling are also discussed. These efforts include reducing the mesh-dependence of spray models and lessening the computational burden of combustion chemistry solvers by using an adaptive multi-grid chemistry model with code parallelization. Features of popular engine CFD codes that are categorized into open source code and commercial software are also described. The chapter concludes with discussion of the new challenges that engine CFD modelling will be facing in the near future.

Basic Approach

In-cylinder flows of diesel engines are typically compressible turbulent flows. Turbulence by itself remains one of the most complex fundamental problems of fluid dynamics. The complexity of in-cylinder flows is further increased due to the injection of a high-pressure spray and the resulting evaporation of the droplets due to multi-phase and multi-component nature of the problem. Once the combustion occurs, the additional requirement of solving reacting flows can increase the difficulty by orders of magnitude due to the vast number of participating chemical species. However, the behaviour of the fluid is still described by classical physics and is governed by several basic equations, including the continuity (mass conservation), momentum (Navier-Stokes equations), energy, and turbulence (i.e., k-ε equations) equations. These equations are supplemented by thermal and caloric equations of states (i.e., ideal gas law). Assumptions and simplifications are usually made for modelling the multi-component mixture viscosity, Fick's law of mass diffusion, and Fourier's law of enthalpy (or energy) transport, depending on the details of the models.

For the gas-liquid flows, both Eulerian-Eulerian and Eulerian-Lagrangian (i.e., Discrete Droplet/Particle) methods can be used to solve two-phase flow problems. Due to the large dimensionality of the problem, the former method awaits "next generation" spray and atomization models. Accordingly, the Eulerian-Lagrangian method still dominates and is widely used in current engine CFD simulations. The Eulerian-Lagrangian approach treats the gas phase as continuous and the liquid phase as consisting of discrete particles, separately. Thus, the gas phase flow is described by the Eulerian formulation and the liquid phase is described using the Lagrangian approach, in which liquid droplets are represented as assemblages of identical particles using the discrete particle or parcel method (Dukowicz 1980). The present implementation of the Lagrangian spray model is based on Kelvin-Helmholtz (KH) and Rayleigh-Taylor (RT) instability analyses (Reitz 1987, Beale and Reitz 1999) and the "blob injection concept" (Reitz and Diwakar 1987). These

numerical models are relatively efficient and can provide statistical information about the distributions of particle size, velocity, and position, which are usually in reasonable agreement with experimental measurements if the models are appropriately tuned. Mass, momentum, and heat transfer between the gas and liquid phases are accounted for through source terms in the corresponding governing equations.

The governing equations of the gas phase are partial differential equations (PDE's). Thus, numerical methods are needed to discretise the equations. The methods include (but are not restricted to) finite volume, finite difference, and finite element methods. They all use a finite-difference mesh or grid to split the computational region into smaller sub-regions to approximate a continuous domain, and the discretised governing equations are then solved inside each of these portions of the domain.

Mesh generation is critical to multi-dimensional CFD engine modelling due to the fact that the mesh quality has a large impact on the numerical stability of CFD solvers and the mesh density can influence the simulation results, depending on the mesh-dependence of the numerical models. Distinguished by the connectivity of neighbouring grids, computational meshes are classified into structured meshes, unstructured meshes, and their hybrids. A structured mesh is characterized by regular connectivity that allows CFD solvers to see the neighbour relationships between connected cells based on their storage arrangements. Typical structured meshes are quadrilaterals and hexahedra in 2-D and 3-D space, respectively. The structured mesh saves storage space, but it is difficult to mesh complex geometries, such as the joints of manifolds, valves, and glow plugs of diesel engines. An unstructured mesh is characterized by irregular connectivity which requires a substantially larger storage space since the neighbour connectivity also needs to be explicitly stored. But the unstructured mesh can easily deal with more complex engine geometries.

The finite volume method is the most prevalent numerical approach in engine CFD codes, such as in open source codes such as KIVA and OpenFOAM, and other commercial CFD software. Its popularity comes from two aspects: its inherent formulation ensures the conservation of quantities such as mass, momentum, energy, and species; it is also easily formulated to allow for unstructured meshes. The finite volume method converts volume integrals in a PDE that contains a divergence term to surface integrals using the divergence theorem, and source terms can be directly volume-integrated. The surface integration then ensures that these terms are evaluated as fluxes at the surfaces of each finite volume. Because the values of the fluxes entering a control volume are identical to their leaving values, conservation can be guaranteed. The finite difference method discretises the governing PDE's in both time and space. It replaces derivatives of PDE's with approximately equivalent difference quotients. Two sources contribute to errors of this method. The first is round-off error due to computer rounding of decimal quantities, and the second is truncation error from using difference quotients to express derivatives when high order terms are discarded. Using higher order

differences helps to reduce the truncation error; however, the numerical stability condition becomes stricter. Explicit differencing schemes require smaller time-steps to satisfy the Courant condition in order to maintain convergence, and thus implicit schemes are usually employed. The finite element method is based on converting PDE's to ordinary difference equations (ODE's) in order to obtain their solution by utilizing standard integration techniques. It finds more applications in structural analysis of engine bodies, and it is seldom applied to solve engine flows primarily due to the special care needed to ensure conservative solutions.

Using the aforementioned basic approaches, the complex in-cylinder physical and chemical processes of diesel engines can be solved using a series of closely coupled sub-models that describe the turbulent flow, spray injection, droplet evaporation, combustion, pollutant formation and heat transfer. They are discussed as follows.

Turbulence Modelling

It is critical to resolve in-cylinder flow motions at both large and small scales in modelling diesel engines. The in-cylinder flows are compressible turbulent flows due to the high-speed gas exchange processes and the piston compression. Various models and methods have been proposed for solving turbulent flows, including Reynolds-averaged Navier-Stokes (RANS), Large Eddy Simulation (LES), and Probability Density Function (PDF) methods, and Direct Numerical Simulation (DNS). Considering the computational expense and the solutions of interest, RANS and LES are most prevalent in engine simulations.

RANS models

Due to their relatively high efficiency and acceptable accuracy, RANS-based turbulence models still play a dominant role in engine simulations nowadays, especially for engineering practices. In the context of engine simulations, RANS models specifically referred to are the k-ε model and its variants, although other types of RANS models, such as Reynolds Stress Model (RSM) (Launder *et al*. 1975), can be found in very few studies (*e.g.*, Lebrère and Dillies 1996).

In RANS models, the Reynolds equations are solved for the mean velocity field, i.e., all turbulent fluctuations about the local mean are modelled. The closure terms, the Reynolds stresses, are determined by a turbulence model, such as the k-ε model which is based on the turbulent viscosity hypothesis (Pope 2000). The k- ε model belongs to the class of two-equation models (as compared to one-equation models in which only the turbulent kinetic energy k is solved), in which model transport equations are solved for two turbulence quantities – the turbulent kinetic energy k and its dissipation rate ε (Pope 2000). The turbulent viscosity is expressed by $\nu_t = C\mu\ k^2/\varepsilon$ where $C\mu$ is a model constant given as 0.09. In the

standard k-ε equations the model constants are evaluated with reference to benchmark experiments.

In early studies, the standard k-ε model was widely used in engine CFD codes, such as in the KIVA II code (Amsden et al. 1989). Considering the moving boundary in engines, a source term that accounts for length scale changes with velocity dilation was added to the ε equation. An additional source term is used to introduce the interaction of a spray with the turbulence in both the k and ε equations.

Yakhot and Orszag (1986) used the Renormalization Group (RNG) theory to form an improved formula for the ε equation and proposed the RNG k- ε model. Their deviation depended on the RNG theory and ε-expansion (Yakhot and Smith 1992). The RNG theory does not include any experimentally adjustable parameters. Therefore, the model constants in the deduced RNG k- ε equations are given more rigorous mathematical meanings. Since its appearance, the RNG k- ε model has been applied to model both low- and high-Reynolds number turbulent flows with great success. In IC engines, although the Mach number of the in-cylinder flow is very low, the moving piston causes the fluid undergo large density variations. With such flow behaviour, the original RNG k- ε model cannot be directly applied. Therefore, Han and Reitz (1995) further modified the ε equation to account for the effect of compressible turbulent flows in engine environments. In their analysis, in-cylinder flows were assumed to be low Mach number flows with rapid distortion and isotropic (spherical) mean strain. The effects of both the pressure dilation and dilatation dissipation that appear in the k equation were deemed to be negligible due to the assumption of isotropic distortion at very low Mach number, and thus the k equation remained as formulated in the original RNG k-ε model. The ε equation was similar to that of the standard one, but focus was placed on modifying a model constant, which accounts for velocity dilation and was determined through the analysis of rapid spherical distortion. In the same study, they showed that with the modified RNG k- ε model simulated engine compressing/expanding flows agreed well with available experimental observations and that the large scale flow structures which are affected by the spray and the squish flows, were consistent with endoscope combustion images. Kong *et al*. (1995) reported that a good quantitative agreement between measured and predicted NOx and soot emission data were obtained with the use of the modified RNG k-ε model. Since then, this RNG k-ε model has been widely adopted into many engine CFD codes and applied to various simulations (Han *et al*. 1996, Kaario *et al*. 2002).

Large Eddy simulation (LES)

Although the pioneering work on LES by Smagorinsky (1963) and Lilly (1967) appeared several decades ago, until recently (2000s) LES has not been widely employed in modelling engine flows. This is because in terms of computational expense, LES lies between Reynolds-stress models and DNS (Pope 2000), which prevented it from being applied to engineering problems in times when computational

power was very limited. Thanks to the rapid development of computer technology, LES has now found more applications in engine simulations. The basic idea of LES is to solve for large-scale eddies (i.e., those that can be resolved on the computational mesh) explicitly and to model the effect of smaller-scale motions (sub-grid scale) on large meshes through the use of a sub-grid scale (SGS) model. Early applications of LES in engine turbulent flows were reviewed by Celik *et al*. (2001). The review revealed that even with relatively coarse grids LES captures many more interesting features of in-cylinder flows, such as the large coherent vortical flow structures developed during the intake stroke. In more recent studies, many researchers have shown that LES offers significant advantages over RANS (Lee *et al*. 2002, Shetaji *et al*. 2005, Jhavar and Rutland 2006, Hu *et al*. 2007) in that LES resolves more flow details, better represents a local mixing field, and is able to reveal engine cycle-to-cycle variations (Fogleman *et al*. 2004). In many cases of LES in engine simulations, the same sub-models, such as wall models, spray models, and turbulent combustion models have been retained with only the k-ε derived turbulence scales being replaced by the scales from the LES sub-grid scale model (Haworth 2005). Therefore, the advantages of LES may not be fully obtained. Further improvements of use of LES in engine simulations will depend on the corresponding development of these sub-models. To take full advantage of the power of LES, not only sound physical modelling is required but also careful numerical implementations, such as high-order numerical schemes and a high-resolution computational mesh. However, the resulting high computational cost may prevent LES from being widely used for practical engine simulations of this time and in the near future. Hence, efforts are needed to compromise between reducing computational expense and benefiting from LES features. Recent research (Pomraning and Rutland 2002, Jhavar 2007, Hu 2008) showed that the dynamic structure LES model can give promising results on coarse meshes.

Spray and Evaporation Modelling

As briefly discussed in the section “Basic Approach”, the Lagrangian Drop Eulerian Fluid (LDEF) approach is the most prevalent methodology used in multi-dimensional CFD codes to treat the interaction of gas-liquid phases that result from high-pressure injection of liquid fuels in diesel engines. In LDEF models, sprays are represented by discrete computational parcels. Each of these parcels represents a group of droplets that have the same characteristics, and they undergo break-up, collision, and coalescence processes whose competition determines the size and position distribution of the droplets. An evaporation model is also needed to calculate the vaporization rate of liquid droplets based on their sizes and the thermal conditions that they are subject to. Interactions due to mass, momentum, and heat transfer between the gas (described using the Eulerian method) and

liquid phases are accounted for using source terms in the corresponding governing equations. Popular spray and evaporation models are reviewed in this section.

Spray models

In the study of Reitz and Diwakar (1987), atomization and drop break-up were treated as indistinguishable processes within the dense spray near the nozzle exit. Accordingly, atomization was prescribed by injecting drops ('blobs') which underwent subsequent breakup, collision, and coalescence processes. This method established a basic framework for calculating spray behaviour using CFD techniques, and has been broadly adopted in engine CFD codes since it was proposed. In their study, the atomization model assumed that the injected drops had a radius equivalent to the effective nozzle-hole radius and the initial axial velocity of the drops was set equal to the injection velocity. The breakup model employed two breakup regimes based on experimental measurements to determine the new drop characteristics. In Reitz's later study (1987), significant improvements were made to the previous model in several aspects: a linear stability analysis was used to describe the instability at the liquid-gas interface and to predict the breakup of the liquid jet, and the method broadened to describe various regimes of jet breakup; the product drops were distinguished from the parent drop by having different drop sizes, which had a significant effect on the fuel vapour distribution in a high-pressure spray. Since then, a variety of instability theories have been used to model the atomization and breakup processes of spray jets, and modifications to these models have been the subject of many studies. These studies include use of the Taylor Analogy Breakup (TAB) model (O'Rourke and Amsted 1987), Kelvin-Helmholtz (KH) instability and Rayleigh-Taylor (RT) instability models (Patterson and Reitz 1998, Beale and Reitz 1998), and their hybrids (Pelloni and Bianchi 1999). The KH/RT hybrid model (Beale and Reitz 1998) is reviewed here.

In the KH/RT hybrid model, the KH theory is used to predict the initial breakup of the injected blobs or the intact liquid core. Then the RH theory is introduced to account for the instability caused by the acceleration normal to the interface of the liquid spray drop and its surrounding gas. Together with the KH model, the RT model is used to predict the secondary breakup of the droplets.

In the KH model, a parent parcel with radius, r, breaks up to form new droplets with radius, r_c, such that

$$r_c = B_0 \Lambda_{KH} \tag{15.1}$$

where B_0 is a constant equal to 0.61 and the wavelength Λ_{KH} corresponds to the KH wave with the maximum growth rate Λ_{KH} given by

$$\Lambda_{KH} = \frac{9.02r(1+0.45\sqrt{Z})(1+0.4T^{0.7})}{(1+0.865We_g^{1.67})^{0.6}} \tag{15.2}$$

$$\Omega_{KH} = \frac{0.34 + 0.38We_g^{1.5}}{(1+Z)(1+1.4T^{0.6})}\sqrt{\frac{\sigma}{\rho_f r^3}} \tag{15.3}$$

In the equations, the gas Weber number is defined as $We_g = \rho_g U_r^2 r/\sigma$ and the Ohnesorge number, Z, is

$$Z = \frac{\sqrt{We_l}}{\mathrm{Re}_l} \tag{15.4}$$

U_r is the relative velocity between the liquid drop and the gas, and σ is the surface tension, and ρ_g and ρ_f are the gas and fuel densities, respectively. The liquid Weber number is $We_l = \rho_f U_r^2 r/\sigma$ and the liquid Reynolds number is $Re_l = \rho_f U^2 r/\mu_f$, where μ_f is the liquid fuel viscosity. The Taylor number, T, is calculated

$$T = Z\sqrt{We_g} \tag{15.5}$$

Due to the loss of mass during drop stripping, the parent reduces in diameter and the rate of change of the radius of the parent parcel is calculated using

$$\frac{dr}{dt} = \frac{r - r_c}{\tau_{KH}} \tag{15.6}$$

where τ_{KH} is the breakup time given by

$$\tau_{KH} = \frac{3.726B_1 r}{\Omega_{KH}\Lambda_{KH}} \tag{15.7}$$

B_1 is a constant that can have values ranging between 10 and 60, and it is usually calibrated with experiments.

The RT model is only employed to influence the drops beyond the break-up length L_b, which is calculated from Levich theory as

$$L_b = C_b d_0 \sqrt{\frac{\rho_f}{\rho_g}} \tag{15.8}$$

where C_b is an adjustable constant which is chosen such that $C_b = B_1/2$ to keep the breakup length approximately equal to that calculated from the KH equations for inviscid flows.

Similar to the KH theory, the size of the new droplets are also determined by the wave instability. In the RT model, the frequency of the fastest growing wave is given by

$$\Omega_{RT} = \sqrt{\frac{2}{3\sqrt{3\sigma}} \frac{[-g_t(\rho_f - \rho_a)]^{1.5}}{\rho_f + \rho_a}} \tag{15.9}$$

where g_t is the acceleration in the direction of travel. The corresponding wave number is

$$K_{RT} = \sqrt{\frac{g_t(\rho_f - \rho_a)}{3\sigma}} \tag{15.10}$$

The wavelength corresponding to the fastest wave growth rate is $2\pi C_{RT}/K_{RT}$, where C_{RT} is an adjustable constant of the order 0.1. The radius of the droplet is compared to the RT wavelength and once the wavelength is smaller than the droplet diameter, RT waves are assumed to be growing on the surface of the droplet. The wave growth time is compared to the breakup time, defined by

$$\tau_{RT} = \frac{C_\tau}{\Omega_{RT}} \tag{15.11}$$

where C_τ is an another constant usually set to unity. If the wave growth time is greater than the breakup time, the drop is assumed to breakup with a new radius given by

$$r_c = \frac{\pi C_{RT}}{K_{RT}} \tag{15.12}$$

It is noted that in both KH and RT models, the number of droplets in the computational domain is adjusted based on mass conservation of the liquid phase once the breakup occurs. Due to its simplicity and with a great deal of successful applications, this hybrid model has been adopted into many engine CFD codes, such as KIVA and STAR-CD.

The interaction between drops that result from spray atomization and breakup is crucial to decide the spatial fuel distribution in diesel combustion simulations. Inter-drop collisions are normally modelled as two-body interaction processes and a sequence of such binary interactions can represent collisions involving three or more participating bodies. To describe the complex physical interactions of drop collision dynamics, a model is needed to solve for the probability of occurrence of a collision and to predict the outcome of the collided drops.

The classic O'Rourke model (O'Rourke 1981) is one of the most widely used collision model in LDEF spray simulations. In the O'Rourke model, the possibility of collision is based on the drop number density and the relative velocity between the drops. Collisions are allowed to occur for two parcels only if they are in the same cell. The model considers two outcomes for a collision, i.e., coalescence

and grazing separation. A formula for the efficiency of coalescence is defined in the model, which is derived from the argument that for coalescence to be permanent, the rotational energy of the combined mass formed by the colliding drops should be less than the surface energy required to reform the drops (Brazier-Smith *et al*. 1972). The collision outcome: coalescence or grazing separation, is determined stochastically by considering whether a randomly generated number (between 0 and 1) is less or greater than the square root of the coalescence efficiency. For resulting drops, mass, momentum and energy conservation laws are applied to calculate their sizes and velocities after the collision.

The simplicity of the O'Rourke collision model has contributed to its popularity in multi-dimensional engine CFD codes. However, the shortcomings of this model cannot be neglected. Many experiments have shown that there are more outcomes from a collision than just the two that are considered in the O'Rourke model, and thus extended models for those outcomes are needed. Also the model assumes that only parcels within the same cell can collide, which is a further limitation. This is also the reason that the O'Rourke collision model exhibits severe dependency on mesh size. Efforts to improve the O'Rourke model have appeared in the literature. A radius of influence (ROI) method proposed by Munnannur (2007) has shown a much reduced mesh-dependence, as discussed in section "Mesh Independent Spray Models". The dependency of the collision model on mesh size is one of the reasons that the results of LDEF spray models more-or-less depend on the grid size on which the models are solved. The other reason is that an inadequate mesh resolution results in under-prediction of spray momentum, which is particularly severe in the near nozzle region. This mesh-dependence issue is also addressed in section "CFD Codes for Engine Simulation".

Evaporation models

Once the fuel spray breaks up into small droplets, evaporation takes place rapidly from the surface of the droplets. In IC engine applications, the ranges of pressures and temperatures are broad, and evaporation models have to properly predict the behaviour of vaporizing droplets and sprays. These models are categorized into single component fuel evaporation models and multi-component fuel evaporation models that are distinguished by how they treat the fuel composition in the droplets, as their names suggest. The multi-component models can be further classified into two types, i.e., continuous multi-component (CMC) models and discrete multi-component (DMC) models. To simplify the complex heat and mass transfer processes of droplet evaporation, several assumptions are often used in these models, such as the liquid droplet is treated as a perfect sphere; no absorption of the ambient gas into the liquid droplet is considered; radiation and second order effects such as the Soret and Dufour effects are assumed to be negligible.

For simplicity, fuels are usually represented as a single component fuel in most evaporation models in multi-dimensional engine CFD simulations. For example, tetradecane ($C_{14}H_{30}$) is normally used as a surrogate fuel for diesel and gasoline is represented by iso-octane (C_8H_{18}) in many cases. These species are chosen because

they have similar physical properties, such as density and surface tension, to diesel and gasoline. However, these similarities do not guarantee that the complex behaviour of the vaporization of multi-component fuels can be truly revealed. It has been pointed out that the preferential vaporization of light-end components in multi-component fuels affects greatly the fuel distribution near the spray and this cannot be represented by single component fuel models (Lippert 1999). Therefore, multi-component evaporation models have been of much interest in engine CFD simulations.

Zhu and Reitz (2002) employed the thermodynamics of continuous systems to treat liquid mixtures and developed a continuous multi-component (CMC) model for engine applications. In their model, the liquid composition and the consequent properties were represented and described by continuous probability density functions, i.e., the Γ distribution for both liquid and vapour phases. The distribution function was only a function of the molecular weight of the studied fuel, and its shape was controlled by two parameters. The parameters were chosen so that the calculated distillation curves with the distribution reproduce best the corresponding ASTM D-86 experimental data for the fuel. Relations for the properties of the high-pressure sub- and super-critical vaporization processes were also formulated in order to consider droplet evaporation under a wide range of engine environments. The model was found to better characterize the characteristics of the droplet vaporization process of complex liquid mixtures.

Since there is only one additional distribution function needed to represent fuel properties, the CMC model enables a reduction of computational load while maintaining the predictability of the complex behaviour of the vaporization of multi-component fuels. However, when it is applied to combustion simulations, especially with detailed chemistry, it is difficult to model the consumption of individual components appropriately. Ra and Reitz (2008) proposed a discrete multi-component (DMC) model so that the individual components of the fuel during the evaporation process can be tracked and thus can be coupled with corresponding reaction kinetics. In the DMC model, the Dirac delta function was used to represent the general distribution function for the composition of the discrete fuel mixture system. An explicit expression for the heat flux from the surrounding gas to the droplet-gas interface was also derived. The inter-diffusion of fuel vapour and the surrounding gas were taken into consideration. The model was successfully implemented into a multi-dimensional CFD code for engine combustion simulations and improved results of combustion characteristics and emissions were seen.

It should be noted that for simplicity in all these evaporation models, fuel vapour is assumed to be uniformly distributed in the computational cell containing the drop, and thus a potential mesh-dependency from the evaporation models is introduced. But this dependency is usually not as severe as those caused by the spray and collision models in practical simulations due to the large number of vapourising drops in the cell.

Combustion Modelling

In engine environments, the combustible mixture is subject to a turbulent flow and, once mixed, undergoes subsequent elementary reactions which convert the fuel vapour to complete and incomplete combustion products with the accompanying release heat. So, in diesel engine simulations, combustion modelling mainly deals with two processes: first, low-temperature chemistry, which leads to auto ignition and produces intermediate species, and second, these intermediate species trigger high-temperature reactions that contribute the main heat release, as well as further complete and incomplete combustion products. Another important task for combustion models is to properly account for the significance of the effect of turbulence on the combustion processes. Various combustion models have been proposed for engine simulations under a variety of operating conditions. This section reviews two combustion models widely used in diesel CFD simulations, the Shell/ Characteristic Time Combustion (CTC) model and direct integration of chemical kinetics. Since the k-ε turbulence model still plays a dominant role in multi-dimensional engine CFD simulations, it is the basis of the present discussion of the combustion models. For other turbulence models, such as LES, the reader is referred to relevant literature, such as a general diesel combustion model formulated in the context of LES, proposed by Hu (2008).

Shell/CTC model

The Shell/CTC model is a widely used combustion model due to its simplicity (thus efficiency) and acceptable accuracy for conventional diesel combustion. Its tunable model constants extend its applicable range without sacrificing physical sense. This makes the model very attractive and useful for solving engineering problems. The model involves two sub-models: the Shell model which simulates the auto-ignition of hydrogen fuels, and the CTC model which calculates the species conversion rate and main heat release of high temperature reactions.

Based on the theory of chemical kinetics, the reaction rate of elementary gas-phase reactions can be described in Arrhenius form. However, a single general Arrhenius expression for a single generic reaction is not able to describe the complex cool flame and two-stage ignition phenomena that are observed during the auto ignition of hydrocarbon fuels, and thus multi-step reactions are normally required. The Shell model (Halstead *et al*. 1977) employs multi-step generic reactions to predict the auto ignition of hydrocarbon fuels, and it was implemented into engine simulations with some modifications by Kong and Reitz (1993).

The Shell model consists of five generic species and eight generic reactions of the form

$$
\begin{aligned}
&RH + O_2 \xrightarrow{K_q} 2R^* && \text{(a)}\\
&R^* \xrightarrow{K_p} R^* + P + Heat && \text{(b)}\\
&R^* \xrightarrow{f_1 K_p} R^* + B && \text{(c)}\\
&R^* \xrightarrow{f_4 K_p} R^* + Q && \text{(d)}\\
&R^* + Q \xrightarrow{f_2 K_p} R^* + B && \text{(e)}\\
&B \xrightarrow{K_b} 2R^* && \text{(f)}\\
&R^* \xrightarrow{f_3 K_p} \text{termination} && \text{(g)}\\
&2R^* \xrightarrow{K_t} \text{termination} && \text{(h)}
\end{aligned}
\qquad (15.13)
$$

The five generic species *RH, R**, *B, Q,* and *P* represent fuel, radicals formed from the fuel, branching agents, labile intermediate species, and oxidized products, respectively, and O_2 is oxygen. In the Shell model, reaction (a) initializes the ignition process. The formed radicals then undergo propagation via reactions (b)–(e). Reaction (f) degenerates the branching process that converts the intermediate species *B* to the branching agent R^*, and R^* is terminated in reactions (g) and (h). Special care was taken to maintain the build-up of the branching agent *B* in Kong and Reitz's study (1993), and it was shown that the reaction rate of Reaction (d) limits the subsequent chain branching and it was the most influential factor on the predicted ignition delay. The model constant f_4 is therefore usually tuned to match experimental data. Although turbulence is not considered to directly affect the reaction rates in the Shell model, the indirect influence of turbulence is reflected through the local concentrations of the involved species due to turbulent transport.

The shell ignition model is used only for the low-temperature chemistry. Once a pre-specified temperature, i.e., ~1,000 K, is reached, it is deemed that the ignition stage is completed and the subsequent high-temperature reactions are then simulated using the CTC model. Extending the use of the CTC model, which was originally developed for SI engine modelling (Abraham *et al*. 1985), Kong *et al*. (1995) combined the Shell ignition model and the CTC model to simulate the overall combustion processes in a diesel engine. With this combustion model, the species conversion rate is calculated based on the thermodynamic equilibrium value of its mass fraction and the characteristic time to reach such equilibrium, expressed as

$$\frac{dY_m}{dt} = -\frac{Y_m - Y_m^*}{\tau_c} \qquad (15.14)$$

In the equation, Y_m is the mass fraction of species *m* and Y_m^* is the local and instantaneous thermodynamic equilibrium value of the mass fraction. The characteristic time τ_c is assumed to be the same for the seven species (fuel, O_2, N_2, CO_2,

CO, H_2 and H_2O) considered, and it is the sum of a laminar timescale τ_l and a turbulent timescale τ_t, given by

$$\tau_c = \tau_l + f\tau_t \tag{15.15}$$

The laminar timescale τ_l is derived from a single droplet auto-ignition experiment of Arrhenius form, which represents the chemistry timescale of the overall reaction that converts the fuel to combustion products. In equations (15.14) and (15.15), it is seen that the role of turbulence in the combustion is introduced through the timescale τ_t. In other words, turbulence mixing determines how fast a species *m* approaches its equilibrium state. Using the *k-ε* turbulence model, the turbulence timescale τ_t is related by the eddy turnover time

$$\tau_t = C_2 k / \varepsilon \tag{15.16}$$

where C_2 is a model constant of an order of 0.1, which is tunable in order to better match measured engine pressure traces and heat release data, as well as emissions which are determined by the species conversion rates. The progressive influence of turbulence on combustion after ignition has occurred is accounted for using a delay coefficient *f* of equation (15.15), and it is given by

$$f = \frac{1 - e^{-r}}{0.632} \tag{15.17}$$

where r is the ratio of the amount of products to that of total reactive species (i.e., all except N_2) and it is an indicator of the completeness of combustion.

By tuning the aforementioned model constants against experiments, the Shell/CTC model is able to provide satisfactory overall results (pressure trace and heat release rate) in parametric studies of diesel engines. Its relative simplicity and acceptable accuracy, particularly the high computational efficiency, have favoured its wide spread use in engine optimization studies for conventional diesel combustion (*e.g.,* Shi and Reitz 2008). However, recent research (Singh *et al*. 2006) has shown that the performance of Shell/CTC model deteriorates when the combustion mode of a diesel engine enters the region of low-temperature premixed combustion (LTC) in which the effect of chemistry dominates. This is largely due to the over-simplified chemical kinetics, such that the Shell/CTC model is not able to predict reasonable trends of unburned hydrocarbons (UHC), carbon monoxide (CO), as well as other intermediate species of interest.

Direct integration of chemical kinetics

In contrast to the Shell/CTC model, direct integration of the chemical kinetics resolves the species conversion rates by considering detailed chemistry for modelling engine combustion processes. The solutions provide the combustion source terms

in the energy and species transport equations. Turbulence may or may not play a role at the sub-grid scale in the model, depending on if the computational cells are treated as well stirred reactors (WSR) or partially stirred reactors (PaSR).

In a combustion system a chemical kinetics mechanism is used to define the reaction pathways and the associated reaction rates leading to the change of species concentrations and heat release. An elementary chemical reaction of arbitrary complexity can be represented by

$$\sum_{j=1}^{N} \nu_{ji}^{'} X_j \Leftrightarrow \sum_{j=1}^{N} \nu_{ji}^{''} X_j \qquad \text{for} \quad \text{i=1, 2, …, M} \tag{15.18}$$

where $\nu_i^{'}$ and $\nu_i^{''}$ are the stoichiometric coefficients of the reactants and products, respectively, and X is the arbitrary specification of all chemical species for the M reactions. Since a species is usually involved in multiple reactions in a chemical kinetics mechanism, its production rate is the sum of its consumption and generation rates in the associated reactions, which can be expressed by a set of ODE's, given as

$$\frac{d[X_j]}{dt} = \sum_{i=1}^{M} (\nu_{ji}^{''} - \nu_{ji}^{'})(k_f \prod_{j=1}^{N} [X_j]^{\nu_{ji}^{'}} - k_r \prod_{j=1}^{N} [X_j]^{\nu_{ji}^{''}}) \qquad \text{for} \quad \text{i=1, 2, …, M} \tag{15.19}$$

where $[X_j]$ is the concentration of species X_j , and k_f and k_r are the forward and reverse rate coefficients for the ith elementary reaction, which are a function of temperature T and take the Arrhenius form as follows.

$$k = AT^{-b} \exp(-E / RT) \tag{15.20}$$

In the expression of the reaction rate coefficients, the constants A, b, and E are the pre-exponential factor, temperature-dependence factor, and activation energy, which are determined from experiments, and R is the universal gas constant. In a chemical kinetic mechanism, the reaction rate coefficients can range over several orders of magnitude. Also, due to the non-linear Arrhenius expression, the direct integration of chemical kinetics model usually involves solving a very stiff system of ODE's. This increases the computational effort considerably when a large number of species is included in the model.

The CHEMKIN code (Kee *et al*. 1991) is the most popular chemistry solver for the chemical kinetics problems described above for engine CFD codes (Kong *et al*. 2001), and its performance relies heavily on its ODE solver (DVODE). As compared to the Shell/CTC model, the direct integration of chemical kinetics can increase the computational expense by an order of magnitude or more, depending on the size of the chemical kinetics mechanism. A complete list of reactions that describe the chemical kinetics of even simple hydrocarbon fuels normally involves thousands of species and reactions. To solve a chemical kinetics mechanism of this

size for every computational cell would make the computational time unacceptable. Thus, skeletal mechanisms (containing of the order of 100 species and reactions) that are derived from their corresponding detailed mechanisms are usually employed to save computational expense while maintaining prediction accuracy. Other efforts for increasing the computational efficiency of the direct integration of chemical kinetics approach are discussed in Section 15.8.

As stated above, if a computational cell is treated as a well stirred reactor (i.e., perfectly mixed fuel/air), no turbulence effect on the combustion rate is considered at the sub-grid scale. This assumption has been shown to be effective in modelling Homogeneous Charge Compression Ignition (HCCI) engine combustion (Kong *et al*. 2001). For conventional diesel combustion, the reaction rate coefficients of a few elementary reactions are allowed to be tuned with the justification that uncertainties of these coefficients may result from the reduction of the chemical kinetics mechanism and other experimental uncertainties. It has also been shown in many studies (Kong *et al*. 2007) that this approach also performs very well under conventional diesel combustion conditions. In order to account for turbulence-chemistry interactions when the approach of direct integration of chemical kinetics is applied to study diesel combustion, the computational cells can also be assumed to be just partially stirred. The basic idea and physical meaning of the PaSR are similar to those of the CTC model. In the PaSR model, a "segregation" factor □ that is formulated by considering the turbulence and chemistry timescales is used to account for the imperfect, unresolved molecular diffusion processes in the reactor. The reader is referred to the studies of Nordin (2001) and Tao and Chomiak (2002) for more details.

Beyond the two combustion models discussed above, many other combustion models have been proposed for engine simulations. The major differences between the models are the treatment of the role of turbulence in the combustion process, the description of flame structure, and the use of chemical kinetics. For instance, in the Eddy Breakup (EBU) model (Spalding 1971) and its variants, the Eddy-Dissipation Model (EDM) (Magnussen and Hjertager 1976) and in the hybrid EBU/Arrhenius model (such as the CTC model), the burning rate of combustible mixture is mainly determined by the turbulent mixing rate, instead of by the rate of chemical reactions. The turbulence timescale is usually used as the control parameter of the mean chemical conversion rate in these models, which is characterized by the breakup or turnover time of turbulence eddies. However, with the direct integration of the chemical kinetics approach, it is normally assumed that the turbulent mixing rate is ultra-fast, and thus the burning rate of the mixture is largely controlled by the chemical kinetics of the reactions. Using flamelet models, the structure of a turbulent flame is described as a laminar flame subject to the same aero-thermo-chemical conditions and the primary effect of turbulence on combustion is to increase the effective flame surface area. For the non-premixed combustion in diesel engines, the Representative Interactive Flamelet (RIF) model (Peters 2000) is a very attractive approach that decouples chemical kinetics and turbulence, while maintaining tight local coupling between chemical

kinetics and molecular transport (Haworth 2005). Although not used widely, the Conditional Moment Closure (CMC) model (De Paola *et al*. 2008) and the Probability Density Function (PDF) methods (Zhang 2004) have also been proposed for engine combustion simulations.

Many studies have been conducted to evaluate or compare these combustion models for engine simulations. The general conclusions are that none of them can perform equally well over the entire range of engine conditions of interest and it is necessary to tune the model constants while maintaining their physical meanings to expand the range of applicability of combustion models. For example, in a recent study of Singh *et al*. (2006), the Shell/CTC, RIF, and direct integration with detailed chemistry combustion models were compared against optical diagnostic data for multi-mode combustion in a heavy-duty DI diesel engine. They showed that all three combustion models gave reasonable predictions of the cylinder pressure and heat release rate trends for the investigated cases, and the direct integration with detailed chemistry model performed better under low temperature and premixed combustion modes, as expected. Since each model has its own applicable ranges, it is thought that their combinations may help to extend their applicability. Efforts to develop hybrid or universal combustion models are described in the study of Tan and Reitz (2004).

Pollutant Emissions Modelling

In-cylinder pollutant reduction by optimizing the combustion system can help the engine industry to meet more-and-more stringent emission standards. Therefore, reliable emission modelling in an engine CFD code is essential for its practical use in engine design and development. For a conventional diesel engine, nitric oxide (NO_x) and soot emissions are the pollutants of most concern. For advanced combustion concepts, such as HCCI, it has been demonstrated that both NOx and soot emissions are substantially reduced, but with the price of increased carbon monoxide (CO) and unburned hydrocarbons (UHC) emissions. This section reviews the most widely used models and surveys methods for the predictions of these emissions in multi-dimensional CFD codes.

NO_x modelling

The formation of NOx in a diesel engine is primarily determined by the local temperature, oxygen concentration, as well as residence time. Consequently, to predict well engine-out NOx emissions requires that all three aspects are accurately resolved in CFD modelling and a good chemical kinetics model is also crucially necessary. With extensive understanding of its chemical kinetics, quantitative prediction of NOx formation becomes possible with engine CFD codes that include detailed chemistry. The thermal NOx reactions include

$$\begin{aligned} &O+N_2 \Leftrightarrow NO+N \quad (1)\\ &N+O_2 \Leftrightarrow NO+O \quad (2)\\ &N+OH \Leftrightarrow NO+H \quad (3) \end{aligned} \tag{15.21}$$

However, four different routes, including the thermal route, the prompt (Fenimore) route, the N_2O route, and the fuel-bound nitrogen route have been identified as important in the formation of NOx (Bowman 1993). Petroleum fuels contain negligible nitrogen, and thus the fuel-bound nitrogen route is usually not considered in engine CFD simulations. It is also noted that in engine simulations, the quantity of NOx is normally represented by NO, and a scale factor of 1.533 (the ratio of the molecular weight of NO_2 to NO) is used to convert NO to NOx, which is consistent with ASTM standards. The extended Zeldovich mechanism (Heywood 1988) for the thermal NO, as formed by the three elementary reactions in equation (15.21), describes the chemical kinetics of NO formation at high temperatures. The extended Zeldovich mechanism has been well adopted in engine simulations, especially for conventional diesel engines in which the in-cylinder gases are subjected to very high temperatures. However, under rich combustion conditions the prompt (Fenimore) route of NO formation can be prominent. This is because the radical CH, which is formed as an important intermediate of rich combustion, reacts with the nitrogen to form hydrocyanic acid (HCN), which reacts further to NO (Warnatz *et al*. 2006). Under low temperatures and lean combustion conditions, the molecular nitrogen N_2 is attacked by O atoms and with the presence of a third-body molecule M (which can be any molecule in the system) nitrous oxide (N_2O) is formed and subsequently reacts with O atoms to form NO.

It is obvious that in order to correctly predict the NOx emissions of diesel engines operating under a wide range of conditions, the prompt and N_2O routes of NO formation are needed to supplement the thermal route. A complete list of elementary reactions for NO formation involves over a hundred reactions, such as seen in GRI 3.0 mechanism for methane combustion (Smith *et al*. 2008) and the extended Leeds methane oxidation mechanism (Hughes *et al*. 1999). The size of the detailed mechanism of NO formation is beyond the computer time limit of practical engine CFD simulations, so mechanism reduction is needed. Sun (2007) extracted 12 important reactions including 4 species from the GRI 3.0 mechanism for the description of NO formation. He showed that the reduced NO mechanism performed similarly with the original detailed one under various conditions. In recent research by Sjöberg and Dec (2008), a NOx-induced combustion-phasing run-away phenomenon was found in HCCI engines when testing at high-load conditions. It was attributed to the fact that the combustion phasing was advanced by NOx contained in EGR and residual gases. The authors have numerically investigated this phenomenon and found that the reaction $HO_2 + NO \Leftrightarrow NO_2 + OH$ plays a significant role. This indicates that this reaction has to be included in reduced NO chemical kinetics mechanisms to account for its influence on fuel ignition.

Soot modelling

Soot formation processes in a diesel engine are much more complicated than chemical-kinetic-controlled NOx formation. It involves both chemical and physical processes, including the chemical kinetics leading to soot precursors (acetylene, benzene, and polycyclic aromatic hydrocarbons (PAHs)), particle nucleation, surface growth, surface oxidation, particle coagulation, and particle dynamics. A complete understanding of the complex phenomena of soot formation is still under experimental exploration, and thus modelling soot formation becomes very challenging.

For engineering practice, most soot modelling in engine CFD codes usually only considers the chemical process, which directly correlates gas-phase soot precursors with engine-out soot emissions. For example, the two-step soot models. In two-step soot models, two competing processes, namely soot formation and oxidation, are considered of the form

$$\frac{dM_s}{dt} = \frac{dM_{sf}}{dt} - \frac{dM_{so}}{dt} \tag{15.22}$$

where M_s, M_{sf}, and M_{so} represent the mass of the net soot produced, soot formed, and soot oxidized, respectively. In the study of Nishida and Hiroyasu (1989), two equations of Arrhenius form were used to calculate soot formation and oxidation rates following.

$$\begin{aligned} \frac{dM_{sf}}{dt} &= A_f M_{fg} P^{0.5} \exp(-\frac{E_{sf}}{RT}) \\ \frac{dM_{so}}{dt} &= A_o M_s \frac{P_{O_2}}{P} P^{1.8} \exp(-\frac{E_{so}}{RT}) \end{aligned} \tag{15.23}$$

where E_{sf} and E_{so} are given values of 12,500 kcal/kmol and 14,000 kcal/mol. A_f and A_o are determined by calibrating with measured soot emissions.

As seen in the equation, the soot formation rate is directly linked to the concentration of fuel vapour M_{fg} and the soot oxidation rate is a linear function of the oxygen partial pressure P_{o2}. This two-step soot model was found to give relatively low peak in-cylinder soot concentrations. Patterson *et al*. (1994) attributed this to the soot oxidation rate equation, and thus replaced it with a more realistic soot oxidation model adopted from Nagle and Strickland-Constable (1962), in which carbon oxidation occurs by two mechanisms whose rates depend on surface chemistry, involving more reactive A sites and the less reactive B sites. With more understanding of soot formation, the use of fuel vapour as the soot precursor in the formation equation also became questionable. Also, when detailed chemistry was employed in engine simulations, the fuel vapour can no longer be used as the indicator of soot formation since it soon decomposes to other smaller intermediate hydrocarbons once low-temperature occurs. In this context, Kong

et al. (2007) considered a more realistic soot precursor, acetylene C_2H_2, to replace the fuel vapour in their soot formation formula, and the values of activation energy were changed correspondingly. Due to their simplicity and moderate accuracy, two-step soot models have been widely used in engine CFD codes. It should not be expected to obtain quantitative predictions of soot emissions from such simplified soot models for a wide range of engine operating conditions. However, qualitative description of sooting tendencies can be captured fairly well if the model constants are fine tuned against existing measured data for the investigated engines.

To improve the soot formation models and also to broaden the range of applicability of soot models, Tao *et al*. (2004) proposed a phenomenological soot model which is based on four global stages: particle nucleation, surface growth, surface oxidation, and particle coagulation. In the first stage, diacetylene (C_4H_2) and naphthalene were used as inception species for soot nucleation. The soot surface growth was described using an active site model proposed by Frenklach and Wang (1991). The Nagle and Strickland-Constable's O_2 oxidation model (1962) and Neoh *et al*.'s OH oxidation model (1984) were both used to describe the soot surface oxidation. Finally, soot coagulation was simulated using two empirical equations. This soot model was validated against measured data from n-heptane spray combustion under diesel-like conditions, and the spatial and temporal soot distributions were well predicted. Based on the structure of this phenomenological soot model, Tao *et al*. (2005) further proposed a nine-step soot model for diesel engine simulations, with which successful applications were also reported in their later study for diesel engines operated over a wide range of conditions (Tao *et al*. 2009).

Since, as stated above, soot formation in diesel engines involves very complex chemical and physical processes, complete models for these processes in multi-dimensional engine CFD simulations would incur unacceptable computational expense. For the foreseeable future, phenomenological models can still be very useful. Improvements to these models are needed to better predict the size distribution of engine-out soot emissions in order to accommodate anticipated demands of meeting stricter legislations.

CO and UHC modelling

Modelling CO and UHC emission has received growing attention as low temperature combustion is attracting more interest in diesel applications. CO forms in fuel-rich regions due to low oxidation rates resulting from the large amount of EGR gases needed to suppress the combustion temperature. In addition, CO is found in lean regions that are too cool for complete combustion. The kinetically controlled CO mechanism is well understood, which is fully described in the skeletal or detailed fuel oxidation mechanisms used in engine CFD simulations (Park and Reitz 2007). The key issue of predicting CO emissions is to have a correctly predicted fuel-air mixing rate. This depends on having reliable turbulence and spray models, as well as adequately-resolved engine geometries to account for their influence on the flow patterns that secondarily affect the mixing process. UHC is

the consequence of the incomplete combustion of fuels. In diesel engines, UHC forms due to both over-mixing and under-mixing of the fuel sprays (Heywood 1988). Another source of UHC is wall quenching whose influence is largely determined by the degree of spray impingement on the combustion chamber walls. Early injections, which are required to prepare a well-mixed fuel charge, may result in a portion of the injected fuel entering the crevice region, and the trapped fuel can escape the main combustion stage, and then reenter the squish region during the expansion stroke. The escaped unburned fuels finally contribute to the engine-out UHC emissions. It is obvious that to model the complex UHC formation processes, all these possible causes need to be considered. The crevice flow can be simulated using a phenomenological crevice flow model, such as the one proposed by Reitz and Kuo (1989) for engine CFD modelling. The crevice flow can be also directly simulated by using an additional crevice mesh attached to the main computational domain. It has been found by the authors' study that the strength of the corner vortex (which affects the mixing rate) caused by the pushed-out crevice flow is sensitive to the width and length of the crevice mesh. This indicates that the geometry of the crevice volume needs to be carefully meshed. The spray-wall interaction model together with the heat transfer model that accounts for heat conduction through the liquid wall fuel film are crucial to model UHC formation due to the wall quenching, as discussed next.

Heat Transfer Modelling

As discussed in the previous section, heat transfer between the in-cylinder flows and the cylinder walls can significantly influence engine emissions, such as UHC. In addition, heat transfer also has substantial influence on engine performance and efficiency. In most cases, convective heat transfer of the gas phase is the main contributor to the heat flux from the in-cylinder flows to cylinder walls. Therefore, convective heat transfer has been of primary interest in engine heat transfer models. However, in a high temperature environment, especially when a large volume of soot is formed in the cylinder, the heat flux due to radiation becomes very important. Furthermore, if the spray impingement becomes severe, heat conduction due to the resulting fuel film cannot be neglected. An early review of engine heat transfer is found in Borman and Nishiwaki's study (1987). Widely used and newly developed engine heat transfer models for multi-dimensional CFD simulations are briefly reviewed here.

To resolve the details of the gas-phase convective heat transfer in engines, the very thin thermal boundary layers have to be resolved in order to obtain the velocity and temperature profiles in the near wall region. This requires use of a very fine mesh resolution, which can make CFD simulations become impractical. A practical way of removing the requirement for fine meshes while maintaining physically correct predictions of the convective heat transfer is to use velocity and

temperature wall functions. The classical temperature wall function was based on assumptions of a steady and incompressible flow without source terms under which the Reynolds analogy is valid. The traditional wall function formulations also assume a constant Prandtl number across the entire boundary layer. Han and Reitz (1997) pointed out that these assumptions and simplifications were questionable when such wall functions were applied to engines in which the flow compressibility must be considered. A curve-fit technique was employed in Han and Reitz's (1997) study to construct a simplified function of dimensionless viscosity to the turbulent Prandtl number. This enabled a direct integration to be performed of the one-dimensional energy equation, so that an analytic solution of the temperature profile can be obtained and used for calculating the convective heat transfer. The proposed heat transfer model was applied to SI and DI engines, and satisfactory agreement between the predicted wall heat fluxes and measured data was obtained under both firing and motoring conditions.

As shown in the study of Abraham and Magi (1997), the radiant heat loss characteristics are strongly correlated with the soot concentration and temperature in engines. Recent research of Musculus (2004) has shown that the radiation heat loss has a measurable influence on in-cylinder temperatures and NOx emissions. The research demonstrates the significance of radiation heat transfer models in engine CFD simulations. The Discrete Ordinates Method (DOM) is a well adopted method that solves the Radiation Transfer Equation (RTE) for the intensity of radiation in a set of ordinates, and the RTE and its boundary conditions are found in (Fiveland 1988). The summation of the intensity of radiation of each ordinate is substituted into the energy equation, and the effect of radiation heat transfer on the spatial temperatures is thus revealed. For applications of DOM in engine simulations, the studies of Abraham and Magi (1997), Wiedenhoefer and Reitz (2003), and Smith (2008) are examples. It should be noted that since in-cylinder soot acts as a blackbody in the radiation heat transfer model, the quantity of soot predicted by the emissions model is influential on the calculated radiant heat loss.

With advanced injection timing required to obtain better-mixed fuel/air, an increased amount of injected fuel can impinge on the engine walls due to the low gas density and corresponding long spray penetration. When the liquid fuel films are formed, the convective heat transfer between the gas phase and the liquid phase, the heat conduction between the liquid film and the wall, as well as the energy used to vaporize the fuel must all be considered in engine CFD simulations. The geometrical dimensions of the fuel films, such as their thickness and area, depend on the dynamical characteristics of the impinging sprays and their interactions with the engine walls. The evolution of the fuel films during the various engine strokes is affected by the local thermal and dynamical conditions, such as the turbulence strength and wall temperature. A good review on this topic is given by Kong (2007). Jia *et al*. (2008) compared three widely used spray/wall interaction models, i.e., the O'Rourke and Amsden model (2001), the Bai and Gosman model (1995), and the Han, Xu, and Trigui model (Han *et al.* 2000), for early injected sprays under HCCI-like conditions. They concluded that neither of the models

outperformed the others, and all of them need to be further improved for predictions of the film thickness and the corresponding vapour distribution. The inaccuracy of these models was attributed to the fact that the conditions under which the experiments were conducted for the model derivation and validation are usually different from the actual engine environment.

Efficient Multi-dimensional Simulation of Diesel Engine Combustion with Detailed Chemistry

This section presents three approaches that can be used in efficient multi-dimensional simulation of diesel engine combustion. The approaches include a newly developed Adaptive Multi-grid Chemistry (AMC) model which allows a fine mesh to be used to allow adequate resolution for the spray simulations, while dramatically reducing the number of cells that need to be computed by chemistry solvers. The second approach to improve efficiency uses a recently developed a set of spray models which reduce numerical grid size dependencies; thus enabling the simulation of DI combustion on relatively coarse meshes to save computing time. The third approach parallelizes the chemistry solver based on the computing load so that simulations can be performed on relatively coarse meshes on multiple processors.

Adaptive multi-grid chemistry (AMC) model

As stated before, solving the detailed chemistry in combustion systems is essentially to solve groups of extremely stiff ODE's. The numerical time step may be required to be comparable to the smallest characteristic time scale of change of chemical species for reasons of stability and/or accuracy (Reitz 1980). In practical engine CFD simulations with directly solved chemistry by integrating the stiff ODE's, the computational time spent on the chemistry solver can be over 75% of the total running time depending on the size of the chemistry mechanism. This has motivated many efforts for reducing the computational time of chemistry solvers to increase the overall efficiency of multi-dimensional engine CFD modelling with detailed chemistry. These efforts include replacing the time consuming direct integration by using more efficient search methods based on tabulated combustion chemistry, such as the *in situ* adaptive tabulation (ISAT) proposed by Pope (1997); using a semi-implicit ODE solver to reduce the integration time, as proposed by Liang *et al*. (2007); adaptively determining the size of chemical kinetic mechanism for different combustion stages (Liang *et al*. 2009); and multi-grid or multi-zone techniques.

The multi-grid or multi-zone techniques have achieved great success for certain classes of problems (Aceves *et al*. 2000, Flowers *et al*. 2003, Babajimopoulos *et al*. 2005). It was reported that an order of magnitude timing reduction was obtained for HCCI engine combustion. Shi and Reitz (2008) extended the use of the

multi-grid technique to simulate direct injection (DI) engines and proposed an Adaptive Multi-grid Chemistry (AMC) model which is discussed next.

The basic idea of multi-grid techniques is to group thermodynamically similar (in terms of pressure, temperature, species composition) cells in engine combustion simulations in order to reduce the calling frequency to the chemistry solver. Two key steps are involved: (1) mapping (grouping) eligible cells together and solving the grouped cells with the chemistry solver, (2) redistributing the group information back onto individual cells so that the gradients can be preserved.

Adaptive multi-grid mapping technique

The key of mapping appropriate cells into a group is to find appropriate measures of similarity, as well as to establish the grouping criteria. In a computational cell assumed to be a WSR, the temperature, pressure, and species fractions describe the composition space that determines the reaction progress. Due to the temperature sensitivity of chemical reactions, it is obvious that temperature should be used as one of the grouping criteria. In the low Mach number flows typical of DI and HCCI engines, pressure gradients are small, and thus the pressure is not needed as a grouping criterion. Strictly grouping cells with similar composition requires a search and comparison for every individual species, but this is not practical because of two concerns. Firstly, the search expense would be too large and thus would reduce the computational efficiency of the multi-grid model. Secondly, it is difficult to define an appropriate criterion of similarity for each species and thus to efficiently group as many cells as possible. Hence, it is necessary to define an indicator that represents both composition information and combustion progress. The so-called progress equivalence ratio (Babajimopoulos *et al*. 2005) is introduced, which is defined by

$$\phi = \frac{2C^{\#}_{-CO_2} + H^{\#}_{-H_2O}/2 - z'C^{\#}_{-CO_2}}{O^{\#}_{-CO_2-H_2O} - z'C^{\#}_{-CO_2}} \tag{15.24}$$

In this equation, the superscript # denotes the number of atoms of each species. The equivalence ratio is defined based on complete combustion, but the products CO_2 and H_2O are excluded, as indicated by the subscripts in the ϕ expression. z' defines the proportion of fuel oxygen to fuel carbon, and for hydrocarbon fuels without oxygen, z' is zero. For DI engines, because significant gradients of species mass fraction can exist, there is no guarantee that cells with similar equivalence ratio contain similar mass fractions of each species, especially for those cells that are distributed in very different physical locations. Therefore, it is necessary to limit the searching area in order to better group cells that have similar species composition. Due to convection and diffusion, neighbor cells can have similar thermodynamic conditions, as well as species composition. In particular, in the early stages of combustion when large gradients, such as temperature gradients exist, the similarity may merely exist among closely adjacent cells and therefore the grouping process needs to be limited to a narrow region. However, as time

progresses energy and species are transported and mixed such that there is a trend toward local uniformity. Correspondingly, the grouping process can be extended to larger and larger regions. This means that the grouping region should be determined adaptively.

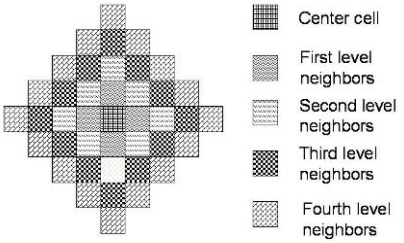

Fig. 15.1 Adaptive multi-grid grouping (Adapted from Shi *et al*. 2009)

Accordingly, a temperature inhomogeneity criterion was used as the indicator for assessing the grouping region adaptively, where

$$\sigma_T = \sqrt{\frac{1}{n-1}\sum_{i=1}^{n}(T_i - \overline{T})^2} \tag{15.25}$$

In equation (15.25), $\overline{T}$ denotes the average in-cylinder temperature and T_i is individual temperature of each of the n cells. The concept of adaptive neighbour search is further illustrated in Fig. 15.1 using a 2-D schematic mesh. It can be seen that the first level search only covers the four adjacent cells (six if 3-D mesh) of the reference cell. If the in-cylinder temperature inhomogeneity is below pre-specified values, the search can then be expanded to the second level or higher. The maximum search level was limited to four, where a maximum of 129 cells can be reached using the fourth level search in 3-D block structural mesh. It should be noted that a similar treatment could also be applied to unstructured meshes. In this case, a convenient approach would be to pre-define a representative search radius and to define the search level as a multiplier used to adjust the search area accordingly.

In the research of Shi *et al*. (2009), it has been found that for HCCI engines the grouping procedure can also be applied regardless of the location of the cells as long as they are thermodynamically similar. This is to say the search can be applied to the whole computing domain. Clearly this is due to the assumption of homogeneous charge in the simulation of HCCI engines. In contrast to the neighbor mapping, it is referred to as global mapping. Similar to specifying a criterion of temperature inhomogeneity for the neighbor mapping, by defining a lower value of temperature inhomogeneity global mapping can be regarded as a fifth level

search, although in this case the location of the cells is no longer used as an additional criterion.

Remapping technique

After the cells are mapped into a group and the group is allowed to react using the averaged conditions, it is not possible to exactly remap the mass fractions of each species back onto the original cells, because that requires solving the complete chemistry for each cell. Thus, an algorithm is needed to redistribute the species back to the cells, such that the gas properties of each cell remapped from the group would be comparable with those if the chemistry of each cell were to be solved individually.

A straightforward way of remapping the information of groups back onto their cells is to assign the mean value of the group's characteristics to each included cell. This means that all the cells in a group would have the same gas properties. It is obvious that this procedure would introduce artificial diffusion to the species continuity equations if significant composition gradients were present among the grouped cells. This relatively inaccurate method has proven to be inapplicable even for HCCI simulations (Shi *et al*. 2009).

Babajimopoulos *et al*. (2005) proposed an improved method that attempts to preserve gradients of temperature and species composition. The method is described as follows. First, before the mapping procedure, a new quantity, ch, is defined using the number of C and H atoms of all participating species, except the combustion products, CO_2 and H_2O, where

$$ch = 2C^{\#}_{-CO_2} + \frac{H^{\#}_{-H_2O}}{2} \tag{15.26}$$

The ch number of a group is the sum of the ch number of all cells in that group. After the chemistry calculation, all species, except CO_2, H_2O, O_2, and N_2 are assigned back to the group's cells based on ch. In this case, the mass of species k in an individual cell is obtained from the ratio

$$m_{k,cell} = m_{k,group} \frac{ch_{cell}}{ch_{group}} \tag{15.27}$$

In this way, the mass of each species in the group is also conserved. Consequently, some cells can have more or fewer C or H atoms than before the mapping process, and thus the rest of the cells in the group need to be adjusted to maintain the total number of C and H atoms in that group. After that, O_2 is distributed to maintain the total number of O atoms in each cell and adjustment of N_2 is used to conserve the mass of each cell. Since after the remapping process the mass fraction of each species in each cell is known, the change of the specific internal energy of each cell can be obtained from the difference between the internal energy of formation of the species present in the cell before the grouping

process and that after the remapping process. The cell temperature can be computed from the updated specific internal energy and the mass fraction of species. This method is called the gradient-preserving remapping method.

Mesh-independent spray models

The increased application of computational fluid dynamics to combustion problems incorporating detailed chemistry and the desire for rapid generation of results causes a need to use coarser computational meshes. Furthermore, as CFD is applied to a wider range of applications from small bore light-duty engines to large bore ship engines, the solutions must be able to yield accurate results over a wide range of grid sizes.

The requirement of short runtimes and the resulting use of coarse computational grids pose a problem for the solution of the spray physics because the drop sizes are often orders of magnitude smaller than the size of a computational cell. Because the spray is not completely resolved on the computational mesh, sub-grid spray models are required in order to describe the physics associated with the injection event.

The solution to spray problems involves modelling of a two-phase flow process and thus includes the complications of dealing with the interfaces between interacting fluids. In the fuel injection process the droplets make up the liquid phase and the entrained air and vaporized fuel make up the vapour phase. Figure 15.2 shows the conceptual spray process presented by Abani *et al*. (2008). As discussed previously, a popular solution method is the Lagrangian-Drop and Eulerian-Fluid (LDEF) approach first presented by Dukowicz (1980).

Severe mesh dependency has been observed in the calculation of droplet drag using the LDEF approach. In the standard LDEF implementation in engine CFD codes, such as KIVA, the particle relative velocity is defined as the difference between the particle velocity and the gas phase velocity at the nearest node. When coarse computational grids are used the size of the cell is much larger than the area occupied by the spray resulting in a dampening of the momentum transfer between the droplets and surrounding gas phase. The poor prediction of the momentum coupling results in an under prediction of the gas-phase momentum and a resulting underprediction of the spray penetration. This problem is most severe in the near nozzle region where the droplets are very close together and occupy only small portions of the Eulerian mesh. Figure 15.3 from Abani *et al*. (2008) depicts the damping of momentum transfer due to inadequate mesh resolution. Abraham (1997) showed that accurate modelling of the near nozzle region required grid resolution on the order of the orifice diameter. However, it is not feasible from a computational time standpoint to solve engine problems on such a fine mesh. Furthermore, a fundamental assumption of the LDEF approach is that the volume fraction of droplets in each cell is small, i.e., the void fraction is near one. The use of near droplet size meshes may violate this assumption. Therefore, it is of much interest to investigate methods that allow accurate spray simulation without using an exceedingly fine grid size. The method used in this investigation

was proposed by Abani and Reitz (2007) where the droplets are solved in the traditional fashion while the entrained air is modelled using turbulent gas-jet theory.

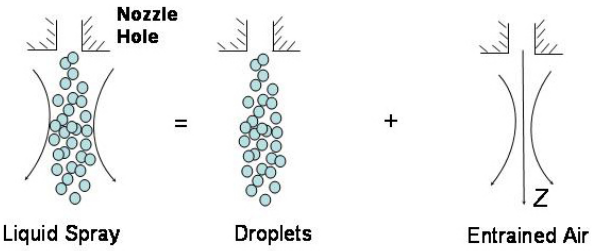

Fig. 15.2 Schematic of spray process (Adapted from Abani *et al*. 2008)

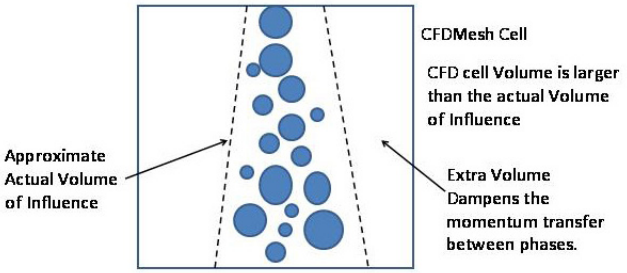

Fig. 15.3 Illustration of damping of momentum transfer due to inadequate mesh resolution (Adapted from Abani *et al*. 2008)

Further grid size dependency exists in LDEF spray simulation in the widely used O'Rourke collision model (O'Rourke 1981). In the O'Rourke model collisions are only considered between droplets which are located in the same collision cell. For simplicity the Eulerian CFD cell is often taken to be the collision cell. Thus, a change in the CFD mesh size results in a change in the possible number of collisions. Schmidt and Rutland (2004) have shown that the use of a separate collision mesh greatly reduced mesh dependency in spray problems. In the present implementation, the approach of Munnannur (2007), where a radius of influence (ROI) that is not based on the cell size, is adopted to assign possible collision partners for each parcel.

Gas-Jet spray model

Abani *et al*. (2008) showed that mesh size dependency can be reduced by using turbulent gas-jet theory to model the air entrained by the injected fuel. Their approach was to assume that the relative velocity of between a droplet and the gas

phase was equal to that between the droplet and a turbulent gas-jet with the same mass and momentum as that of the injected fuel. This approach imposes the axial component for the gas phase velocity as a function of distance from the nozzle in the near nozzle region, which is used in the droplet acceleration equation given by:

$$\frac{dU}{dt} = \frac{3}{8} C_D \frac{\rho_g}{\rho_l r_d} \left| U - V_{gas} \right| \left(U - V_{gas} \right) \tag{15.28}$$

Here U is the droplet velocity vector, C_D is the droplet drag coefficient and is a function of Reynolds number, ρ_g and ρ_l are the gas and liquid phase densities respectively, r_d is the droplet radius, V_{gas} is the gas phase velocity vector given as $V_{gas} = (V_x, Vy, Vz)$ where V_y and V_z are components perpendicular to the spray axis and obtained from the Eulerian gas phase solution. Finally, V_x, the axial component of the gas phase velocity is found from gas-jet theory (Abraham 1996) as:

$$V_x = \min \left[U_{inj,} \frac{3 U_{inj} d_{noz} \sqrt{\frac{\rho_l}{\rho_g}}}{K_{entr} x} \left(\frac{1}{\left(1 + \frac{12 r^2}{K_{entr}^2 x^2} \right)^2} \right) \right] \tag{15.29}$$

where U_{inj} is the effective injection velocity, d_{noz} is the nozzle diameter, K_{entr} is a model constant taken to be 0.7 as suggested by Abani *et al*. (2008), x is the position downstream of the nozzle on the spray axis, and r is the radial position ($r^2 = y^2 + z^2$).

Grid independent collision model

Munnannur (2007) reduced grid size dependencies of the O'Rourke collision model by employing a radius of influence (ROI) method. The ROI is a distance around a parcel which contains other possible collision partners, thus allowing mesh independent collision calculations without the added complexity of a separate collision mesh. The droplets are then allowed to collide with any other droplet within their collision volume regardless of what CFD cell the droplet is located in.

Furthermore, Munnannur (2007) implemented a method for merging parcels in order to reduce the computational time required in the collision calculations based on the method presented by Lapenta (2002). Simple binary merging cannot conserve mass, momentum, and energy simultaneously, however a ternary merge followed by a binary split allows the conservation of mass, momentum, and energy. In that implementation parcels in a collision volume are sorted by ascending mass, next the velocities of each group of three neighbouring parcels in the mass sorted list are compared using equation (15.30), and finally groups of parcels having velocity errors $\varepsilon_{vel\,i,\,j}$ less than 0.1 are merged into two parcels, where

$$\varepsilon_{\text{vel i,j}} = \frac{\left|u_i - u_j\right|}{\left|u_i\right| + \left|u_j\right|} \tag{15.30}$$

Code parallelization

As the cost of computers dramatically decreases, code parallelization becomes a very effective approach of saving computing times in engine CFD simulations. Traditional parallelization of CFD codes is based on domain decomposition, i.e., evenly distribute the total number of computational cells to the available processors. However, under some circumstances, cells that have to be computed using the chemistry solver are not distributed in space in a homogeneous fashion. For instance, the cells that have lower temperature or lower concentration of combustible species than a specified criterion can be skipped. Even though they may be distributed evenly in space, the computing time of integrating the stiff ODE's that describe the chemical reactions might be very different because of their different stiffness. In some cells, the ODE's may be stiffer and thus require more iterations than other cells. This indicates that a load balancing strategy is needed to improve the parallelization efficiency. A good load-balancing scheme has to keep the processors doing useful computations for as much of the time as possible, i.e., to minimize the waiting time of all processors. A load-balancing scheme that is based on historical uses of computing resources is described below (Shi *et al*. 2009).

When a detailed reaction mechanism is solved in a CFD code, most of the CPU time is spent on that part. In addition, the communication time of the input and output data of chemistry solvers is small in the overall simulations. Therefore, usually only the chemistry computation is parallelized. In the load balancing parallel scheme, before the chemistry solver is called, all cells that need to be computed using the chemistry solver are listed. In the initial step, those cells are evenly assigned to the available processors. Then, the time required by a processor can be defined as the ratio of the number of cells computed by this processor and the CPU time taken in the previous time step:

$$P_i^{n+1} = \frac{N_{ckcell,i}^n}{t_i^n} \tag{15.31}$$

where, superscript n denotes the time step; subscript i indicates the i-th processor. Starting from the next time step, the cells can be assigned based on the time spent in processor P_i^{n+1}:

$$N_{ckcell,i}^{n+1} = \frac{P_i^{n+1}}{\sum_{i=1}^{N_{cpu}} P_i^{n+1}} \mathrm{N_{ck}} \tag{15.32}$$

in which N_{ck} is the total number of cells required in the chemistry computation. In this way, a dynamic balance between the processors is achieved. To smooth the process, a relaxation factor, α, is introduced in equation (15.33) as

$$P_i^{n+1} = \alpha P_i^n + (1-\alpha)\frac{N_{ckcell,i}^n}{t_i^n} \tag{15.33}$$

The load-balancing scheme is also especially useful for heterogeneous computer clusters with different machine hardware.

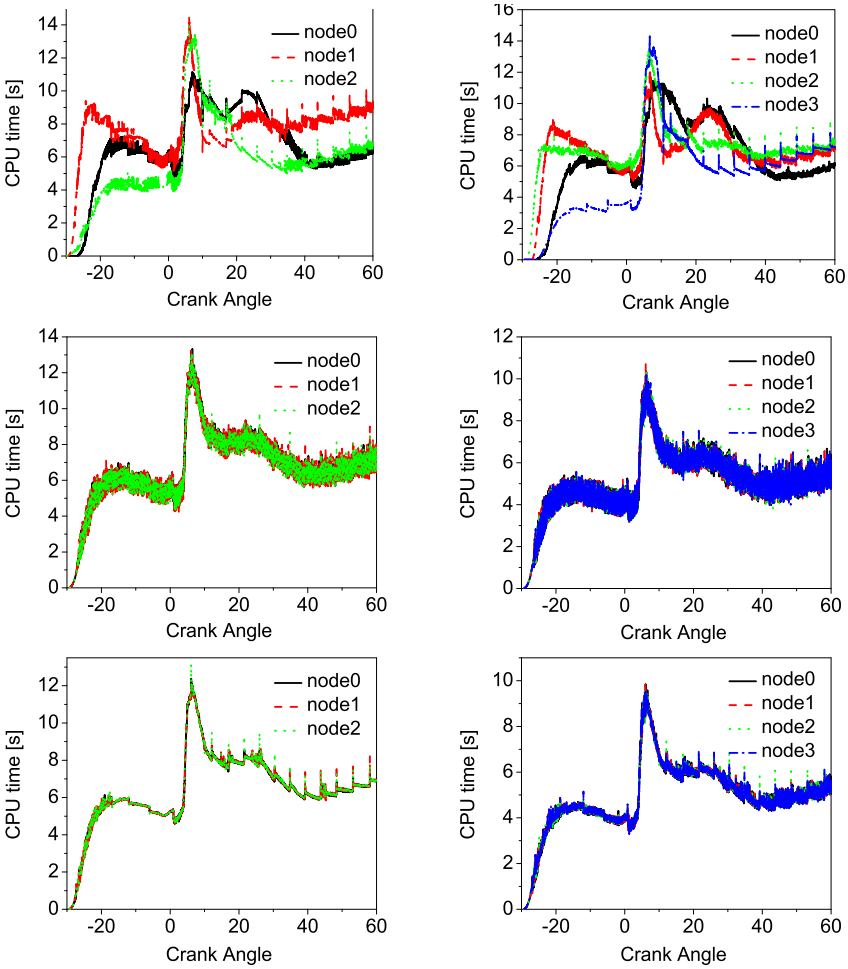

Fig. 15.4 CPU time consumed by each node with different schemes: top: domain decomposition; middle: load balancing without relaxation factor (α = 0); bottom: load balancing with relaxation factor α = 0.5. Left column: 3 CPUs; right column: 4 CPUs

The implementation of the parallel code was tested on a HSDI engine. Figure 15.4 shows the CPU time consumed by each node at each time step in parallel computations. The left column uses three processors, and the right column uses four processors. The first row uses the conventional domain decomposition method. As aforementioned, the computation load is not well scaled. At the beginning, the combustion mainly occurs in the central region of the combustion chamber. Therefore, the processor(s) in the middle array, which is the dashed line in the left column, and the dashed line and dotted line in the right column, need(s) more CPU time to complete the job(s). As the main combustion region expands, the CPU time consumed by the processors varies and is not well scaled.

The second and third rows employ the load-balancing scheme described above. The second row does not consider the relaxation factor, i.e., $\alpha = 0$. The CPU time of the processors is well scaled, but subject to significant fluctuation. With the implementation of the relaxation technique, these fluctuations are successfully removed, as illustrated in the third row of Fig. 15.4. A better scalability is then achieved. Figure 15.5 summarizes the longest time that the processors consumed at each time step, and this is the bottleneck time of all the processors. The area under the curve is the total wall time of the parallel computation. Compared to the original domain decomposition method, the current load-balancing scheme greatly improves the efficiency and scalability of the parallel code. The relaxation technique works very well with the load-balancing scheme.

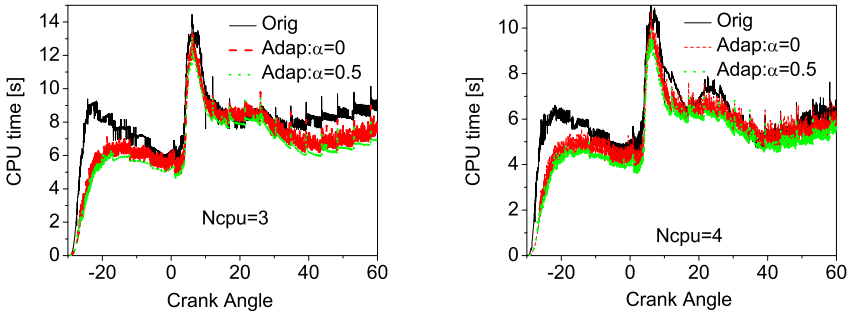

Fig. 15.5 Profile of the longest time the processors consumed (bottle-neck time) at each time step

CFD Codes for Engine Simulation

The increasing confidence of using CFD techniques in engine designs depends on continuously improved CFD codes in terms of their fidelity and ease-of-use. Two pioneering works including the KIVA family of CFD codes (developed at Los Alamos National Laboratory (LANL) in the United States) and the STAR-CD family of CFD codes (developed at Imperial College in Great Britain) have made tremendous contributions in bringing CFD techniques to engine simulations. Both

of these codes are being continuously developed by researchers worldwide and their efforts have yielded a great deal of innovative models whose applications also have benefited other engineering areas, such as turbines and ramrockets. Since its initiation, the KIVA code has been kept in an open source form, which facilitates its further developments. Recently, another open source CFD code, OpenFOAM, has attracted increasing interest from the engine community. STAR-CD has become commercial software offered by CD-adapco. The other main competitors in commercial engine CFD software are FIRE, FLUENT, and VECTIS. All of these CFD codes are briefly reviewed here.

Open source codes

KIVA has evolved from its original release in 1985 to its latest version KIVA 4. The family contains KIVA (1985), KIVA II (1989), KIVA 3 (1993), KIVA 3V (1997), KIVA 3V release 2 (1999), and KIVA 4 (2006). KIVA is developed in FORTRAN language, and the detailed description of its governing equations, numerical schemes, and the original sub-models can be found in the KIVA II report (Amsden *et al*. 1989). The KIVA II code enhanced its preceding versions by improving its computational accuracy and efficiency and its ease-of-use. The KIVA II equations and numerical solution procedures are more general, so that it can be applied for various studies of reaction flows. The meshing methodology of KIVA II prevented it from efficiently solving flows in complex geometries. Thus, KIVA 3 was developed to overcome this drawback by introducing a block-structured mesh with connectivity defined through indirect addressing, and a corresponding efficient storage method was introduced (Amsden 1993). In 1993, the KIVA 3V code was released with a special focus of treating motions of vertical or canted valves in IC engines (Amsden 1997). In KIVA 3V the RNG k-ε turbulence model also became a standard option and other improvements were made to the wall heat transfer and soot models. The subsequent version of KIVA 3V, KIVA 3V release 2, added many new features to enhance the robustness, efficiency, and usefulness of the overall program for engine modelling, such as an automatic restart of the cycle with a reduced time step in case the code tends to crash, a deactivation option for a port region when it is not used in the engine cycle, an improved wall film model, etc. (Amsden 1999). In all these KIVA versions, structured meshes are required to discretise engine geometries.

Many efforts have been made to enable the KIVA programs to simulate flows in complex engine geometries, but there are limitations of a structured mesh for describing detailed engine geometries. Compared to structured meshes, unstructured grids can be composed of a variety of elements including hexahedra, prisms, pyramids, and tetrahedral, and thus provide an easier route in the discretisation of physical domains (Torres and Trujillo 2006). In this context, the newly developed KIVA 4 code employs unstructured meshes and, in response to this change, modifications and new numerical schemes have been integrated. KIVA 4 is comparable in computational efficiency to KIVA 3V and also maintains the full generality of previous versions. In particular, in the use of the latest physics sub-models for

multi component vaporization, wall impingement, Lagrangian liquid film movement, drop breakup, etc. (Torres and Trujillo 2006).

KIVA provides an open platform on which researchers worldwide can implement and test their models for engine simulations. However, relatively complicated mesh generation processes and the lack of user-friendly interface have weakened the popularity of KIVA recently. The structural programming language of KIVA, FORTRAN (mainly FORTRAN 77 and 90), is extensively used in scientific computations due to its efficiency and ease-of-programming. However, limited by the FORTRAN language itself, KIVA cannot adopt objective-oriented programming concepts in its structure. Thus, implementation and testing of new models, especially changes of the numerical integration scheme, can result in a large workload. Using a concurrent version control system, such as the CVS (http://www nongnu.org/cvs/) relaxes some of these difficulties and significantly enhances the robustness of the continuously improved code.

OpenFOAM stands for Open Field Operation and Manipulation. Capabilities of this free open source CFD toolbox are not only restricted to simulating complex fluids flows involving chemical reactions, turbulence and heat transfer, but it is also able to calculate solid dynamics, electromagnetic and even financial problems. OpenFOAM facilitates CFD research in that it is an object-oriented software toolkit, which separates the handling of physics from numerical discretisation techniques. Therefore, more emphasis can be placed on developing and validating the physics of models. It employs an unstructured mesh and thus it is able to handle complex geometries, such as diesel engines. Its utility library provides various interfaces that can convert mesh files of popular CFD codes, such as KIVA, FLUENT, STAR-CD, and etc. Post-processing can also be done using third-body software by converting OpenFOAM result files to corresponding formats. Recent research has pioneered the use of OpenFOAM in engine simulations (Jasak *et al*. 2004, D'Errico *et al.* 2007, Kärrholm *et al*. 2008). The current OpenFOAM version 1.6 contains three solvers to deal with engine problems, including dieselFoam for simulating reacting or non-reacting diesel sprays, dieselEngineFoam for simulating reacting flows of diesel engines, as well as engineFoam mainly for SI engines. The use of OpenFOAM in solving engine problems is still in an initialization stage. Many existing physical models need to be integrated into the OpenFOAM code and to be systematically validated. Issues associated with the complicated topological changes of a moving mesh, such as moving valves in engines, still need further efforts. In addition, to appreciate the powerful functionalities of OpenFOAM needs professional skills and knowledge in objective-oriented programming and CFD fundamentals. This may limit widespread applications of OpenFOAM in engine simulations.

Commercial software

As compared to open source codes, commercial CFD software for engine simulations has superiority in ease-of-use. Their user-friendly graphic interfaces enables fast modelling and solving of engineering problems, and expertise is not necessarily required. They also provide their own mesh generators or have complete functionalities of using mesh files from other popular third-body mesh software, which expedites the mesh generating process. Technique support from software vendors or directly from software firms can help solve customers to address difficulties in a timely fashion. As a result, commercial CFD software has found more applications in engine design, development, and production in the automotive industry. STAR-CD, AVL FIRE, FLUENT, and VECTIS are the most preferred multi-dimensional CFD software in industry. A search of the database of technical papers of SAE international (www.sae.org) reflects that the former three commercial codes have close popularity, followed by VECTIS. But the fact is that none of them exceeds the number of applications of KIVA, which somewhat indicates the role of open source CFD codes in engine simulations in both academia and industry R&D throughout the past decades. The main reasons are that commercial CFD software is usually much more expensive to purchase, maintain, and update. They are often "black boxes" for users so that their flexibility is weak.

Future and Challenge

Engine CFD modelling has received growing attention since its initiation. As continuously improved physical models and mathematical methods are developed, the credibility of CFD modelling is also better recognized. This has made CFD modelling an indispensable tool in engine design, development, and production as a means of saving cost and time. However, there still remain big challenges to quantitatively predict engine performance and emissions using CFD modelling.

The mesh generation process still requires a relatively large workload, and to describe detailed engine geometries, including features such as valve recess and glow plugs adds additional difficulties. More advanced and user-friendly automatic mesh generation tools will favour wider applications of engine CFD modelling.

Inspite of the significant progress to-date, spray and evaporation models need to be improved in several aspects. First, detailed nozzle flow models are needed to provide complete initial conditions for spray models to better resolve the atomization of sprays. Second, although efforts have been made as discussed in the preceding sections, the mesh-dependency of spray and evaporation models may still result in inconsistent calculations for engines of different sizes. Third, to describe the different vaporizing characteristics of commercial fuels sourced from various places, improvements of evaporation models are necessary.

Inaccurate predictions of CFD models can usually be traced to insufficient description of physical phenomena. But, in the first place, even the physics of

some complex processes is not completely understood. Combustion physics in turbulent flows still challenges many modellers and experimentalists around the world. In the context of engine applications, the interaction of turbulence and chemical kinetics is of much interest to CFD modelling. Precise NOx predictions have been seen in many modelling works thanks to well-understood NOx formation mechanisms, but the prediction of soot emissions is relatively poor due to lack of a full understanding of its interacting physical and chemical formation processes in engine environments. To further explore these phenomena, advanced laser diagnostic techniques are needed for model development and validation.

It is true that the speed of computers has increased rapidly, but this does not necessarily mean that engine simulations using CFD tools take less computing time since CFD models are continuously improved. For instance, to capture more detailed flow structures at the sub-grid scale, LES turbulence models are preferred to perform on smaller meshes than those using RANS models. To reduce truncation errors, high order numerical schemes are also necessary. So, methodologies that can be applied to engine CFD models to reduce computational expense, while maintaining prediction accuracy will always be of much interest.

Demands from innovative engine techniques and advanced applications will continue to stimulate interest in developing new models. In the near future, the production of engines that feature HCCI combustion modes will likely become to a reality. Bio fuels will partially replace conventional fuels to ensure the sustainability of IC engines in automobiles. These will require more fundamental understandings of fuel chemistry. To further reduce emissions from diesel engines, a higher injection pressure is needed. Correspondingly, new spray models may be necessary to describe the resulting new atomization and breakup mechanisms. Stricter emission regulations may challenge CFD modelling as more detailed characteristics of engine emissions are legislated, such as the size of particulate matter.

References

Abani N and Reitz R D (2007) Unsteady turbulent round jets and vortex motion. Phys Fluids 19: 125102.1-125102.13

Abani N, Kokjohn L S, Park S W, and *et al*. (2008) An improved spray model for reducing numerical parameters dependencies in diesel engine CFD simulations, SAE paper 2008-01-0970

Abraham J, Bracco F V, and Reitz R D (1985) Comparisons of computed and measured premixed charge engine combustion. Combust. Flame 60: 309–322

Abraham J (1996) Entrainment characteristics of transient jets. Numer Heat Tranf A-Appl 30:347–364

Abraham J (1997) What is adequate resolution in the numerical computation of transient jets. SAE paper 970051

Abraham J and Magi V (1997) Modeling radiant heat loss characteristics in a diesel engine. SAE paper 970888

Amsden A A, Ramshaw J D, O'Rourke P J and Dukowicz J K. (1985) KIVA: A computer program for two- and three-dimensional fluid flows with chemical reactions and fuel sprays. Los Alamos National Lab. Report, LA-10245-MS

Amsden A A, O'Rourke P J and Butler T D (1989) KIVA-II - A computer program for chemically reactive flows with sprays. Los Alamos National Laboratory Report LA-11560-MS

Amsden A A (1993) A KIVA program with block-structured mesh for complex geometries. Los Alamos National Laboratory Report LA-12503-MS

Amsden A A (1997) KIVA-3V: A block-structured KIVA program for engines with vertical or canted valves. Los Alamos National Laboratory Report LA-13313-MS

Amsden A A (1999) KIVA-3V, Release 2, improvements to KIVA-3V. Los Alamos National Laboratory Report LA-UR-99-915

Aceves S M, Flowers D L, Westbrook C K, and *et al*. (2000) A multi-zone model for prediction of HCCI combustion and emissions. SAE paper 2000-01-0327

Babajimopoulos A, Assanis D N, Flowers D L, and *et al*. (2005) A fully coupled computational fluid dynamics and multi-zone model with detailed chemical kinetics for the simulation of premixed charge compression ignition engines. Int J Engine Res 6: 497–512.

Bai C and Gosman A D (1995) Development of methodology for spray impingement simulation. SAE paper 950283

Beale J C and Reitz R D (1999) Modeling spray atomization with the Kelvin-Helmholtz/ Rayleigh-Taylor hybrid model. Atom Sprays 9: 623–650

Borman G L and Nishiwaki K (1987) Internal combustion engine heat transfer, Prog Energy Combust Sci 13: 1–46

Bowman C T (1993) Control of combustion-generated nitrogen oxide emissions: Technology driven by regulation. Proc Comb Inst 24: 859

Brazier-Smith P R, Jennings S G, and Latham J (1972) The interaction of falling rain drops: coalescence. Proc R Soc London, Ser A 326: 393–408

Celik I, Yavuz I, and Smirnov A (2001) Large eddy simulations of in-cylinder turbulence in internal combustion engines: a review. Int J Engine Res 2: 119–148

De Paola G, Mastorakos E, Wright Y M, and Boulouchos K (2008) Diesel engine simulations with multi-dimensional conditional moment closure. Combust Sci Tech 180: 883–899

D'Errico G, Ettorre D, and Lucchini T (2007) Comparison of combustion and pollutant emission models for DI diesel engines. SAE paper 2007-24-0045

Dukowicz J K (1980) A particle-fluid numerical model for liquid sprays. J Comput Phys 35: 229–253

Fiveland W A (1988) Three-dimensional radiative heat-transfer solutions by the discrete-ordinates method. J Thermophys 2: 309–316

Flowers D L, Aceves S M, Martinez-Frias J, and *et al*. (2003) Effect of mixing on hydrocarbon and carbon monoxide emissions prediction for iso-octane HCCI engine combustion using a multi-zone detailed kinetics solver. SAE Paper 2003-01-1821

Fogleman M, Lumley J, Rempfer D, and Haworth D (2004) Application of the proper orthogonal decomposition to datasets of IC engine flows. J of turbulence. doi: 10.1088/1468-5248/5/1/023

Frenklach M and Wang H (1991) Detailed modeling of soot particle nucleation and growth. Proc Combust Inst 23:1559–1566

Halstead M, Kirsh L, and Quinn C (1977) The autoignition of hydrocarbon fuels at high temperatures and pressures - fitting of a mathematical model. Combust. Flame 30:45–60

Han, Z, and Reitz, R D (1995) Turbulence modeling of internal combustion engines using RNG k-ε models. Comb Sci Tech 106: 267–295

Han Z, Uludogan A, Hampson G J and Reitz R D (1996) Mechanism of soot and NOx emission reduction using multiple-injection in a diesel engine. SAE Paper 960633

Han Z and Reitz R D (1997) A temperature wall function formulation for variable-density turbulent flows with application to engine convective heat transfer modeling. Int J Heat Mass Transfer 40: 613–625

Han Z, Xu Z, and Trigui N (2000) Spray/wall interaction models for multidimensional engine simulation. Int J Engine Res 1:127–146

Haworth D C (2005) A Review of turbulent combustion modeling for multidimensional in-cylinder CFD. SAE paper 2005-01-0993

Heywood J B (1988), Internal combustion engine fundamentals. McGraw-Hill.
Hu B, Jhavar R, Singh S, and *et al*. (2007) Combustion modeling of diesel combustion with partially-premixed conditions. SAE paper 2007-01-0163
Hu B (2008) Development of a general diesel combustion model in the context of large eddy simulation. Ph. D. Dissertation, University of Wisconsin-Madison
Hughes K J, Turányi T, Pilling M J, and Tomlin A S (1999) http://www.chem.leeds.ac.uk/Combustion/Combustion.html . Accessed 20 NOV 2008
Jasak H, Weller H, and Nordin N (2004) In-cylinder CFD simulation using a C++ object-oriented toolkit. SAE Paper 2004-01-0110
Jhavar R and Rutland C J (2006) Using large eddy simulations to study mixing effects in early injection diesel engine combustion. SAE paper 2006-01-0871
Jhavar R (2007) Using large eddy simulations to study DI-HCCI diesel engine flow structure, mixing, and combustion. Ph.D. Dissertation, University of Wisconsin-Madison
Jia M, Peng Z, Xie M, and *et al*. (2008) Evaluation of spray/wall interaction models under the conditions related to diesel HCCI engines. SAE paper 2008-01-1632
Kaario O, Larmi M., Tanner F. (2002) Relating integral length scale to turbulent time scale and comparing k-ε and RNG k-ε turbulence models in diesel combustion simulation. SAE paper 2002-01-1117
Kärrholm F P, Tao F, and Nordin N (2008) Three-dimensional simulation of diesel spray ignition and flame lift-off using OpenFOAM and KIVA-3V CFD codes. SAE Paper 2008-01-0961
Kee R J, Rupley F M and Miller J A (1991) CHEMKIN-II: A Fortran chemical kinetics package for the analysis of gas-phase chemical kinetics. Sandia National Laboratory Report SAND 89-8009
Kong S C and Reitz R D (1993) Multidimensional modeling of diesel ignition and combustion using a multistep kinetics model. J Eng Gas Turbines Power 115: 781–789
Kong S C, Han Z, and Reitz R D (1995) The development and application of a diesel ignition and combustion model for multidimensional engine simulation. SAE Paper 950278
Kong S C, Marriott C D, Reitz R D, and Christensen M (2001) Modeling and experiments of HCCI engine combustion using detailed chemical kinetics with multidimensional CFD. SAE paper 2001-01-1026
Kong S C, Sun Y, and Reitz R D (2007) Modeling diesel spray flame lift-off, sooting tendency and NOx emissions using detailed chemistry with phenomenological soot model. J Eng Gas Turbines Power 129: 245–251
Kong S C (2007) Drop/wall interaction criteria and their applications in diesel spray modeling. Atom Sprays 17: 473–499
Lapenta G (2002) Particle rezoning for multidimensional kinetic particle-in-cell simulations. J Comput Phys 181:317–337
Launder B E, Reece G J and Rodi W (1975) Progress in the development of a Reynolds-Stress turbulent closure. J Fluid Mech 68:537–566
Lebrère L and Dillies B (1996) Engine flow calculations using a Reynolds Stress Model in the Kiva-II code. SAE Transaction 105: 133–155
Lee D, Pomraning E, and Rutland C J (2002) LES modeling of diesel engines. SAE paper 2002-01-2779
Liang L, Jung C, Kong S-C, and Reitz R D (2007) Development of a semi-implicit solver for detailed chemistry in I.C. engine simulations. J Eng Gas Turbines Power 129: 2271–278
Liang L, Stevens J G, and Farrell J T (2009) A dynamic adaptive chemistry scheme for reactive flow computations. Proc Combust Inst, doi: 10.1016/j.proci.2008.05.073
Lippert A M (1999) Modeling of multi-component fuels with application to sprays and simulation of diesel engine cold start. Ph.D. dissertation, University of Wisconsin-Madison
Lilly D K (1967) The representation of small-scale turbulence in numerical simulation experiments. In: Goldstine H H (Ed.). Proc IBM scientific computing symp on environmental sciences, Yorktown Heights, NY

Magnussen B F and Hjertager H (1976) On mathematical modelling of turbulent combustion with special emphasis on soot formation and combustion. Proc Combust. Institute 16: 719–729
Musculus M P B (2004) On the correlation between NOx emissions and the diesel premixed burn SAE paper 2004-01-1401
Munnannur A (2007) Droplet collision modeling in multi-dimensional engine spray computations. Ph.D. Dissertation, University of Wisconsin-Madison
Nagle J and Strickland-Constable R F (1962) Oxidation of carbon between 1000–2000 C, Proc of the Fifth Carbon Conf 1: 265–325
Neoh K G, Howard J B, Sarofim A F (1984) Effect of oxidation on the physical structure of soot. Proc Combust Inst 20: 951–957
Nishida K and Hiroyasu H (1989) Simplified three-dimensional modeling of mixture formation and combustion in a D.I. diesel engine. SAE paper 890269
Nordin, N. (2001) Complex chemistry modeling of diesel spray combustion. Ph.D. Dissertation, Chalmers University of Technology
O'Rourke P J (1981) Collective drop effects in vaporizing liquid sprays. Ph.D. Dissertation, Princeton University
O'Rourke P J and Amsden A A (1987) The Tab method for numerical calculation of spray droplet break-up. SAE paper 872089
O'Rourke P J and Amsden A A (2001) The spray/wall interaction submodel for the KIVA-3 wall film model. SAE paper 2001-01-0271
Park S W and Reitz R D (2007) Numerical study on the low emission window of homogeneous charge compression ignition diesel combustion. Combust Sci Tech 179: 2279–2307
Patterson M A, Kong S C, Hampson G J, and Reitz R D (1994) Modeling the effects of fuel injection characteristics on diesel engine soot and NOx emissions. SAE paper 940523
Patterson M A and Reitz R D (1998) Modeling the effects of fuel spray characteristics on diesel engine combustion and emissions. SAE paper 980131
Pelloni P and Bianchi G M (1999) Modeling the diesel fuel spray break-up by using a hybrid model. SAE paper 1999-01-0226
Peters N (2000), Turbulent Combustion. Cambridge University Press, Cambridge, UK
Pomraning E and Rutland C J (2002) A dynamic one-equation non-viscosity LES model. AIAA Journal 44:689–701
Pope S B (1997) Computationally efficient implementation of combustion chemistry using *in situ* adaptive tabulation. Combust Theory Model 1: 41–63
Pope S B (2000) Turbulent flows. Cambridge University Press, Cambridge, UK
Reitz R D (1980) Computations of laminar flame propagation using an explicit numerical method. 18th Symposium (International) on Combustion / The Combust Inst, Pittsburgh, PA: 433–442
Ra Y and Reitz R D (2008) A vaporization model for discrete multi-component fuel sprays. Int J Multiph Flow, doi:10.1016/j.ijmultiphaseflow.2008.10.006
Reitz R D (1987) Modeling atomization processes in high-pressure vaporizing sprays. Atom Sprays Tech 3: 309–337
Reitz R D and Diwakar R (1987) Structure of high pressure fuel sprays. SAE Transaction 96:492–509
Reitz R D and Kuo T W (1989) Modeling of HC emissions due to crevice flows in premixed-charge engines. SAE paper 892085
Schmidt D P and Rutland C J (2004) Reducing grid dependency in droplet collision modeling. J Eng Gas Turbines Power 126: 227–233.
Shethaji T A, Rutland C J, Barths H, and *et al*. (2005) Assessment of RANS and LES turbulence models: turbulent flow past a backward-facing step and multidimensional simulation of in-cylinder flows. SAE paper 2005-01-0202
Shi Y and Reitz R D (2008) Optimization study of the effects of bowl geometry, spray targeting and swirl ratio for a heavy-duty diesel engine operated at low- and high-load. Int J Engine Res 9: 325–346

Shi Y, Hessel R P, and Reitz R D (2009) An adaptive multi-grid chemistry (AMC) model for efficient simulation of HCCI and DI engine combustion. Combust Theory Model, 13: 83–104

Shi Y, Kokjohn S L, Ge H W, and Reitz R D (2009) Efficient multidimensional simulation of HCCI and DI engine combustion with detailed chemistry. SAE paper 2009-01-0701

Singh S, Reitz R D and Musculus M P B (2006) Comparison of the Characteristic Time (CTC), Representative Interactive Flamelet (RIF), and direct integration with detailed chemistry combustion models against optical diagnostic data for multi-mode combustion in a heavy-duty DI diesel engine. SAE paper 2006-01-0055

Sjöberg M and Dec J E (2008) Influence of fuel autoignition reactivity on the high-load limits of HCCI engines. SAE paper 2008-01-0054

Smagorinsky J (1963) General circulation experiments with the primitive equations: I. The basic equations. Mon Weather Rev 91: 99–164

Smith G P, Golden D M, Frenklach M, and *et al*. http://www.me.berkeley.edu/gri_mech/. Accessed 19 NOV 2008

Spalding D B (1971) Mixing and chemical reaction in steady confined turbulent flames. Proc Combust Institute 13: 649–657

Sun Y (2007) Diesel combustion optimization and emissions reduction using adaptive injection strategies (AIS) with improved numerical models, Ph.D. Dissertaion, University of Wisconsin-Madison.

Tan Z and Reitz R D (2004) Development of a universal turbulent combustion model for premixed and direct injection spark/compression ignition engines. SAE paper 2004-01-0102

Tao F and Chomiak J (2002) Numerical investigation of reaction zone structure and flame liftoff of DI diesel sprays with complex chemistry. SAE paper 2002-01-1114

Tao F, Golovitchev V I, and Chomiak J (2004) A phenomenological model for the prediction of soot formation in diesel spray combustion. Combust Flame 136: 270–282

Tao F, Liu Y, Rempel, Ewert B H, and *et al*. (2005) Modeling the effects of EGR and injection pressure on soot formation in a high-speed direct-injection (HSDI) diesel engine using a multi-step phenomenological soot model. SAE paper 2005-01-0121

Tao F, Reitz R D, Foster D E, and Liu Y (2009) Nine-step phenomenological diesel soot model validated over a wide range of engine conditions. Int J Therm Sci, 48: 1223–1234

Torres D J and Trujillo M (2006) KIVA-4: An unstructured ALE code for compressible gas flow with sprays. J Comput Phys 219: 943–975

Warnatz J, Mass U, Dibble R W (2006) Combustion: physical and chemical fundaments, modeling and simulation, experiments, pollutants formation. Springer

Zhang Y Z (2004) Hybrid particle/finite-volume PDF methods for there-dimensional time-dependent flows in complex geometries. Ph.D. Dissertation, Pennsylvania State University

16 Multi-dimensional Modelling of Diesel Combustion: Applications

Yu Shi and Rolf D. Reitz

Engine Research Center, University of Wisconsin-Madison

Abstract Various successful applications have proven the reliability of using multi-dimensional CFD tools to assist in diesel engine research, design and development. Those applications can be categorized as follows: using CFD tools to reveal details about invisible (or technically difficult and/or costly) in-cylinder processes of diesel combustion, so that guidance can be provided to improve engine designs in terms of emissions reduction and fuel economy; innovative combustion concepts can be evaluated numerically prior to experimental tests to reduce the number of investigated parameters and thus costs; important design parameters can be discovered by modelling engines of different sizes to establish engine size-scaling relationships and thus non-dimensionalize engine designs; by integration with optimization methodologies, CFD tools can also directly impact the design of optimum engine systems, such as piston geometry and injection parameters. Each of these aspects is described by relevant case studies in this chapter. The corresponding simulations were conducted with an improved version of the KIVA-3v2 code.

To demonstrate the capability of engine CFD modelling in diesel engine design, development, and production, three representative case studies are discussed in this chapter. The first case investigates the UHC/CO emissions trends for a light-duty diesel engine under low-temperature combustion conditions. The CFD tool used for this study is an improved version of the KIVA-3v2 code which features the RNG turbulence model (Han and Reitz 1995), the KH/RT spray model (Beale and Reitz 1999), a detailed chemistry solver with the newly developed PRF mechanism (Ra and Reitz 2008), and other improved sub-models. In addition, recently developed techniques for reducing the computational expense of multi-dimensional CFD engine simulations are also integrated into the KIVA code and are used for the first case. In the second case, engine size-scaling relationships are assessed for a light-duty and a heavy-duty diesel engine with consideration of turbulence and chemistry timescales. The last case shows how CFD tool can optimize engine designs when coupled with optimization methodologies. In this case study, the same KIVA code is used, but with a simple combustion model, the shell/CTC model (Kong *et al*. 1995), in order to reduce the extensive computation time that is required for thousands of individual simulations.

P.A. Lakshminarayanan and Y.V. Aghav, *Modelling Diesel Combustion*, Mechanical Engineering Series, DOI 10.1007/978-90-481-3885-2_16,

Case Studies

The discussion about the three cases in this section shares the same structure where the problem of each case is first described together with its research background. It is followed by list(s) of engine specifications and a description of the research approach for that case. In the last part of each case study, the simulation results are discussed in detail so that the insight gained from each type of simulation is naturally demonstrated.

Study of UHC/CO emissions trends

Problem description: low-temperature combustion in a light-duty diesel engine using an efficient engine simulation code with detailed chemistry

Recent efforts to reduce pollutant emissions and fuel consumption have resulted in the development of many advanced combustion concepts. Among them, low-temperature combustion is attracting more interest since it has been proven in many studies that the low-temperature combustion helps the combustion processes avoid from NO_x and soot formation environments (Kimura *et al*. 2001, Lee *et al*. 2007, Park and Reitz 2007). In practical applications, Premixed Charge Compression Ignition (PCCI) (Lee *et al*. 2007, Nevin *et al*. 2007), which realizes low temperature combustion by injecting fuel very early to produce a premixed fuel-air charge prior to the ignition, and Modulated Kinetics (MK) (Kimura *et al*. 1999, 2001), which requires late injection with a large amount of cooled recycled exhaust gases to delay ignition timing and thus lower the combustion temperature, are seeing a promising future. However, these approaches usually result in higher unburned hydrocarbons (UHC) and CO emissions compared to conventional diesel combustion. As discussed in Chapter 15, possible reasons are the cylinder wall wetting due to early injections and the low oxidation rate due to over-lean mixture and low combustion temperatures.

To achieve low-temperature combustion in a diesel engine, a highly dilute environment is usually required, namely, low inhomogeneity of the in-cylinder charge and low oxygen concentration (~10%) with a large EGR rate (~60%). Experimental studies of Kook *et al*. (2005, 2006) and Opat *et al*. (2007) found a unique behavior of the UHC/CO emissions while performing injection sweeps for diesel engines operating in dilute environments. The unique behavior showed that for the investigated engines there exist injection timings that correspond to minimum values of CO emission throughout the injection sweeps, termed the CO "sweet spot". This finding provides a valuable guideline for designing PCCI diesel engines.

Advanced combustion strategies use many parameters (injection pressure, number of injection pulses, EGR rate, boost, etc.) to control the combustion process in order to achieve ultra-low emissions and fuel consumption. The vast number of variables in these combustion strategies necessitates a large number of iterations to achieve an optimal engine design via parametric studies. Because experimental engine design is a time consuming process, the expense of optimizing engine designs

in the lab is becoming more and more costly. With the increasing prediction ability of engine simulation tools, engine design aided by relatively low cost CFD modelling is becoming more popular in both industry and academia. To quantitatively predict engine power, performance and emissions trends, multi-dimensional CFD tools coupled with chemistry solvers, as discussed in Chapter 15, are required. However, the computational expense of the simulation may become very large if numerous cases need to be studied. Therefore, there is a need to reduce the computational expense of engine simulations using CFD tools coupled with chemistry solvers. In this section, the three approaches that were introduced in Chapter 15 are integrated into an improved CFD code to study the above discussed UHC/CO emissions trends for low-temperature combustion in a light-duty diesel engine.

Engine specifications and investigation approach

The studied engine in this section is a light-duty diesel engine, M16 (Table 3.2) for passenger cars, and its specifications and operating conditions are listed in Tables 16.1 and 16.2, respectively.

Table 16.1 Specifications of engine M16

Displacement (L)	0.4774
Bore (mm)	82.0
Stroke (mm)	90.4
CR	16.6:1
IVC (°ATDC)	–132
EVO (ATDC)	112
Number of holes	7
Injection angle ( )	155

Table 16.2 Operating conditions of engine M16

Speed (rev/min)	2,000
Injection pressure (bar)	860
IMEP (bar)	5.5
EGR (%)	65
Equivalence ratio	0.95
SOI (ATDC)	–39 to –21

Before the injection sweep parametric study listed in Table 16.2, the CFD code was well calibrated with a representative case, and thereafter all calibrated model constants were kept the same throughout the study. An in-house code was employed to iteratively determine the engine inlet valve closing (IVC) conditions based on available measured intake temperature, pressure and gas composition data. It was also found that in the calibration that the start-of-injection command was 4.8° advanced from the physical SOI (start of Injection i.e., start of mass flow from

injector) at the 2,000 rev/min engine speed, and thus the model inputs were adjusted accordingly for all cases. The study of this section is divided into two phases: in the first phase, the study demonstrates that the current CFD code can qualitatively capture emissions trends, and the CO "sweet spot" is revealed and explained in detail; in the second phase, the effectiveness of three approaches for efficient simulation of diesel combustion (i.e., the adaptive multi-grid chemistry model, mesh-independent spray models, and code parallelization, as discussed in Chapter 15) are compared with respect to their computational efficiency and prediction accuracy. All simulations were conducted on computers with the same configuration (Intel P4 3.0 GHz and 2G bytes memory) and the wall clock time was recorded. Due to the geometrical symmetry of the 7-hole injector, a 51.4° sector mesh was employed for the simulations. The fine mesh used in the first and second phase had 32,600 cells of size of approximately 1.0 mm at BDC, and the coarse mesh used for the second phase had about 10,600 cells of size of 2.5 mm. Both meshes are depicted in Fig. 16.1.

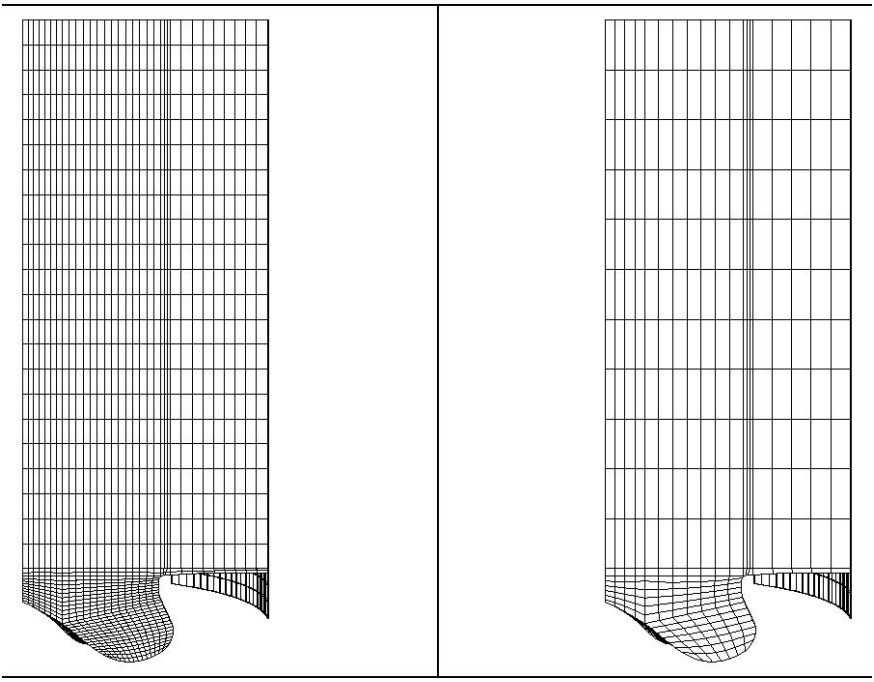

Fig. 16.1 Computational meshes (fine mesh: the left; coarse mesh: the right)

Results and discussion

Simulations for the injection sweep were performed using the fine mesh to investigate the emissions trends. NO_x, soot, CO and UHC emissions are reported in Fig. 16.2a–d as a function of injection timings, respectively. Although UHC and soot emissions are over-predicted and under-predicted for late injection timings,

the KIVA CFD code correctly predicts emissions trends over the entire range of the injection timings. More significantly, the CO "sweet spot", and especially the accompanying UHC "sweet" spot, are revealed, as seen in the experiments. This gives strong confidence of using the simulation results to further explore the formation processes of UHC/CO through in-cylinder visualization. Three cases including the boundaries of the injection sweep, namely, SOI = –21 and SOI = –39, as well as the "sweet spot" timing SOI = –33, are studied in detail as follows.

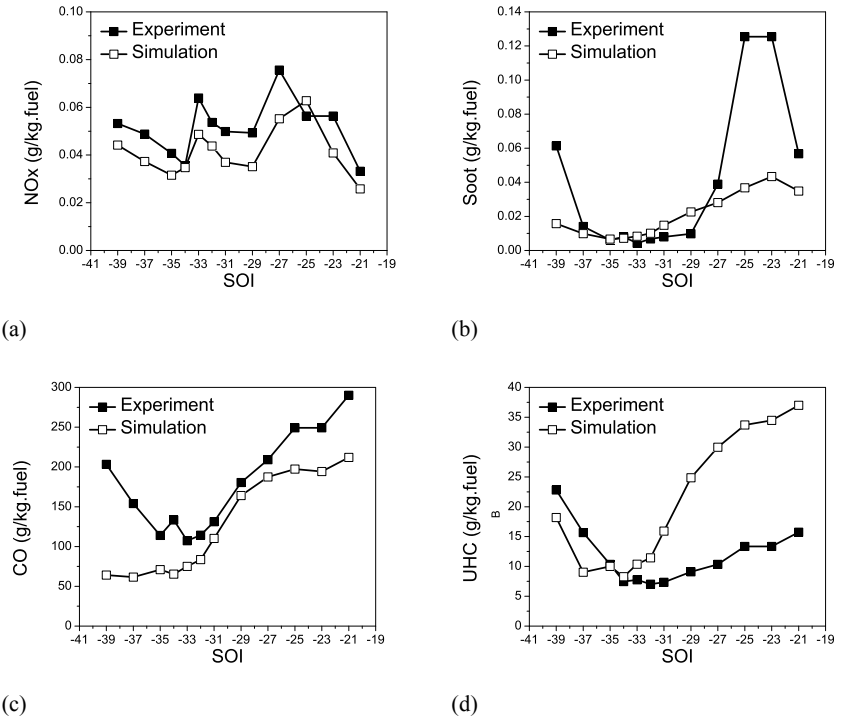

Fig. 16.2 Comparison of simulation and experimental measurement for engine-out emissions of engine M16. (a) NO_x emissions. (b) Soot emissions. (c) CO emissions. (d) UHC emissions

Figure 16.3a illustrates the pressure traces and heat release rates for the three cases. Correspondingly, their combustion phasings are depicted in Fig. 16.3b expressed as the percentage of total heat release as a function of crank angle. The ignition delay (I.D.) is defined as the crank angle between ten percent heat release and the physical injection timing. Figure 16.3b shows that it decreases as the injection timing advances. A shorter ignition delay indicates a shorter time for mixing the spray with the ambient gases before the combustion, which can deteriorate the oxidation rate of fuel and its combustion product CO during the combustion processes. However, if the mixing time alone could explain UHC/CO formation processes under the present highly dilute low-temperature combustion

conditions, it would be expected to see a monotonic shape of the UHC/CO emissions trends. The phenomenon of UHC/CO emissions for low-temperature diesel combustion was investigated using a phenomenological engine spray model by Opat *et al*. (2007) and Siewert (2007) who showed that the increasing CO seen as the injection timing advanced coincided with increasing amounts of liquid fuel that missed the bowl, and the increasing CO with retarded injection timings was due to the fact that less than 100% of the fuel was vaporized prior to fuel ignition. In light of this, in-cylinder visualization by post-processing the simulation results was employed to investigate the mixing related phenomena, such as spray impingement, turbulence interaction, and combustion, as shown in Figs. 16.4 and 16.5.

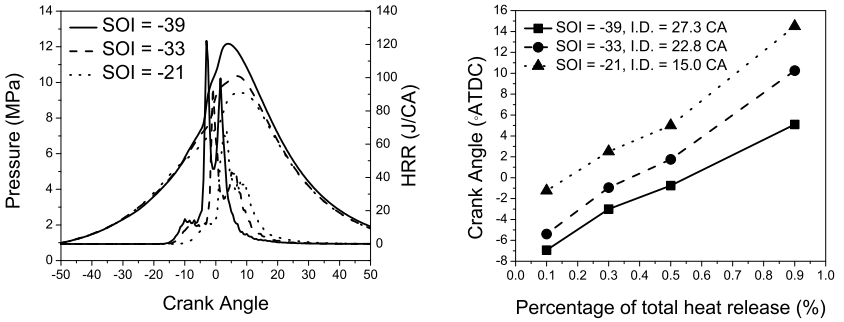

(a) (b)

Fig. 16.3 Comparison of the three representative cases. (a) Pressure trace and heat release rate. (b) Combustion phasing

It is observed in Fig. 16.4 that for the case of SOI = –33, the sprays target the piston bowl lip that splits the spray plumes into two regions, i.e., the squish and the piston bowl. Therefore, the air can be effectively used to mix the spray and thus enhances combustion in both regions. On the contrary, for the late injection case, the high temperature zone is mainly located in the piston bowl where the combustion occurs and its peak combustion temperature is also the lowest due to the locally rich stoichiometry. These are the primary reasons that higher UHC and CO are found for this case. For the early injection case, the combustion temperature is the highest among the three cases, and thus it benefits CO and UHC oxidation. The simulation predicts less CO than the experimental measurement, as shown in Fig. 16.2c for the early injection cases, which is attributed to complex fuel impingement events are not fully captured by the current spray impingement model. But the emission trend that UHC increases as the injection timing advances (before SOI = –34) is well revealed by the simulations, as shown in Fig. 16.2d. It is seen in the first and the second plot of the case of SOI = –39 in Fig. 16.4 that

part of fuel enters the crevice region before combustion, and this trapped fuel is therefore the main contributor of the engine-out UHC emissions.

In-cylinder velocity fields and CO mass fraction distributions of the three cases are also illustrated in Fig. 16.5 on vertical planes through the axis of the sprays. The tumble motion projected on the plane highly depends on the injection timing since it is seen that each case has complex and quite different flow patterns, especially near TDC. As a result, the locations of the high CO regions are also much different. For example, at the crank angle of 12 ATDC, they are located in the squish region for the early injection case, in the squish and bowl regions for the "sweet spot" case, and in the bowl region for the late injection case.

These findings from both experiments and simulations suggest that for highly dilute low-temperature combustion diesel engines it is necessary to optimize the injection timing to match the piston bowl design in order to achieve low UHC/CO emissions. Extensive studies of Opat *et al*. (2007) found that the position of the CO "sweet spot" shifts with changes of injection pressure and swirl ratio, which indicates that these are additional parameters that need to be optimized for diesel engines operated in dilute environments.

The computer time for the above cases is about 45 h. Thus, further parametric or optimisation studies of the combustion system would require a huge amount of computing resources. The following section demonstrates the capability of efficient engine CFD codes for such problems.

The AMC model was integrated into the KIVA code and it was applied to study the previous cases using the fine mesh. As seen in Fig. 16.6a using the AMC model the computational time is reduced by a factor of three to four for each case, as compared to the full chemistry model. For a representative case of SOI = –21 in Fig. 16.6b, the pressure trace and heat release rate predicted by the AMC model agree excellently with the full chemistry model, and both of them match the experimental results very well. This was also true for all other cases over the entire injection timing sweep. In addition, the results of the AMC model are also quantitatively consistent with those of the full chemistry simulations in terms of emissions, as shown in Fig. 16.5c–f.

The implementation of the mesh-independent spray model enables simulations of DI engine combustion on a coarse computational mesh, while maintaining the relatively high accuracy of a fine mesh. Simulations on the same cases discussed in the previous section were conduced using the original spray models and the updated spray models on both coarse and fine computational meshes. In order to assess the performance of the spray models only, the AMC model was deactivated to isolate its effect. After verifying that the updated spray models were able to predict less mesh-dependent results, the AMC model was then activated to show further capacity of reducing computational time using the current efficient KIVA code.

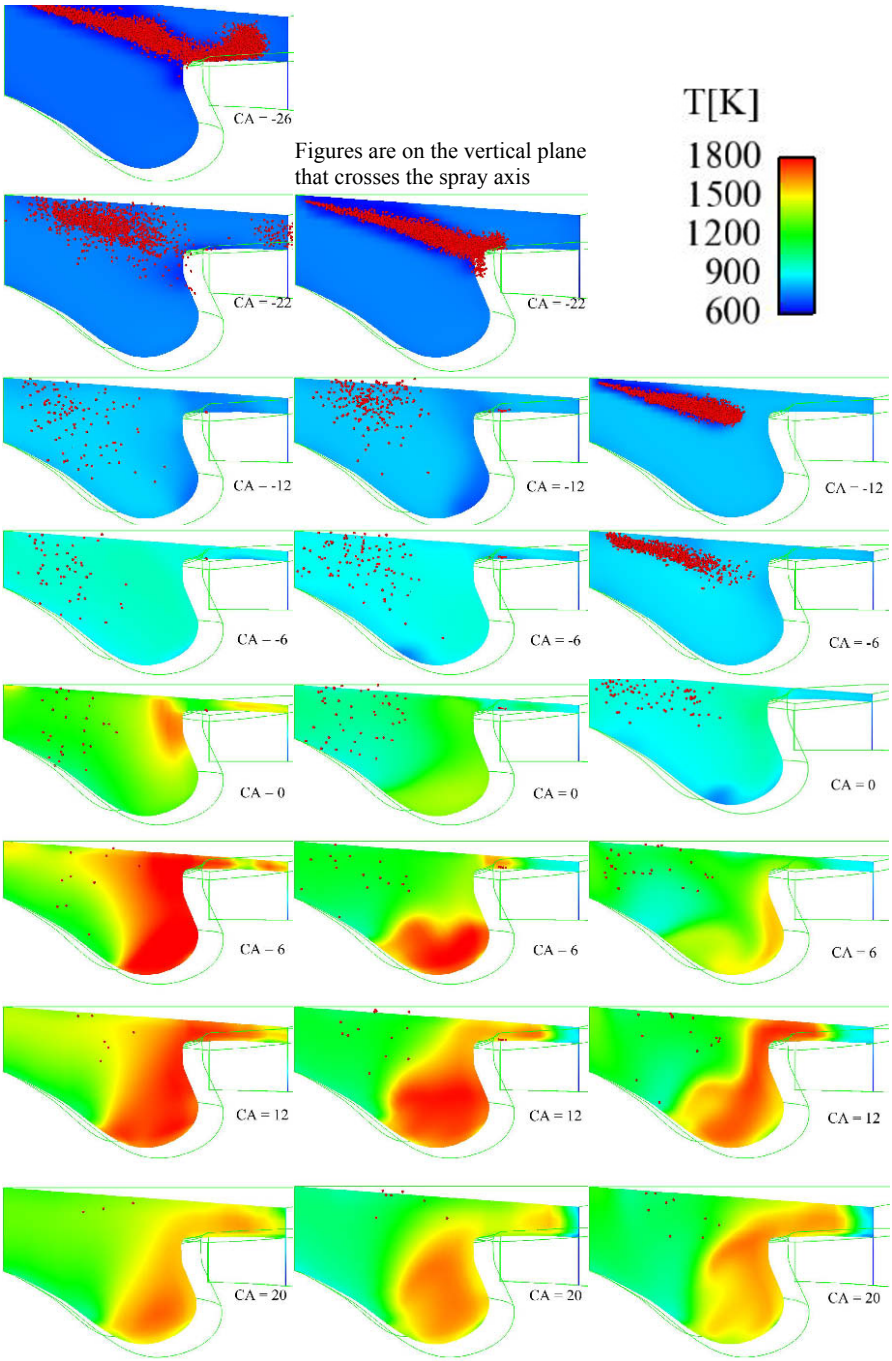

Fig. 16.4 CFD computed distributions of sprays and temperature fields for SOI = –39 (left), –33 (middle), –21 (right) cases

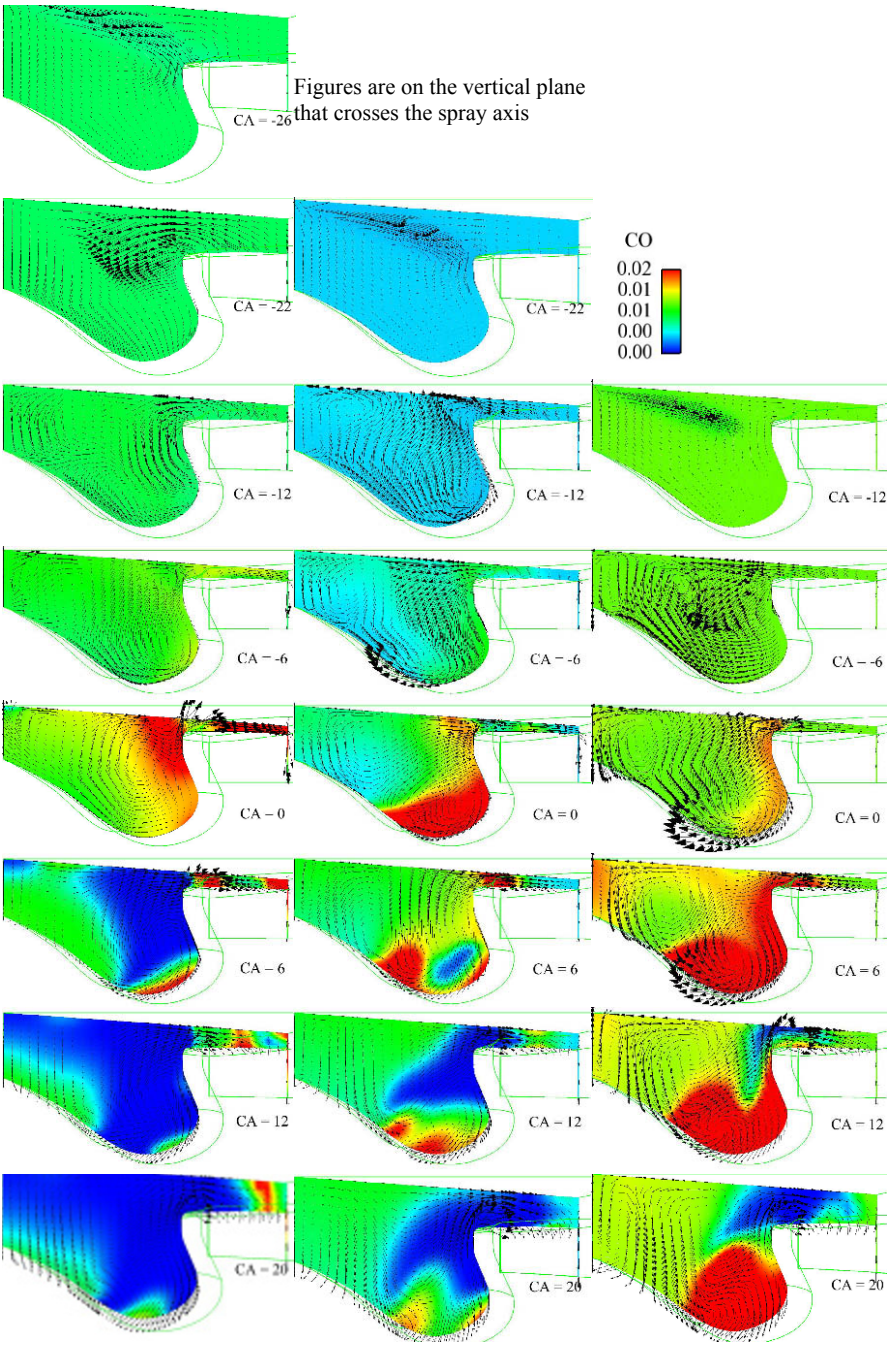

Fig. 16.5 CO mass fraction and velocity for SOI = –39 (left), –33 (mid), –21 (right)

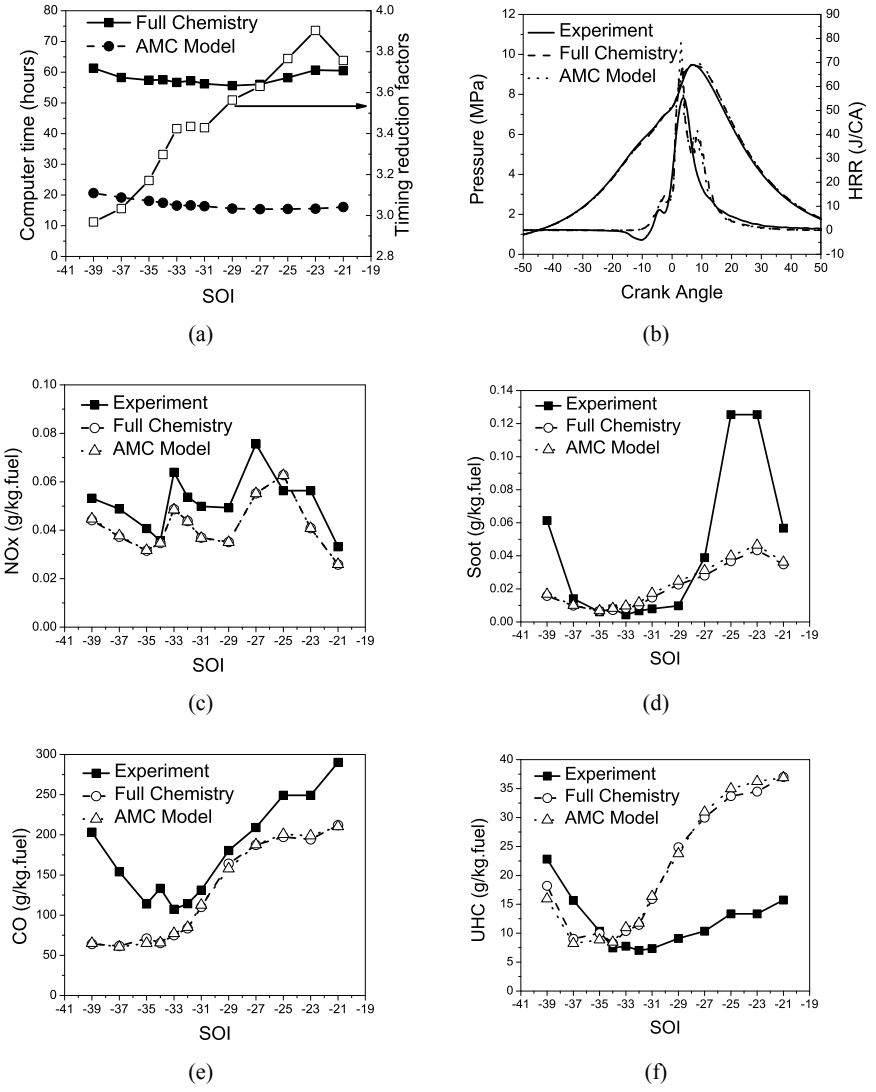

Fig. 16.6 Comparison of experimental results with simulated results using the fine mesh W/ and W/O the AMC model. (a) Computational time. (b) Pressure trace and heat release for SOI = –21. (c) NO_x emissions. (d) Soot emissions. (e) CO emissions. (f) UHC emissions

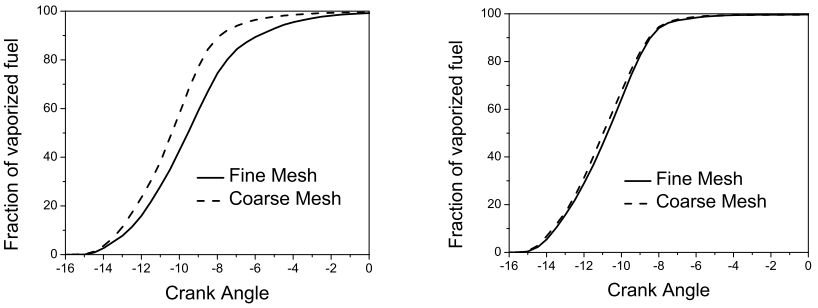

Fig. 16.7 Comparison of fraction of vaporized fuel using the original spray model and the mesh-independent spray model. (a) The original spray model. (b) The mesh-independent spray model

As shown in Fig. 16.7a, for the selected case of SOI = –21, using the original spray models produces very different results of vaporized fuel fraction between the fine mesh and the coarse mesh, and the difference is reduced significantly when updated spray models were applied (Fig. 16.7b). Therefore, it can be anticipated that the updated spray models would produce similar results of combustion characteristics and emissions when the mesh size is changed. This is proved by comparing Fig. 16.8 with Fig. 16.9, which shows that compared to the original spray model, the code with the updated spray models predicts more similar results between the coarse mesh and the fine mesh in terms of emission trends and quantities. It can be observed in Figs. 16.8 and 16.9 that the improvement is more prominent for early injection cases. Since NO_x is mainly a function of temperature, the agreement in Figs. 16.8a and 16.9a is the best, as can be expected. In addition to temperature, the local concentration and gradients of species composition also play crucial roles in the formation of soot, UHC, and CO. Therefore, even though a similar distribution of fuel on a large scale can be achieved using the updated spray model on the fine and coarse meshes, the coarse mesh results in lower local concentrations and gradients and thus leads to slightly different emission results. This is further confirmed by Fig. 16.8c and d that show that using the coarse mesh produces lower emissions in general. The differences are also attributed to the spray impingement model used in this study, which is not mesh-independent. This suggests that in order to further improve the mesh-independence of the current code, effort needs to be placed on developing a sub-grid evaporation model for the application of coarse meshes and reducing the mesh-dependence of the current spray impingement model.

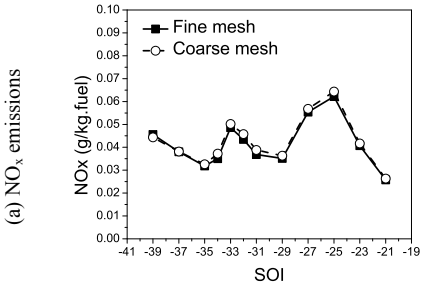

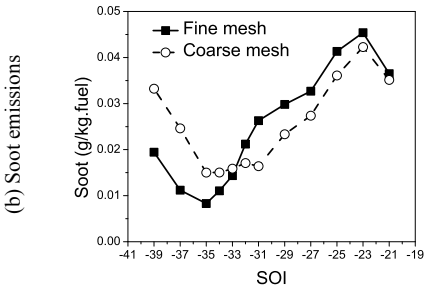

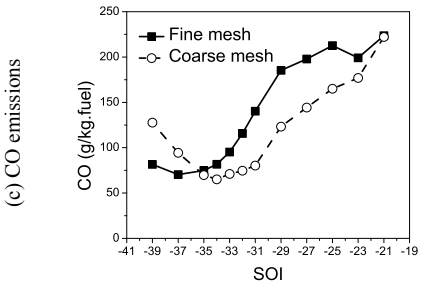

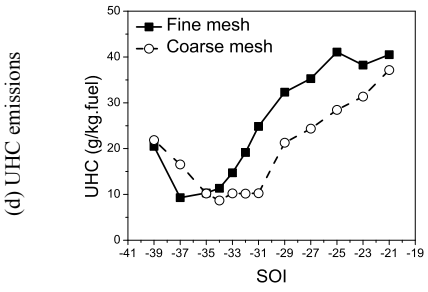

Fig. 16.8 Original spray model

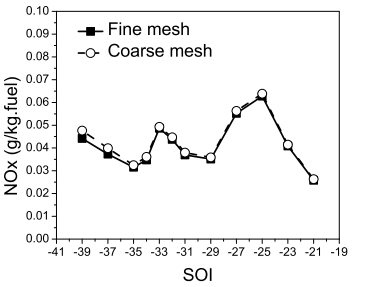

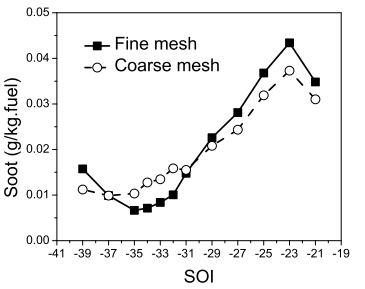

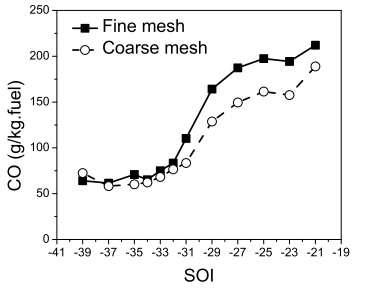

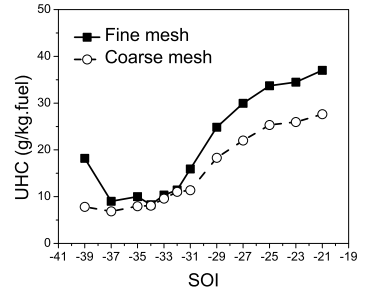

Fig. 16.9 Mesh-independent spray model

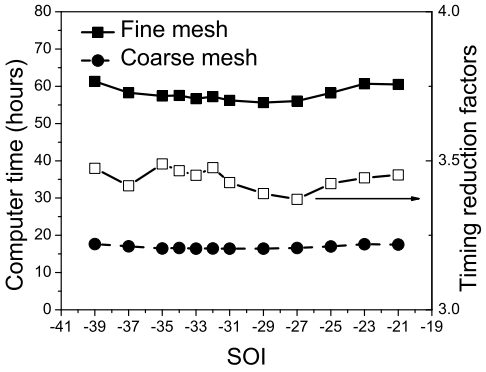

Fig. 16.10 Comparison of computational time using different meshes and the mesh-independent spray model

It is seen in Fig. 16.10 that the reduction of computational time roughly scales with the number of cells of the fine and coarse meshes, which is easily understood.

To further reduce computational time, the AMC model was activated for simulations using the coarse mesh. Similar to the results that were demonstrated in Fig. 16.6 for the fine mesh, the AMC model predicts very consistent results with the full chemistry model for the coarse mesh as shown in Fig. 16.11a–d. A tremendous computer time reduction (an order of magnitude) was obtained by combining these two schemes, as shown in Fig. 16.11e.

It is noted that the cost of computers has reduced dramatically in the past decades. The popularity of parallel computing in engine CFD simulations thus increases with the continuously decreasing cost of computers. Therefore, the AMC model and the mesh-independent spray model have been implemented into a parallel version of the KIVA3v2 code to explore its ability further.

The previous simulations were repeated using the coarse mesh on two and four processors, respectively. Because the parallelized code produces identical results to its series version, only the comparison of computing times is discussed. Parallelizing the simulations on two processors took an average of 3.7 h for each run, which is reduced from 5.8 h if a single processor is used (Fig. 16.12). If four processors were employed, the average computing time was further reduced to 2.6 h. As mentioned earlier, for the current code only the chemistry solver was parallelized, and the computing time spent on the master processor for the CFD calculation could not be further reduced by using more processors. Therefore, in order to utilize more processors while maintaining code efficiency, it would also be necessary to parallelize the CFD calculation of the KIVA code. The increasing network burden caused by more frequent communication between processors would also reduce the efficiency of the parallelized code if more processors were used. The communication burden to the network could be reduced if the parallelization was conducted on a single CPU with multiple cores. In that case,

processors exchange data through the internal high-speed bus system instead of an external network. Figure 16.12 compares the computational times.

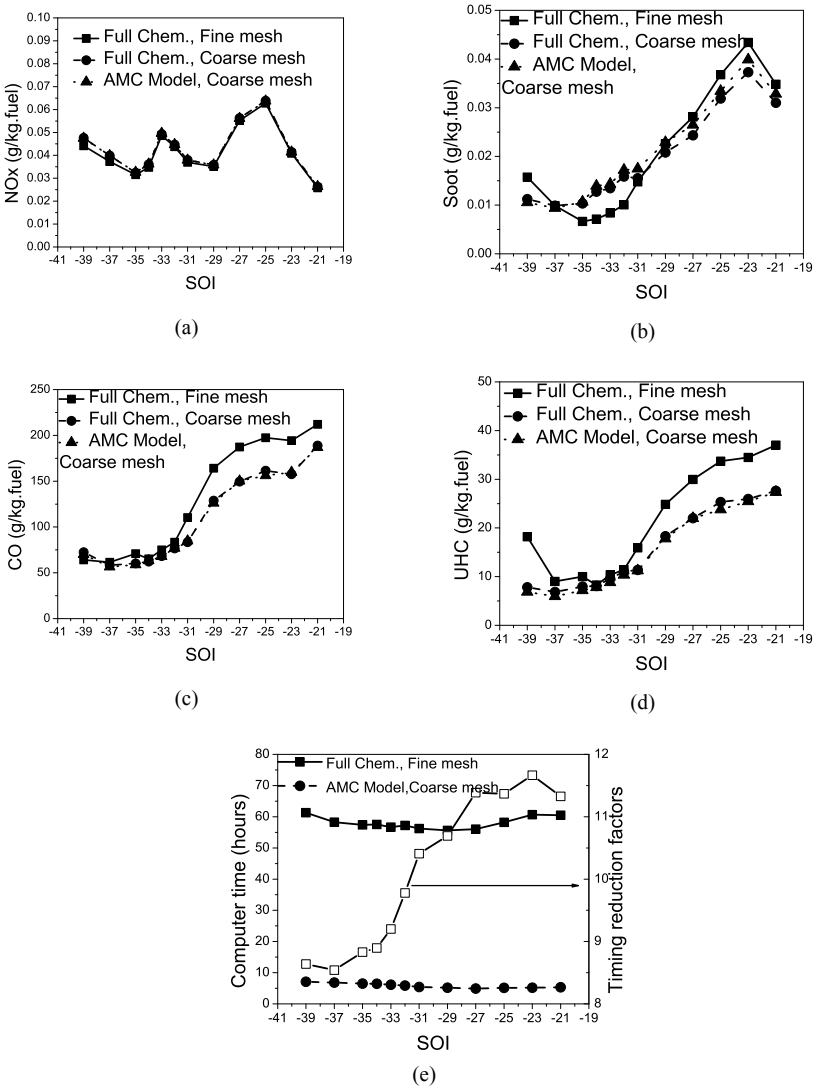

Fig. 16.11 Comparison of simulated results using the mesh-independent spray model and AMC model on fine and coarse meshes. (a) NO_x emissions. (b) Soot emissions. (c) CO emissions. (d) UHC emissions. (e) Computational time

It is seen that by combining all three approaches, it is possible to reduce the computational time by a factor of more than twenty (indicated by the open symbols in the figure) for a DI engine case. The computational expense of simulating

combustion using detailed chemistry is reduced to the same level as of using the relatively simple Shell/CTC model discussed in Chapter 15. This allows for significantly more productive engine optimizations using CFD tools with detailed chemistry.

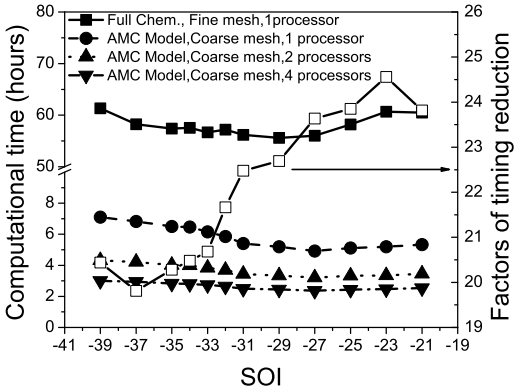

Fig. 16.12 Comparison of computational time using multiple processors, engine M16

Study of engine size-scaling relationships for a light-duty and a heavy-duty diesel engine

Problem description

Currently engine design work must be repeated for different engines that share essentially similar features. This motivates a study of the relationships between large diesel engines (such as off-road heavy-duty engines) and small engines (such as high speed auto engines) based on CFD simulation results. Initial work was proposed by Bergin *et al*. (2005) who argued that similar combustion between different engine sizes could be obtained by scaling a few basic engine geometry parameters, namely the engine speed and the mass of fuel injected. Later, Stager and Reitz (2007) extended Bergin's work and created additional rules to scale the spray development and combustion characteristics. The scaling rules were applied to two ideally scaled engines where the small engine was obtained by halving the linear dimensions of the larger engine. They concluded that the scaling rules worked well over a range of injection timings for engines with low temperature combustion, and the results also suggested that three regimes could be defined where turbulence and chemical kinetics timescales played different roles in influencing combustion and emissions.

This section describes scaling studies on two production diesel engines (Table 3.2) – a light-duty engine, S16 (~0.5 L displacement) and a heavy-duty engine, L16 (~2.5 L displacement). The small engine, S16 was taken as the baseline engine on which the scaling arguments were applied in order to obtain scaling parameters for defining a scaled large-bore engine, L16. The study also extends

the applications of scaling rules to more engine operating conditions in order to understand the effects of turbulence and chemistry timescales over a broader range in more detail.

Engine specifications and investigation approach

The investigated engines are a light-duty engine and a heavy-duty engine, which are single-cylinder experimental engines (Table 3.2) corresponding to respective production models. The original specifications of these two engines are described in Table 16.3.

Table 16.3. Original engine specifications

Engine type	Small, S16	Large, L16
Bore (mm)	82.0	137.16
Stroke (mm)	90.4	165.1
Bowl diameter (mm)	51.3	98.0
Connecting rod length (mm)	145.0	261.6
Squish height (mm)	0.67	1.57
Displacement (L)	0.477	2.439
Compression ratio	16.53	16.1
Swirl ratio	2.2~5.6	0.5
IVC	–142 ATDC	–143 ATDC
EVO	142 ATDC	130 ATDC
Injection pressure (bar)	1,600	1,500
Number of holes	8	6
Nozzle holes diameter (μm)	133	158

The two engines S16, L16 differ in many geometrical parameters and injection related variables, as indicated in Table 16.3. Figure 16.13 shows a comparison of the piston profiles of the two engines, which shows that the engines also feature different bowl curves. The small engine, S16 has a deep bowl design with vertical sidewall, but the bowl shape of the large engine, L16 is shallow and the curved chamber wall is relatively closer to the cylinder wall.

To eliminate the differences in bowl geometrical similarity the baseline piston bowl profile of the small engine, S16 was scaled to produce the bowl profile for a modified large engine, L16 in this study. Correspondingly, other parameters, such as the injection related parameters and operating conditions were scaled based on the scaling arguments, as discussed next. As is well known, the process of spray development has a primary effect on the performance and pollutant formation in diesel engines. In order to obtain similar spatial and temporal distributions of the vapour fuel, it is necessary to ensure that the transient spray plume trajectory scales. Here the temporal distribution of fuel represents its spatial distribution at a certain crank angle.

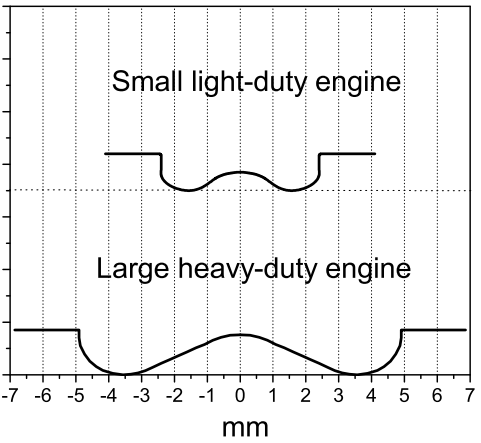

Fig. 16.13 Original piston bowl profiles (Adapted from Shi and Reitz 2008a)

This at least requires the spray penetration to be scaled. The spray penetration is defined as the distance the penetrating tip of the liquid-phase fuel travels in the combustion chamber before and during vaporization. The first scaling argument about the spray penetration is based on the empirical equations derived by Hiroyasu *et al*. (1978), which are given as

$$s = 0.39\sqrt{\frac{2\Delta p}{\rho_l}}t \quad , \quad 0 < t < t_{break} \tag{16.1}$$

$$s = 2.95\left(\frac{\Delta p}{\rho_a}\right)^{1/4}\sqrt{d_0 t} \quad , \quad t \geq t_{break} \tag{16.2}$$

$$\theta = 0.05\left(\frac{{d_0}^2 \rho_a \Delta p}{{\mu_a}^2}\right)^{1/4} \tag{16.3}$$

where:

$$t_{break} = 28.65\frac{\rho_l d_0}{\sqrt{\rho_A \Delta p}}$$

s = spray penetration tip length
ρ_l = liquid fuel density
ρ_a = air density

Δp = pressure drop across the injector
t = time
d_0 = injector nozzle orifice diameter
t_{break} = transient time from SOI to the jet breakup
θ = spray angle
μ_a . = air dynamic viscosity.

The second scaling argument is based on the flame lift-off length of diesel fuel jets. It is defined as the distance from the injector to the reaction zone where the jet stabilizes once the initial auto-ignition phase is over. The flame lift-off has a strong effect on diesel combustion, because it allows air to be entrained and pre-mixed with the fuel jet upstream of the lift-off length, which affects the combustion and soot formation processes downstream (Dec 1997, Siebers *et al*. 2002, Pickett *et al*. 2005). Pickett *et al*. (2005) extended Siebers' study (Sieber et al. 2002) on lift-off length and studied the relationships between ignition processes and the lift-off length. A power-law relationship of the lift-off length to various parameters was summarized in their paper (2005) based on an extensive database obtained using #2 diesel fuel. The expression is

$$H = CT_a^{-3\,74}\rho_a^{-0\,85}d_0^{\,0\,34}U^1Z_{ST}^{\,-1} \tag{16.4}$$

where:
H = lift off length
C = proportionality constant
T_a = ambient temperature
ρ_a = ambient gas density
U = injection velocity
ZST = stoichiometric mixture fraction.

The scaling argument about the swirl ratio is based on its influence on the spray plume, which is also obtained from Hiroyasu's study (1978). Two factors were proposed to supplement the empirical equations of spray penetration and angle in quiescent air in order to consider the fact that the spray is bent by air swirl. These two dimensionless correlation factors are defined as:

$$C_s = \left(1 + \frac{\pi r_s Ns}{30u_0}\right)^{-1} \tag{16.5}$$

$$C_\theta = \left(1 + \frac{\pi r_s Ns}{30u_0}\right)^2 = \frac{1}{C_s^{\,2}} \tag{16.6}$$

where C_s and C_θ are proportional to the reduction in axial penetration and the azimuthal deflection of the spray axis, respectively, and

r_s = swirl ratio

N = engine speed

s = spray penetration

u_0 = initial fuel jet velocity

It is apparent that the correlation factors should be equal in scaled engines in order to obtain scaled spray penetration.

The last scaling argument is to assume that scaled engines have the same combustion and thermal efficiency and their power output should be scaled by the mass of fuel injected into the cylinders, which is calculated from

$$m = \rho_l \frac{\pi}{4} d_0^2 U \Delta t \tag{16.7}$$

where:

m = mass of fuel injected

ρ_l = liquid fuel density

d_0 = injector nozzle orifice diameter

U = injection velocity (assumed constant)

Δt = injection duration

Scaled engines should have the same ambient conditions and fuel properties, and consequently these parameters can be removed from the scaling arguments discussed above, such as ambient temperature, fuel density, etc. equations (16.2), (16.4), and (16.7) are closed with respect to the parameters of injection velocity, nozzle orifice diameter, and injection duration in real time. Solving these equations simultaneously such that the power output is constant, and the spray penetration and flame lift-off length scale directly with the scaling factor yields the scaling relations in Table 16.4.

It is well known that the thermal efficiency of a diesel engine is correlated with its compression ratio. In order to match the thermal efficiency of the scaled engines, it is necessary to keep the same compression ratio. This presents two options, which are either to use the relation of the displacement volume to scale the TDC volume, or to use the TDC volume to scale the IVC volume. It was demonstrated in the study of Shi and Reitz (2008a) that the TDC volume scaling performed better than the displacement volume scaling, and thus it is discussed next. The specifications for the scaled engines are listed in Table 16.5, which is either derived from the scaling relationships shown in Table 16.4, or from the original values described in Table 16.3. It should be noted that since the stroke of the two engines S16, L16 is not scaled in proportional to their piston diameter, the IVC timing of the engine must be adjusted to have the same effective compression ratios for both engines.

Table 16.4 Scaling relations

Parameter	Scaling factor length	Scaling factor volume
M	L^3	V
S	L	$V^{1/3}$
H	L	$V^{1/3}$
d_0	L	$V^{1/3}$
A	L^2	$V^{2/3}$
T	$L^{1/3}$	$V^{1/9}$
U	$L^{2/3}$	$V^{2/9}$
Speed	$L^{-1/3}$	$V^{-1/9}$
Mean piston Speed	$L^{2/3}$	$V^{2/9}$
valve-lifts	L	$V^{1/3}$

Table 16.5 Scaled parameters for the TDC volume scaled engines

Engine type	Small engine, S16 (scaled)	Large engine, L16 (scaled)	Scaled?
Bore (mm)	82.0	137.16	N/A
Stroke (mm)	90.4	165.1	N/A
Bowl diameter (mm)	51.3	85.9	Yes
Connecting rod length (mm)	145.0	261.6	N/A
Squish height (mm)	1.33	2.23	Yes
Displacement (L)	0.477	2.439	No
TDC volume (L)	0.0359	0.1682	Yes
Geometrical compression ratio	14.3	15.5	No
Effective compression ratio	13.3	13.3	Yes
Swirl ratio	1.8	1.8	Yes
IVC	–142 ATDC	–126 ABTDC	Yes
EVO	142 ATDC	130 ATDC	No
Injection pressure (bar)	755	1,500	Yes
Number of holes	8	8	Yes
Nozzle holes diameter (μm)	137	229	Yes
Included spray angle	130	130	Yes

In addition to the scaling arguments described above, a few issues need to be addressed for numerically studying the scaled engines. First, the injection rate shape of the two engines has to be the same in order to deliver the scaled amount of fuel into the cylinders. Second, more heat transfer from the small engine, S16 due to its larger area/volume ratio has to be compensated for. The higher heat loss of the small engine, S16 is balanced by increasing its IVC temperature. The

increment of the intake temperature of the small engine, S16 was determined such that the motoring pressure trace of the small engine, S16 matched that of the scaled large engine under the same compression ratio, and the increment was found to be 10 K for the present study. Finally, the mesh-dependency issue has to be carefully considered to minimize its influence on the simulation results for engine of different sizes. This was accounted for by using a proper mesh size for both engines, such that either increasing or decreasing the mesh size would have consistent small changes in the simulation results. With these considerations, together with the scaling arguments, the engine operating conditions for studying the scaling relationships is shown in Table 16.6.

Table 16.6 Operating conditions of the TDC volume scaled engines: A, B, C low-, mid-, and high-load, respectively

		Small engine	Large engine	
Engine type		(scaled)	(scaled)	Scaled?
Speed (rpm)		2,000 (3,000 for case C)	1,685 (2,502 for case C)	Yes
Gross IMEP (bar)	A	4.5	4.5	Yes
	B	7	7	Yes
	C	10	10	Yes
Equivalence ratio	A	0.25	0.25	Yes
	B	0.75	0.75	Yes
	C	0.75	0.75	Yes
EGR rate (%)	A	55	55	Yes
	B	55	55	Yes
	C	25	25	Yes
Oxygen (vol%)	A	17.93	17.93	Yes
	B	11.97	11.97	Yes
	C	17.65	17.65	Yes
IVC Temperature (K)	A	380	370	Yes
	B	380	370	Yes
	C	380	370	Yes
IVC Pressure (bar)	A	1.79	1.736	Yes
	B	1.791	1.732	Yes
	C	1.791	1.732	Yes
Injected fuel (mg/cyc.)	A	11	51.5	Yes
	B	22.2	104	Yes
	C	32.5	151	Yes
Injection duration (CA)	A	6.2	6.2	Yes
	B	12.4	12.4	Yes
	C	18	18	Yes

Results and discussion

Simulations were conducted over a SOI sweep to investigate the effect of turbulence and chemistry timescales, and their interactions. With the TDC volume scaling, the pressure, heat release rate, and the scaled spray penetration (see the inset plots) for both engines S16, L16 at low-load (Case A in Table 16.6) match very well over the SOI sweep, as shown in Figs. 16.14a–c.

As indicated in Figs. 16.14a–c, the pressure traces of the scaled large engine, L16 are close to those of the small engine, L16 over the broad range of injection timings, as well as its scaled heat release rates. However, because the IVC timing of the large engine, L16 needs to be altered to match the effective compression ratio, its compression processes differ slightly from those of the small engine, S16, but no noticeable influence of this discrepancy was seen on the combustion and emissions. This indicates that the current scaling argument regarding the engine power output works fairly well. The small inset plots in Figs. 16.14a–c are included to show that the scaled liquid spray penetrations in the large engine, L16 also agree with those in the small engine, L16, which further supports the scaling argument for spray penetration.

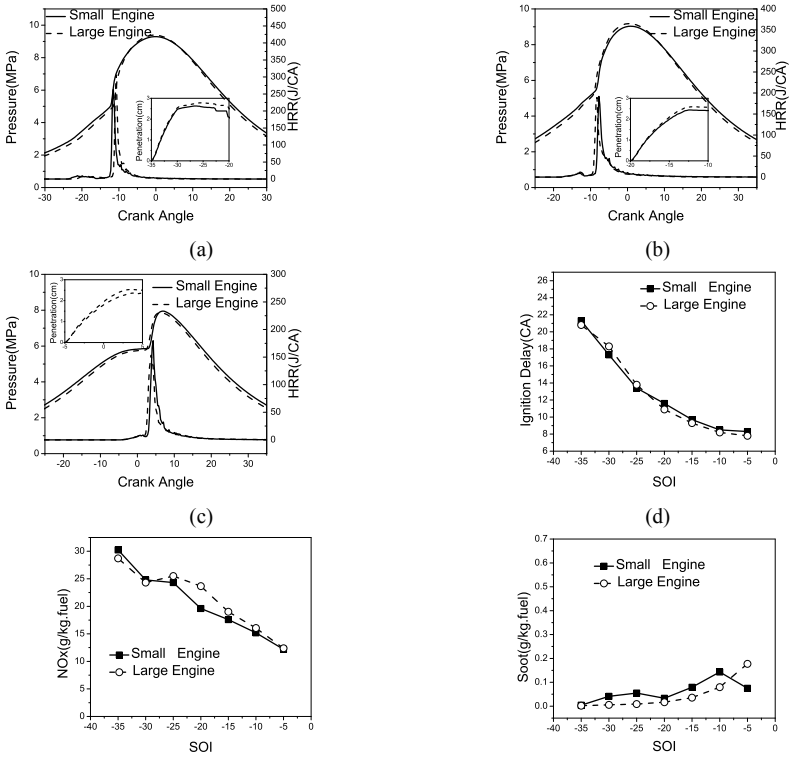

Fig. 16.14 Comparison of the TDC volume scaled engines at low-load. (a) SOI = –35 ATDC. (b) SOI = –20 ATDC. (c) SOI = –5 ATDC. (d) Ignition delay. (e) NO_x emissions. (f) Soot emissions

The results of the TDC volume scaling at mid-load (Case B in Table 16.6) are not as good as those of the low-load cases with respect to the differences in the emissions trends, which are shown in Fig. 16.15. In general, the large engine, L16 produces more NO_x and soot emissions. The discrepancy of soot emissions increases as the SOI timing is retarded, but the difference in NO_x emissions decreases.

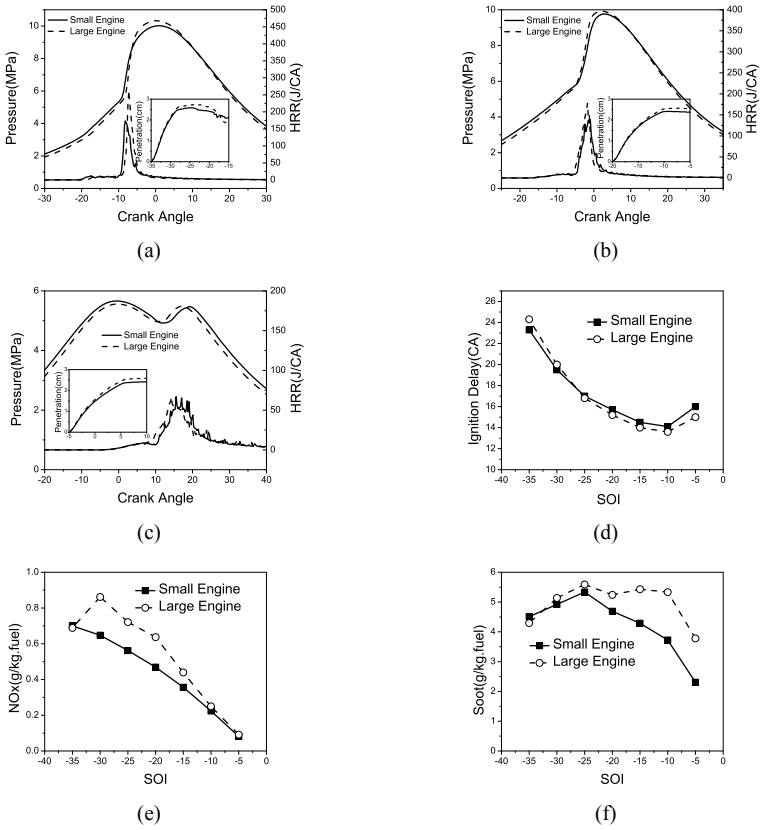

Fig. 16.15 Comparison of the TDC volume scaled engines at mid-load. (a) SOI = –35 ATDC. (b) SOI = –20 ATDC. (c) SOI = –5 ATDC. (d) Ignition delay. (e) NO_x emissions. (f) Soot emissions

The injection duration of the low-load case (6.2 CA) is about half that of the mid-load case (see Tables 16.4 and 16.6). The short injection duration reduces the time of spray jet flow interaction with the ambient turbulent flow. This leaves more time for the transport of evaporated fuel by turbulence and bulk flow. Figure 16.14d reveals that the ignition delay is larger than the injection duration for all SOI timings, which allows time for mixing before combustion. The combustion process should be expected to scale if the chemistry timescale is more influential since the engine speeds are similar and the gas temperature was adjusted by 10 K to give similar ignition times. Therefore, the explanation of better matching of the

combustion characteristics and emission trends in the two engines, S16, L16 at low-load can be understood. The longer injection duration at mid-load, and thus the longer time of interaction of the jet flow with the bulk flow and the weaker effect of the chemistry on the emission formation and oxidation processes are reasons that the emissions are less scaled.

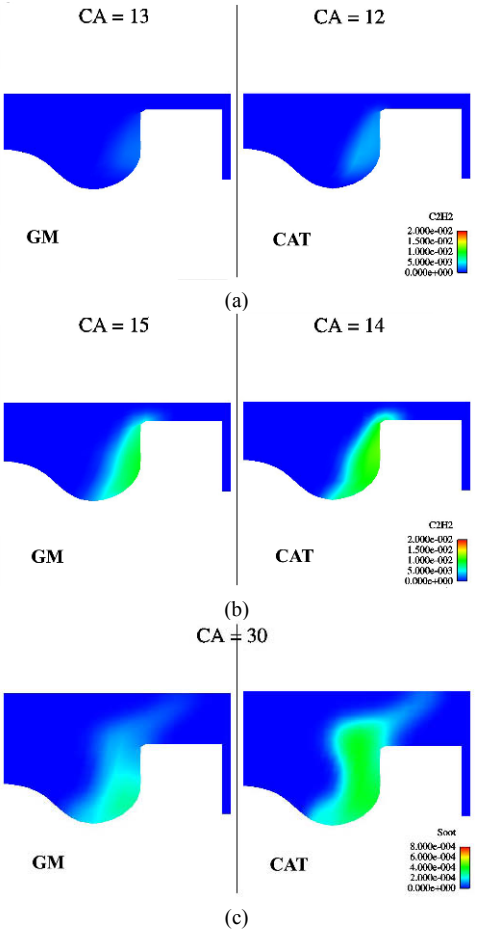

Fig. 16.16 Distributions of C_2H_2 and soot mass fraction (SOI = −5 ATDC). (a) C_2H_2. (b) C_2H_2. (c) Soot (Shi and Reitz 2008a)

In this study, acetylene (C_2H_2) is taken as the precursor of soot formation, and higher concentration areas of C_2H_2 correspond to more soot production propensity. Before acetylene was formed, the distributions and quantities of the local temperature, evaporated fuel, as well as oxygen concentration were found to be very similar in the two engines. However, a comparison between Figs. 16.16a and b regarding the C_2H_2 mass fraction reveals that in the same 2°CA span, more C_2H_2

is generated in the large engine (note that the large engine is shown 1°CA ahead of the small engine because of its slightly earlier ignition). This directly results in more soot emissions in the large engine shown in Fig. 16.16c. The large engine has lower speed based on the current scaling laws, and therefore longer real time for 1°CA. The C_2H_2 formation reactions are fast under conditions of high temperature and low oxygen concentration, and thus the differences in C_2H_2 are due to mixing effects and oxidation. For early injection cases, the chemistry timescale of reactions of C_2H_2 is relatively large due to the lower local temperatures. The better-scaled soot emissions trend for the low-load case was primarily due to the effect of the soot oxidation process, whose chemistry timescale is much larger than soot formation (or C_2H_2 formation). Based on this discussion, it is expected that scaled engines operated at a higher speed would produce smaller differences in soot emissions. This is proved in Fig. 16.16 that shows less discrepancy of soot emissions between the two engines when operated at high speed for Case C listed in Table 16.6 with engine speeds of 3,000 and 2,502 rev/min, respectively.

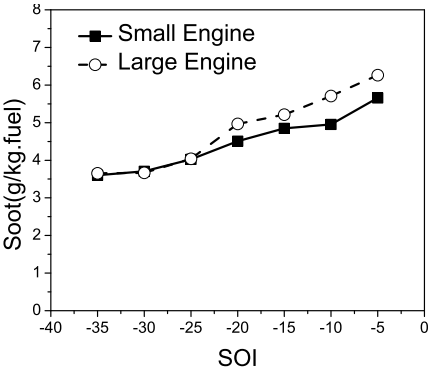

Fig. 16.17 Comparison of soot emissions of engines at high speed (engine speed 3,000 and 2,502 rev/min for the small S16 and large L16 engines, respectively)

From the above study, it is seen that the engine size-scaling arguments have been validated using the KIVA CFD code. Global performance results, such as the pressure trace and heat release rates are well scaled based on the scaling laws. Soot emissions for the large engine, L16 operated at mid- or high-load conditions do not scale as well as at light load. This is due to the fact that the soot formation process, which is controlled by chemistry timescales, at mid- or high-load is more significant compared to that at light-load, in which the soot oxidation, which is controlled by turbulence mixing timescales, dominates. Therefore, at different engine speeds (or different real time) the different timescales that control the net soot emissions contribute to the poor-scaled soot emissions for engines operated at mid- or high-load. For the low-load operating condition, better scaling of soot emissions was seen because sufficient time is available for oxidation. The large engine, L16 has longer time available for reactions compared to the higher speed

small engine. Therefore, more NO_x is produced, especially in cases with early injection timings where the gas remains at higher temperature for larger distributions. Hence, higher EGR ratios may be needed to suppress the NO_x formation. Unscaled heat losses and NO_x can be compensated for by slightly increasing the intake temperature of the small size engine, S16. Thermal management of the cooling system can be used to scale the heat losses for engines of different sizes.

Optimisation of a heavy-duty engine at low- and high-loads

Problem description

Although many researchers have shown that low temperature combustion is a very promising strategy to reduce both NO_x and soot emissions in diesel engines, it has been found (as also seen in the first case study) that UHC and CO emissions are usually high. The rapid pressure rise rate occurring in PCCI engines also narrows its available operating conditions, and its application to the high-load operating condition is limited due to unacceptable engine knock. The control of the onset of combustion remains an additional challenge for the application of low temperature combustion, because the start of combustion is primarily determined by chemistry processes. Therefore, it is still of much interest to further investigate the traditional combustion regime for heavy-duty engines to improve their performance and to reduce emissions.

Genetic Algorithm (GA) search techniques have become one of the mainstream optimization methods and are now increasingly used in engine design. Wickman *et al*. (2001) conducted a study of engine combustion chamber geometry optimization for a small bore and a large bore engine with a Single Objective Genetic Algorithm (SOGA), and they achieved improved fuel economy and emissions for the two investigated engines. Bergin *et al*. (2005) applied SOGA to their study of large diesel engines and discovered a promising new concept called “spin-spray” combustion. 2006 non-road emissions targets were met by optimizing the spray events without other means of emissions reduction. But SOGA demonstrates dependency on the choice of merit function and, unfortunately, the definition of an appropriate merit function is usually unclear to the decision maker prior to the optimization process of a multi-objective problem. This motivates interest in studies and application of Multi-Objective Genetic Algorithms (MOGA). MOGA is becoming a prominent method for use in optimization and design. Genzale *et al*. (2007) investigated a heavy-duty diesel engine operated at low-load and under low temperature combustion conditions, and a set of optimized combinations of the spray targeting, bowl geometry and swirl ratio was revealed. Shi and Reitz (2008b) assessed three widely applied MOGAs for optimizing a heavy-duty diesel engine operated at high-load. In their research, the Non-dominated Sorting Genetic Algorithm II (NSGA II) (Deb *et al*. 2002) with a large population size was found to perform better for use in engine optimization, and an optimal injection strategy and better matching of the piston geometry with the spray plume were also identified.

For any combustion process, boundary and initial conditions are two influential aspects, and particularly the preparation of the fuel-air mixture also critically influences compression ignition combustion. Combustion and pollution formation are significantly affected by the mixing processes in diesel engines, and thus it is necessary to identify a better method to match the boundary conditions, such as matching the piston geometry with the spray plume geometry, as well as to ensure good initial conditions, such as those due to the initial flow motions like swirl.

For a diesel engine operated at different loads, the in-cylinder thermal conditions vary considerably, which results in different spray behaviors, combustion characteristics, and pollutant formation. It can be anticipated that different injection strategies and matching of the piston geometry and spray plume are needed for engines under different operating conditions in order to reduce emissions and fuel consumption. This case study presents an optimization study of a heavy-duty diesel engine operated at both low-load and high-load for better understanding of the effects of bowl geometry, spray targeting, and swirl ratio on engine operation. A non-parametric regression analysis tool (Lin and Zhang 2003, Liu *et al*. 2006) is also used to post-process the optimized results to provide more visible relations between design parameters and objectives.

Engine specifications and investigation approach

The geometric specifications and fuel injector parameters of the heavy-duty engine, H16 (Table 3.2) are summarized in Table 16.7. The operating conditions correspond to 20% and 95% load at high speed, respectively (Table 16.8).

Table 16.7 Specifications of Engine H16

Combustion chamber	Quiescent, direct injection
Swirl ratio	0.5
Bore × stroke (mm)	137.16 × 165.1
Bowl width (mm)	97.8
Displacement (L)	2.44
Connection rod length (mm)	261.6
Geometric compression ratio	16.1:1
Fuel injector nozzles	8 holes, equally spaced
Spray pattern included angle	154
Rail pressure (bar)	1,600
Nozzle orifice diameter (mm)	0.217

The primary goal of the present study is to find optimal combustion boundary conditions, i.e., combustion chamber (bowl) shapes, for a heavy-duty engine, H16 at low-load and high-load. In addition, optimal combinations of spray targeting and swirl ratio levels as a function of combustion chamber shape were searched for simultaneously in order to further understand the effects of the initial flow

conditions and the spray development on combustion, with the objectives of reducing both NO_x and soot emissions and improving fuel economy.

A total of nine parameters, including the injector spray angle, swirl ratio, SOI, and six different parameters that define the bowl geometry were studied for the high-load case. An additional parameter of injection pressure was applied to the low-load case. The compression ratio was kept fixed as 16.1 and the six bowl geometric parameters enable a search of a wide range of bowl shapes, and also allow for the consideration of reentrant-type bowls. The number of geometry parameters used gives a reasonable search space using the Kwickgrid methodology (Wickman *et al*. 2001), although more parameters are available in the grid generator to define the bowl shapes. Figure 16.18 illustrates the six bowl geometry parameters optimized in this study.

Table 16.8 Baseline operating conditions

Conditions	High-load	Low-load
Speed (rev/min)	1,672	1,672
IVC temperature (K)	385	370
IVC pressure (kPa)	310	153
Load (%)	95	20
Injection quantity (mg/cyc)	229	70.9
EGR level (%)	25	20
Global equivalence ratio	0.60	0.33
O_2 Concentration (vol. %)	17.65	19.52

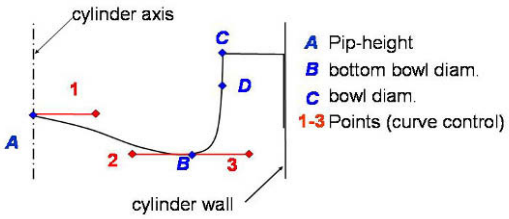

Fig. 16.18 Parameters of bowl geometry (Adapted from Shi and Reitz 2008c)

Table 16.9 provides the ranges of the parameters, which were determined so as to avoid infeasible bowl designs but still to maintain diversity. The spray angles target a wide region of the piston, from the bowl floor up to the bowl lip. Considering the ability of the intake system of the experimental engine, the range of swirl ratio was restricted to a relative narrow range. The SOI range for the high-load operation was determined based on maximum power-output of the baseline design of the engine, and for the low-load case a broader range was considered to

explore more emissions trade-offs. The injection pressure for the high-load case was fixed at 2,000 bar in order to achieve realistic injection durations.

The optimisation process is described in Fig. 16.19, which shows that the genetic algorithm is employed to generate input parameters (in the ranges listed in Table 16.9) for the KIVA CFD code. With these input parameters, the KIVA code evaluates the engine performance and emissions, which provides feedback to the genetic algorithm. The new feedback enables the genetic algorithm to search for optimum input parameters for the next KIVA evaluations. The cycle evolves until satisfactory results are obtained or the optimization process converges (Shi and Reitz 2010). In this study, for each of the two cases, a total of 1,272 cases were simulated.

Table 16.9. List of optimisation parameters and their ranges of engine H16

Parameters	Range	
	High-load	Low-load
A – (% bowl depth)	65–75	65–75
B – (% bowl diameter)	74–80	74–80
C – (% cylinder diameter)	71–84	71–84
1 – Bezier curve control point	0.1–0.7	0.1–0.7
2 – Bezier curve control point	0.3–0.9	0.3–0.9
3 – Bezier curve control point	0.8–1.5	0.8–1.5
Injector spray half-angle	60 –85	60 –85
Swirl ratio	0.5–2.0	0.5–2.0
SOI (ATDC)	–15 to –13	–10 to +10
Injection pressure (bar)	2,000	850–2,000

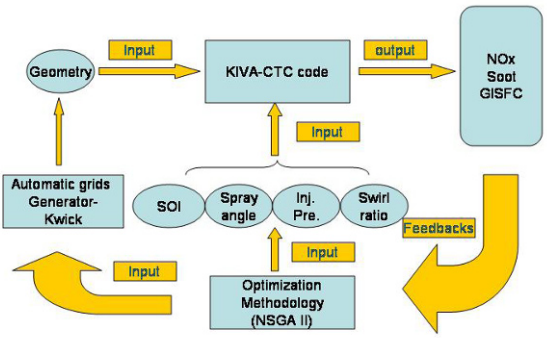

Fig. 16.19 Illustration of optimisation process using genetic algorithm and the KIVA CFD code

Results and discussion

The optimisation studies on the heavy-duty engine, H16 operated at high- and low-load conditions were conducted, and the Pareto solutions (representing optimal designs) with objectives of NO_x, soot, and GISFC were identified. Representative designs for each case were selected from the Pareto Front (formed by all optimum solutions) as the reference designs for use with the non-parametric regression analysis. The response surfaces generated under different engine operating conditions are discussed next. The optimal designs were further explained and examined with additional parametric studies and in-cylinder visualizations in order to validate the present non-parametric regression technique and also to better understand the flow motions, combustion, and pollutant formation processes. Finally, a common optimal piston design was selected to show that an optimum design could be achieved for both high- and low-load operation.

All solutions from each case are plotted in the objective space, as shown by the squares in Figs. 16.20 and 16.21 for the high-load and low-load, respectively, and the optimal solutions are indicated by the circles. It is seen from the optimal solutions in the figures that for each group, designs exist that can simultaneously reduce NO_x and soot emissions while reducing the fuel consumptions, such as Design 2 in Fig. 16.20 and Design 3 in Fig. 16.21.

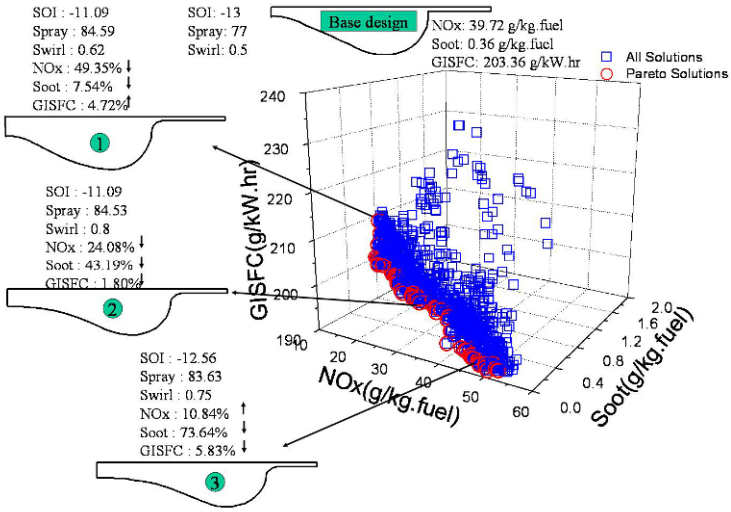

Fig. 16.20 Pareto front and optimal solutions. (a) Solutions for the high-load condition (Adapted from Shi and Reitz 2008c)

Comparison of the low-load optimal designs with the high-load optimal solutions indicates that the Pareto solutions feature different aspects. Firstly, the spray included angles are no longer restricted to high values for the low-load case, although most of the optimal solutions still have flat spray targeting, as seen for the high-load case. Secondly, the effect of bowl size become less important

compared to that of the high-load optimal designs. No small bowl design was found on the Pareto front, and all optimal designs feature mid-range or large bowl diameters and also have a relatively large size of the bowl floor. Thirdly, the Pareto solutions seek high swirl ratios, and most of them are larger than 1.5, but for the high-load optimal solutions, almost all cases feature relatively low swirl ratios. Fourthly, for the low-load condition, high injection pressure does not certainly benefit emissions and fuel economy, and most of optimal solutions have a moderate injection pressure in range of 1,400–1,600 bar. All these observations imply that spray targeting and its matching with the bowl geometry and the initial flows behave differently under high- and low-load conditions. Therefore more details were explored with non-parametric and parametric studies as follows.

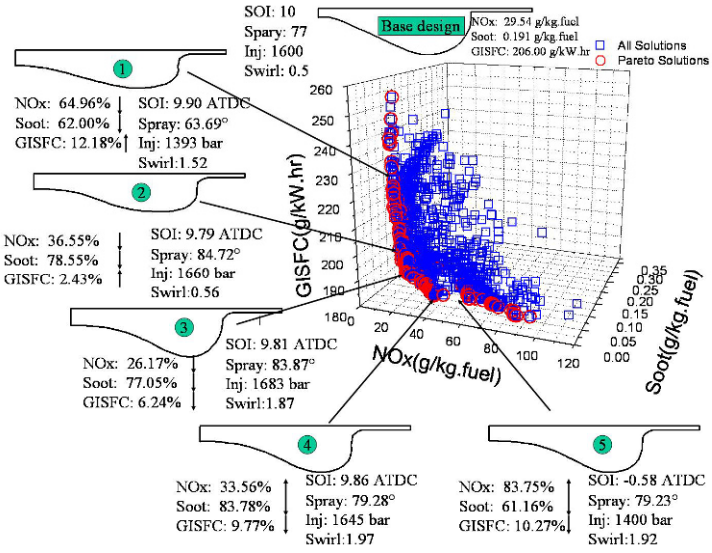

Fig. 16.21 Pareto front and optimal solutions. (b) Solutions for the low-load condition (Adapted from Shi and Reitz 2008c)

Design 2 in Fig. 16.20 for the high-load and Design 3 in Fig. 16.21 for the low-load were selected as reference designs for the non-parametric regression analysis, since they represent optimum designs. It is also noted that for the high-load cases GISFC responded similarly with soot emissions and thus its response surfaces are not provided here. In addition, for both cases, the details of the piston geometry, such as the bowl profile curvatures were found not influential to the objectives and thus they are not further discussed.

Observed in Fig. 16.22 for the high-load condition, the spray included-angle is the most influential parameter for NO_x emissions, and the peak NO_x emissions are found at medium values of the spray angle. In Fig. 16.22b, reduced NO_x emissions are favoured by a low swirl condition. However, changes with swirl ratio are less than those associated with spray angle changes, so that the swirl ratio has a

secondary effect on NO_x emissions. The SOI has less effect on NO_x emissions as compared to the other two. The order of parameters and how significantly they influence soot are the same as that obtained from the response surfaces of NO_x, and the spray angle is still the dominant parameter. Similar to its effect on NO_x, medium values of the spray angle contribute more soot. As shown in Fig. 16.22d, the soot emissions reduce slightly as the swirl ratio increases, for which an inverse trend is seen on NO_x emissions in Fig. 16.22b.

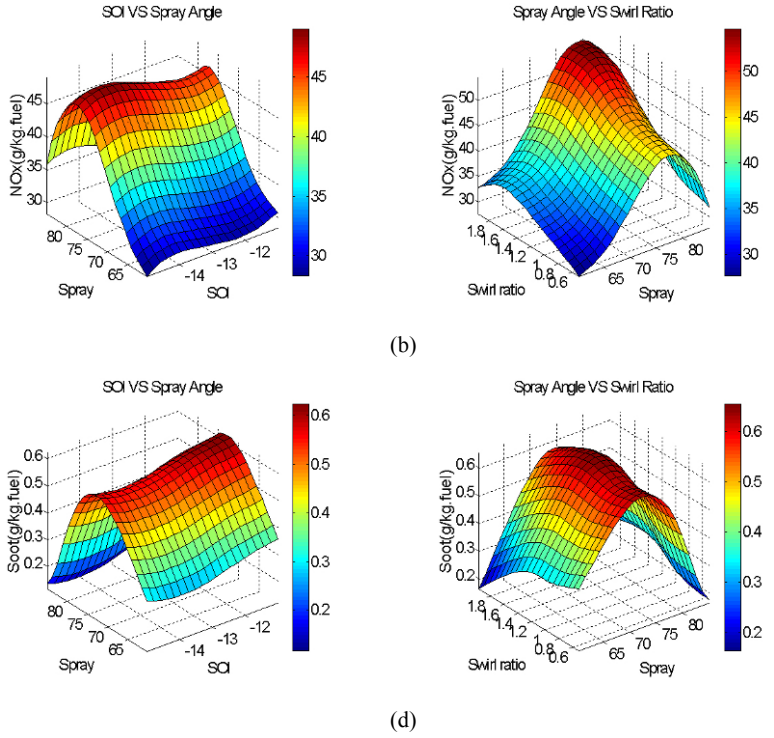

Fig. 16.22 Response surfaces for the large bowl design (Design 2 in Fig. 16.20) under the high-load condition. (a) Interacting of SOI and spray angle on NO_x. (b) Interaction of spray angle and swirl on NO_x (c) Interaction of SOI and spray angle on soot. (d) Interaction of spray angle and swirl on soot (Adapted from Shi and Reitz 2008c)

The response surfaces of NO_x with respect to SOI, spray angle, swirl ratio, and injection pressure and their interacting effects are given in Figs. 16.23a–c. It is observed that retarding SOI has the primary influence of reducing NO_x emissions, which is consistent with experimental observations, since the combustion temperature reduces as the SOI is retarded. But note that after 5°ATDC, the effect of SOI becomes weaker since the surface with respect to spray angle becomes flat. NO_x emissions peak at about 77° spray angle, and this finding is similar to that obtained from the study of the high-load cases. Decreasing injection pressure helps reduce NO_x emissions, as shown in Fig. 16.23e. Compared to the other

parameters, the swirl ratio has the least effect on NO_x emissions, though it can be seen that a high swirl ratio slightly promotes NO_x production in Figs. 16.23b and c.

For the soot emissions, SOI is still an important parameter, but the effects of other parameters become more important than they were on NO_x. As seen in Fig. 16.23d, soot emissions are minimized at about 77° spray angle, opposite to the observation on NO_x. However, retarding SOI also helps to reduce soot emissions, and this is believed to be the reason that most of the Pareto designs for the low-load condition feature very late injection timings. Increasing swirl ratio or injection pressure benefits soot emissions, as seen in Figs. 16.23e and f, which also indicates the difficulty of engine design due to the trade-off between NO_x and soot.

Comparison of Figs. 16.23e–f and g–i demonstrates that GISFC responds differently to the investigated parameters, which is a further challenge to engine design for low-load operation. For example, it was found above that retarding SOI helps reduce both NO_x and soot emissions. However, Fig. 16.23g frustrates this finding in that the late injection timing deteriorates fuel economy significantly. However, it is also seen that if a large spray angle is employed, the effect of SOI on GISFC weakens. Therefore, in order to obtain both emissions reduction and fuel economy, a combination of large spray angle and late injection is needed. Figure 16.23i illustrates that GISFC decreases as the injection pressure increases. Furthermore, the effect of swirl ratio is again seen to be the least.

For a practical engine the combustion chamber geometry and the spray included angle cannot be varied easily. Thus it is of interest to seek a compromise optimal design for both conditions. It is desired to achieve emissions reduction and improved fuel consumption at both high-load and low-load by optimising other flexible design parameters, such as the swirl ratio and the injection timing and pressure. It was shown in Fig. 16.20 that high-load Design 2 reduced emissions and fuel consumption simultaneously, compared to the baseline design. In addition, it is also observed that its combustion chamber shape shares similar features with Design 3 in Fig. 16.21 for the low-load optimisation. Therefore, Design 2 and its corresponding spray angle (84.53°) were selected to conduct a study under the low-load condition. The three cases listed in Table 16.10 were studied, and the results are given in Table 16.11.

Table 16.10 Parametric study for the low-load condition using the second high-load piston design in Fig. 16.20

Parameters	SOI(ATDC)	Spray( )	Swirl	Inj. Pre. (bar)
Case 1	9.81	84.53	1.87	1,683
Case 2	9.81	84.53	0.8	1,683
Case 3	9.81	84.53	0.8	1,200

Compared to the results from the original optimised bowl design, Cases 1 and 2 are seen in Table 16.11 to reduce both NO_x and soot emissions, without sacrificing fuel economy significantly. This indicates that optimal piston designs exist for both high-load and low-load conditions, but it would be necessary to provide

different swirl ratios through intake system design and to employ different injection pressures and timings, for example by using a common-rail injection system to accommodate the different loads in order to achieve clean and highly efficient combustion.

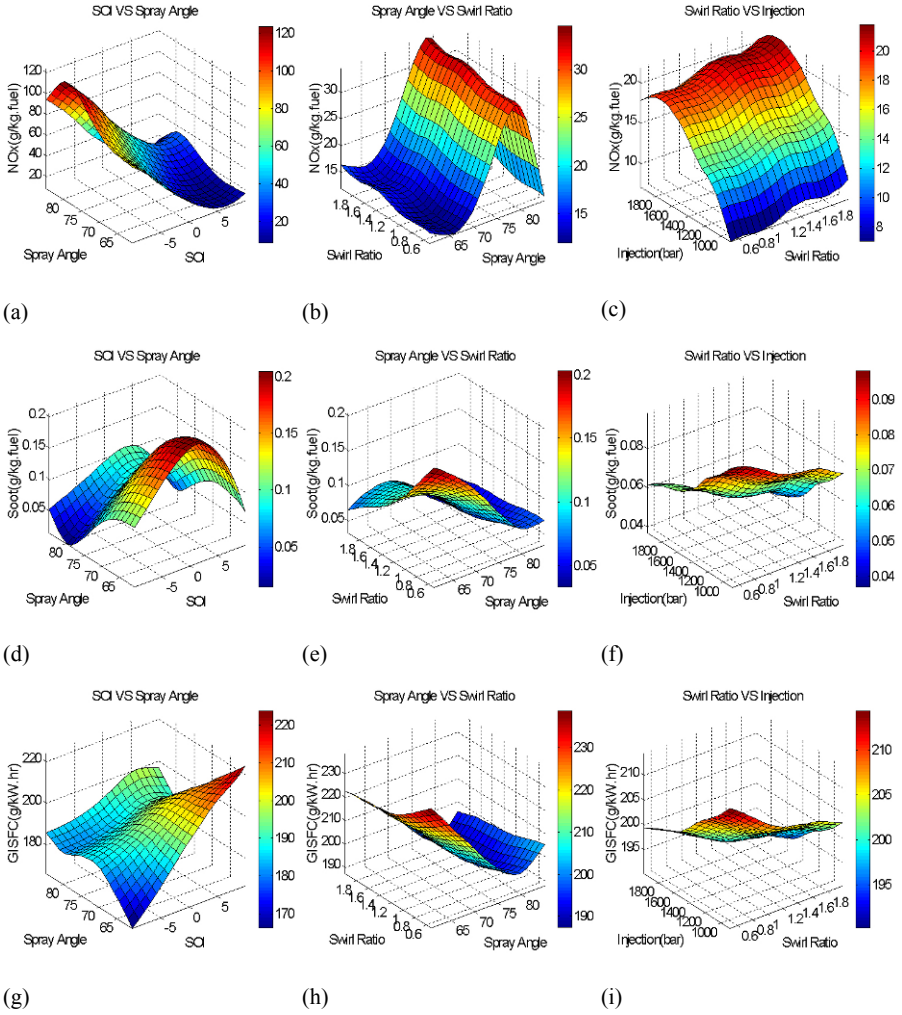

Fig. 16.23 Response surfaces for the large bowl design (Design 3 in Fig. 16.21) under the low-load condition. (a) SOI and spray angle on NO_x. (b) Spray angle and swirl on NO_x. (c) Swirl and injection pressure on NO_x. (d) SOI and spray angle on soot. (e) Spray angle and swirl on soot. (f) Swirl and injection pressure on soot. (g) SOI and spray angle on GISFC. (h) Spray angle and swirl on GISFC. (i) Swirl and injection pressure on GISFC (Adapted from Shi and Reitz 2008c)

Table 16.11 Results of parametric study for the low-load condition using the second high-load piston design in Fig. 16.20

Objectives	NO_x (g/kg.fuel)	Soot (g/kg.fuel)	GISFC (g/kW.h)
Case 1	20.34	0.049	196.21
Case 2	17.32	0.047	201.00
Case 3	13.12	0.078	211.93

It is concluded from this case study that the use of MOGA enables an efficient search of global optimal solutions with conflicting objectives. The use of non-parametric regression analysis together with the GA optimisations helps to quantify the influences of design parameters on the optimal objectives. The optimization showed that the high-load operating condition is more sensitive to the combustion chamber geometrical design compared to the low-load condition. This was revealed by examining the optimal solutions for the high-load optimization, in which the Pareto cases feature a broad range of bowl sizes and geometries. By choosing an optimal combustion chamber design from the high-load optimization study and varying swirl ratio, injection timing and pressure, excellent performing designs were also found using the high-load optimal chamber geometry for the low-load condition. This suggests that engine optimization studies for all operating loads should start with an optimization study of piston geometry, spray targeting for the high-load condition. Then further optimization on the spray injection event and swirl ratio should be conducted for the low-load condition.

References

Beale J C and Reitz R D (1999) Modeling spray atomization with the Kelvin-Helmholtz/ Rayleigh-Taylor hybrid model. Atom Sprays 9: 623–650

Bergin M J and Reitz R D (2005) Soot and NO_x emissions reduction in diesel engines via spin-spray combustion. ILASS American, 18th Annual Conference on Liquid Atomization and Spray Systems, Irvine, CA

Bergin M J, Hessel R P, and Reitz R D (2005) Optimization of a large diesel engine via spin spray combustion. SAE paper 2005-01-0916

Deb K, Pratap A, Agarwal S, and Meyarivan T (2002) A fast and elitist multiobjective genetic algorithm: NSGA-II. IEEE Transactions on Evolutionary Computation 6: 182–197

Dec J E (1997) A conceptual model of DI diesel combustion based on laser-sheet imaging. SAE Transaction 106: 1319–1348

Genzale C L, Reitz R D, and Wickman D D (2007) A computational investigation into the effects of spray targeting, bowl geometry and swirl ratio for low-temperature combustion in a heavy-duty diesel engine. SAE paper 2007-01-0119

Han, Z, and Reitz, R D (1995) Turbulence modeling of internal combustion engines using RNG k-ε models. Comb Sci Tech 106: 267–295

Hiroyasu H, Kadota T, and Arai M (1978) Supplementary comments: fuel spray characterization in diesel engines. Combustion Modeling in Reciprocating Engines Symposium, General Motors Research Laboratories, 1978

Kimura S, Aoki O, Kitahara Y, Ogawa H, and *et al*. (1999) New combustion concept for ultraclean and high-efficiency small DI diesel engines. SAE paper 1999-01-3681

Kimura S, Aoki O, Kitahara Y, and Aiyoshizawa E (2001) Ultra-clean combustion technology combining a low-temperature and premixed combustion concept for meeting future emission standards. SAE paper 2001-01-0200

Kong S C, Han Z, and Reitz R D (1995) The development and application of a diesel ignition and combustion model for multidimensional engine simulation. SAE Paper 950278.

Kook S, Bae C. Miles P C. and *et al*. (2005) The influence of charge dilution and injection timing on low temperature diesel combustion and emissions. SAE paper 2005

Kook S, Bae C, Miles P C, and *et al*. (2006) The effect of swirl ratio and fuel injection parameters on CO emission and fuel conversion efficiency for high-dilution, low temperature combustion in an automotive diesel engine. SAE paper 2006-01-0197

Opat R, Ra Y Gonzalez D M A, and *et al.* (2007) Investigation of mixing and temperature effects on HC/CO emissions for highly dilute low temperature combustion in a light-duty diesel engine. SAE paper 2007-01-0193

Lee S, Gonzalez M A, and Reitz R D (2007) Effects of engine operating parameters on near stoichiometric diesel combustion characteristics. SAE paper 2007-01-0121

Lin Y and Zhang H H (2003) Component selection and smoothing in smoothing spline analysis of variance models. Institute of Statistics Mimeo Series 2556, NUCS, 2003

Liu Y, Lu F, and Reitz R D (2006) The use of non-parametric regression to investigate the sensitivities of high-speed direct injection diesel emissions and fuel consumption to engine parameters. Int J Engine Res 7: 167–180

Nevin R M, Sun Y, Gonzalez M A, and Reitz R D (2007) PCCI investigation using variable intake valve closing in a heavy duty diesel engine. SAE paper 2007-01-0903

Park S W and Reitz R D (2007) Numerical study on the low emission window of homogeneous charge compression ignition diesel combustion. Combust Sci Tech 179: 2279–2307

Pickett L M, Siebers D L, and Idicheria C A (2005) Relationship between ignition processes and the lift-off length of diesel fuel jets. SAE paper 2005-01-3843

Ra Y and Reitz R D (2008) A reduced chemical kinetic model for IC engine combustion simulations with primary reference fuels. Combust. Flame 155: 713–738

Shi Y and Reitz R D (2008a) Study of diesel engine size-scaling relationships based on turbulence and chemistry scales. SAE paper 2008-01-0955

Shi Y and Reitz R D (2008b) Assessment of optimization methodologies to study the effects of bowl geometry, spray targeting and swirl ratio for a heavy-duty diesel engine operated at high-load. SAE paper 2008-01-0949

Shi Y and Reitz R D (2008c) Optimization study of the effects of bowl geometry, spray targeting and swirl ratio for a heavy-duty diesel engine operated at low- and high-Load. Int J Engine Res 9: 325–346

Shi Y and Reitz (2010) Assessment of multi-objective genetic algorithms with different niching strategies and regression methods for engine optimization and design. J Eng Gas Turbines Power 132(1)

Siebers D L, Higgins B, and Pickett L M (2002) Flame lift-off on direct-injection diesel fuel jets: oxygen concentration effects. SAE paper 2002-01-0890

Siewert R M (2007) A phenomenological engine model for direct injection of liquid fuels, spray penetration, vaporization, ignition delay, and combustion. SAE paper 2007-01-0673

Stager L A and Reitz R D (2007) Assessment of diesel engine size-scaling relationships. SAE paper 2007-01-0127

Wickman D D, Senecal P K, and Reitz R D (2001) Diesel engine combustion chamber geometry optimization using genetic algorithms and multi-dimensional spray and combustion modeling. SAE paper 2001-01-0547

Appendices

Appendix I: Estimation of Products of Combustion from the Interferogram

It is assumed that when the mixture fraction ($C(r, x)$) is greater than the concentration at rich limit ($C_{R\cdot L\cdot}$) a part of the fuel vapour combines with available air according to a ratio determined by $C_{R\,L}$ and the rest of the fuel remains in pure vapour form. Referring to Fig. A.1:

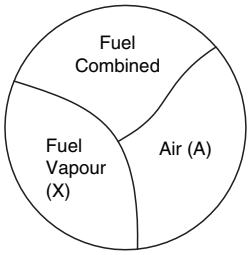

Fig. A.1 Fuel, vapour and air in the spray

By definition of the rich limit

$$\frac{y}{y+A} = C_{R\,L} \tag{A.1}$$

$$\text{Also } \frac{x+y}{x+y+A} = \textit{Mixture fraction} \tag{A.2}$$

$$\begin{aligned} C_f &= \textit{Concentration of fuel vapour} \\ &= \frac{x+y}{x+y+A} \\ &= C(r,x) - \frac{C_{R\,L}}{1-C_{R\,L}} \end{aligned} \tag{A.3}$$

Appendix II: Estimation of Concentration of Fuel Vapour in the Vapourising and Combusting Spray from the Interferogram

Let T = Temperature

n = Refractive index

ρ = Density

K = Gladstone-Dale constant

M = Molecular weight

and Cf = Concentration of fuel vapour

Subscripts *f, b, ∞, r* refer to fuel vapour, products of combustion, the surroundings (reference, air) and the point in the jet. From (Dent *et al.* 1977) for any point r in the burning jet

$$n_r = \rho_{mix}\left[C_f K_f + (1 - C_f)K_b + 1\right] \tag{A.4}$$

Similarly,

$$n_\infty = \rho_\infty K_\infty + 1 \tag{A.5}$$

Also

$$\rho_\infty = \frac{p M_\infty}{R T_\infty} \tag{A.6}$$

$$\rho_{mix} = \frac{p}{R T_r}\left(\frac{C_f}{M_f} + \frac{C_b}{M_b}\right) \tag{A.7}$$

Here R is the universal gas constant and $C_b = 1 - C_f$

Substituting equations (A.5), (A.6), (A.7) in (A.4),

$$T_r = \frac{T_\infty}{M_\infty} \frac{C_f + (1 - C_f)K_b}{\left[K_\infty - \frac{(n_r - n_\infty)}{\rho_\infty}\right]\left[\frac{C_f}{M_f} + \frac{(1 - C_f)}{M_b}\right]} \tag{A.8}$$

Appendix III: Estimation of Mass and Heat Transfer Functions

Transfer number, B (Spalding 1977):

By Reynolds Analogy between the mass and thermal boundary layers (Fig. 5.7)

$$\frac{m_{vap,\,o} - m_{vap,\infty}}{1 - m_{vap,o}} = B_M = B_H = \frac{C_{vap}\left(T_\infty - T_o\right)}{L} \tag{A.9}$$

Here, m = Mass concentration

T = Temperature

L = Latent heat of vaporisation+ sensible heat to change liquid from sub-cooled condition to vapour at saturation temperature

C = Specific heat

B = Transfer number

and subscripts

vap = Vapour

o = At the interface of liquid and vapour

∞ = Bulk gases

H = Heat transfer

and M = Mass transfer

Appendix IV: Vapour Pressure of Diesel and Fuels A & B and B*

Vapour pressure of diesel, and fuels *A, B, B**

$$P_{vap} = 7.9 \times 10^9 \exp\left(\frac{-5440}{T_s}\right) \tag{A.10}$$

Vapour pressure of highly viscous, less volatile fuel, G,

$$P_{vap} = 4.1 \times 10^{11} \exp\left(\frac{-8400}{T_s}\right) \tag{A.11}$$

Where T_s = saturation temperature

Appendix V: Calculation of Tangential Velocity of Air in the Piston Cavity from the Inlet Swirl Number

The cylinder head is assembled on the cylinder liner in a steady flow rig. The inlet of a blower is connected to the liner von Thien (1965). The air is sucked from the atmosphere through the inlet port to create a swirling flow in the liner. This is measured by a fan anemometer. The valve lift is varied in steps. The measured rate of airflow is Q m/s. A diesel engine of swept volume, V would inhale air at a rate of V per one stroke (i.e.) V per half revolution, i. e., 2 V per revolution in a steady rig. If the engine speed is n rpm, the engine flow rate will be nV/30. The ratio of speed of air rotor to the engine speed is defined as the swirl number.

$$swirl\ \ number at a\ valve\ lift = \frac{anemometer\ speed \times V}{30\,Q} \tag{A.12}$$

A valve lift history typical of diesel engines is used to calculate the integrated swirl number at the end of the inlet stroke. This value is the characteristic swirl number of a diesel engine.

Appendix VI: Momentum of Useful Air of the Three Different Combustion Cavities Described in Kuo *et al.* (1988)

.	Type	Speed	Momentum of useful air (x 1E4) (kg m/s)	Total fuel Momentum (× 1 E4) (kgm/s)	ISFC (g/kW – h)	EIC (g/kg fuel)
1.	R	1,000	2.46	1.25	185	1.48
2.		1,300	3.36	1.165	173	0.86
3.		1,500	3.87	1.305	174	1.01
4.		1,800	4.62	1.305	169	1.35
5.		2,400	5.9	1.195	171	3.86
6.	S1	1,000	2.7	1.07	174	0.66
7.		1,300	3.36	1.165	173	1.56
8.		1,500	3.89	1.435	170	1.06
9.		1,800	4.66	1.395	174	1.81
10.		2,400	6.29	1.275	177	7.34
11.	S2	1,000	1.80	1.09	189	0.7
12.		1,300	2.01	1.27	176	0.57
13.		1,500	2.38	1.305	176	0.65
14.		1,800	3.12	1.24	173	0.63

15.		2,400	4.03	1.3	175	2.58
16.	R	1,500	3.5	2.97	219	31.6
17.		1,500	3.5	1.91	188	7.58
18.		1,500	3.82	1.07	174	0.83
19.		1,500	2.87	0.705	174	0.68
20.	S1	1,500	3.87	2.89	198	9.7
21.		1,500	3.88	2.05	185	3.62
22.		1,500	3.88	1.115	169	0.86
23.		1,500	3.31	0.675	170	0.58
24.	S2	1,500	3.39	5.84	206	6.1
25.		1,500	3.39	1.91	186	1.57
26.		1,500	1.93	1.205	186	0.61
27.		1,500	1.93	0.67	184	0.96

Appendix VII: Momentum of Useful Air for Engines A8, B8, C8 and D8

Type	Speed (rpm)	Injector hole Size (mm)	No of Injector holes	Average injection velocity (m/s)	Total fuel momentum (kg m/s)	Useful mass (kg)	Velocity of solid rotor at bowl (rad m/s)	ISFC (g/kW h)	EIC (g/kg fuel)
A8	2,200	0.22	4	159	2.08E-3	1.4E-4	36	183	2.316
B8	1,500	0.28	4	150	5.98E-3	5E-4	32	177	0.570
	2,000			165	6.57E-3		42.5	175	0.210
	2,000			171	6.98E-3		42.5	174	0.620
	2,200			165	6.71E-3		46.7	173	1.660
	2,500			187	7.51E-3		53.1	178	0.631
	2,500			190	8.25E-3		53	180	2.436
C8	2,000	0.28	4	168	7.63E-3	6.4E-4	50	174	1.629
	2,050			177	6.7E-3		51	174	0.647
	1,600			151	8 E-3		40	191	2.460
	1,200			152	8.9E-3		30	201	4.098
D8	2,013	0.25	5	180	4.31E-3	3.85E-4	30.0	181	0.831
	2,042			177	3.98E-3		30.5	181	0.503
	2,051			157	2.99E-3		30.6	175	0.442
	1,800			149	3.51E-3		26.8	176	1.206
	1,607			172	4.12E-3		24.0	182	0.718
	1,200			178	4.36E-3		17.9	198	1.389

Appendix VIII: Estimation of Spray Properties and Impingement Parameters

From Lakshminarayanan and Dent (1983),

$$\text{Penetration of free spray } s = \sqrt{8 C_d u_{inj} d_e t_{soi}} \left(\frac{T_o}{T_{surr}} \right)^{\frac{1}{4}} \quad \text{(A.13)}$$

Penetration of free spray with swirl (Heywood 1988),

$$\frac{s_{sn}}{s} = \left(1 + \frac{\pi n_{sn} Ns}{30 u_{inj}} \right) \quad \text{(A.14)}$$

$$\text{Penetration of wall spray, } S_{wall} = 0.75 \sqrt{u_{inj} d_e t_{imp}} \left(\frac{T_o}{T_{surr}} \right)^{\frac{1}{4}} \quad \text{(A.15)}$$

Here,

s	=	Penetration of spray
u_{inj}	=	Velocity of fuel jet at the exit of the nozzle
d_e	=	Equivalent diameter of orifice = do (ρ f /ρ a) 1/2
d_o	=	Diameter of nozzle hole
ρ_f	=	Density of fuel
ρ_a	=	Density of charge air
t_{soi}	=	Time after start of injection
T_{ref}	=	Reference temperature, 294 K
T_{surr}	=	Surrounding temperature
C_d	=	Coefficient of discharge of the nozzle
s_{sn}	=	Penetration of spray
R_{sb}	=	Radius of combustion cavity
N	=	Speed of engine
t_{imp}	=	Time at which impingement occurs

Similarly, the impingement distance available can be calculated by using a simple geometric correlation as follows (Fig. A.2),

$$s_{wall} = \left(\frac{R_{sb}}{\sin \theta} \right) \quad \text{(A.16)}$$

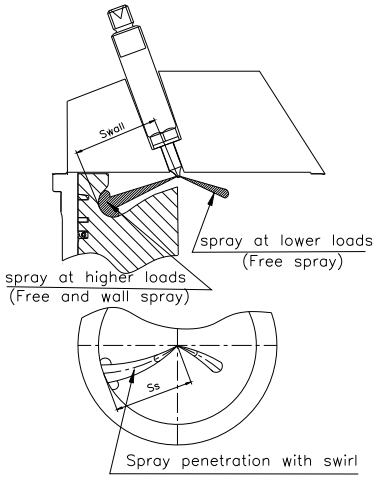

Fig. A.2 Comparison of engine sprays

Where, S_{wall} = Penetration of wall spray

θ = Half spray angle

The duration of injection is calculated from injection pressure diagrams. The time in crank degrees required for impingement is evaluated by comparing the spray penetration with impingement distance,

$$S_{sn} = S_{wall} \tag{A.17}$$

Differentiating equations (A.13) and (A.15), we obtain the velocity of the free spray and wall jet as follows,

$$u_{free} = \sqrt{8 C_d u_{inj} d_e} \frac{1}{2\sqrt{t_{soi}}} \left(\frac{T_o}{T_{surr}} \right)^{\frac{1}{4}} \tag{A.18}$$

$$u_{wall} = 0.75\sqrt{u_{inj} d_e} \frac{1}{2\sqrt{t_{imp}}} \left(\frac{T_o}{T_{surr}} \right)^{\frac{1}{4}} \tag{A.19}$$

In other words, the kinetic energy input to the portion of the fuel in the wall jet is less by a factor, C_{wall} given by the ratio of the kinetic energy of the spray along the wall and the free spray.

$$C_{wall} = \left(\frac{u_{wall}}{u_{free}} \right)^2 \tag{A.20}$$

Appendix IX: Calculation of Fuel Injection Rate

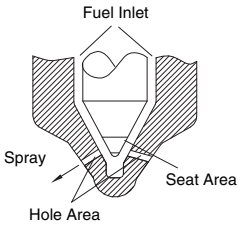

Fig. A.3 Flow area available for fuel flow

The rate of injection can be obtained by simulation of the fuel injection equipment or using sophisticated devices. Alternatively, it can be obtained from experimental data if available, as in case of engines studied in the present work. The instantaneous flow area around the needle seat obtained from the measured needle lift and the total area of the spray-holes are considered as two orifices in series as shown in Fig. A.3. Then fuel line pressure, cylinder pressure and needle lift are considered as inputs for further analysis. A typical measurement of fuel pressure, cylinder pressure and needle lift for a data point is shown in Fig. A.4.

The rate of fuel injection at any instant is calculated using the effective area of flow through the two orifices A_n, and the pressures at the injector entry, P_f and measured in the cylinder P_{cyl}. A flow coefficient, C_d of 0.7 is reasonable for the spray holes.

The instantaneous injection rate, $dm_f/d\theta$

$$\frac{dm_f}{d\theta} = c_d \, \rho_f \, A_n \sqrt{\frac{2\left(P_f - P_{cyl}\right)}{\rho_f}} \tag{A.21}$$

In the present work, the heat release rate is modelled as a strong function of the rate of fuel injection. Therefore, the accuracy of estimation of the fuel injection rate is important, especially in the first regime of combustion.

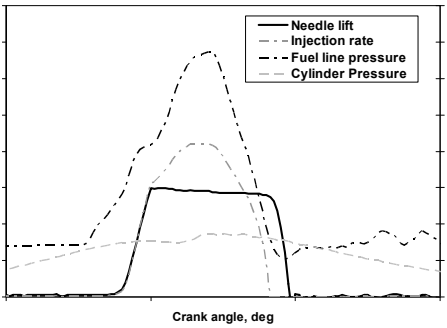

Fig. A.4 Experimental estimation of injection rate

Appendix X: Influence of Nozzle Features

The terms 'KF' and 'HE' used in this thesis refer to spray hole-manufacturing signatures of nozzles (Fig. A.5). The nozzles with conical spray holes are termed as k-Factor (KF) nozzles. Sometimes the spray holes are finished by hydro grinding process, know as hydro-erosion, HE. In case of VCO nozzle, the spray holes are on seat of needle. Therefore, they have lesser discharge coefficient and larger flow variations. The smoother entry of spray in the holes improves discharge coefficient of the spray holes. In addition, the hydro-grinding process is with close loop control that reduces nozzle-to-nozzle variation.

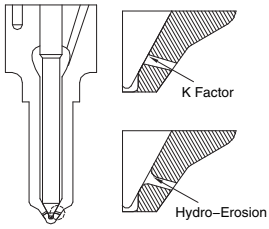

Fig. A.5 Explanation of KF and HE nozzles

The nozzles hole is defined as base orifice size with % HE or k-Factor. This effect is considered as enlargement of orifice diameter over base diameter.

$$N_f = HE \text{ or } N_f = \frac{k_{Factor}}{10} \tag{A.22}$$

The HE and k-Factor are defined below:

$$\%HE = \frac{flow\ \ after\ \ HE - flow\ \ before\ \ HE}{flow\ \ before\ \ HE} \tag{A.23}$$

$$k\ Factor = \frac{d_{inlet} - d_{outlet}}{10\mu m} \tag{A.24}$$

Example 1: Base hole-size is 0.19 mm with HE of 10.5%. Then effective area of nozzle, A_o;

$$A_o = \frac{\pi\, d_o^2\,(1 + N_f)}{4} = \frac{\pi\, 0.19^2\,(1 + 0.105)}{4} \tag{A.25}$$

Example 2: Base hole-size is 0.19 mm with k-Factor of 1.5. Then effective area of nozzle, A_o;

$$A_o = \frac{\pi\, d_o^2\,(1 + N_f)}{4} = \frac{\pi\, 0.19^2\,(1 + 0.15)}{4} \tag{A.26}$$

Appendix XI: Henry's Constant Hc for Fuel (n-Octane) in Oil

Following Kaiser *et al.* (1980), the engine lubricant was assumed to be Squalane (C_{30} H_{62}), which closely resembled the base hydrocarbon of the SAE 5W20 oil, used by them in their bomb experiments, because of availability of data for HC for various paraffins dissolved in Squalane over a range of temperatures (Chappelow and Praushnitz 1974). Unfortunately, no values are reported for any paraffin beyond a-butane. Therefore, the following procedure was adopted for determining HC for n-octane in Squalane. The data from reference (Table I, Chappelow and Praushnitz 1974) was plotted as $\log_e$ (HC) against molecular weight of the paraffin listed over the temperature range of the data. The result is shown in Fig. A.6. The data show an approximately linear variation of Log $_{10}$ (HC) with molecular weight at constant temperature. The value of HC for octane in Squalane was obtained by extrapolation.

It is recognized that the process of extrapolation is prone to error and that the use of n-octane as the fuel instead of iso-octane, which is more representative of commercial fuel, could introduce some error due to their differing solubility. However, in the absence of any more representative data the extrapolation procedure was adopted, and HC obtained by this procedure for n-octane in Squalane over a range of temperatures is shown plotted in Fig. A.7. It can be expressed as:

$$\log_{10}(HC) = -1.921 + 0.013\,(T - 300) \tag{A.27}$$

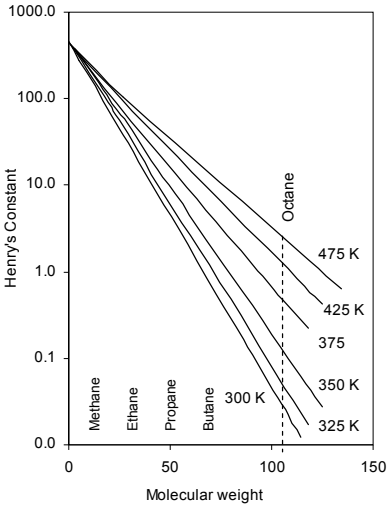

Fig. A.6 Variation of Henry's constant for range of paraffins dissolved in Squalane (C_{30} H_{62}) (Data from Chappelow and Praushnitz 1974)

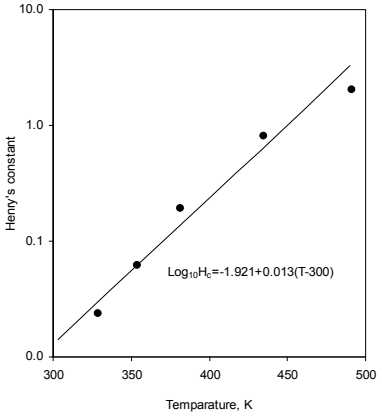

Fig. A.7 Variation of Henry's constant with temperature for Octane dissolved in Squalane (C_{34} H_{62})

Appendix XII: Evaluation of g_F^* and g_G^*

Molecular diffusion through the effective penetration depth is assumed. Hence:

$$g_F^* = \frac{\rho D}{\delta} \tag{A.28}$$

where D is the mass diffusion coefficient for fuel vapour in oil and is taken from reference (Kaiser *et al.* 1982).

$$D = 7.4\times10^{-8} M^{0.5} T V^{-0.6} \mu^{-1} \quad cm^2\ s^{-1} \tag{A.29}$$

Here, M = Molecular weight of oil
= 422
V = Molar volume of fuel vapour
= 176 cm^3/ mole
T = Temperature K
μ = Absolute viscosity of oil centipoise

Here, μ is obtained from Walther's equation (Schilling 1968) which can be expressed as

$$\log_{10}\left[\log_{10}\left(\mu/\rho + 0.6\right)\right] = 7.686 - 3.01\log_{10}\tau \tag{A.30}$$

Evaluation of g_G* was obtained from assuming the Reynolds Analogy between heat and mass transfer which implies a Levis Number of unity under these conditions.

$$g_G^* = h / C_p \tag{A.31}$$

Here, h is heat transfer coefficient evaluated from Woschni's correlation (1967). Of particular interest here, is the velocity term in the Woschni's equation:

$$\left[C_1 U_P + C_2 \frac{V_s T_1}{P_1 V_1}\left(P - P_o\right)\right] \quad m\ s^{-1} \tag{A.32}$$

Here, C_1 and C_2 are constants: U_p is the mean piston speed; V_s the cylinder volume; P_1, V_1 and T_1 are pressure, volume and temperature at some reference state in the engine cylinder. ($P - P_o$) is the difference between the fired and motored cylinder pressure at any crank angle. For the same engine speed, the influence of gas motion due to change of intake valve geometry, will result in changes in h and g* through ($P - P_o$).

Appendix XIII: In-Cylinder Oxidation of HC

The choice of a limiting temperature of 1,100 K above which oxidation of fuel desorbed from the oil film can be considered complete is justified as follows. It is

assumed that the fuel desorbed into the burned gas zone remains in the boundary layer at a film temperature, which is the mean of the burned gas temperature (T_b) and the will temperature (T_w). The concentration of oxygen (m_{O2}) in the boundary layer is assumed what remains after stoichiometric combustion in the bulk of the burned gas zone, and for a lean mixture can be expressed as:

$$m_{o_2} = 0.23\left[(A/F) - (A/F)_{ST}\right]/\left[1 + A/F\right] \tag{A.33}$$

When the mixture is rich $m_{O2} = 0$.

A/F is the overall engine air fuel ratio and the subscript ST refers to a stoichiometric mixture.

The net rate of increase of fuel in the boundary layer (dm_{net}/dt) is the difference between rates of that desorbed (dm_D/dt) and oxidized (dm_{net}/dt). The net incremental fuel mass over a time step Δt can be expressed as:

$$m_{nett_{t+\Delta t}} = \left[\left(m_{D_{t+\Delta t}} - m_{D_t}\right) + m_{nett_t}\right] - dm_c/dt.\,\Delta t \tag{A.34}$$

Here, $\dfrac{dm_c}{dt} = \dfrac{d[HC]}{dt}\,(Boundary\ layer\ volume \times Molecular\ weight\ of\ fuel)$ (A.35)

The oxidation of hydrocarbon $d[HC]/dt$ is considered to be represented by the rate equation used by Lavoie and Blumberg (1980) for HC oxidation which has the form

$$\frac{d[HC]}{dt} = C_R\, A[O_2] \exp\left[\frac{-E}{RT}\right] \quad moles\,cm^{-3}\,s \tag{A.36}$$

Here, $C_R = 2$

$A = 6.7 \times 1015$ cm^3/mols

and $E = 37{,}230$ cal/mol.

$[HC] = m_{net}$ / [Boundary Layer Volume × Molecular weight of Fuel]
moles cm^{-3}

$[O_2]$ in moles/cm^3 is obtained from the oxygen mass fraction m_{O2} and the burned gas volume.

Figure A.8 shows the rates of desorption and oxidation plotted against film temperature and crank angle, for the baseline operating condition, While Fig. A.9 shows the variation in total HC against the same ordinates

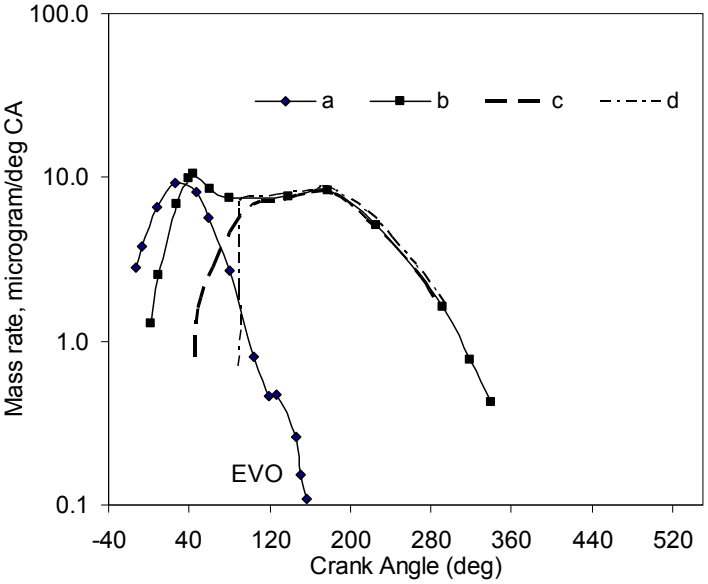

Fig. A.8 Rates of absorption and desorption, oxidation and net in-cylinder HC accumulation, b = HC desorbed by oil , c = HC desorbed – HC oxidized according to Arrhenius relation ship, d = HC desorbed – HC modeled to oxidize if temperature is beyond 1,000 K and not oxidized if the temperature is less than 1,000 K

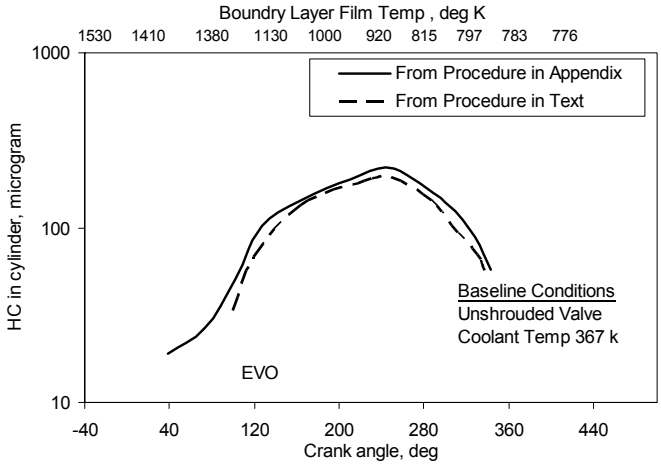

Fig. A.9 Comparison of simple HC oxidation assumption and approximate desorption oxidation model

Also plotted is the net fuel (HC) present in the cylinder based on the assumption that all HC desorbed when the film temperature is above 1,100 K is completely oxidized. It will be seen that this assumption is quite reasonable.

Appendix XIV: Estimation of Wall Surface Temperature

It is known (Lavoie *et al.* 1980, Wentworth 1968) that cylinder wall temperature strongly affects HC emission from an engine. This effect is discussed in the paper in relationship to the Henry Number, which increases with increasing temperature, and the direct effect of temperature on oil film thickness through the kinematic viscosity of the oil.

The cylinder wall temperature is highest near the head and lowest at the crankcase. To obtain a representative cylinder wall temperature for use in the model, the cycle average of the cylinder wall area in contact with the cylinder charge (A) is computed. The total heat loss per cycle $\oint \dot{Q}\, dt$ is computed and the heat transfer conductance of the cylinder liner and the coolant U, is taken from Lavoie *et al.* (1980) and has a value of 1.89 kW/m^2 K.

$$\therefore T_{wall} = T_{coolant} + \frac{1}{\tau}\frac{\oint \dot{Q}\, dt}{\bar{A}U} \tag{A.37}$$

Here τ = the cycle time

$$A = \oint \sum_i A_i dt \tag{A.38}$$

A_i = the instantaneous area of sleeve in contact with zone i.

$$\dot{Q} = \sum_i \dot{q}''_i A_i \tag{A.39}$$

Here $\dot{q}_i''$=the instantaneous heat flux from zone i across the cylinder liner and is estimated from Woschni's correlation (1967).

In order to compute T_{wall} instantaneous heat fluxes and dress must be available. Therefore, a wall temperature of 450 K was initially assumed to obtained values of A_i and $\dot{q}_i''$ to start the interaction.

Appendix XV: Experimental Data on HC Emissions from DI Diesel Engines

Engine	Speed	Power	Fuel injected (mg)		HC measured		Air-fuel ratio	delay
	rpm	kW	per cycle	During delay	ppm	mg/cycle/cylinder		(ms)
A10	1,400	39.7	43.70	13.10	250	0.12	21.58	0.71
	1,400	31.0	37.90	17.00	212	0.11	24.88	0.77
	1,400	20.7	27.00	17.30	211	0.11	34.93	0.77
	1,500	42.5	46.90	13.90	238	0.12	19.88	0.56
	1,500	33.1	32.70	14.30	225	0.11	28.51	0.56
	1,500	22.1	30.30	20.30	205	0.10	30.77	1.22
	2,200	55.5	43.50	14.10	307	0.15	21.13	0.45
	2,200	38.8	31.00	14.90	252	0.12	29.65	0.38
	2,200	26.7	16.90	10.20	263	0.13	54.39	0.53
	2,200	4.9	10.40	8.50	346	0.17	88.38	0.64
	2,300	56.1	45.70	16.80	206	0.10	19.88	0.54
	2,300	38.0	29.60	12.30	237	0.12	30.69	0.62
	2,300	25.4	16.50	9.40	266	0.13	55.05	0.36
	2,300	4.9	12.20	8.30	387	0.19	74.46	0.54
	2,500	56.8	40.90	12.50	208	0.10	21.95	0.47
	2,500	27.6	16.70	10.20	258	0.12	53.75	0.53
	2,500	5.5	11.40	10.40	384	0.18	78.74	0.73
B10	2,200	48.5	47.32	5.49	190	0.13	30.30	0.53
	2,200	72.8	67.28	4.32	162	0.12	24.60	0.46
	1,500	60.6	72.88	3.54	121	0.10	23.20	0.56
	1,500	49.6	57.80	3.96	149	0.11	28.80	0.67
	1,500	33.0	40.60	6.75	168	0.11	37.70	0.78
	1,500	11.0	15.92	3.40	193	0.11	59.40	0.78
C10	2,210	60.6	64.10	32.20	305	0.27	22.66	1.02
	2,211	46.6	49.80	34.80	383	0.31	29.17	1.13
	2,207	31.6	34.90	31.00	405	0.30	41.62	1.10
	2,204	0.0	16.40	16.40	646	0.40	50.24	1.21
	1,508	46.1	70.20	36.50	346	0.26	19.15	1.33
	1,507	35.8	53.90	38.70	374	0.26	24.94	1.38
	1,500	24.3	41.60	39.10	361	0.23	32.31	1.50
	610	0.0	78.60	78.60	447	0.22	15.39	4.37
D10	2,000	23.1	32.50	25.80	560	0.22	23.69	1.04
	2,000	17.6	26.60	22.30	520	0.20	28.95	0.92
	2,000	11.8	24.00	19.50	480	0.18	32.08	1.04
	2,000	5.9	21.10	18.20	620	0.23	36.49	0.92

	1,319	8.7	29.10	22.80	480	0.19	26.63	0.95
	1,298	17.8	48.70	36.70	690	0.29	15.91	1.28
	1,300	12.9	28.50	24.70	540	0.22	27.19	0.83
E10	1,500	86.2	50.80	27.50	113	0.23	28.10	1.11
	1,500	57.6	34.10	27.90	136	0.24	34.80	1.28
	1,500	29.7	21.60	21.40	208	0.33	50.00	1.39
	1,500	8.6	12.20	12.10	232	0.34	72.50	1.44
F10	1,500	39.0	27.90	23.00	565	0.24	26.70	1.28
	1,500	25.8	20.30	19.50	583	0.25	38.60	1.33
	2,500	78.7	39.40	26.70	214	0.09	19.02	0.53
	2,500	37.7	20.70	15.80	473	0.20	37.40	0.57
	2,500	9.0	8.30	8.00	470	0.20	78.20	0.60
G10	1,600	90.4	65.00	14.30	65	0.05	21.61	1.33
	2,500	115.4	86.00	3.10	60	0.06	13.95	0.67
H10	700	–	17.14	15.00	400	0.46	138.90	2.02
	1,300	–	17.17	15.00	500	0.57	138.90	1.47
	1,300	–	17.18	14.00	400	0.46	138.80	1.41
	1,300	–	17.17	9.00	150	0.17	138.80	1.09
	1,300	–	17.17	13.00	250	0.29	138.80	1.35
	1,300	–	17.17	15.00	450	0.52	138.80	1.47
	1,300	–	17.17	14.00	510	0.59	138.80	1.46
	1,300	–	25.13	10.00	200	0.23	95.00	1.31

References

Chappelow CC, Praushnitz JM (1974) Solubilities of Gases in High Boiling Hydrocarbon Solvents. AIChE Journal 20

Dent JC, Keightley JD, DeBoer CD (1977) Application of interferometry to air fuel measurements. SAE Paper No. 770825

Heywood JB (1988) A text book on Internal Combustion engine fundamentals. McGraw-Hill International edition

Kaiser EW, Adamczyk AA, Lavoie GA (1980) The Effect of Oil Layers on the Hydrocarbon Emissions Generated During Closed Vessel Combustion. 18th International Symposium on Combustion

Kaiser EW, Lorusso JA, Lavoie GA, Adamczyk AA (1982) The Effect of Oil Layers on the Hydrocarbon Emissions from Spark Ignited Engines. Combust. Sci. Technol., 28

Kuo TW, Henningsen S, Wu KJ (1988) Evaluation of four mixing correlations for performance and soot emission characteristic of a small open chamber diesel engine. SAE 880599

Lakshminarayanan PA, Dent JC (1983) Interferometric Studies of Vapourising and Combusting Sprays. SAE 830244

Lavoie GA, Blumberg PN (1980) A Fundamental Model for Predicting Fuel Consumption NO and HC Emissions of the conventional Spark Ignition Engine. Combust. Sci. Technol., 21

Lavoie GA, Lorusso JA, Adamczyk AA (1980) Hydrocarbon Emissions Modelling for Spark Ignition Engines. Symposium on Combustion Modelling in Reciprocating Engines, General Motors Research Laboratories, Nov 1978. Plenum Press, London

Schilling A (1968) Motor Oils and Engine Lubrication. Scientific Publications (GB) Ltd

Spalding DB (1977) Combustion and Mass transfer. chapters 4, 6, 11, Pergamon Press, Oxford
von Thien (1965) Entwicklungsarbeiten an Ventilkanalen von Viertakt Dieselmotoren. Osterreichen Ingenieur Zeitschrift, Heft 9, Jg 8, Springer
Wentworth JT (1968) Piston and Ring Variables Affect Exhaust Hydrocarbon Emissions. SAE 680109, SAE Transactions 77
Woschni G (1967) A Universally Applicable Equation for the Instantaneous Heat Transfer Coefficient in the Internal Combustion Engine. SAE 670931, SAE Transactions 76

Index